

**QUANTITATIVE DROUGHT RECONSTRUCTION IN THE PACIFIC NORTHWEST
FROM LAKE SEDIMENT RECORDS AND PREDICTIVE MODELS**

by

Byron Anthony Steinman

Arts Bachelor, Harvard University, 2000

Submitted to the Graduate Faculty of
Arts and Sciences in partial fulfillment
of the requirements for the degree of
Doctor of Philosophy

University of Pittsburgh

2011

UNIVERSITY OF PITTSBURGH
SCHOOL OF ARTS AND SCIENCES

This dissertation was presented

by

Byron Anthony Steinman

It was defended on

April 1st, 2011

and approved by

Daniel J. Bain, Assistant Professor, Geology and Planetary Science

William Harbert, Professor, Geology and Planetary Science

Michael F. Rosenmeier, Assistant Professor, Geology and Planetary Science

Dissertation Advisor: Mark B. Abbott, Associate Professor, Geology and Planetary Science

Copyright © by Byron Anthony Steinman

2011

QUANTITATIVE DROUGHT RECONSTRUCTION IN THE PACIFIC NORTHWEST FROM LAKE SEDIMENT RECORDS AND PREDICTIVE MODELS

Byron Anthony Steinman, PhD

University of Pittsburgh, 2011

Water resources in the American west are under mounting stress due to increasing demand, receding glaciers, and diminishing winter snowpack amounts. By understanding past aridity patterns, we can improve the ability of global climate models to predict regional hydroclimatic conditions in the coming decades and centuries. Such forecasting is critical to the development of sound water allocation policies. To produce accurate forecasts, global climate models rely on paleo-proxy evidence to constrain climate parameters that govern, for example, important potential changes in the El Niño Southern Oscillation and its associated impacts on extratropical precipitation and drought patterns in response to future anthropogenic climate forcing. Lake sediment oxygen isotope records are one such form of paleo-proxy evidence, providing valuable information about past climatic conditions on time scales ranging from years to millennia. Here a numerical lake-catchment model defined by a system of twelve ordinary differential equations is developed and used to describe the physical processes controlling lake-catchment hydrology and oxygen isotope dynamics. This model is applied to Castor Lake and Scanlon Lake, central Washington, and used to conduct simulations designed to characterize lake hydrologic and isotopic responses to mean state and stochastic hydroclimatic variability. Ultimately, the Castor Lake sediment oxygen isotope record is interpreted using an ensemble of Monte Carlo lake model simulations to produce a probabilistic, quantitative reconstruction of precipitation amounts over the past 1500 years. This reconstruction indicates that the Medieval

Climate Anomaly (MCA) (950–1250 BP) was a relatively wet period and that the Little Ice Age (LIA) (1450–1850 BP) was relatively dry, suggesting that the MCA was characterized by a La Niña like state of the tropical Pacific and the LIA was characterized by El Niño like conditions. These results are the first quantitative, probabilistic estimate of paleo-precipitation using lake sediment oxygen isotope records from the interior Pacific Northwest, and will provide a resource for the parameterization of climate models designed to investigate future Pacific Ocean responses to anthropogenic forcing and the associated influence on aridity patterns in the American west.

TABLE OF CONTENTS

1.0	THE ISOTOPIC AND HYDROLOGIC RESPONSE OF SMALL, CLOSED-BASIN LAKES TO CLIMATE FORCING FROM PREDICTIVE MODELS: APPLICATION TO PALEOCLIMATE STUDIES IN THE UPPER COLUMBIA RIVER BASIN	1
1.1	INTRODUCTION	3
1.2	METHODS	5
1.2.1	Study sites	5
1.2.2	Model structure	8
1.2.3	Hydrologic mass-balance equations	10
1.2.4	Infiltration, runoff, and inflow model sub-routines	12
1.2.5	Lake mixing model and outseepage sub-routines	14
1.2.6	Lake evaporation and catchment evapotranspiration model sub-routines	16
1.2.7	Isotope mass balance equations	17
1.2.8	Model inputs	19
1.2.9	Lake and climate monitoring data	20
1.3	RESULTS	21
1.3.1	Seepage estimation simulations	21

1.3.2	Catchment model calibration.....	23
1.3.3	Model sensitivity to climate variables	26
1.3.4	Temperature sensitivity tests	26
1.3.5	Relative humidity sensitivity tests	27
1.3.6	Precipitation sensitivity tests.....	28
1.4	DISCUSSION.....	29
1.4.1	The influence of hypsography and seepage on lake water $\delta^{18}\text{O}$ values..	29
1.4.2	Residence time response to hydrologic forcing	31
1.4.3	Seepage model considerations.....	32
1.5	CONCLUSIONS.....	34
2.0	THE ISOTOPIC AND HYDROLOGIC RESPONSE OF SMALL, CLOSED-BASIN LAKES TO CLIMATE FORCING FROM PREDICTIVE MODELS: SIMULATIONS OF STOCHASTIC AND MEAN STATE PRECIPITATION VARIATIONS.....	36
2.1	INTRODUCTION	37
2.2	METHODS.....	39
2.2.1	Study sites and regional climate	39
2.2.2	Model structure.....	40
2.2.3	Mean state precipitation forcing simulation structure.....	41
2.2.4	Stochastic precipitation forcing simulation structure	41
2.3	RESULTS	43
2.3.1	Simulation of mean state precipitation forcing.....	43
2.3.2	Simulation of combined mean state and stochastic precipitation forcing.	

	44
2.3.3	Simulation of combined mean state and stochastic precipitation forcing within hypothetical lakes.....	50
2.3.4	Simulation of variance changes in stochastic precipitation forcing.....	56
2.4	DISCUSSION.....	56
2.4.1	Lake responses to mean state precipitation forcing.....	56
2.4.2	Lake responses to combined mean state and stochastic precipitation forcing	57
2.4.3	Hypothetical lake responses to combined mean state and stochastic precipitation forcing	59
2.4.4	Lake responses to variance changes in stochastic precipitation forcing	60
2.5	CONCLUSIONS.....	61
2.5.1	Implications for paleoclimate studies.....	61
3.0	HYDROLOGIC AND ISOTOPE MASS BALANCE MODEL SIMULATIONS OF LAKE OUTSEEPAGE AND IMPLICATIONS FOR LAKE RESPONSES TO HYDROCLIMATIC VARIATIONS	64
3.1	INTRODUCTION	65
3.2	METHODS.....	67
3.2.1	Model development, study sites, and regional climate	67
3.2.2	Process based outseepage submodel structure	67
3.2.3	Altered hypsography simulations.....	68
3.2.4	Steady state simulation structure	69
3.3	RESULTS.....	70

3.3.1	Volumetric outseepage submodel configuration	70
3.3.2	Exponential outseepage configuration 1	71
3.3.3	Exponential outseepage configuration 2	73
3.3.4	Exponential outseepage configuration 3	74
3.3.5	Alternate hypsography configuration	76
3.4	DISCUSSION.....	77
3.4.1	The volumetric configuration	77
3.4.2	Exponential configurations	78
3.4.3	Transient $\delta^{18}\text{O}$ responses	80
3.4.4	Future work.....	80
3.5	CONCLUSIONS.....	81
4.0	SMALL LAKE ISOTOPIC AND HYDROLOGIC RESPONSES TO 20 TH CENTURY CLIMATE VARIABILITY: COMPARISON OF OBSERVED AND MODELED SEDIMENT CORE OXYGEN ISOTOPE RECORDS AND LAKE LEVEL VARIATIONS.....	83
4.1	INTRODUCTION	83
4.2	METHODS.....	85
4.2.1	Study sites and regional climate	85
4.2.2	Lake and catchment elevation maps	85
4.2.3	CL sediment core recovery and sampling	87
4.2.4	CL sediment core chronology	88
4.2.5	SL sediment core recovery and sampling.....	88
4.2.6	SL sediment core chronology.....	95

4.2.7	Model structure.....	95
4.2.8	20 th century weather datasets	98
4.2.9	20 th century simulations	102
4.3	RESULTS	102
4.3.1	Castor Lake age model.....	102
4.3.2	Scanlon Lake age model.....	104
4.3.3	Modeled and orthophotograph derived lake surface elevation changes (1945–2007).....	105
4.3.4	Modeled lake level changes (1900–2007).....	107
4.3.5	Measured 20 th century $\delta^{18}\text{O}$ records.....	108
4.3.6	Modeled 20 th century $\delta^{18}\text{O}$ records	110
4.4	DISCUSSION.....	111
4.4.1	CL authigenic carbonate formation	111
4.4.2	SL authigenic carbonate formation.....	113
4.4.3	Model accounting for the timing of authigenic carbonate formation ..	113
4.4.4	Comparison of observed and modeled lake surface elevation	114
4.4.5	The influence of precipitation and temperature on lake level	115
4.4.6	The influence of stochastic variance on long term lake levels and $\delta^{18}\text{O}$ values.....	116
4.4.7	Comparison of observed and modeled $\delta^{18}\text{O}$ records.....	117
4.5	CONCLUSIONS	118
5.0	SMALL LAKE ISOTOPIC AND HYDROLOGIC RESPONSES TO 20TH CENTURY CLIMATE VARIABILITY: SIMULATIONS OF MEAN STATE AND	

STOCHASTIC CLIMATE VARIATIONS WITH NON-CONSTANT INITIAL CONDITIONS.....	119
5.1 INTRODUCTION	119
5.2 METHODS.....	121
5.2.1 Study sites	121
5.2.2 Model structure.....	121
5.2.3 Mean state RH, temperature, and precipitation forcing simulations ..	122
5.2.4 Stochastic temperature and precipitation forcing simulations.....	123
5.2.5 Initial condition forcing simulations	125
5.3 RESULTS	126
5.3.1 Simulations of mean state change in hydroclimate.....	126
5.3.2 Simulations of variations in stochastic temperature.....	127
5.3.3 Simulations of variations in stochastic precipitation.....	129
5.3.4 Initial condition sensitivity simulations (mean state)	130
5.3.5 Initial condition sensitivity simulations (random)	133
5.4 DISCUSSION.....	133
5.4.1 Simulations of mean state variations in RH, temperature, and precipitation.....	133
5.4.2 Simulations of variations in stochastic RH, temperature, and precipitation.....	140
5.4.3 Simulations of unknown initial conditions	142
5.5 CONCLUSION	145

6.0	CENTURY SCALE PRECIPITATION IN THE PACIFIC NORTHWEST FROM OXYGEN ISOTOPES IN LAKE SEDIMENT.....	148
6.1	INTRODUCTION	148
6.1.1	Study sites	153
6.2	DISCUSSION AND CONCLUSIONS.....	155
6.3	MATERIALS AND METHODS.....	161
6.3.1	Castor Lake model structure	161
6.3.2	Hydrologic mass-balance equations	162
6.3.3	Isotope mass-balance equations.....	164
6.3.4	Removal of source water $\delta^{18}\text{O}$ influences	165
6.3.5	Authigenic carbonate formation.....	165
6.3.6	Lime Lake sediment core recovery and sampling	167
6.3.7	Lime Lake chronology	168
6.3.8	Lime Lake $\delta^{18}\text{O}$ record.....	169
6.3.9	20th century weather datasets	171
6.3.10	Monte Carlo simulations	172
6.3.11	Monte Carlo results and comparison to 20th century observations	178
	BIBLIOGRAPHY	181

LIST OF TABLES

Table 1.1	CL and SL hydrologic model parameters and initial values for the continuous input (2005–2008) simulations	6
Table 1.2	Monthly model input data.....	8
Table 1.3	Model variables and parameters	9
Table 1.4	Relative humidity and temperature sensitivity test results	27
Table 2.1	Average summer lake variables for each simulation period in response to stochastic variations and changes in mean state precipitation.....	50
Table 4.1	Air photo data	87
Table 4.2	Observed and modeled 20 th century lake surface elevation and volume data	106
Table 4.3	20 th century lake model simulation results	108
Table 5.1	20 th century steady state and stochastic climate change simulation data.....	127
Table 5.2	Initial condition sensitivity simulation data.....	136
Table 6.S1	Lime Lake age model data.....	168

LIST OF FIGURES

Figure 1.1	Map of Washington State showing the approximate location of the study area. Topography of the Castor and Scanlon Lake catchments and surrounding area	5
Figure 1.2	Global meteoric water line, measured $\delta^{18}\text{O}$ and δD values for Castor Lake and Scanlon Lake surface waters and local meteoric waters	7
Figure 1.3	Simulated Castor Lake steady state water $\delta^{18}\text{O}$ and lake-level change with and without delayed catchment water inflow.....	22
Figure 1.4	Simulated Scanlon Lake steady state water $\delta^{18}\text{O}$ and lake-level change with and without delayed catchment water inflow.....	23
Figure 1.5	Castor Lake and Scanlon Lake calibrated, uncalibrated, and measured lake surface water $\delta^{18}\text{O}$ and δD values between August 2005 and October 2008	24
Figure 1.6	Castor Lake and Scanlon Lake average summer month surface water $\delta^{18}\text{O}$ values and lake levels from precipitation sensitivity tests.....	28
Figure 1.7	Scanlon Lake responses to a 50% decrease and a 50% increase in precipitation	31
Figure 1.8	Castor Lake responses to a 50% decrease and a 50% increase in precipitation.....	32
Figure 1.9	Scanlon Lake responses to a 50% decrease in precipitation and increased outseepage. Castor Lake responses to a 50% increase in precipitation and altered hypsography	33

Figure 2.1	Depth and lake water $\delta^{18}\text{O}$ value changes at SL and CL in response to mean state precipitation changes	44
Figure 2.2	SL responses to the superimposition of stochastic variations and a mean state precipitation decrease of 50%	46
Figure 2.3	SL responses to the superimposition of stochastic variations and a mean state precipitation increase of 50%	47
Figure 2.4	CL responses to the superimposition of stochastic variations and a mean state precipitation decrease of 50%	48
Figure 2.5	CL responses to the superimposition of stochastic variations and a mean state precipitation increase of 50%	49
Figure 2.6	CL2 responses to the superimposition of stochastic variations and a mean state precipitation increase of 50%	52
Figure 2.7	SL2 responses to the superimposition of stochastic variations and a mean state precipitation decrease of 50%	53
Figure 2.8	CL responses to changes in the variance of stochastic precipitation changes.....	54
Figure 2.9	SL responses to changes in the variance of stochastic precipitation changes	55
Figure 3.1	Exponential outseepage functions	68
Figure 3.2	Observed Castor Lake hypsography and adjusted Castor Lake hypsography data....	69
Figure 3.3	Volumetric (VOL) outseepage configuration results	71
Figure 3.4	EXP1 configuration results.....	72
Figure 3.5	EXP2 configuration results.....	74
Figure 3.6	EXP3 configuration results.....	75
Figure 3.7	EXP4 configuration results.....	76

Figure 3.8	Combined Castor Lake summer average lake level and $\delta^{18}\text{O}$ values from all simulations.....	77
Figure 4.1	Air photo of the Castor Lake catchment on 07/01/2006 superimposed with catchment topography and lake bathymetry (5 m contours).....	89
Figure 4.2	Air photo of the Castor Lake catchment on 07/03/1952 superimposed with catchment topography and lake bathymetry (5 m contours).....	90
Figure 4.3	Air photo of the Scanlon Lake catchment on 07/01/2006 superimposed with catchment topography and lake bathymetry (5 m contours)	91
Figure 4.4	Air photo of the Scanlon Lake catchment on 07/03/1952 superimposed with catchment topography and lake bathymetry (5 m contours)	92
Figure 4.5	Air photo of Castor Lake on 07/03/1952 and 07/01/2006 superimposed with catchment topography and lake bathymetry (0.5 m contours)	93
Figure 4.6	Air photo of Scanlon Lake on 07/03/1952 and 07/01/2006 superimposed with catchment topography and lake bathymetry (0.5 m contours)	94
Figure 4.7	Castor Lake and Scanlon Lake total and unsupported ^{210}Pb and ^{137}Cs activity values. Castor Lake age model. Scanlon Lake age model developed using ^{210}Pb , ^{137}Cs and ^{14}C	100
Figure 4.8	Local weather station data relationships.....	101
Figure 4.9	20 th century precipitation temperature values estimated for Castor and Scanlon lakes. Castor Lake and Scanlon Lake modeled 20 th century depth, monthly aragonite $\delta^{18}\text{O}$ values, and average June–September aragonite $\delta^{18}\text{O}$ values.....	103
Figure 4.10	Castor Lake and Scanlon Lake 20 th century modeled and observed water surface elevations and associated error estimates	107

Figure 4.11 Modeled and observed sediment $\delta^{18}\text{O}$ values for Castor Lake	109
Figure 4.12 Modeled and observed sediment $\delta^{18}\text{O}$ values for Scanlon Lake.....	110
Figure 5.1 Continuous 20 th century annual total precipitation and average temperature datasets applied in model simulations.....	124
Figure 5.2 CL average summer sediment $\delta^{18}\text{O}$ values from mean state sensitivity simulations	128
Figure 5.3 CL average summer depth values from mean state sensitivity simulations.....	129
Figure 5.4 SL average spring/summer sediment $\delta^{18}\text{O}$ values from mean state sensitivity simulations.....	131
Figure 5.5 SL average spring/summer depth values from mean state sensitivity simulations ..	132
Figure 5.6 CL and SL average spring/summer sediment $\delta^{18}\text{O}$ values from stochastic forcing simulations.....	134
Figure 5.7 CL and SL average spring/summer depth values from stochastic forcing simulations	135
Figure 5.8 CL average summer month $\delta^{18}\text{O}$ values from initial condition sensitivity simulations and observed sediment core $\delta^{18}\text{O}$ measurements	138
Figure 5.9 SL average spring/summer month $\delta^{18}\text{O}$ values from initial condition sensitivity simulations and observed sediment core $\delta^{18}\text{O}$ measurements.....	139
Figure 5.10 CL and SL average summer month depth values from initial condition sensitivity simulations.....	141
Figure 5.11 CL and SL average summer month $\delta^{18}\text{O}$ values from initial condition sensitivity simulations.....	143

Figure 5.12 CL and SL average summer month volume values from initial condition sensitivity simulations.....	145
Figure 6.1 PDSI reconstruction correlation map for the western United States.....	151
Figure 6.2 Castor Lake and Lime Lake sediment $\delta^{18}\text{O}$ records, the Castor Lake and Like Lake $\Delta\delta^{18}\text{O}$ record, and PDSI reconstruction data.....	152
Figure 6.3 SOI and PDO index values and associated precipitation amounts in eastern Washington. 20 th century $\Delta\delta^{18}\text{O}$ values related to precipitation amounts in eastern Washington.....	157
Figure 6.4 Niño3 and PDO reconstructions of Mann et al. (2009) compared to the lake sediment and model derived precipitation reconstruction	160
Figure 6.S1 Global meteoric water line, local evaporation line and water sample $\delta^{18}\text{O}$ measurements from the period of observation (2005–2011).....	154
Figure 6.S2 Lime Lake age model.....	169
Figure 6.S3 Monthly precipitation data applied in the Monte Carlo simulations.....	173
Figure 6.S4 Monthly temperature data applied in the Monte Carlo simulations.....	175
Figure 6.S5 Monthly relative humidity data applied in the Monte Carlo simulations	178
Figure 6.S6 $\delta^{18}\text{O}$ results from the Monte Carlo simulations	179
Figure 6.S7 Monte Carlo simulation results relating 20 year average $\Delta\delta^{18}\text{O}$ values to 20 year average winter/spring precipitation amounts.....	180
Figure 6.S8 20 year average observed and modeled winter/spring precipitation for the Castor Lake region over the 20 th century.....	180

LIST OF EQUATIONS

Equation 1.1	$\frac{dV_L}{dt} = \Sigma I - \Sigma O$	8
Equation 1.2	$\frac{d(V_L \delta_L)}{dt} = \Sigma I \delta_I - \Sigma O \delta_O$	8
Equation 1.3	$\frac{dRES_{SL}}{dt} = F_P + F_{IN} + F_{DLM} - F_E - F_{SLM} - F_{SOS}$	10
Equation 1.4	$\frac{dRES_{DL}}{dt} = F_{SLM} - F_{DLM} - F_{DOS}$	10
Equation 1.5	$\frac{dRES_{SS}}{dt} = F_{SSI} - F_{SSE} - F_{SSD}$	10
Equation 1.6	$\frac{dRES_{DS}}{dt} = F_{SSD} - F_{DSE} - F_{DSD}$	11
Equation 1.7	$\frac{dRES_{IN}}{dt} = F_{RO} + F_{DSD} - F_{IN}$	11
Equation 1.8	$\frac{dRES_{SP}}{dt} = F_{SF} - F_{SM}$	11
Equation 1.9	$F_{SF} = \begin{cases} F_R & T_a \leq 0 \\ 0 & T_a > 0 \end{cases}$	12
Equation 1.10	$F_{SM} = \begin{cases} 21(-2 - T_a) \times CA \times dt^{-1} & RES_{SP} > 21(-2 - T_a) \times CA \\ RES_{SP} \times dt^{-1} & RES_{SP} \leq 21(-2 - T_a) \times CA \end{cases}$	12

$$\text{Equation 1.11 } F_{SSI} = \begin{cases} (F_R + F_{SM}) \times dt^{-1} & RES_{SS} < CA \times AWC_{SS} \\ (F_R + F_{SM})0.5 \times dt^{-1} & RES_{SS} \geq CA \times AWC_{SS} \text{ and } RES_{DS} < CA \times AWC_{DS} \dots 12 \\ 0 & RES_{SS} \geq CA \times AWC_{SS} \text{ and } RES_{DS} \geq CA \times AWC_{DS} \end{cases}$$

$$\text{Equation 1.12 } F_{SSE} = \begin{cases} CA \times PET \times dt^{-1} & RES_{SS} > CA \times PET \\ RES_{SS} \times dt^{-1} & RES_{SS} \leq CA \times PET \dots 13 \end{cases}$$

$$\text{Equation 1.13 } F_{SSD} = (RES_{SS} - CA \times AWC_{SS}) \times dt^{-1} \dots 13$$

$$\text{Equation 1.14 } F_{DSE} = \begin{cases} (CA \times PET - F_{SSE}) \times dt^{-1} & RES_{DS} > CA \times PET - F_{SSE} \\ RES_{DS} \times dt^{-1} & RES_{DS} \leq CA \times PET - F_{SSE} \dots 13 \end{cases}$$

$$\text{Equation 1.15 } F_{DSD} = (RES_{DS} - CA \times AWC_{DS}) \times dt^{-1} \dots 13$$

$$\text{Equation 1.16 } F_{RO} = \begin{cases} (F_R + F_{SM}) \times dt^{-1} & RES_{SS} \geq CA \times AWC_{SS} \text{ and } RES_{DS} \geq CA \times AWC_{DS} \\ (F_R + F_{SM})0.5 \times dt^{-1} & RES_{SS} \geq CA \times AWC_{SS} \text{ and } RES_{DS} < CA \times AWC_{DS} \dots 14 \\ 0 & RES_{SS} < CA \times AWC_{SS} \end{cases}$$

$$\text{Equation 1.17 } F_{IN} = RES_{IN} \times C_{IN} \times dt^{-1} \dots 14$$

$$\text{Equation 1.18 } F_{SLM} = \begin{cases} 0 & M < 9 \\ RES_{SL} \times dt^{-1} & M \geq 9 \dots 15 \end{cases}$$

$$\text{Equation 1.19 } F_{DLM} = \begin{cases} (SVC - RES_{SL}) \times dt^{-1} & M < 9 \\ 0 & M \geq 9 \dots 15 \end{cases}$$

$$\text{Equation 1.20 } F_{SOS} = C_{SR} \times RES_{SL} \times dt^{-1} \dots 16$$

$$\text{Equation 1.21 } F_{DOS} = C_{SR} \times RES_{DL} \times dt^{-1} \dots 16$$

$$\text{Equation 1.22 } E = \left(\begin{array}{l} 0.051(1 - ALB) \times R_s \times (T_a + 9.5)^{(1/2)} - 2.4 \left(\frac{R_s}{R_a} \right)^2 + \\ 0.052(T_a + 20) \times \left(1 - \frac{RH}{100} \right) \times (a_u - 0.38 + 0.54WS) \end{array} \right) \times 30 \dots 16$$

Equation 1.23
$$PET = \left(\begin{array}{l} 0.051(1 - ALB) \times R_s \times (T_a + 9.5)^{(1/2)} - 2.4 \left(\frac{R_s}{R_a} \right)^2 + \\ 0.048(T_a + 20) \times \left(1 - \frac{RH}{100} \right) \times (0.5 + 0.536WS) \end{array} \right) \times 30 \dots\dots\dots 16$$

Equation 1.24
$$\delta_E = \frac{\alpha^* \delta_L - h_n \delta_A - \epsilon_{tot}}{1 - h_n + 0.001 \epsilon_{kin}} \dots\dots\dots 17$$

Equation 1.25
$$h_n = RH \times \frac{e_{s-a}}{e_{s-w}} \dots\dots\dots 18$$

Equation 1.26
$$e_{s-a} \text{ and/or } e_{s-a} = 6.108 \text{EXP} \left(\frac{17.27T}{T + 237.7} \right) \dots\dots\dots 18$$

Equation 1.27
$$\delta_A = \delta_p - \epsilon_{eq} \dots\dots\dots 18$$

Equation 1.28
$$\ln \alpha = 0.35041 \times \left(\frac{10^6}{T_w^3} \right) - 1.6664 \times \left(\frac{10^3}{T_w^2} \right) + 6.7123 \left(\frac{1}{T_w} \right) - 7.685 \times 10^{-3} \dots\dots\dots 18$$

Equation 1.29
$$\begin{aligned} \ln \alpha &= 1.1588 \times \left(\frac{T_w^3}{10^9} \right) - 1.6201 \times \left(\frac{T_w^2}{10^6} \right) \\ &+ 0.79484 \times \left(\frac{T_w}{10^3} \right) + 2.9992 \times \left(\frac{10^6}{T^3} \right) - 161.04 \times 10^{-3} \end{aligned} \dots\dots\dots 18$$

Equation 1.30
$$\alpha^* = 1/\alpha \quad \alpha^* < 1 \dots\dots\dots 18$$

Equation 1.31
$$\epsilon_{eq} = 1000 \times (1 - \alpha^*) \dots\dots\dots 18$$

Equation 1.32
$$\epsilon_k = C \times (1 - h_n) \dots\dots\dots 18$$

Equation 3.1
$$F_{OSSx} = OS_{EXPx} \times SA_{Sx} \dots\dots\dots 68$$

Equation 4.1
$$F_{OF} = \begin{cases} RES_{SL} + RES_{DL} - 424562 & RES_{SL} + RES_{DL} > 424562 \\ 0 & RES_{SL} + RES_{DL} \leq 424562 \end{cases} \dots\dots\dots 96$$

Equation 4.2
$$1000 \ln \alpha_{Aragonite-H_2O} = 20.44(10^3 T^{-1}) - 41.48 \dots\dots\dots 97$$

Equation 4.3
$$1000 \ln \alpha_{Calcite-H_2O} = 18.03(10^3 T^{-1}) - 32.42 \dots\dots\dots 97$$

Equation 4.4	$\alpha_{A-B} = \frac{1000 + \delta_A}{1000 + \delta_B}$	97
Equation 4.5	$\delta_{VSMOW} = 1.03086 \times \delta_{VPDB} + 30.86$	97
Equation 4.6	$\Omega = \frac{a_{Ca} a_{CO3}}{K_{sp}} > 1$	112
Equation 5.1	$\left(\frac{\text{Annual total P in year X}}{\text{20th century average annual P}} - 1 \right) \times (1.5 \text{ or } 0.5) + 1 = \text{APM}$	123
Equation 5.2	$\left(\frac{\text{Annual average T in year X}}{\text{20th century average annual T}} - 1 \right) \times (1.5 \text{ or } 0.5) + 1 = \text{ATM}$	123

1.0 THE ISOTOPIC AND HYDROLOGIC RESPONSE OF SMALL, CLOSED-BASIN LAKES TO CLIMATE FORCING FROM PREDICTIVE MODELS: APPLICATION TO PALEOCLIMATE STUDIES IN THE UPPER COLUMBIA RIVER BASIN

Simulations conducted using a coupled lake-catchment, hydrologic and isotope mass-balance model indicate that small, closed-basin lakes in north-central Washington are isotopically sensitive to changes in precipitation, relative humidity, and temperature. Most notably, model simulations predicted inconsistent lake responses to precipitation changes due to differences in lake outseepage rates and surface area to volume (SA:V) ratios. Greater outseepage within model experiments resulted in increased sensitivity to changes in mean precipitation. Moreover, simulations suggest that, in lakes with appreciable outseepage, SA:V ratio changes resulting from lake-level variations control the direction of changes in lake water oxygen isotope composition ($\delta^{18}\text{O}$). Specifically, in lakes with a SA:V ratio that increases at higher lake levels, steady state $\delta^{18}\text{O}$ values will increase in response to greater long term average precipitation. These results suggest that closed-basin lakes with low outseepage rates will exhibit a transient isotopic response to stochastic variability in hydrologic forcing but will not strongly respond at steady state to variation in mean hydrologic conditions. Conversely, closed-basin lakes with appreciable outseepage will exhibit strong isotopic responses to both stochastic variability and variation in mean hydrologic conditions (i.e., mean precipitation, relative humidity and temperature control of catchment hydrologic inputs to the lake). These

relationships provide a mechanism for explaining inconsistencies in the isotopic responses of lakes within a given region to hydrologic forcing, and demonstrate that semi-quantitative models for describing the relationship between lake hydrologic and isotopic responses to climate variability are not appropriate for all closed-basin lakes.

1.1 INTRODUCTION

The hydrologic and chemical evolution of a lake is subject to a complex array of climate and catchment controls that can be mathematically described and related using numeric mass-balance models. Previous modeling studies have examined the influence of changes in climate (relative humidity, precipitation, temperature, solar insolation, wind speed, etc.) on the isotopic composition of lake water by simulating hydrologic and isotopic fluxes through time (Hostetler and Benson 1994; Gibson et al. 2002; Shapley et al. 2008). These climate variables, as well as catchment parameters and basin morphology, control water balance and lake residence time, and therefore define the temporal extent of magnitude of lake response to climate dynamics. As such, mass-balance models can be used to interpret lake sediment oxygen isotope ($\delta^{18}\text{O}$) records by characterizing lake sensitivity to specific climate variables, and to investigate underdetermined aspects of lake hydrologic systems (such as outseepage and throughflow rates), and therefore are useful to both paleoclimatologists (Rowe and Dunbar 2004; Jones et al. 2007; Rosenmeier et al. In press) and water resources scientists (Sacks 2002).

In the seasonal, drought prone climate of north-central Washington, small, closed-basin lakes (i.e., lakes with low rates of outseepage and no surficial outflow) exhibit hydrologic and isotopic instability. This instability arises primarily from the inflow of isotopically light surface runoff from snowmelt and spring precipitation, and from evaporative enrichment of isotopes throughout the summer and early fall. In these lakes, the low salinity and isotopic depletion of runoff results in early spring water column stratification that is then weakened by wind action, diffusion, and evaporative enrichment in subsequent months. The persistent isotopic and chemical instability of closed-basin lakes in north-central Washington precludes the application

of standard steady-state analytical models and necessitates the use of numerical models to quantitatively describe lake response to climate change.

In this paper, a coupled lake and catchment numeric mass-balance model is presented that simulates the hydrologic and isotopic response of two small, closed-basin lakes, Castor Lake and Scanlon Lake, to changes in the primary drought controlling climate variables (i.e., precipitation, relative humidity, and temperature). This relatively simple model is similar to the (Hydrologic-isotopic-balance (HIBAL) model for application to paleolake systems) model of Benson and Paillet (2002) in that it incorporates observed mixing depths and meteorological data to predict near surface and deeper lake water isotopic and hydrologic responses to climate forcing. To account for hydrologic inputs directly from the surrounding catchment (a component not represented in the HIBAL system) the model presented here incorporates catchment sub-routines that describe snowpack, runoff, and soil moisture volume changes through time. Of the more sophisticated coupled lake-catchment models that are well established in the literature (e.g., the calibration free, one-dimension thermal model of Hostetler and Bartlein (1990)) none are applicable to non-freshwater lakes because they do not account for changes in solute concentrations, an important driver of seasonal lake stratification in oligosaline and mesosaline lakes such as Castor and Scanlon. The model presented here is structured to be computationally simple and applicable to a much wider range of lake types, particularly small, closed systems in seasonal climates with stratification regimes influenced by salinity changes.

The Castor and Scanlon Lake model simulations presented here utilized meteorological data from local and regional weather stations, catchment area and soil survey data, and lake depth and $\delta^{18}\text{O}$ values as initial conditions (i.e., initial model variable inputs). Catchment models for each lake were calibrated by adjusting an inflow delay constant until differences

between model estimates obtained using continuous weather station data and measured monthly lake levels and surface water $\delta^{18}\text{O}$ values from the same period (June 2005 to December 2008) were minimized. Following calibration, model simulations were conducted to determine lake sensitivity to changes in temperature, relative humidity, and precipitation, and to describe the potential for variations in outseepage and hypsography to affect lake water isotopic composition.

1.2 METHODS

1.2.1 Study sites

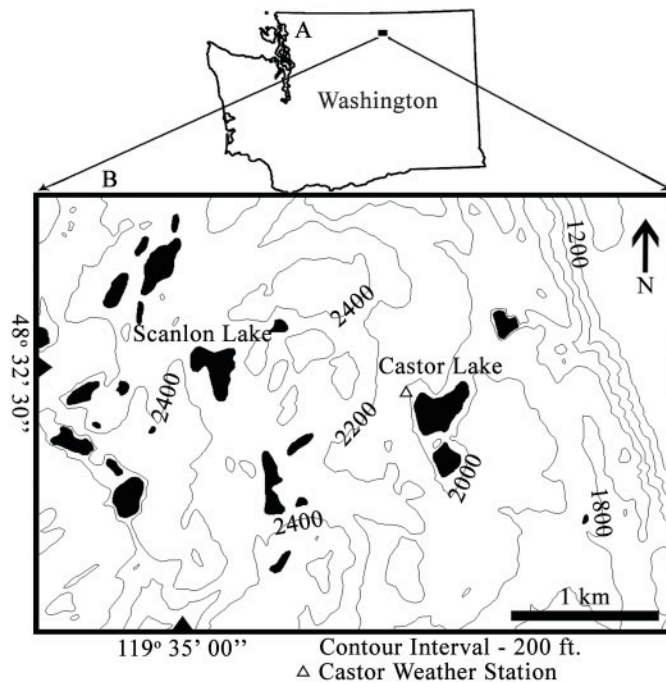


Figure 1.1 (A) Map of Washington State showing the approximate location of the study area. (B) Topography of the Castor and Scanlon Lake catchments and surrounding area.

Table 1.1 CL and SL hydrologic model parameters and initial values for the continuous input (2005–2008) simulations.

Catchment parameters	Value		Reservoir	Initial value (m ³)	
	CL	SL		CL	SL
<i>CA</i> (km ²)	0.86	0.49	<i>RES_{SL}</i>	216,000	120,000
<i>AWC_{SS}</i> (cm)	2.3	2.3	<i>RES_{DL}</i>	77,500	10,000
<i>AWC_{DS}</i> (cm)	2.3	2.3	<i>RES_{SS}</i>	0	0
<i>C_{IN}</i>	0.21	0.21	<i>RES_{DS}</i>	0	0
<i>C_{SR}</i>	0.016	0.007	<i>RES_{IN}</i>	10,000	2500
			<i>RES_{SP}</i>	0	0

Scanlon Lake (SL) and Castor Lake (CL) are located in the ‘lime belt region’ of Okanogan County, Washington, on a terrace margin of the Okanogan River (Figure 1.1). The landscape is characterized by shrub-steppe, evergreen, and secondary deciduous vegetation, and numerous small, perched lakes and seasonal wetlands. Bedrock is principally limestone with mixed calcareous sedimentary rock. Similar to most small lakes in this region, CL and SL are kettle lakes that formed during the retreat of the late Pleistocene Cordilleran ice sheet. The lake catchments are small (< 1 km²) (Table 1.1) and occupy a topographic high isolated from regional groundwater. Lake salinity varies with depth and season between ~1 and 4 mS cm⁻² and 3 and 20 mS cm⁻² for CL and SL, respectively. No evidence exists for organized drainage at SL, and overflow occurs along the northeastern margin of CL only in the spring of very wet years. As a consequence, evaporative losses dominate the hydrologic budgets of both lakes (Figure 1.2).

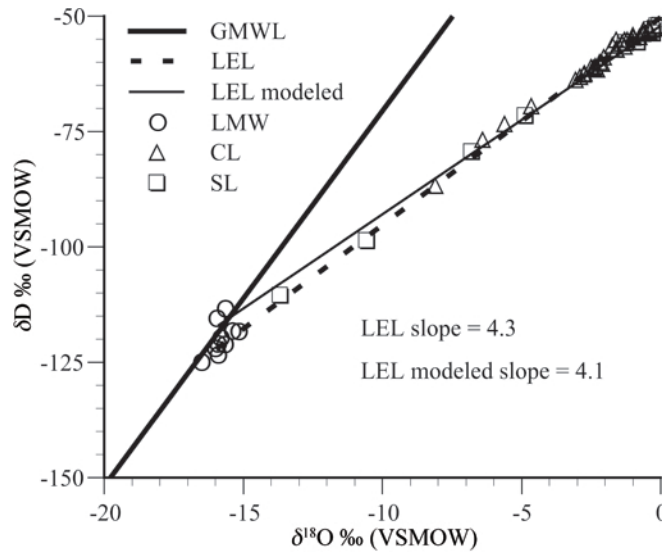


Figure 1.2 Global meteoric water line (GMWL), measured $\delta^{18}\text{O}$ and δD values for Castor Lake (open triangles) and Scanlon Lake (open squares) surface waters, local meteoric waters (LMW, open circles) and slopes of observed and modeled local evaporation lines (LEL and LEL modeled, respectively).

The seasonal, semi-arid climate of north-central Washington is largely controlled by interactions between the Pacific westerlies and the Aleutian low pressure and north Pacific high-pressure systems (Bryson and Hare 1974). In the winter months, the Aleutian low strengthens and moves southward, bringing cool, moist air to the Washington coast. In the summer months, the Aleutian low weakens, moves northward, and is replaced by the north Pacific high. These winter (cool, moist) and summer (warm, dry) air masses are pushed eastward, over the Cascade Mountains, by the Pacific westerlies, leading to a highly seasonal and interannually variable climate (Table 1.2).

Table 1.2 Monthly model input data.

Month	Precip. ^a (mm)	Temp. ^a (°C)	RH ^b (%)	Solar rad. (MJ m ⁻² d ⁻¹)	Wind speed ^b (m s ⁻¹)	δ ¹⁸ O _P (‰)	δD _P (‰)	Stratification depth (m)		Lake-air temp. offset (°C)	
								CL	SL	CL	SL
Jan	34	-4.3	84	2.5	1.3	-15.7	-119	0	0	9.2	7.3
Feb	29	-1.4	77	6.1	1.3	-15.1	-118	0	0	4.1	2.2
Mar	24	3.7	64	12.2	1.5	-15.2	-113	0	0	2.8	2.2
Apr	23	8.5	56	22.3	1.5	-12.9	-96	0.5	0.5	5.2	9.8
May	27	12.6	56	26.4	1.5	-10.6	-82	1.5	1.5	2.5	8.7
Jun	31	16.2	54	30.9	1.4	-10.2	-84	3.25	3.25	4.3	7.8
Jul	14	19.6	46	31.3	1.4	-10.0	-81	6.0	5.0	2.5	4.0
Aug	12	18.9	48	25.1	1.3	-10.6	-86	6.0	5.0	2.5	3.1
Sep	13	14.3	54	16.5	1.3	-9.8	-76	6.0	5.0	3.5	3.4
Oct	20	7.8	67	8.7	1.2	-12.0	-88	6.0	5.0	4.7	3.7
Nov	36	1.0	81	3.6	1.2	-14.4	-111	0	0	5.3	3.3
Dec	45	-3.0	86	2.2	1.2	-15.7	-116	0	0	6.2	3.8
Coeff. of var. ^c	0.28	0.12	0.06	0.04	0.06						

^a Average from Omak NCDC weather station (1900–2007)

^b Average from Omak AgriMet weather station (1989–2007)

^c Coefficient of variation of the annual average over the period of measurement

1.2.2 Model structure

The hydrologic and isotope mass-balance of a lake can be described by the following equations:

$$\frac{dV_L}{dt} = \Sigma I - \Sigma O \quad (1.1)$$

$$\frac{d(V_L \delta_L)}{dt} = \Sigma I \delta_I - \Sigma O \delta_O \quad (1.2)$$

where V_L is lake volume, ΣI and ΣO are the total surface and below ground inflows to and outflows from a lake, and δ is the isotopic composition of the inflows and outflows. These equations provide the basis for a hydrologic and isotope mass-balance model that is defined by a

system of twelve ordinary differential equations compiled using numerical modeling software. Specifically, the model equations, as well as variables and parameters (Table 1.3), integrate a system of lake and catchment water reservoirs (notated as RES in the equations that follow) and volumetric fluxes (F) to the reservoirs, including a two-layer (surface and deep) model sub-routine for soil moisture availability and a two-layer (surface and deep) sub-routine for lake stratification described by separate differential equations. Snowpack and inflow reservoirs are also used to simulate water transfer delays associated with winter freezing and water mass travel time along slower flow paths.

Table 1.3 Model variables and parameters.

RES_{SL}	Surface lake reservoir, m^3	AWC_{SS}	Available water capacity surface soil, m
RES_{DL}	Deep lake reservoir, m^3	AWC_{DS}	Available water capacity deep soil, m
RES_{SS}	Surface soil reservoir, m^3	PET	Potential evapotranspiration, $m\ month^{-1}$
RES_{DS}	Deep soil reservoir, m^3	C_{IN}	Catchment inflow delay constant, unitless
RES_{IN}	Inflow reservoir, m^3	SVC	Surface lake volume control, m^3
RES_{SP}	Snowpack reservoir, m^3	C_{SR}	Seepage constant, unitless
F_P	Precipitation on the lake surface, m^3	ALB	Lake surface albedo, unitless
F_{IN}	Catchment inflow to the lake, m^3	R_s	Solar radiation, $MJ\ m^{-2}\ d^{-1}$
F_E	Evaporation from the lake surface, m^3	R_a	Extraterrestrial solar radiation, $MJ\ m^{-2}\ d^{-1}$
F_{SOS}	Shallow lake outseepage, $m^3\ month^{-1}$	RH	Relative humidity, %
F_{DOS}	Deep lake outseepage, $m^3\ month^{-1}$	a_u	Penman wind function constant, unitless
F_{SLM}	Shallow lake mixing, $m^3\ month^{-1}$	WS	Wind speed, $m\ s^{-1}$
F_{DLM}	Deep lake mixing, $m^3\ month^{-1}$	δ_E	Isotopic composition of evaporation, ‰
F_R	Rainfall on catchment, $m^3\ month^{-1}$	α^*	Reciprocal of α , ‰^{-1}
F_{SM}	Catchment snowmelt, $m^3\ month^{-1}$	δ_L	Isotopic composition of the lake surface, ‰
F_{SSI}	Surface soil infiltration, $m^3\ month^{-1}$	h_n	Normalized relative humidity, %
F_{SSE}	Surface soil evapotranspiration, m^3	δ_A	Isotopic composition of atm. moisture, ‰
F_{SSD}	Surface soil drainage to deep soil, m^3	ϵ_{tot}	Total isotopic separation, ‰
F_{DSE}	Deep soil evapotranspiration, m^3	ϵ_{eq}	Equilibrium isotopic separation, ‰
F_{RO}	Catchment runoff, $m^3\ month^{-1}$	ϵ_k	Kinetic isotopic separation, ‰
F_{DSD}	Deep soil drainage, $m^3\ month^{-1}$	ϵ_{s-a}	Saturation vapor pressure-air, millibars
F_{SF}	Snowfall, $m^3\ month^{-1}$	ϵ_{s-w}	Saturation vapor pressure-water, millibars
T_a, T_w	Air temperature, water temperature, $^{\circ}C$	α	Equilibrium isotopic fractionation factor, ‰
CA	Catchment area, m^3	C	Kinetic isotopic fractionation, ‰

1.2.3 Hydrologic mass-balance equations

The model calculates mass-balance through time for near surface and deep lake waters (RES_{SL} and RES_{DL} , respectively) by the volumetric addition of direct precipitation over the lake area (F_P) and inflow from the catchment (F_{IN}), and subtraction of lake water evaporation (F_E) and outseepage through shallow lake and deep lake sediments (F_{SOS} and F_{DOS}). Lake water mass-balance is also controlled by surface and deep water mixing fluxes (F_{SLM} and F_{DLM} , respectively) associated with the establishment and breakdown of lake stratification (Equations 1.18, 1.19). The lake water mass-balance is described by the following equations, utilizing the notation above:

$$\frac{dRES_{SL}}{dt} = F_P + F_{IN} + F_{DLM} - F_E - F_{SLM} - F_{SOS} \quad (1.3)$$

$$\frac{dRES_{DL}}{dt} = F_{SLM} - F_{DLM} - F_{DOS} \quad (1.4)$$

where direct precipitation over the lake surface area (again, F_P , $F_P = F_{SF} + F_R$) is specifically determined by monthly and/or daily precipitation inputs (*see* Section 1.2.8). Evaporation from the lake surface, in turn, is estimated by a combination radiation-aerodynamic Penman equation (Equation 1.22).

Soil water mass-balance is determined by the amount of rainfall and snowmelt over the catchment surface area (excluding the lake surface area) (F_R and F_{SM} , Equations 1.9, 1.10), catchment evapotranspiration (Equations 1.12, 1.23), infiltration (Equation 1.11), and, ultimately, losses to sub-surface flow (Equation 1.15) and/or runoff (Equation 1.16) to the lake. Within the model, this mass-balance is defined by two reservoir and flux systems:

$$\frac{dRES_{SS}}{dt} = F_{SSI} - F_{SSE} - F_{SSD} \quad (1.5)$$

$$\frac{dRES_{DS}}{dt} = F_{SSD} - F_{DSE} - F_{DSD} \quad (1.6)$$

where RES_{SS} and RES_{DS} are the volumes of water stored within surface and deeper soil reservoirs, and F_{SSI} , F_{SSE} , F_{SSD} , and F_{DSE} (Equations 1.11–1.14) denote surface soil infiltration from precipitation, evapotranspiration from the soil surface, surface soil drainage to the deep soil reservoir, and evapotranspirative loss from deep soil, respectively. Any water in excess of the aforementioned fluxes is assumed to recharge a so-called inflow reservoir (RES_{IN} , Equation 1.7, below) via deep soil drainage (F_{DSD} in Equation 1.6, above, and Equation 1.7). RES_{IN} is not meant to represent a reservoir in nature but rather is an empirical construct designed to allow the model to simulate water transport along slower flow paths.

Hydrologic mass-balance within the inflow reservoir is also controlled by runoff (F_{RO}) generated by catchment rainfall (F_R , Equation 1.9) and/or melt of the catchment snowpack (F_{SM} , Equations 1.9, 1.10) in excess of soil water storage:

$$\frac{dRES_{IN}}{dt} = F_{RO} + F_{DSD} - F_{IN} \quad (1.7)$$

with the entire balance of excess water ultimately reaching the lake via combined surface and sub-surface inflows (F_{IN}) following a fixed retention time (i.e., residence time) in the catchment (identified as an inflow delay constant, C_{IN} , described below). Catchment snow cover (i.e., snowpack reservoir size, RES_{SP}) is determined simply by a balance between accumulation and melt:

$$\frac{dRES_{SP}}{dt} = F_{SF} - F_{SM} \quad (1.8)$$

where F_{SF} is snowfall and F_{SM} is a temperature-controlled snowmelt flux component based on the model of Vassiljev et al. (1995):

$$F_{SF} = \begin{cases} F_R & T_a \leq 0 \\ 0 & T_a > 0 \end{cases} \quad (1.9)$$

$$F_{SM} = \begin{cases} 21(-2 - T_a) \times CA \times dt^{-1} & RES_{SP} > 21(-2 - T_a) \times CA \\ RES_{SP} \times dt^{-1} & RES_{SP} \leq 21(-2 - T_a) \times CA \end{cases} \quad (1.10)$$

wherein snowfall is generated at air temperatures (T_a) less than or equal to 0°C, and melt occurs at temperatures greater than -2°C at a rate equivalent to 21 mm per °C per month.

1.2.4 Infiltration, runoff, and inflow model sub-routines

The two layer soil model sub-routine (introduced above, in Equations 1.5, 1.6) controls the partitioning of catchment water between soil storage, runoff, and subsurface flow. This system of equations is derived, in part, from the two layer soil models of Palmer (1965) and Vassiljev et al. (1995). Within the sub-routine, surface soil infiltration (F_{SSI}) occurs with rainfall (F_R) and/or snowmelt (F_{SM}) until the maximum available water capacity of the catchment is reached (i.e., the surface soil and deep soil reservoirs are saturated) according to the following equations:

$$F_{SSI} = \begin{cases} (F_R + F_{SM}) \times dt^{-1} & RES_{SS} < CA \times AWC_{SS} \\ (F_R + F_{SM}) 0.5 \times dt^{-1} & RES_{SS} \geq CA \times AWC_{SS} \text{ and } RES_{DS} < CA \times AWC_{DS} \\ 0 & RES_{SS} \geq CA \times AWC_{SS} \text{ and } RES_{DS} \geq CA \times AWC_{DS} \end{cases} \quad (1.11)$$

where CA is the area of the catchment and AWC_{SS} and AWC_{DS} are the surface soil and deep soil layer available water capacities. With saturation of the surface soil and undersaturation of the deep soil, catchment water is partitioned evenly (i.e., $F_{SSI} = (F_R + F_{SM}) 0.5$, above) between surface soils and runoff (Equation 1.16). When available water capacity is maximized in both reservoirs, soil water infiltration ceases ($F_{SSI} = 0$).

Evapotranspirative flux from the soil surface (F_{SSE}) is determined by potential evapotranspiration (PET , Equation 1.23) and the total availability of water stored within the catchment:

$$F_{SSE} = \begin{cases} CA \times PET \times dt^{-1} & RES_{SS} > CA \times PET \\ RES_{SS} \times dt^{-1} & RES_{SS} \leq CA \times PET \end{cases} \quad (1.12)$$

When the surface soil water reservoir exceeds total catchment PET , evapotranspiration from surface soils occurs at the potential rate and excess water infiltrates deep soil. In contrast, evapotranspiration is reduced from the potential value to the volume of the surface soil water reservoir if PET demand is not met.

Water in excess of surface soil evapotranspiration (F_{SSE}) and available water capacity (AWC_{SS}) is transferred into the underlying deep soil layer from the overlying surface soil layer (RES_{SS}) according to the equation:

$$F_{SSD} = (RES_{SS} - CA \times AWC_{SS}) \times dt^{-1} \quad (1.13)$$

where, again, F_{SSD} is the surface soil drainage flux. The deep soil layer reservoir, in turn, is subject to evapotranspirative losses in step with evapotranspiration from the surface soil reservoir:

$$F_{DSE} = \begin{cases} (CA \times PET - F_{SSE}) \times dt^{-1} & RES_{DS} > CA \times PET - F_{SSE} \\ RES_{DS} \times dt^{-1} & RES_{DS} \leq CA \times PET - F_{SSE} \end{cases} \quad (1.14)$$

Any water remaining within the deep soil layer in excess of evapotranspiration demand and available water capacity (AWC_{DS}) is then transferred to the inflow reservoir (Equation 1.7) as a deep soil drainage flux (F_{DSD}):

$$F_{DSD} = (RES_{DS} - CA \times AWC_{DS}) \times dt^{-1} \quad (1.15)$$

All catchment precipitation and snowmelt is directly transferred to the lake inflow reservoir, RES_{IN} , as runoff, F_{RO} , under conditions of both surface and deep soil saturation ($RES_{SS} \geq CA \times AWC_{DS}$ and $RES_{DS} \geq CA \times AWC_{DS}$). Under conditions of surface soil saturation and deep soil layer undersaturation, catchment precipitation and snowmelt is evenly partitioned as a flux to the inflow reservoir as runoff (i.e., $F_{RO} = (F_R + F_{SM}) 0.5$) and a flux of water to the deep soil layer (F_{SSD} , Equation 1.13, above). No runoff is generated when surface soil layer water stores fall below available water capacity:

$$F_{RO} = \begin{cases} (F_R + F_{SM}) \times dt^{-1} & RES_{SS} \geq CA \times AWC_{SS} \text{ and } RES_{DS} \geq CA \times AWC_{DS} \\ (F_R + F_{SM}) 0.5 \times dt^{-1} & RES_{SS} \geq CA \times AWC_{SS} \text{ and } RES_{DS} < CA \times AWC_{DS} \\ 0 & RES_{SS} < CA \times AWC_{SS} \end{cases} \quad (1.16)$$

The flux of surface water runoff and deep soil water (F_{IN}) from the inflow reservoir (RES_{IN}) to the lake, then, is governed by the equation:

$$F_{IN} = RES_{IN} \times C_{IN} \times dt^{-1} \quad (1.17)$$

where the inflow delay constant, C_{IN} , is empirically derived through the model calibration process described below (*see* Section 1.3.2).

1.2.5 Lake mixing model and outseepage sub-routines

To approximate the effects of seasonal stratification on surface water isotope content, a two layer (surface and deep) lake model was developed in which the volume of each layer is controlled by monthly mixing depths determined from observations of lake temperature and salinity profiles over a three year period.

The seasonal cycle of lake surface water evolution starts in mid-fall as evaporation rates decrease, rain saturates the surface soil, and the first runoff of the hydrologic year occurs. In the

late fall, the onset of lake freezing leads to the formation of a low salinity ice layer that thickens throughout the winter and early spring, until thaw and ice breakup occur. At this time, runoff and subsurface inflow from rainfall and snowmelt contribute isotopically light, low salinity water to the lake surface layer while wind action begins to force mixing with the isotopically heavy deep lake water layer below. By mid spring, the influx of freshwater begins to decrease and increasing evaporation rates result in renewed isotopic enrichment of the lake surface layer.

To simulate this process, the thickness of the lake surface water layer is independently controlled by a time dependent mixing component that is applied to the hypsographic relationships. This mixing component defines surface layer volume at any total lake depth and at any time of year, with the resulting difference between surface layer volume and total volume defining the volume of the deep layer. In this way, the total volume of the lake is always equal to the sum of the deep layer and surface layer volumes. In the late fall, the surface layer thickness is ‘reset’ to zero for three months, which forces all water into the deep lake reservoir. This has the effect of completely mixing the lake and, due to the small influx of water from the catchment during this time, leads to surface water isotope values approximately equal to that of runoff. The equations that govern the flow between the surface and deep layers are described as follows:

$$F_{SLM} = \begin{cases} 0 & M < 9 \\ RES_{SL} \times dt^{-1} & M \geq 9 \end{cases} \quad (1.18)$$

$$F_{DLM} = \begin{cases} (SVC - RES_{SL}) \times dt^{-1} & M < 9 \\ 0 & M \geq 9 \end{cases} \quad (1.19)$$

where M is the month (0–11, with 0 = January and 11 = December) and SVC is surface lake volume control determined by lake stratification profiles.

Outseepage from the lakes is determined strictly as a function of lake volume and outseepage rate estimates:

$$F_{SOS} = C_{SR} \times RES_{SL} \times dt^{-1} \quad (1.20)$$

$$F_{DOS} = C_{SR} \times RES_{DL} \times dt^{-1} \quad (1.21)$$

1.2.6 Lake evaporation and catchment evapotranspiration model sub-routines

The evaporation and evapotranspiration models applied in this study are the simplified versions of the modified Penman equations proposed by Valiantzas et al. (2006) and are described as follows:

$$E = \left(\begin{array}{l} 0.051(1 - ALB) \times R_s \times (T_a + 9.5)^{(1/2)} - 2.4 \left(\frac{R_s}{R_a} \right)^2 + \\ 0.052(T_a + 20) \times \left(1 - \frac{RH}{100} \right) \times (a_u - 0.38 + 0.54WS) \end{array} \right) \times 30 \quad (1.22)$$

$$PET = \left(\begin{array}{l} 0.051(1 - ALB) \times R_s \times (T_a + 9.5)^{(1/2)} - 2.4 \left(\frac{R_s}{R_a} \right)^2 + \\ 0.048(T_a + 20) \times \left(1 - \frac{RH}{100} \right) \times (0.5 + 0.536WS) \end{array} \right) \times 30 \quad (1.23)$$

where E and PET are evaporation and potential evapotranspiration in mm day^{-1} , ALB is the albedo of the lake (0.08, Equation 1.22) and surrounding grass (0.25, Equation 1.23) surfaces, T_a is average daily temperature in $^{\circ}\text{C}$, R_s is average daily incoming solar radiation in $\text{MJ m}^{-2} \text{d}^{-1}$, R_a is average daily extraterrestrial radiation in $\text{MJ m}^{-2} \text{d}^{-1}$, RH is average daily relative humidity expressed as a percentage, a_u is the Penman wind function constant, and WS is average daily wind speed in m s^{-1} (E and PET values are set to zero when $T_a \leq 0$). This simplified version of the Penman equation was chosen on the basis of available meteorological data and the fact that,

when applied to small lakes in seasonal climatic settings, it produces results that compare favorably to those of the energy budget method for calculating evaporation (Rosenberry et al. 2007a; 2007b). Note that E and PET values are multiplied by thirty in order to convert from daily to monthly estimates.

1.2.7 Isotope mass-balance equations

The reservoir and flux structure of the isotope mass-balance model is identical to that of the hydrologic model and follows the equations of Dincer (1968), Gonfiantini (1986), and Gat (1995). Within the model, oxygen and hydrogen isotope values, in standard delta (δ) notation as the per mil (‰) deviation from Vienna Standard Mean Ocean Water (VSMOW), are calculated for each reservoir at each time step and are multiplied by the corresponding hydrologic flux to determine the isotope mass-balance of any given water mass.

The isotopic composition of moisture evaporating from the lake surface (δ_E) is estimated by the linear resistance model of Craig and Gordon (1965):

$$\delta_E = \frac{\alpha^* \delta_L - h_n \delta_A - \varepsilon_{tot}}{1 - h_n + 0.001 \varepsilon_{kin}} \quad (1.24)$$

where α^* is the reciprocal of the equilibrium isotopic fractionation factor, δ_L is the isotopic composition of lake water, h_n is the ambient humidity normalized to lake water temperature, δ_A is the isotopic composition of atmospheric moisture, ε_{tot} is the total per mil isotopic separation ($\varepsilon_{eq} + \varepsilon_k$), ε_{eq} is the equilibrium isotopic separation, and ε_k is the kinetic isotopic separation.

Normalized relative humidity is calculated from the saturation vapor pressure of the overlying air (e_{s-a}) and the saturation vapor pressure at the surface water temperature (e_{s-w}) in millibars:

$$h_n = RH \times \frac{e_{s-a}}{e_{s-w}} \quad (1.25)$$

$$e_{s-a} \text{ and/or } e_{s-a} = 6.108 \text{EXP} \left(\frac{17.27T}{T + 237.7} \right) \quad (1.26)$$

Atmospheric moisture (δ_A) is assumed to be at isotopic equilibrium with precipitation (Gibson et al. 2002):

$$\delta_A = \delta_P - \varepsilon_{eq} \quad (1.27)$$

The equilibrium isotopic fractionation factor (α) and the reciprocal of the equilibrium isotopic fractionation factor (α^*) for oxygen (Equation 1.28) and hydrogen (Equation 1.29) are calculated using the equations of (Horita and Wesolowski 1994):

$$\ln \alpha = 0.35041 \times \left(\frac{10^6}{T_w^3} \right) - 1.6664 \times \left(\frac{10^3}{T_w^2} \right) + 6.7123 \left(\frac{1}{T_w} \right) - 7.685 \times 10^{-3} \quad (1.28)$$

$$\ln \alpha = 1.1588 \times \left(\frac{T_w^3}{10^9} \right) - 1.6201 \times \left(\frac{T_w^2}{10^6} \right) + 0.79484 \times \left(\frac{T_w}{10^3} \right) + 2.9992 \times \left(\frac{10^6}{T^3} \right) - 161.04 \times 10^{-3} \quad (1.29)$$

$$\alpha^* = 1/\alpha \quad \alpha^* < 1 \quad (1.30)$$

where T_w is the temperature (degrees K) of the lake surface water. The per mil equilibrium isotopic separation (ε_{eq}) of oxygen and hydrogen follows accordingly:

$$\varepsilon_{eq} = 1000 \times (1 - \alpha^*) \quad (1.31)$$

Kinetic fractionation (ε_k) is controlled by molecular diffusion and the moisture deficit ($1 - h_n$) over the lake surface (Merlivat and Jouzel 1979):

$$\varepsilon_k = C \times (1 - h_n) \quad (1.32)$$

where C is the experimentally derived isotopic separation value of 14.3‰ for oxygen and 12.4‰ for hydrogen (Vogt 1976; Araguás-Araguás et al. 2000) and h_n is the humidity normalized to the temperature of the lake surface water.

1.2.8 Model inputs

Steady state and continuous model simulations utilized monthly and daily weather data from two sites located within ~10 km and 200 meters elevation of CL and SL. Specifically, average monthly temperature and precipitation were calculated using ~100 years of data from National Climatic Data Center weather stations at Omak (1930 to present) and Conconully (1900 to present). Monthly and daily average values for relative humidity and wind speed, and daily average values for solar insolation were derived from twenty years of data collected at Omak by the Pacific Northwest Cooperative Agricultural Weather (AgriMet) Network. All climate input data were linearly corrected using two years of daily Campbell® Scientific weather station data from CL. Monthly average values for incoming solar radiation were calculated using the method of Valiantzas et al. (2006). One year (2007) of lake water temperature measurements from Solinst® Leveloggers® were used to derive monthly surface water temperature offsets from average air temperature. Monthly $\delta^{18}\text{O}$ and δD values of precipitation were estimated using the interpolated values of Bowen and Wilkinson (2002), Bowen and Revenaugh (2003), and Bowen et al. (2005) and were adjusted in the temperature sensitivity tests by 0.6‰ per 1° Celsius according to Rozanski et al. (1992).

Catchment surface areas were estimated from georeferenced topographic maps (United States Geological Survey 1981) using geographic information system (GIS) software. Specific soil types and their corresponding areas within each catchment were identified from United States Department of Agriculture regional soil report maps and then used to calculate a weighted average available water capacity (*AWC*) for each catchment.

Lake volume-surface area and lake volume-depth relationships were derived from detailed bathymetric surveys completed in 2007. Depth and location data were collected with a

combination GPS receiver and chartplotter (Garmin® GPSMAP® 430S). All data were compiled, gridded, and contoured using 3-D surface mapping software. Best-fit polynomial regression curves were then applied to the software generated hypsographic profiles to produce equations of depth and surface area as a function of lake volume.

1.2.9 Lake and climate monitoring data

Water samples for oxygen and hydrogen isotope analyses were collected from the shorelines of SL and CL, from shallow wells within the lake catchments, and from nearby streams at irregular intervals between June 2005 and December 2008. Isotopic ratios of lake water were measured at the University of Arizona Environmental Isotope Laboratory by CO₂ equilibration with a VG602C Finnigan® Delta S isotope ratio mass spectrometer. The reported precision is 0.1‰ for $\delta^{18}\text{O}$ and 1.0‰ for δD . Lake level at both SL and CL was measured with a Solinst® Levelogger® data logger and corrected for barometric pressure changes recorded by a land-based Solinst® Barologger® device. Each Levelogger® was tied to floats and positioned at the center of each lake approximately one meter below the surface using anchored ropes. Barologger® devices were positioned in the shade approximately ten meters above the lake surfaces. A Campbell® Scientific weather station was deployed near the shoreline approximately three meters above the lake surface of CL in May of 2006. Air temperature, relative humidity, barometric pressure, wind speed and direction, precipitation, and solar insolation were measured at thirty second intervals and recorded every thirty minutes.

1.3 RESULTS

All model simulations were conducted with numerical modeling software using the fourth order Runge-Kutta numerical integration method. In the first series of model simulations (Section 1.3.1), monthly average climate data and modern catchment parameter datasets were used to approximate the monthly and seasonal variability of CL and SL water levels, lake water $\delta^{18}\text{O}$ values, and outseepage rates. In the second sequence of model simulations (Section 1.3.2), outseepage estimates derived from the first set of simulations were combined with continuous daily meteorological data and initial catchment reservoir volumes and characteristics (Table 1.1) to simulate lake level and $\delta^{18}\text{O}$ values over the three-year lake water sampling and monitoring period (2005–2008). Results from these simulations were compared to observations in order to calibrate the catchment sub-model. The model was then adapted to simulate lake water δD evolution over the same three year period in order to independently test the validity of the isotopic sub-model. The third series of simulations (Section 1.3.3) utilized both the outseepage estimates derived from the first set of model tests and the model calibration factor developed from the second set of tests to evaluate the sensitivity of the lakes to each of the primary drought controlling climate variables (i.e., precipitation, relative humidity, and temperature).

1.3.1 Seepage estimation simulations

Initially, outseepage was assigned a value of zero and both lakes were assumed to lose water only by evaporation. In this configuration, evaporative losses were insufficient to balance lake levels and surface water $\delta^{18}\text{O}$ values at or near modern values. Outseepage rates were subsequently increased in a stepwise manner until average annual lake level matched modern

observations for both CL and SL (Figures 1.3, 1.4).

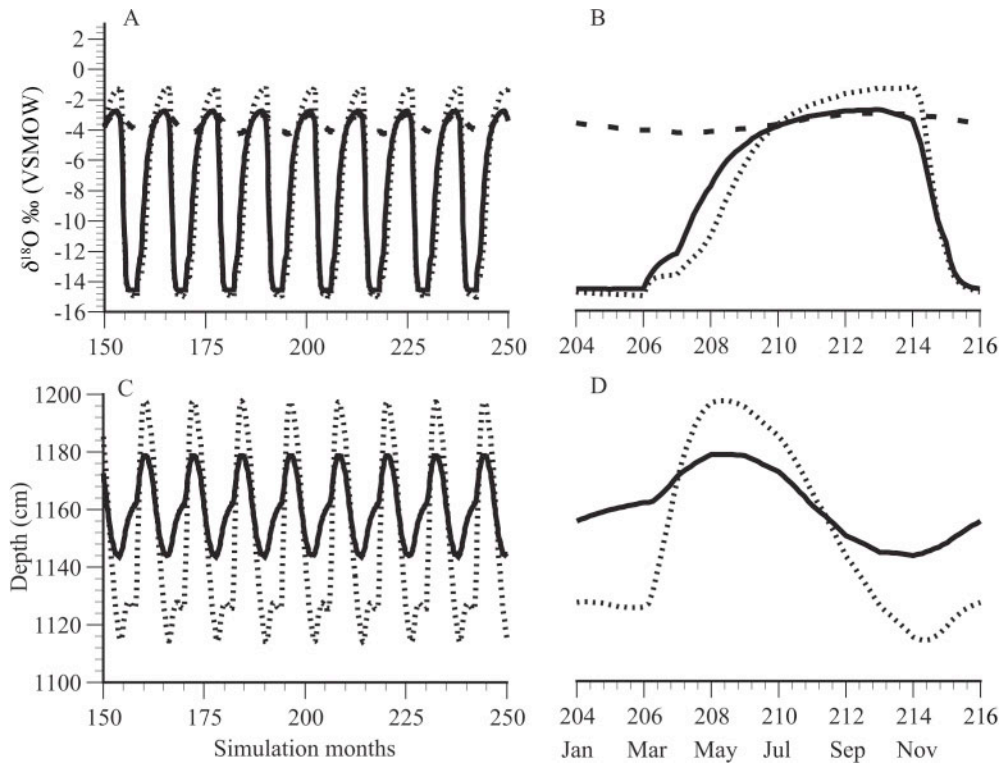


Figure 1.3 (A) Simulated Castor Lake steady state total water column $\delta^{18}\text{O}$ values (coarse dashed line) and surface water $\delta^{18}\text{O}$ values (solid line) with delayed catchment water inflow. Fine dashed line depicts surface water $\delta^{18}\text{O}$ values without delayed inflow. (B) Expanded view of Castor Lake $\delta^{18}\text{O}$ values between model months 204 (Jan) and 216 (Dec) from Figure 1.3A. (C, D) Simulated Castor Lake steady state lake-level change with (solid lines) and without (fine dashed lines) delayed inflow.

Simulations of modern lake level were achieved only by removing $1.5\% \pm 0.3\%$ and $0.5\% \pm 0.3\%$ of monthly lake volume through outseepage at CL and SL, respectively. At these outseepage rates, after applying catchment calibration factors (*see* Section 1.3.2), the simulated lake-level curves reproduced the observed pattern of seasonal water level change ($\sim 0.4\text{m}$) at both sites, with lowest lake levels occurring between October and November and highest lake levels occurring between May and July. The model also reproduced the observed seasonal variations in lake surface water $\delta^{18}\text{O}$ ($\sim 12\text{‰}$ for CL and $\sim 17\text{‰}$ for SL), with minimum values between

November and January and maximum values between July and October. Outseepage estimates were insensitive to catchment calibration, with almost identical average annual lake levels resulting from both calibrated and uncalibrated model configurations.

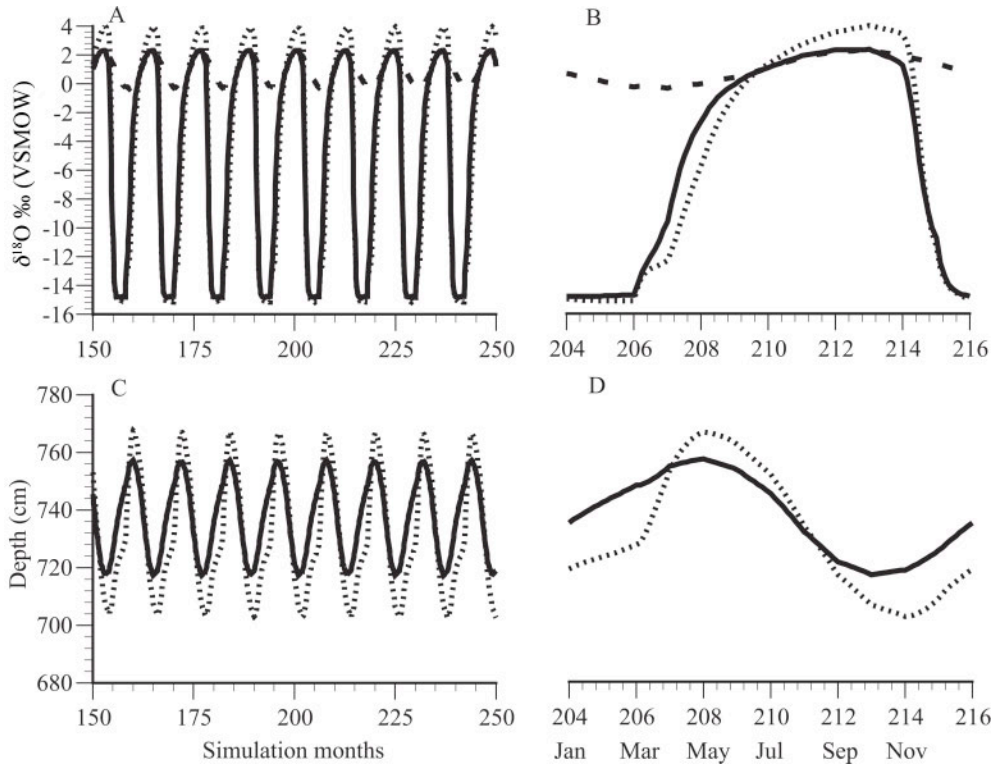


Figure 1.4 Simulated Scanlon Lake steady state total water column $\delta^{18}\text{O}$ values (coarse dashed line) and surface water $\delta^{18}\text{O}$ values (solid line) with delayed catchment water inflow. Fine dashed line depicts surface water $\delta^{18}\text{O}$ values without delayed inflow. (B) Expanded view of Scanlon Lake $\delta^{18}\text{O}$ values between model months 204 (Jan) and 216 (Dec) from Figure 1.4A. (C, D) Simulated Scanlon Lake steady state lake-level change with (solid lines) and without (fine dashed lines) delayed inflow.

1.3.2 Catchment model calibration

The objective of the second set of simulations was to define the inflow delay constant (C_{IN}), in order to calibrate the catchment model, and to refine outseepage estimates. These

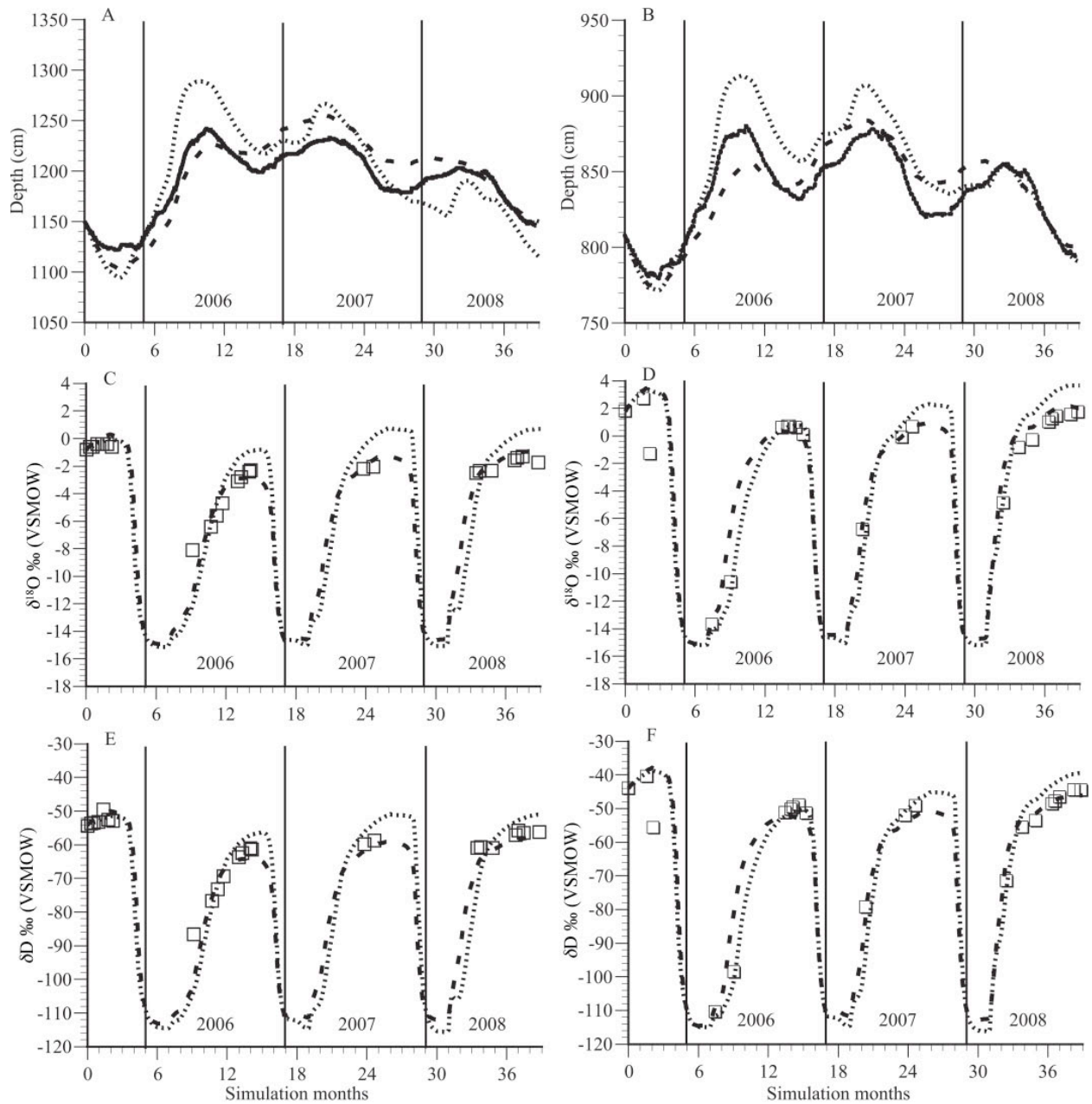


Figure 1.5 (A, B) Castor Lake and Scanlon Lake calibrated (course dashed lines) and uncalibrated (fine dashed lines) lake-level simulations using continuous input data plotted with observed lake-level changes (solid lines). (C, D) Castor Lake and Scanlon Lake calibrated (course dashed lines), uncalibrated (fine dashed lines), and measured (open squares) lake surface water $\delta^{18}\text{O}$ values between August 2005 and October 2008. (E, F) Castor Lake and Scanlon Lake calibrated (course dashed lines), uncalibrated (fine dashed lines), and measured (open squares) lake surface water δD values.

simulations utilized three years (August 2005 to October 2008) of daily climate data from the CL and Omak AgriMet weather stations and initial values for model reservoirs based on steady state values and depth and surface water $\delta^{18}\text{O}$ measurements taken in late July of 2005. In these experiments, an inflow delay constant (Equation 1.17) was applied to each catchment in an effort to simulate expected delays between rainfall and snowmelt within the catchment and lake inflow. The applied inflow delay constant was sequentially adjusted downward from a value of one (i.e., no delay in the transport of water from the catchment to the lake) until the difference between the predicted seasonal lake level and $\delta^{18}\text{O}$ values and the observed lake level and $\delta^{18}\text{O}$ values was minimized (Figure 1.5). After defining the inflow delay constant (0.21), outseepage estimates were adjusted within the range defined by the seepage estimation simulations in order to improve model calibration. Final outseepage estimates were 1.6% and 0.7% of monthly volume for CL and SL, respectively. At both CL and SL, the inflow delay constant that resulted in lake level values most closely matched to observations equates to a catchment residence time of ~ 140 days.

The model was also adapted to predict lake water hydrogen isotope variability over the three-year sampling and monitoring period used for model calibration (Figure 1.5). Modeled lake surface water δD values were similar to measured δD values, and produced a theoretical local evaporation line (LEL) with a slope similar to that derived from lake surface water measurements (Figure 1.2). The ability of the model to simulate hydrogen isotope variability within both CL and SL demonstrates that the improvements in accuracy resulting from calibration are not specific to the oxygen isotope system and that the structure of the hydrologic and isotopic model is widely applicable.

1.3.3 Model sensitivity to climate variables

The objective of the third series of simulations was to determine the hydrologic and isotopic sensitivity of SL and CL to temperature, relative humidity, and precipitation changes. In each set of sensitivity tests, simulations were conducted on a monthly time-step over ~110 model years using modern catchment parameters and average climate data for the 20th century. Between the 501st and 1004th simulation month, corresponding to the beginning (October) of the 42nd and end (September) of the 84th model hydrologic year, respectively, the tested climate parameter was either increased or decreased in a step-wise manner by a constant percentage determined on the basis of the coefficient of variation of the parameter over the 20th century (Table 1.2).

1.3.4 Temperature sensitivity tests

Atmospheric temperature can influence lake hydrologic and isotopic balance by altering evaporative flux from the lake surface, catchment evapotranspiration rates, water column temperature and stratification, normalized *RH* values, and through direct control of the liquid-vapor equilibrium fractionation factor for evaporating water (Equations 1.22–1.32). At mid- and high-latitude sites, atmospheric temperature also influences the isotopic composition of lake water through its effect on the isotopic composition of precipitation.

Atmospheric temperatures 20% above or below average 20th century values resulted in water depth changes of less than ± 0.35 m at SL and less than ± 0.20 m at CL (Table 1.4), suggesting that basin hydrology at both sites is relatively insensitive to temperature changes. Oxygen isotope value shifts of $\sim 1.2\text{‰}$ at both SL and CL, resulting from a 20% temperature

change, were largely a consequence of temperature control on the isotopic composition of precipitation and to a lesser extent on changes in hydrologic and isotopic fluxes.

Table 1.4 Relative humidity and temperature sensitivity test results.

	Model Year	Castor Lake				Scanlon Lake			
		Temp. -20%	Temp. +20%	<i>RH</i> -10%	<i>RH</i> +10%	Temp. -20%	Temp. +20%	<i>RH</i> -10%	<i>RH</i> +10%
$\delta^{18}\text{O}$	40	-3.6	-3.6	-3.6	-3.6	1.4	1.4	1.4	1.4
(‰)	80	-4.8	-2.5	-3.2	-4.1	0.2	2.5	2.3	0.3
Depth	40	1162	1162	1162	1162	739	739	739	739
(cm)	80	1179	1145	1135	1189	771	715	714	770

1.3.5 Relative humidity sensitivity tests

The sensitivity of lakes to changes in relative humidity is largely due to the effect of *RH* on the kinetic fractionation process that occurs during evaporation from the lake surface. Relative humidity also influences lake hydrologic balance by affecting evapotranspiration rates. The hydrologic response of both lakes to a 10% change in *RH* was relatively small (less than ~0.3 m) in comparison to the change in lake water $\delta^{18}\text{O}$ values ($\pm 1.1\text{‰}$ and $\pm 0.5\text{‰}$ at SL and CL, respectively) (Table 1.4), indicating that *RH* sensitivity is primarily a result of isotope fractionation processes rather than hydrologic influence on lake water isotopic composition. Additionally, the more pronounced isotopic response of SL to *RH* changes (relative to CL, a nearly 0.6‰ difference) suggests that lake sensitivity is in part controlled by the proportion of water lost through evaporation, with greater evaporative loss at SL resulting in greater sensitivity to *RH* forcing (*see* evaporative outflow proportion discussion and figures below).

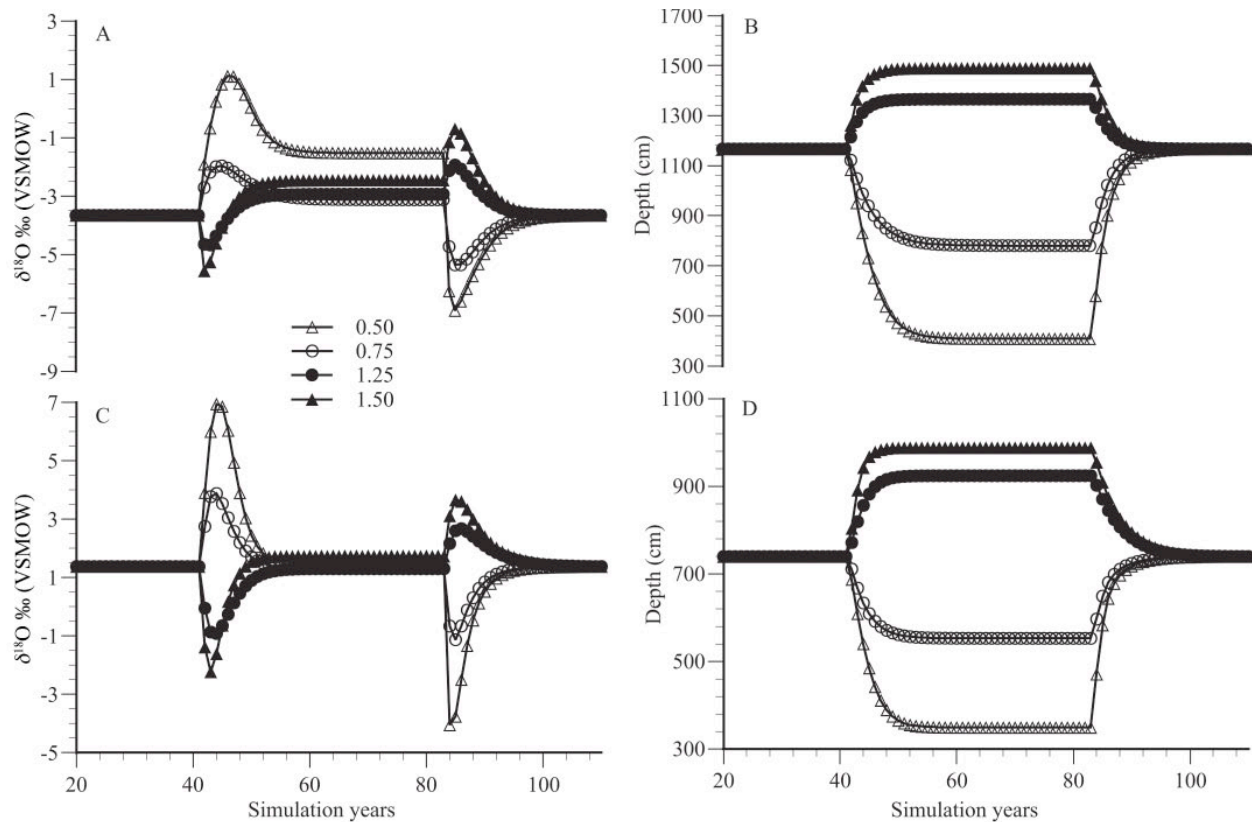


Figure 1.6 (A) Castor Lake average summer month (June, July, August) surface water $\delta^{18}\text{O}$ values and (B) lake levels from precipitation sensitivity tests. (C) Scanlon Lake average summer month (June, July, August) surface water $\delta^{18}\text{O}$ values and (D) lake levels from precipitation sensitivity tests.

1.3.6 Precipitation sensitivity tests

Precipitation rates were incrementally adjusted from 50% to 150% of modern values, reflective of the coefficient of variation of recorded precipitation over the 20th century. In response to a 50% reduction in precipitation, both SL and CL exhibited a marked, but transient (i.e., short-lived) $\delta^{18}\text{O}$ increase of $\sim 5.6\text{‰}$ and $\sim 4.8\text{‰}$, respectively, with CL taking longer to achieve initial maxima and steady state $\delta^{18}\text{O}$ values relative to SL, due in part to the larger volume and consequently slower response time of CL (Figure 1.6). Increased precipitation levels (50% above modern) resulted in transient $\delta^{18}\text{O}$ decreases of $\sim 1.9\text{‰}$ and $\sim 3.6\text{‰}$ at CL and SL, respectively.

1.4 DISCUSSION

1.4.1 The influence of hypsography and seepage on lake water $\delta^{18}\text{O}$ values

In the increased precipitation simulations, both CL and SL achieved initial, transient $\delta^{18}\text{O}$ minima and steady state values relatively quickly (in comparison with the precipitation reduction scenarios) largely as a result of a rapid increase in lake surface area with increasing depth. Moreover, the transient isotopic response was stronger in the decreased precipitation scenarios due to the longer hydrologic equilibration times resulting from relatively gradual decreases in lake surface area with decreasing depth (Figure 1.6).

Under all precipitation scenarios SL exhibited a steady state $\delta^{18}\text{O}$ value that was similar to the value prior to hydrologic forcing (differences ranged from about -0.1 to 0.4‰). In contrast, CL exhibited a steady state value that was considerably different (by as much as 2.1‰) than the value prior to forcing, and, in the case of the +25% and +50% precipitation scenarios, opposite in sign of the transient response (i.e., an increase in steady state water $\delta^{18}\text{O}$ values occurred as a result of a lake-level increase). This apparently contradictory response results from control of lake steady state isotopic response to hydrologic forcing by surface area to volume (SA:V) ratio variation with changing depth and the consequent change in the proportions of water lost through fractionating (evaporation) and non-fractionating (outseepage) hydrologic pathways. For example, in lakes such as SL with a high SA:V ratio (i.e., shallow lakes with a proportionally large surface area), the outseepage rate (C_{SR} in the model) is less influential in determining the proportion of water lost through evaporation because at all depths the SA:V ratio is high. As a consequence, evaporation is the only significant outflow pathway and steady state lake water $\delta^{18}\text{O}$ values are buffered only slightly by outflow through seepage. To that end, as

volumetric adjustments occur at SL in response to hydrologic forcing, minimal changes occur in the proportion of water lost through evaporation (relative to outseepage), thereby resulting in effectively negligible changes in steady state isotopic values (Figure 1.7). At CL, however, the lower overall SA:V ratio and the higher outseepage rate cause the opposite response, in that lake volumetric changes resulting from hydrologic forcing lead to larger proportional changes in water loss through evaporation versus outseepage and consequently substantial variations in steady state $\delta^{18}\text{O}$ values (Figure 1.8). Roberts et al. (2008) predicted similar results (i.e., lakes with appreciable outseepage respond more strongly at steady state to hydrologic forcing) using a schematic model for differential lake response to common water balance forcing.

The influence of the SA:V ratio on steady state lake water $\delta^{18}\text{O}$ values was examined at SL through steady state sensitivity simulations in which outseepage rates were increased to 2.4% of monthly volume (Figure 1.9A, B) and, at CL, through altered hypsographic profiles such that the SA:V ratio decreased with increasing depth above twelve meters (Figure 1.9C, D). In these configurations, precipitation was decreased by 50% at SL and increased by 50% at CL. At SL, the increased outseepage rate simulation resulted in a large increase in the steady state $\delta^{18}\text{O}$ value ($\sim 1.3\text{‰}$). The positive direction of the isotopic response was a result of the increase in the SA:V ratio over the depth interval of the test. At CL, the altered SA:V ratio led to a steady state isotopic response (nearly -0.9‰) with a sign opposite (i.e., negative) that of the original configuration due to the decrease in the percentage of outflow via evaporation resulting from the altered SA:V ratio.

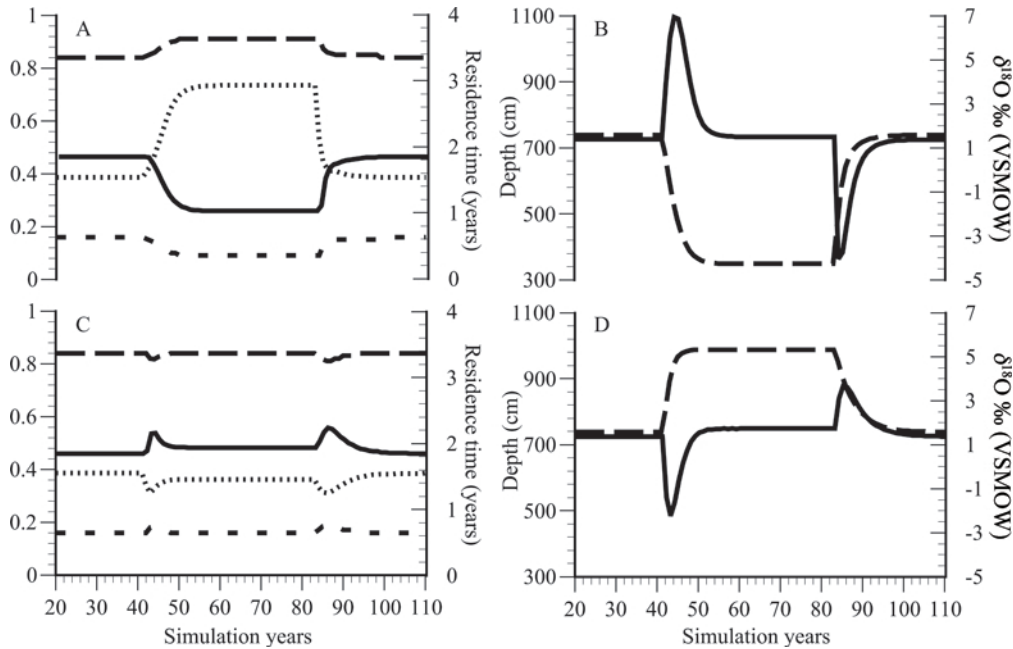


Figure 1.7 Scanlon Lake water residence time (solid line), SA:V ratio (fine dashed line), and percentage of outflow via evaporation (course dashed line) and seepage (medium dashed line) changes resulting from (A) a 50% decrease and (C) a 50% increase in precipitation. Scanlon Lake surface water $\delta^{18}\text{O}$ values (solid line) and lake level changes (course dashed line) resulting from (B) a 50% decrease and (D) a 50% increase in precipitation.

1.4.2 Residence time response to hydrologic forcing

Changes in the SA:V ratio also explain, in part, estimated changes in lake water residence time at CL and SL in response to hydrologic forcing. As lake volume increases, surface area increases to a proportionally greater extent, causing greater volumetric loss through evaporation, a larger outflow-to-volume ratio, and hence a lower residence time. At both SL and CL, for example, a 50% decrease in precipitation results in a substantial increase in the SA:V ratio, and a corresponding decrease in residence time (defined as total lake volume divided by total outflux) as the loss of water through evaporation from the lake surface increases relative to lake volume (Figures 1.7A, 1.8A). At both sites, there is an inverse relationship between the SA:V ratio and residence time, regardless of the volumetric response to hydrologic forcing.

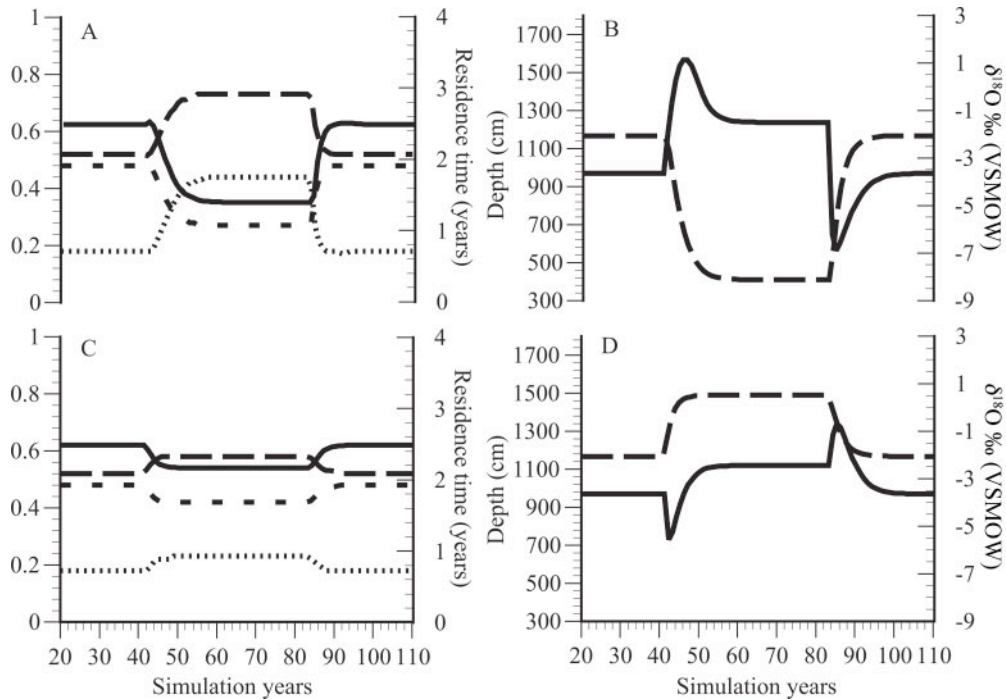


Figure 1.8 Castor Lake water residence time (solid line), SA:V ratio (fine dashed line), and percentage of outflow via evaporation (course dashed line) and seepage (medium dashed line) changes resulting from (A) a 50% decrease and (C) a 50% increase in precipitation. Castor Lake surface water $\delta^{18}\text{O}$ values (solid line) and lake level changes (course dashed line) resulting from (B) a 50% decrease and (D) a 50% increase in precipitation.

1.4.3 Seepage model considerations

In all model simulations, water loss via seepage was determined strictly as a percentage of total lake volume (Equations 1.20, 1.21). At both SL and CL, estimated outseepage fell within the range of values calculated using Darcy's law and generally accepted lake sediment hydraulic conductivity values between 10^{-8} and 10^{-9} m s^{-1} . However, given that lake sediment hydrologic parameters can vary between the littoral and benthic zones, and that seepage rates often decrease exponentially with distance offshore, this simple model for calculating outseepage may not be appropriate in some lakes and may lead to lake level and lake water $\delta^{18}\text{O}$ predictions that differ from observation (Genereux and Bandopadhyay 2001). For example, in lakes with highly

permeable littoral zone sediments, an increase in lake level resulting from a hydrologic forcing could result in a decrease in steady state $\delta^{18}\text{O}$ values regardless of the SA:V ratio change (Almendinger 1990). In lake systems with heterogeneous sediments, outseepage responses to hydrologic forcing may therefore exert greater control on steady state $\delta^{18}\text{O}$ values than lake hypsography.

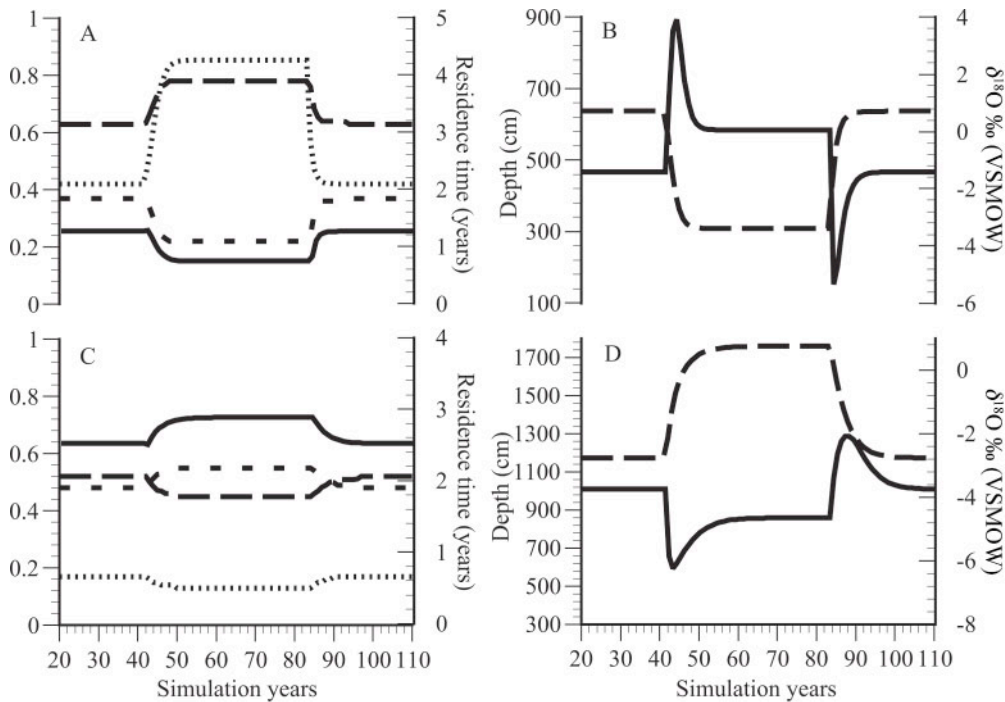


Figure 1.9 (A) Scanlon Lake water residence time (solid line), SA:V ratio (fine dashed line), and percentage of outflow via evaporation (course dashed line) and seepage (medium dashed line) changes resulting from a 50% decrease in precipitation and outseepage increased from 0.7% to 2.4% of monthly lake volume, and (B) consequent lake water $\delta^{18}\text{O}$ values (solid line) and lake-level changes (course dashed line). (C) Castor Lake water residence time (solid line), SA:V ratio (fine dashed line), and percentage of outflow via evaporation (course dashed line) and seepage (medium dashed line) changes resulting from a 50% increase in precipitation and hypsography altered such that the SA:V ratio decreases with depths above twelve meters. (D) Consequent lake water $\delta^{18}\text{O}$ values (solid line) and lake-level changes (course dashed line).

1.5 CONCLUSIONS

Numeric mass-balance models can accurately predict the hydrologic and isotopic evolution of small, closed-basin lake systems on seasonal and interannual time scales when calibrated using modern lake water stratification, surface water isotopic composition, and lake-level change data. At Scanlon and Castor Lakes, north-central Washington, mass-balance model sensitivity tests demonstrate a strong lake water hydrologic and transient isotopic response to precipitation changes. Neither relative humidity nor temperature strongly influence lake hydrologic responses, but do affect steady state lake water $\delta^{18}\text{O}$ values via controls on kinetic and equilibrium isotope fractionation.

The results presented here describe how the isotopic composition of closed-basin lake water is dependent on both initial conditions and input forcing, and that specific lake water $\delta^{18}\text{O}$ values cannot always be ascribed to specific lake hydrologic states. A related inference is that, within an individual lake, the magnitude of the transient isotopic response is at least partly controlled by how quickly the equilibrium lake level and corresponding surface area can be reached, with longer equilibration times resulting in stronger transient isotopic responses. Most importantly, these results demonstrate the potential for inconsistent isotopic responses to drought and/or pluvial conditions between adjacent closed-basin lakes with differing outseepage rates and lake basin morphologies.

Semi-quantitative interpretations of lake sediment $\delta^{18}\text{O}$ records often rely on a somewhat overly simplistic model in which steady state increases (decreases) in closed-basin lake volume resulting from climatically induced changes in precipitation-evaporation balance cause steady state decreases (increases) in closed-basin lake water $\delta^{18}\text{O}$ values. This model is based on several assumptions, most notably that lake basin geometry is approximately conic and, as a

consequence, the SA:V ratio decreases with increasing depth (Benson et al. 1996). This study demonstrates that closed-basin lake steady state isotopic responses are dependent upon interactions between both lake outseepage and basin morphology, and that in lakes with non-standard geometry (i.e., in which the SA:V ratio increases with increasing depth) this basic model relating hydrologic forcing and isotopic response may not apply.

This study also suggests that closed-basin lakes with minimal outseepage will likely exhibit a transient isotopic response to stochastic variability in hydrologic forcing but will not strongly respond to variations in mean hydrologic conditions (i.e., mean precipitation, relative humidity and temperature control of catchment hydrologic inputs to the lake). Conversely, closed-basin lakes with appreciable outseepage and a SA:V ratio that changes with depth will exhibit a strong isotopic response to both stochastic variability in hydrologic forcing and variations in mean hydrologic conditions, with the direction of the SA:V ratio change (either positive or negative with increasing depth) controlling the direction of the steady state isotopic response. These relationships provide a mechanism for explaining inconsistencies in multi-proxy sediment records from regional closed-basin lakes and highlight the need for caution when applying only semi-quantitative models to explain the relationship between climatic forcing and oxygen isotope values in sediments from underdetermined lake systems.

2.0 THE ISOTOPIC AND HYDROLOGIC RESPONSE OF SMALL, CLOSED-BASIN LAKES TO CLIMATE FORCING FROM PREDICTIVE MODELS: SIMULATIONS OF STOCHASTIC AND MEAN STATE PRECIPITATION VARIATIONS

A hydrologic and isotope mass-balance model is applied to two small closed-basin lakes, Castor and Scanlon, in north-central Washington to describe the influence of hydroclimatic forcing on lake hydrologic and isotopic evolution. Simulations of lake responses to the combined effects of stochastic variability (i.e., random interannual fluctuations) and long-term (i.e., multi-decade to century), mean state changes in precipitation were conducted using three hundred years of randomly generated precipitation data as model inputs. Simulation results demonstrate that average (long-term) closed-basin lake water oxygen isotope values are dependent largely upon lake water outseepage (i.e., subsurface outflow) rates, with lower (higher) outseepage resulting in decreased (increased) isotopic sensitivity to long term precipitation changes, and that lake basin surface area to volume (SA:V) ratio changes with depth influence the direction of the isotopic response. Simulation results also suggest that, as average lake level decreases as a consequence of decreasing mean state precipitation amounts, interannual lake water isotopic variability in response to stochastic forcing will increase. Conversely, as average lake level increases in response to increasing mean state precipitation amounts, interannual lake water isotopic variations associated with stochastic forcing will decrease. Additional model experiments demonstrate that increased (decreased) variance in

precipitation leads to increased (decreased) water volume within lakes over the long-term, which (if stochastic variance changes are large enough) could result in decreased (increased) lake water oxygen isotopic sensitivity to stochastic precipitation.

2.1 INTRODUCTION

The oxygen isotope composition of closed-basin lake water is controlled by many factors including net groundwater flux, catchment size and soil characteristics, lake basin morphology, and hydroclimatic forcing through stochastic variability (i.e., random interannual fluctuations) and mean state changes (i.e., changes in multi-decade to century averages) in precipitation, relative humidity, and temperature (Gat 1979; Leng and Marshall 2004; Steinman et al. 2010a). In regions with highly seasonal climate such as the Pacific Northwest, precipitation and evaporation rates substantially vary intra-annually, whereas lake basin morphology, lake seepage rates, and catchment hydrologic parameters such as soil thickness and depth, vary only on decadal and longer time scales, largely in response to inter-annual climate forcing (Johnson and Watson-Stegner 1987; Phillips 1993; Rosenmeier et al. in press). Changes in average climatic states, such as long-term increases in the variance of precipitation about an established annual mean, or the shifting of precipitation from one season to another, add additional complexity to the geochemical evolution and, more specifically, the isotopic composition, of lake water (Vassiljev 1998; Leng et al. 2001; Pham et al. 2009). Only by simulating lake sensitivity to these factors using quantitative models can the isotopic response of closed-basin lakes to climate change be predicted, a fact that has considerable relevance to paleoclimate interpretations of sediment core oxygen isotope ($\delta^{18}\text{O}$) records (Ricketts and Johnson 1996; Cross et al. 2001;

Jones et al. 2005).

Groundwater flow regimes and associated lake seepage rates are of particular importance in the control of steady state lake water $\delta^{18}\text{O}$ values (Donovan et al. 2002; Smith et al. 2002; Shapley et al. 2008). In closed basin systems that are isolated from regional groundwater (i.e., perched lakes), the origin of subsurface inflow is often precipitation falling on or very near the catchment (Almendinger 1993). In seasonal climates, under these conditions, baseflow has an isotopic composition that is approximately equal to the weighted average isotopic composition of mean annual precipitation, and therefore can effectively be considered runoff with an extended transit time (Henderson and Shuman 2009). In contrast, subsurface inflows to lake systems that are not isolated from regional groundwater aquifers can potentially undergo a much more complex isotopic evolution during transport to a lake (Smith et al. 1997).

Subsurface outflow from closed basin lakes occurs as seepage through the lake bed at rates that are typically very low due to the low hydraulic conductivity of silt and clay-rich lake sediment. Outseepage, a potentially minimal hydrologic flux, is in all cases a fundamental control on the steady state isotopic composition of closed-basin lake water in that, through interaction with lake basin morphology, it determines the proportion of water that leaves a lake through fractionating (evaporation) and non-fractionating (outseepage) pathways (Steinman et al. 2010a).

In this study, a numeric, hydrologic and isotope mass balance model was applied to Castor and Scanlon Lakes, north-central Washington, and used to simulate lake water hydrologic and isotopic responses to changes in mean state and stochastic precipitation. In the first set of experiments, intra-annual variations in lake depth and $\delta^{18}\text{O}$ values, as well as inter-annual lake transient and steady state responses to mean state precipitation forcing, were simulated by

applying long-term increases and decreases ($\pm 50\%$) in monthly precipitation values . In the second set of experiments, the model structure was modified to include stochastic changes in precipitation, in order to more realistically simulate hydroclimatic forcing conditions. In this series of tests, a precipitation data set was randomly generated using the mean and standard deviation of 20th century precipitation values recorded at local weather stations and applied over three, one-hundred year periods during which varying long-term precipitation changes were used to simulate the gradual shift from one hydroclimatic mean state to another. To augment these analyses, and to test model derived hypotheses across a diversity of lake morphologies and hydrologic settings, model simulations were also conducted on two hypothetical, hypsographically and hydrologically distinct lakes, representing variations on both Castor and Scanlon Lakes. In the third series of experiments, the standard deviation of interannual precipitation forcing factors (established in the second series of tests) was varied over three, one hundred year periods in order to simulate lake hydrologic and isotopic responses to changes in the variance of stochastic variability in the absence of mean state forcing.

2.2 METHODS

2.2.1 Study sites and regional climate

Scanlon Lake (SL) and Castor Lake (CL) are located in the Limebelt region of north-central Washington on a terrace margin of the Okanogan River. The lake catchments are small ($< 1 \text{ km}^2$) and occupy a topographic high isolated from regional groundwater. Climate in the area is seasonal and semi-arid, and is largely controlled by the interaction between the Pacific

westerlies and the Aleutian low- and north Pacific high-pressure systems.

2.2.2 Model structure

The hydrologic and isotope mass-balance of CL and SL are calculated in the model using the following equations:

$$\frac{dV_L}{dt} = \Sigma I - \Sigma O \quad (1.1)$$

$$\frac{d(V_L \delta_L)}{dt} = \Sigma I \delta_I - \Sigma O \delta_O \quad (1.2)$$

where V_L is lake volume, ΣI and ΣO are the total surface and below ground inflows to and outflows from the lakes, and δ is the isotopic composition of the inflows and outflows. These equations provide the basis for a system of twelve ordinary differential equations, compiled using numerical modeling software, that describe water and isotope dynamics for the lake catchment systems. More specifically, the hydrologic model is defined by six separate differential equations corresponding to unique water reservoirs (catchment groundwater, snowpack, shallow and deep lake volumes, etc.). Volumetric fluxes to the reservoirs are described by model sub-routines for lake stratification, soil moisture availability, snowpack, and surface and subsurface inflow. Additional detail regarding calculation of the flux components as well as all other aspects of the model is provided by Steinman et al. (2010a). All model simulations were conducted with numerical modeling software using the fourth-order Runge-Kutta numerical integration method.

2.2.3 Mean state precipitation forcing simulation structure

In the first series of model simulations monthly average climate data and modern catchment parameter datasets were used to approximate the monthly and seasonal variability of CL and SL water levels, and to evaluate the transient (i.e., short-lived) and longer term, steady state sensitivity of the lakes to precipitation changes. Each set of sensitivity simulations was conducted on a monthly time-step over ~63 model years using modern catchment parameters and average climate data for the 20th century. At the 501st simulation month, the precipitation rate was either increased or decreased by 50% and maintained at the altered value for the remainder of the test in order to simulate large changes in mean hydroclimatic conditions.

2.2.4 Stochastic precipitation forcing simulation structure

To explore the interplay between stochastic variability and mean state change in hydroclimate on closed-basin lake water balance and $\delta^{18}\text{O}$ values, hydrologic forcing simulations were conducted in which randomly adjusted precipitation rates (i.e., stochastic variations in precipitation) were superimposed upon long term changes in mean precipitation levels. Specifically, for each simulation year, a forcing factor was produced using a random number algorithm and applied to each month during the year. Random forcing factors were generated using a standard deviation equal to the coefficient of variation of annual precipitation over the 20th century (0.28) calculated from local weather station data sets (Steinman et al. 2010a). This method is fundamentally similar to that of the more sophisticated daily stochastic weather generators applied by global climate models but is simpler because randomness in monthly,

rather than daily, precipitation and only one climate variable (in this case, precipitation) are simulated (Richardson 1981; Katz 1996; Mearns et al. 1997).

For the combined mean state and stochastic variability tests, steady state conditions were achieved during the first twenty five years of each experiment, after which precipitation rates were randomly adjusted on an inter-annual basis, as described above, to simulate stochastic climate variability. During the first one-hundred year simulation period (i.e., during model years 25 to 125), no mean state precipitation forcing was applied. In the subsequent one-hundred year period (model years 125 to 225), the average precipitation value was gradually increased or decreased toward a fixed percentage ($\pm 50\%$ of modern) to simulate variation in the mean hydroclimate state. During the third one-hundred year simulation period (model years 225–325), precipitation values were held at the adjusted mean state value (again, either 50% above or below modern) achieved at model year 225 to simulate the effects of stochastic variability within an altered long-term average precipitation amount. Only one set of one-hundred stochastic forcing factors was applied in each simulation in order to ensure that the standard deviation of precipitation values in each simulation period were identical, and to thereby maintain consistency in the simulations.

Similarly, to investigate the influence of changes in the variance of stochastic forcing in the absence of mean state change, simulations were conducted in which the standard deviation of randomly adjusted precipitation rates was increased over the course of the tests. The general structure of the stochastic forcing variance change simulations was identical to the combined mean state and stochastic forcing simulations with the exceptions that no mean state forcing was applied and that the standard deviation of the precipitation forcing factors increased from 0.21 to

0.35 (i.e., from -25% to +25% of 0.28, the 20th century coefficient of variation of precipitation) from the first to the third simulation periods, respectively.

2.3 RESULTS

2.3.1 Simulation of mean state precipitation forcing

Steady state simulations predicted extensive intra-annual isotopic variability at SL (Figure 2.1A, B) and CL (Figure 2.1C, D), with $\delta^{18}\text{O}$ variations of approximately 17‰ and 12‰, respectively, between winter and summer months and a maximum summer $\delta^{18}\text{O}$ value at SL ~5‰ greater than that of CL prior to precipitation forcing at model month 501. These predictions are consistent with modern observations of intra-annual hydrologic and isotopic variability at CL and SL (Steinman et al. 2010a).

After a 50% decrease in precipitation at month 501, both CL and SL exhibited transient annual maximum $\delta^{18}\text{O}$ increases of ~5‰ and 6‰, respectively, with CL taking longer (relative to SL) to achieve transient maxima and steady state $\delta^{18}\text{O}$ values. In contrast, after a 50% increase in precipitation, both CL and SL exhibited short-lived maximum annual $\delta^{18}\text{O}$ decreases of ~2‰ and 4‰, respectively. After achieving transient maxima or minima, annual $\delta^{18}\text{O}$ values at both lakes transitioned to new steady state values corresponding to the precipitation change initiated at month 501. In the decreased precipitation scenario, new annual maximum steady state $\delta^{18}\text{O}$ values were higher than the values prior to precipitation forcing, although the values at CL were appreciably higher than at SL (an increase of ~2.6‰ and 0.7‰, respectively). In the increased precipitation scenario, new steady state $\delta^{18}\text{O}$ values were also higher than the values

prior to precipitation forcing, although the increase at SL ($\sim 0.2\text{‰}$) was significantly smaller than that of CL ($\sim 1.3\text{‰}$).

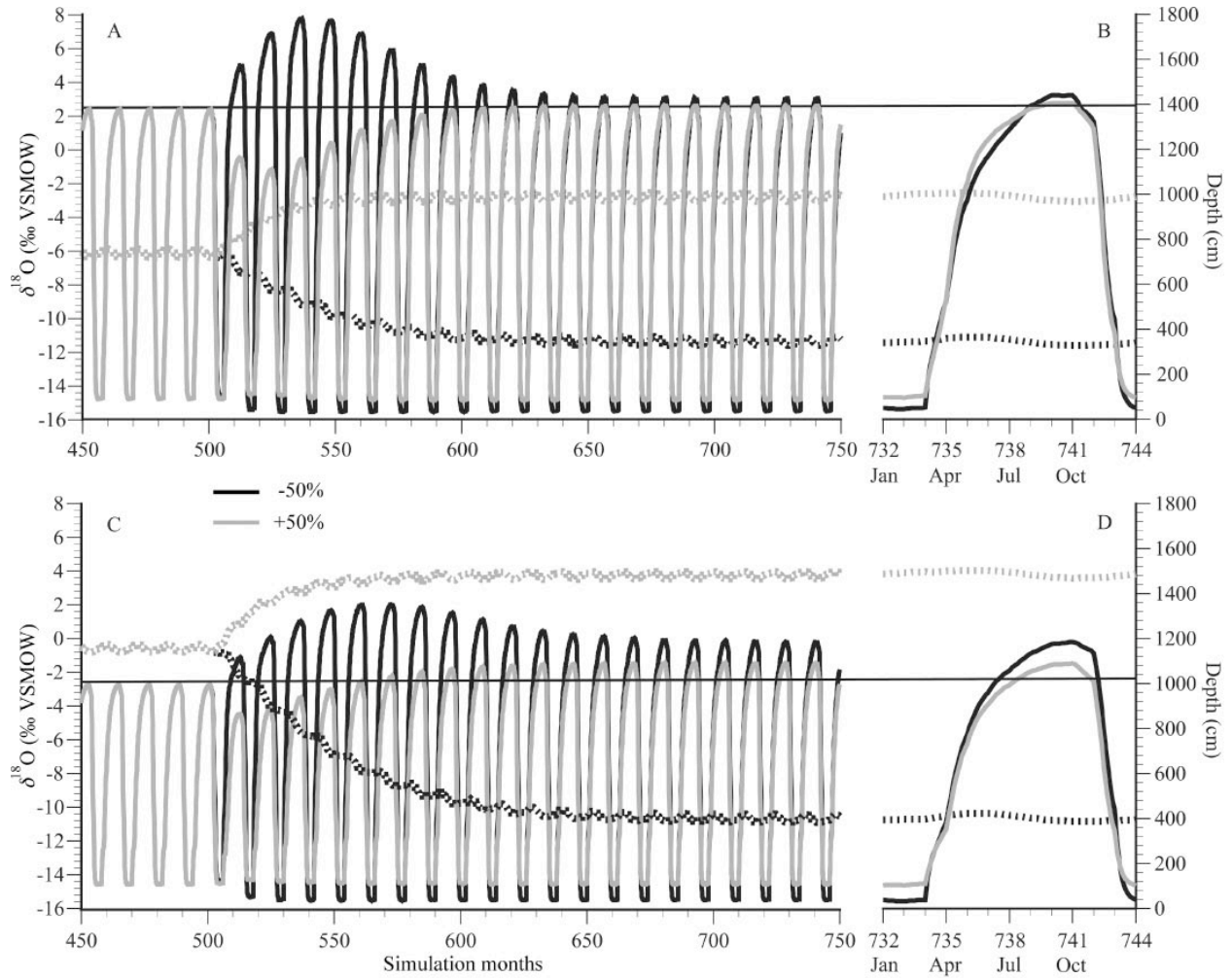


Figure 2.1 Depth (dashed lines) and lake water $\delta^{18}\text{O}$ value changes (solid lines) at SL and CL in response to mean state precipitation increases of 50% (gray lines) and decreases of 50% (black lines) over model simulation months 450 to 750 (A and C, respectively) with an expanded view of model months 732 to 744 (B and D, respectively) following reestablishment of steady state. In both lake simulations precipitation changes were initiated at month 501.

2.3.2 Simulation of combined mean state and stochastic precipitation forcing

Over the course of the SL simulations, stochastic variability in precipitation led to large inter-annual fluctuations in average summer (June–August) lake volume and $\delta^{18}\text{O}$ values. In the

mean state precipitation decrease scenario, the magnitude of these fluctuations increased during the second one-hundred year simulation period and reached a maximum during the third simulation period (Figure 2.2, Table 2.1). Conversely, in the precipitation increase scenario, the magnitude of these fluctuations decreased during the second one-hundred year simulation period and reached a minimum during the third simulation period (Figure 2.3). In response to mean state precipitation change, SL summer average $\delta^{18}\text{O}$ values increased slightly over the course of both simulations, with a larger magnitude increase occurring during the precipitation reduction scenario (Table 2.1).

The response of CL to stochastic variability in precipitation was similar to that of SL, in that the magnitude of inter-annual $\delta^{18}\text{O}$ and lake volume changes increased from the first to the third simulation period in response to a mean state precipitation decrease (Figure 2.4, Table 2.1). In the precipitation increase scenario, the smallest magnitude inter-annual $\delta^{18}\text{O}$ and volume changes occurred during the third one-hundred year period (Figure 2.5, Table 2.1). The response of CL to mean state precipitation changes was, however, different than that of SL, in that average summer $\delta^{18}\text{O}$ values substantially increased from one simulation period to the next in response to mean state precipitation increases and decreases.

At both CL and SL, large changes in residence time, surface area to volume (SA:V) ratio values, and outflow proportions occurred in response to both stochastic and mean state precipitation variability forcing (Figures 2.2–2.5, Table 2.1). In all cases, residence time values exhibited a strong association with lake SA:V ratio values and evaporative outflow proportions, with residence times decreasing in response to increases in evaporative outflow proportions and SA:V ratio values.

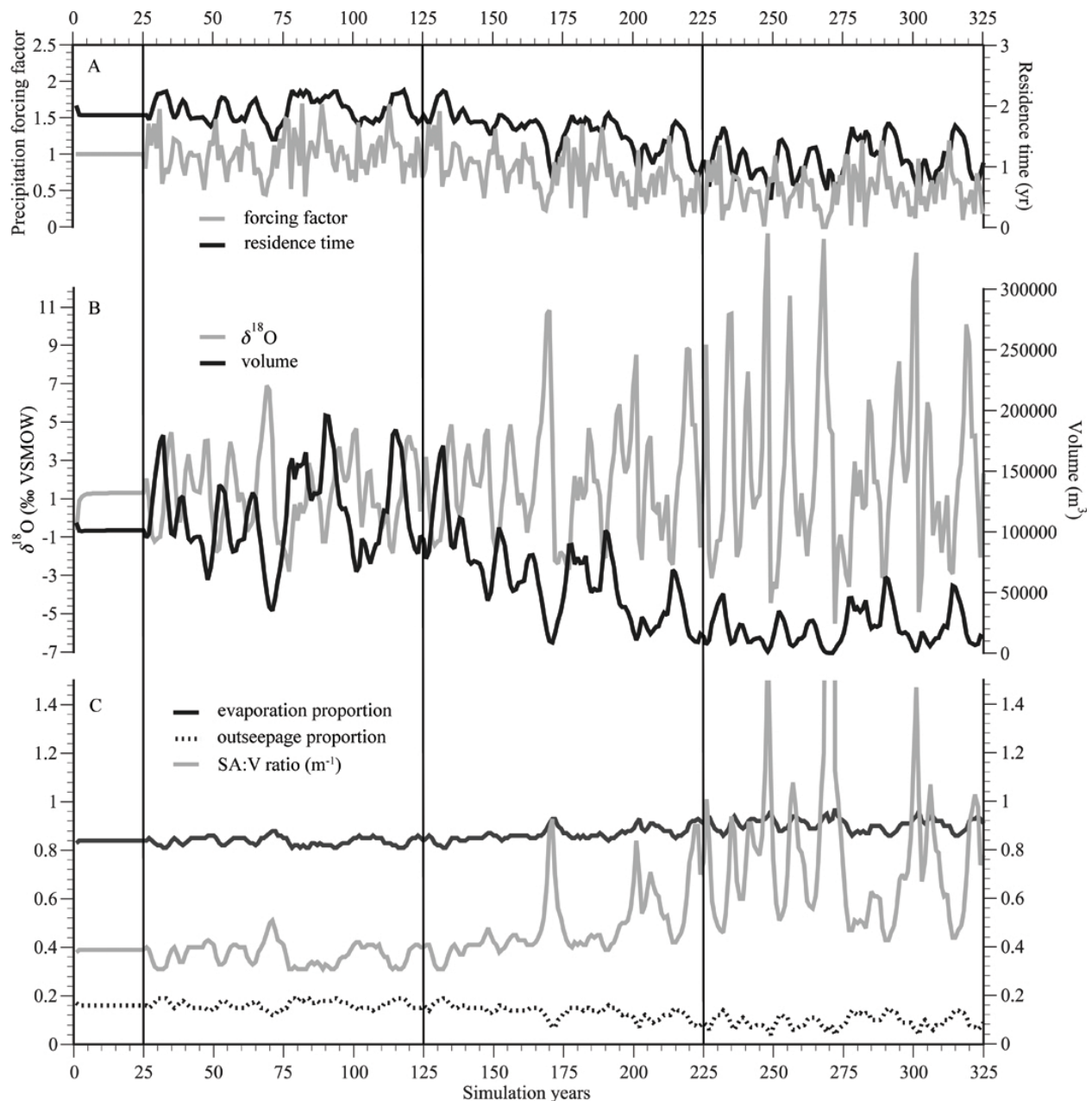


Figure 2.2 SL responses to the superimposition of stochastic variations and a mean state precipitation decrease of 50%. Between years 0 and 25, no changes in precipitation were applied. Between years 25 and 125, precipitation was varied stochastically with a mean and standard deviation equal to observed 20th century values. Between years 125 and 225, mean state precipitation was incrementally decreased by 50% while maintaining stochastic variations applied in years 25 through 125. Between years 225 and 325, mean state precipitation was maintained at a value 50% below the 20th century average while again maintaining the stochastic variations applied in the prior one-hundred year simulation periods. (A) Superimposed stochastic and mean state precipitation forcing factors (gray line) and residence times (black line). (B) Average summer (June–August) surface water $\delta^{18}\text{O}$ values (gray line) and lake volumes (black line) resulting from described precipitation changes. (C) Lake SA:V ratio values (gray line) and the proportions of water lost to evaporation (black line) and outseepage (dashed line). Vertical lines delineate one-hundred year simulation periods identified in Table 2.1.

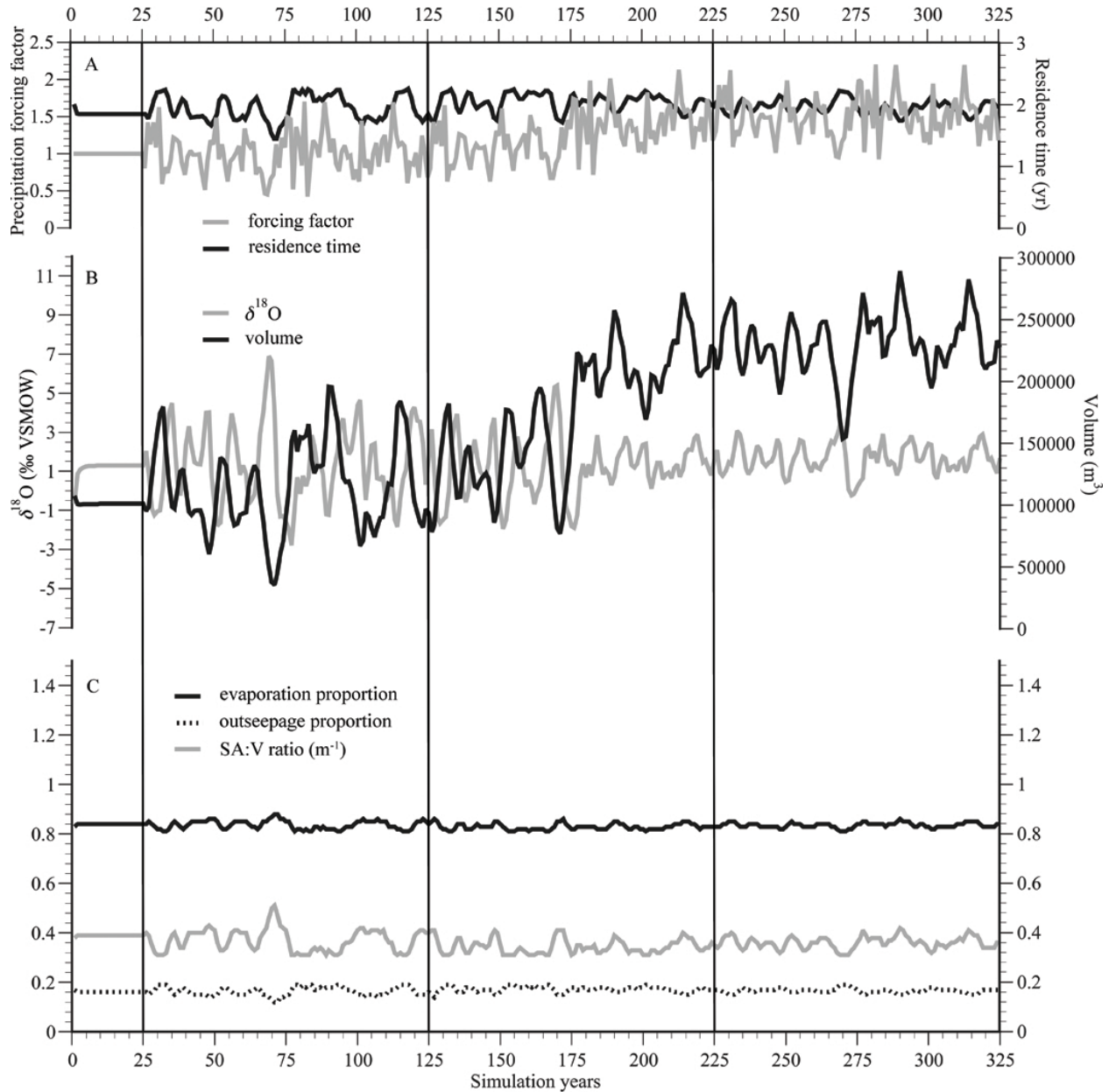


Figure 2.3 SL responses to the superimposition of stochastic variations and a mean state precipitation increase of 50%. Between years 0 and 25, no changes in precipitation were applied. Between years 25 and 125, precipitation was varied stochastically with a mean and standard deviation equal to observed 20th century values. Between years 125 and 225, mean state precipitation was incrementally increased by 50% while maintaining stochastic variations applied in years 25 through 125. Between years 225 and 325, mean state precipitation was maintained at a value 50% above the 20th century average while again maintaining stochastic variations applied in the prior one-hundred year simulation periods. (A) Superimposed stochastic and mean state precipitation forcing factors (gray line) and residence times (black line). (B) Average summer (June–August) surface water $\delta^{18}\text{O}$ values (gray line) and lake volumes (black line) resulting from described precipitation changes. (C) Lake SA:V ratio values (gray line) and the proportions of water lost to evaporation (black line) and outseepage (dashed line).

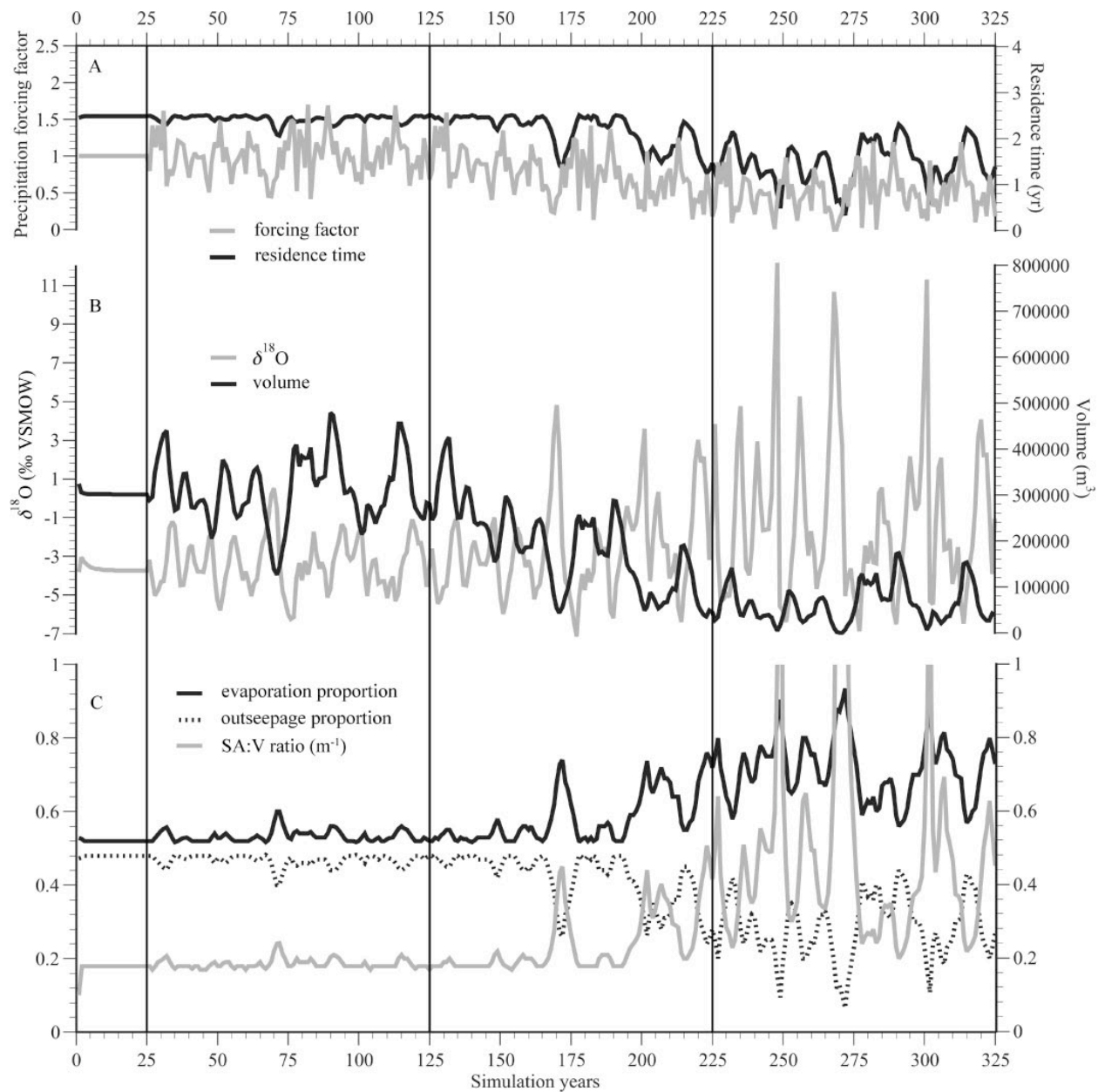


Figure 2.4 CL responses to the superimposition of stochastic variations and a mean state precipitation decrease of 50%. Between years 0 and 25, no changes in precipitation were applied. Between years 25 and 125, precipitation was varied stochastically with a mean and standard deviation equal to observed 20th century values. Between years 125 and 225, mean state precipitation was incrementally decreased by 50% while maintaining stochastic variations applied in years 25 through 125. Between years 225 and 325, mean state precipitation was maintained at a value 50% below the 20th century average while again maintaining stochastic variations applied in the prior one-hundred year simulation periods. (A) Superimposed stochastic and mean state precipitation forcing factors (gray line) and residence times (black line). (B) Average summer (June–August) surface water $\delta^{18}\text{O}$ values (gray line) and lake volumes (black line) resulting from described precipitation changes. (C) Lake SA:V ratio values (gray line) and the proportions of water lost to evaporation (black line) and outseepage (dashed line).

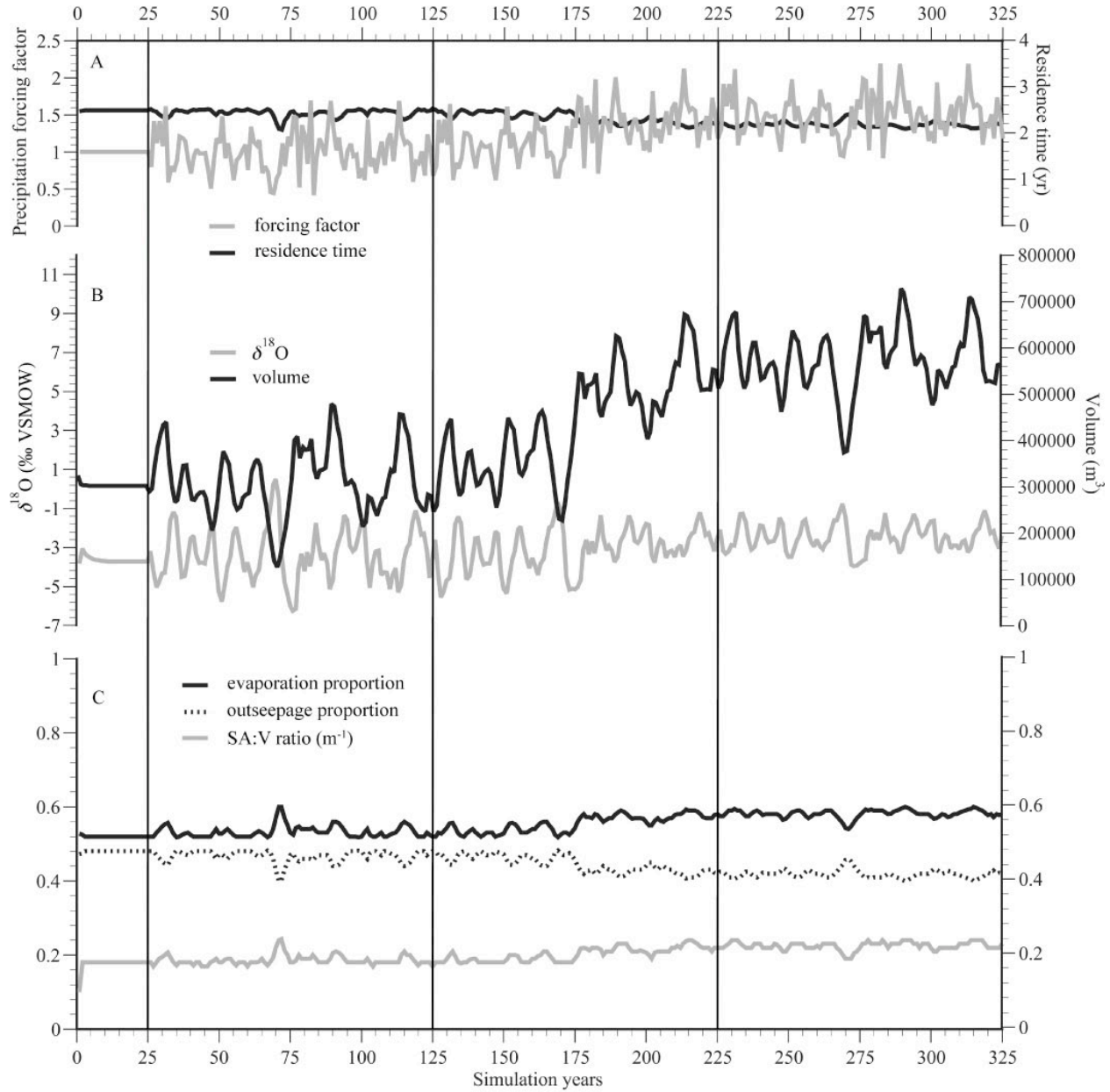


Figure 2.5 CL responses to the superimposition of stochastic variations and a mean state precipitation increase of 50%. Between years 0 and 25, no changes in precipitation were applied. Between years 25 and 125, precipitation was varied stochastically with a mean and standard deviation equal to observed 20th century values. Between years 125 and 225, mean state precipitation was incrementally increased by 50% while maintaining stochastic variations applied in years 25 through 125. Between years 225 and 325, mean state precipitation was maintained at a value 50% above the 20th century average while again maintaining stochastic variations applied in the prior one-hundred year simulation periods. (A) Superimposed stochastic and mean state precipitation forcing factors (gray line) and residence times (black line). (B) Average summer (June–August) surface water $\delta^{18}\text{O}$ values (gray line) and lake volumes (black line) resulting from described precipitation changes. (C) Lake SA:V ratio values (gray line) and the proportions of water lost to evaporation (black line) and outseepage (dashed line).

Table 2.1 Average summer (June–August) lake variables for each simulation (sim.) period in response to stochastic variations and changes in mean state precipitation.

	Mean precip. change	Sim. period	Vol. (m ³)	Avg. inter-annual % vol. change	Depth (cm)	Surface lake $\delta^{18}\text{O}$ (%)	Surface lake $\delta^{18}\text{O}$ standard deviation	Evap. Prop.	Outseep. Prop.	SA:V ratio (m ⁻¹)	Res. time (yr)
CL	0.5 (-50%)	1	311529	9.1	1165	-3.38	1.36	0.53	0.47	0.19	2.43
		2	183828	14.8	857	-2.65	2.36	0.58	0.42	0.24	2.17
		3	62778	35.2	460	-1.13	4.05	0.72	0.28	0.50	1.48
	1.5 (+50%)	1	311529	9.1	1165	-3.38	1.36	0.53	0.47	0.19	2.43
		2	437107	7.3	1337	-3.09	1.10	0.55	0.45	0.20	2.32
		3	573361	5.1	1480	-2.46	0.69	0.58	0.42	0.23	2.18
SL	0.5 (-50%)	1	114216	11.7	762	1.33	1.99	0.84	0.16	0.37	1.94
		2	60339	19.4	581	1.94	2.91	0.87	0.13	0.49	1.58
		3	20600	43.6	372	2.37	4.64	0.91	0.09	0.76	1.12
	1.5 (+50%)	1	114216	11.7	762	1.33	1.99	0.84	0.16	0.37	1.94
		2	174936	8.5	887	1.19	1.48	0.83	0.17	0.34	2.05
		3	230052	5.1	980	1.65	0.74	0.84	0.16	0.36	1.96
CL2	1.5 (+50%)	1	326003	9.3	1196	-3.74	1.41	0.51	0.49	0.17	2.53
		2	508880	7.2	1463	-4.32	1.10	0.48	0.52	0.15	2.70
		3	739698	4.6	1747	-4.65	0.70	0.45	0.55	0.13	2.88
SL2	0.5 (-50%)	1	71467	15.6	641	-1.31	1.73	0.64	0.36	0.43	1.26
		2	39764	26.0	494	-0.42	2.73	0.69	0.31	0.57	1.08
		3	14752	53.5	323	0.83	4.25	0.77	0.23	0.90	0.81
CL*	-25%	1	307005	7.0	1164	-3.51	1.03	0.53	0.47	0.18	2.45
	0	2	310366	9.3	1163	-3.40	1.37	0.53	0.47	0.19	2.43
	+25%	3	315256	11.6	1164	-3.26	1.72	0.54	0.46	0.19	2.41
SL*	-25%	1	110168	9.13	756	1.27	1.54	0.84	0.16	0.37	1.93
	0	2	113633	12.0	761	1.32	2.00	0.84	0.16	0.37	1.94
	+25%	3	116792	14.7	765	1.42	2.47	0.84	0.16	0.37	1.94

*Stochastic forcing variance change simulations. Percentage change in the standard deviations for each 100 year period are displayed in the 'Mean precipitation change' column.

2.3.3 Simulation of combined mean state and stochastic precipitation forcing within hypothetical lakes

Model simulations were also conducted on two hypothetical lakes, representing variations on the bathymetric and outseepage characteristics of Castor and Scanlon Lakes, and denoted CL2 and SL2, respectively. In the CL2 configuration, SA:V ratio values above a depth

of 12 meters were changed such that values decreased with increasing depth (from the actual, opposite, configuration of increasing values with depth increases). In the SL2 configuration the seepage rate was increased to 1.5 times that of CL to a value of 2.4% of monthly lake volume (Steinman et al. 2010a).

In the CL2 configuration, the $\delta^{18}\text{O}$ response to stochastic variability forcing was similar to that of CL, with standard deviations for both configurations within 0.1‰ for all three simulation periods (Figure 2.6, Table 2.1). The lake water $\delta^{18}\text{O}$ response to a mean state precipitation increase was dissimilar, however, with a lower average value (relative to the actual bathymetric configuration of Castor Lake) during the third simulation period. In the CL2 configuration, the SA:V ratio over the third simulation period decreased in response to increasing volume while seepage and evaporation outflow proportions increased and decreased, respectively.

The lake water $\delta^{18}\text{O}$ response to stochastic variability in the SL2 model test was also similar to that of SL, with standard deviations for both configurations within 0.4‰ over all three simulation periods (Figure 2.7, Table 2.1). The lake water $\delta^{18}\text{O}$ responses to mean state precipitation forcing likewise differed, with the average $\delta^{18}\text{O}$ value in the SL2 configuration appreciably lower in all three simulation periods and increasing from one period to the next. Seepage and evaporation outflow proportions of total lake volume were also markedly different between the true Scanlon Lake and SL2 configurations with a higher outseepage proportion and a lower evaporation proportion in the SL2 configuration over all three simulation periods.

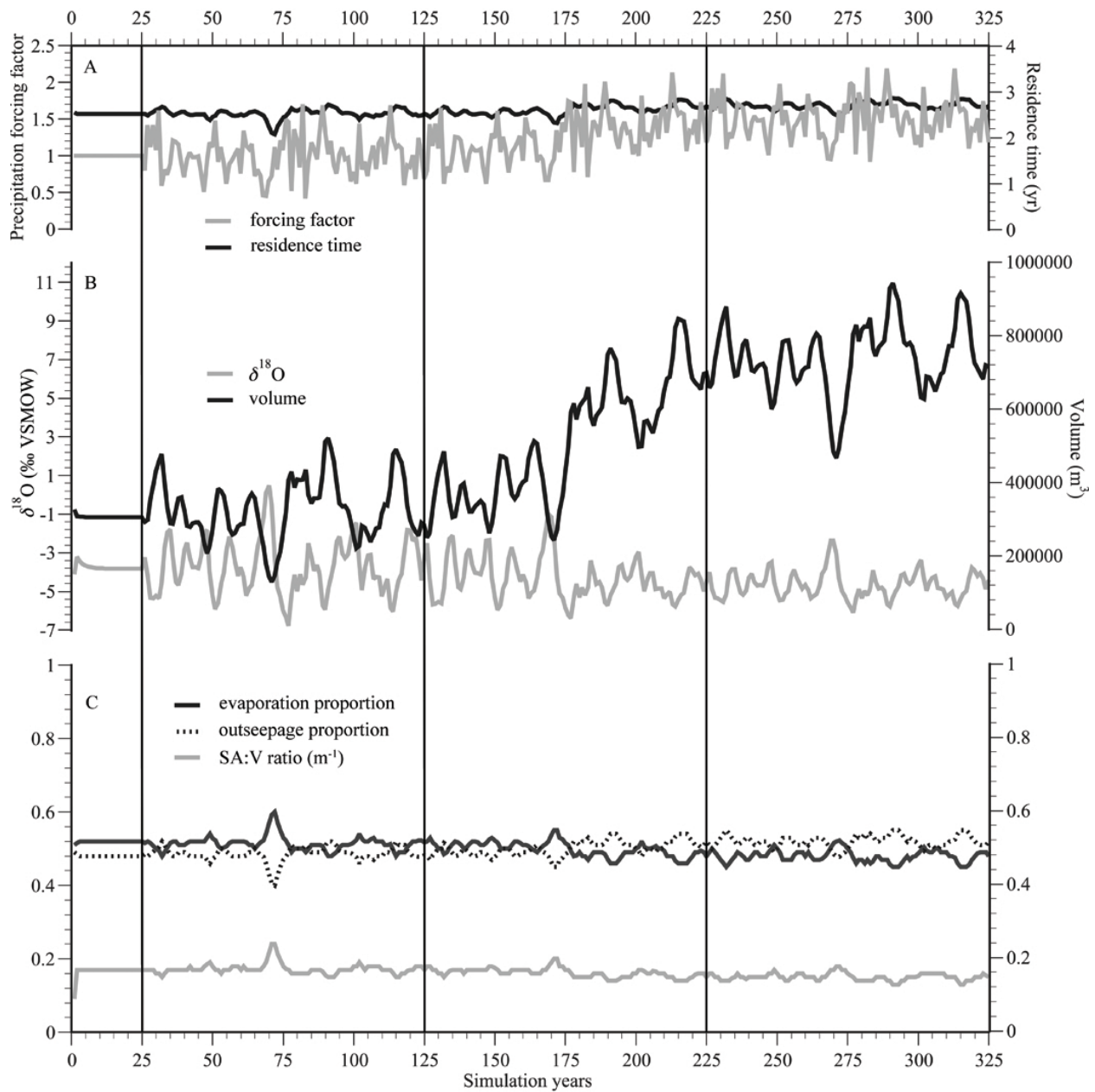


Figure 2.6 CL2 responses to the superimposition of stochastic variations and a mean state precipitation increase of 50%. Between years 0 and 25, no changes in precipitation were applied. Between years 25 and 125, precipitation was varied stochastically with a mean and standard deviation equal to observed 20th century values. Between years 125 and 225, mean state precipitation was incrementally increased by 50% while maintaining stochastic variations applied in years 25 through 125. Between years 225 and 325, mean state precipitation was maintained at a value 50% above the 20th century average while again maintaining stochastic variations applied in the prior one-hundred year simulation periods. (A) Superimposed stochastic and mean state precipitation forcing factors (gray line) and residence times (black line). (B) Average summer (June–August) surface water $\delta^{18}\text{O}$ values (gray line) and lake volumes (black line) resulting from described precipitation changes. (C) Lake SA:V ratio values (gray line) and the proportions of water lost to evaporation (black line) and outseepage (dashed line).

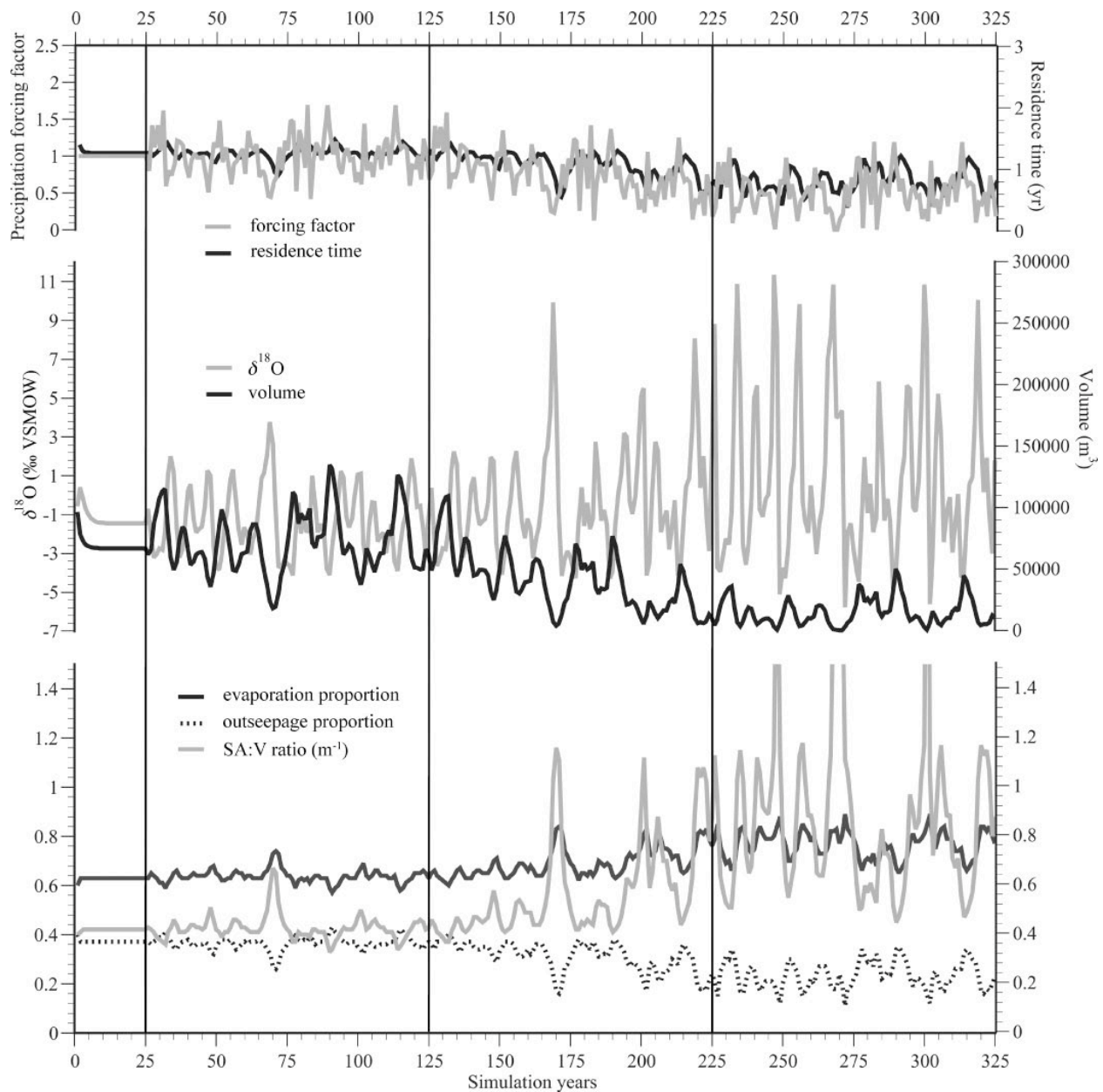


Figure 2.7 SL2 responses to the superimposition of stochastic variations and a mean state precipitation decrease of 50%. Between years 0 and 25, no changes in precipitation were applied. Between years 25 and 125, precipitation was varied stochastically with a mean and standard deviation equal to observed 20th century values. Between years 125 and 225, mean state precipitation was incrementally decreased by 50% while maintaining stochastic variations applied in years 25 through 125. Between years 225 and 325, mean state precipitation was maintained at a value 50% below the 20th century average while again maintaining stochastic variations applied in the prior one-hundred year simulation periods. (A) Superimposed stochastic and mean state precipitation forcing factors (gray line) and residence times (black line). (B) Average summer (June–August) surface water $\delta^{18}\text{O}$ values (gray line) and lake volumes (black line) resulting from described precipitation changes. (C) Lake SA:V ratio values (gray line) and the proportions of water lost to evaporation (black line) and outseepage (dashed line).

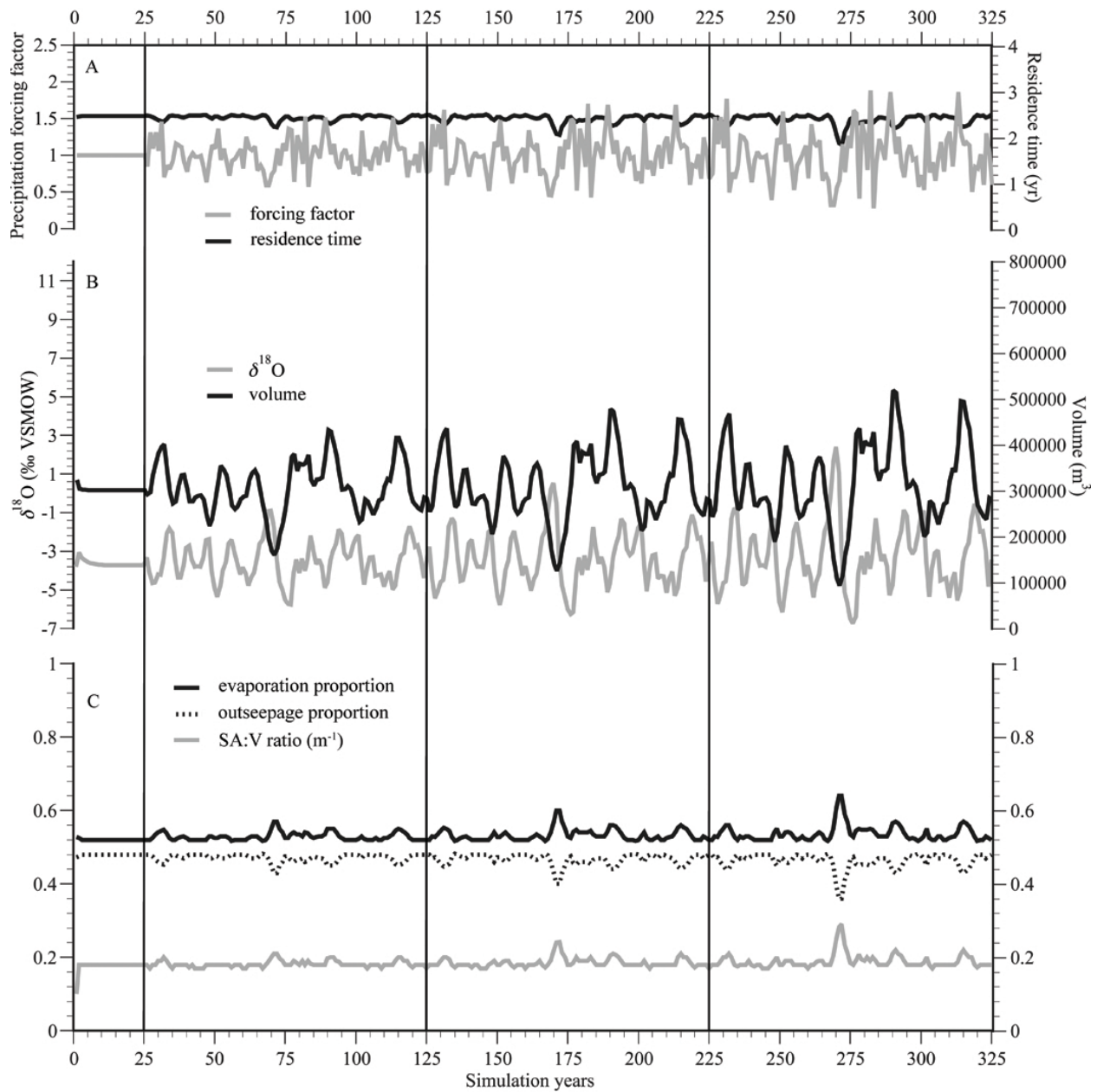


Figure 2.8 CL responses to changes in the variance of stochastic precipitation changes. Between years 0 and 25, no changes in precipitation were applied. Between years 25 and 125, precipitation was varied randomly (stochastically) with a standard deviation 25% lower than the observed 20th century value. Between years 125 and 225, precipitation was varied randomly with a standard deviation equal to the observed 20th century value. Between years 225 and 325, precipitation was varied randomly with a standard deviation 25% greater than the observed 20th century value. (A) Stochastic precipitation forcing factors (gray line) and residence times (black line). (B) Average summer (June–August) surface water $\delta^{18}\text{O}$ values (gray line) and lake volumes (black line) resulting from the described precipitation changes. (C) Lake SA:V ratio values (gray line) and the proportions of water lost to evaporation (black line) and outseepage (dashed line).

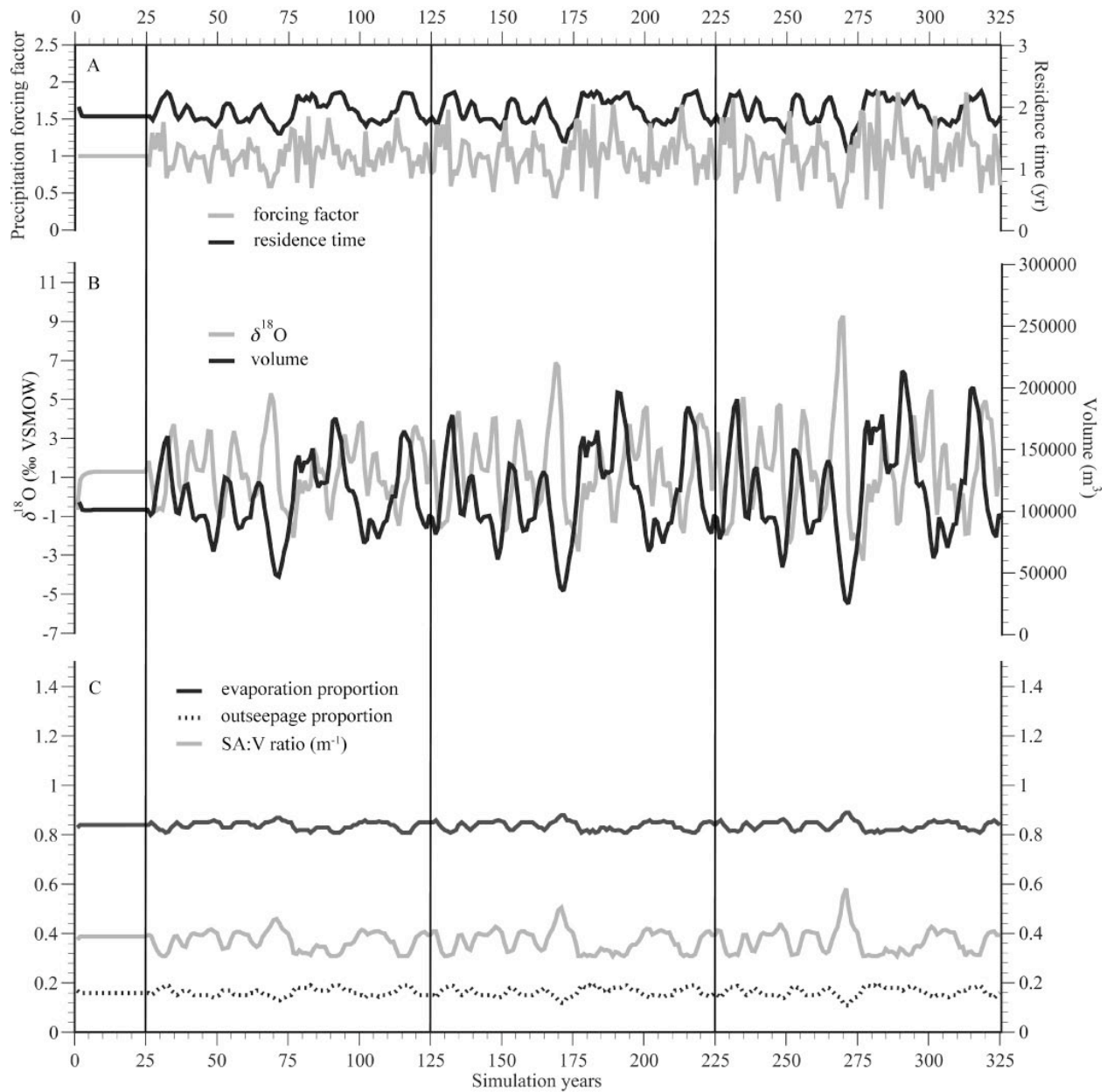


Figure 2.9 SL responses to changes in the variance of stochastic precipitation changes. Between years 0 and 25, no changes in precipitation were applied. Between years 25 and 125, precipitation was varied randomly (stochastically) with a standard deviation 25% lower than the observed 20th century value. Between years 125 and 225, precipitation was varied randomly with a standard deviation equal to the observed 20th century value. Between years 225 and 325, precipitation was varied stochastically with a standard deviation 25% greater than the observed 20th century value. (A) Stochastic precipitation forcing factors (gray line) and residence times (black line). (B) Average summer (June–August) surface water $\delta^{18}\text{O}$ values (gray line) and lake volumes (black line) resulting from the described precipitation changes. (C) Lake SA:V ratio values (gray line) and the proportions of water lost to evaporation (black line) and outseepage (dashed line).

2.3.4 Simulation of variance changes in stochastic precipitation forcing

In the case of both CL and SL, changes in the standard deviation of interannual precipitation forcing led to commensurate changes in the standard deviation of interannual lake water $\delta^{18}\text{O}$ values and volume changes (Figures 2.8, 2.9; Table 2.1). No large scale deviations from mean state values for any of the analyzed lake parameters were observed with the exception of lake volume, which increased by approximately 6% at SL and 3% at CL between the first and third simulation periods.

2.4 DISCUSSION

2.4.1 Lake responses to mean state precipitation forcing

Mean state precipitation simulation results demonstrated that SL has a higher maximum annual $\delta^{18}\text{O}$ value relative to CL as a result of the larger proportion of water lost through evaporation, a fractionating pathway, in comparison to outseepage, a non-fractionating pathway (Table 2.1) (Steinman et al. 2010a). SL also exhibits a stronger transient response to precipitation forcing. The slower equilibration time of CL occurs because the higher residence time and the relatively low SA:V ratio result in inter-annual volumetric fluxes that are, in proportion to lake volume, smaller. This in turn results in a less pronounced transient lake water $\delta^{18}\text{O}$ response and a slower return to steady state conditions. Additionally, CL exhibits a post-transient maximum annual steady state $\delta^{18}\text{O}$ value that is, in both forcing scenarios, larger relative to the pre-forcing value, while SL, in contrast, exhibits a post-transient maximum annual

steady state value that is nearly identical to the pre-forcing value (Figure 2.1). This is again due to disparities in the outflow proportions, in that the greater proportion of seepage outflow at CL (and the consequently smaller evaporative outflow proportion) result in a greater sensitivity of steady state $\delta^{18}\text{O}$ values to SA:V ratio changes with changing depth. Specifically, as lake level either increases or decreases at CL, the SA:V ratio increases, which leads to an increase in the proportion of water leaving the lake through evaporation. At SL, however, the response is different in that the low outseepage rate results in an evaporation outflow proportion that is high regardless of the SA:V ratio, resulting in a minimal steady state $\delta^{18}\text{O}$ change.

2.4.2 Lake responses to combined mean state and stochastic precipitation forcing

A comparison of the SL and CL precipitation variability simulation results reveals several differences between the isotopic and hydrologic responses of the two lakes. Perhaps most notably, in every simulation period of the precipitation change scenarios (both +50% and -50%), the standard deviation of the average summer isotopic $\delta^{18}\text{O}$ values at SL is higher than the corresponding value for CL (Table 2.1). This can be explained by the stronger transient response to hydrologic forcing at SL (*see* Section 2.4.1), which results from the lower volume and residence time and higher SA:V ratio values. A related observation is that, for both SL and CL, as lake volume increases in response to increasing mean state precipitation, the standard deviation of the summer average $\delta^{18}\text{O}$ values decreases, and vice versa. At both CL and SL, as the mean annual precipitation total increases, and the standard deviation of precipitation values remains unchanged, lake level and volume will increase, resulting in volumetric fluxes associated with stochastic variability that are proportionally smaller in comparison to total lake volume. As precipitation amounts decrease, in contrast, the volumetric fluxes associated with

stochastic precipitation changes become larger relative to total lake volume.

The summer average $\delta^{18}\text{O}$ values of CL and SL also show dissimilarities, most notably that in every simulation period, SL $\delta^{18}\text{O}$ values are comparatively higher than CL values. This occurs primarily because SL has a lower outseepage rate and consequently, an evaporative outflow proportion that is higher than that of CL, which leads to greater overall evaporative enrichment of SL lake waters regardless of the precipitation forcing scenario (Table 2.1).

The similarity in the direction of the SL and CL steady state responses to mean state precipitation changes is also conspicuous, in that long-term precipitation increases result in increased lake volumes and summer average $\delta^{18}\text{O}$ values, a somewhat counterintuitive result given that decreasing $\delta^{18}\text{O}$ values are typically associated with increasing lake volumes. This result can be explained by the interplay between the outseepage flux proportions and the SA:V ratio values which at SL and CL increase with increasing depth above ~8.5 and 12 meters, respectively (*see* Section 2.4.1).

The precipitation reduction scenarios provide an example of how the direction of the SA:V ratio can influence lake steady state $\delta^{18}\text{O}$ values. For both SL and CL, over the first half of the second simulation period (simulation years 125–175), lake level decreases while the SA:V ratio varies only slightly, which in turn leads to minimal change in mean state summer average $\delta^{18}\text{O}$ values (Figures 2.2, 2.4). Not until simulation year 175, when lake volume decreases to the extent that the SA:V ratio value begins to increase, does the increase in CL and SL summer average $\delta^{18}\text{O}$ values begin.

Additionally, for both CL and SL, a decrease in residence time occurs in response to 50% increases and decreases in mean state precipitation. In both cases, this can be explained in part by the increase in the SA:V ratio with both increasing and decreasing depth. As volume

increases, surface area increases to a proportionally greater extent, allowing greater volumetric loss through evaporation and a larger lake volume to outflow ratio.

2.4.3 Hypothetical lake responses to combined mean state and stochastic precipitation forcing

In the hypothetical CL2 configuration, in which SA:V ratio values increase with increasing depth above 12 meters, mean state precipitation increases resulted in a decrease in steady state $\delta^{18}\text{O}$ values, a response opposite that of the CL configuration under the same precipitation forcing scenario (Figure 2.6). This opposite response can again be explained by the interplay between SA:V ratio values and outseepage flux proportions. In the CL2 configuration, as lake level increases, SA:V ratio values decrease rather than increase (as in the CL configuration), leading to a decrease in the proportion of water lost through evaporation. Summer average $\delta^{18}\text{O}$ values therefore decrease in response to the decrease in evaporative enrichment and the consequent increase in water lost through outseepage.

In the hypothetical SL2 configuration the outseepage rate was increased by a factor of three (i.e., from 0.007 to 0.021) relative to the estimated value for Scanlon Lake. Consequently, the average summer $\delta^{18}\text{O}$ values prior to mean state precipitation forcing were lower due to the relative decrease in the proportion of water lost through evaporation (Figure 2.7). Just as the small outseepage rate in the SL simulations resulted in a minimal response to mean state hydrologic forcing, the relatively large outseepage rate in the SL2 simulations resulted in a substantial isotopic response. This inference is supported by the large increase in summer average $\delta^{18}\text{O}$ values and in the evaporation outflow proportion observed during the second and third simulation periods (Table 2.1).

2.4.4 Lake responses to variance changes in stochastic precipitation forcing

Hydrologic responses to changes in stochastic precipitation were similar at CL and SL in that an increase in the standard deviation of interannual precipitation values lead to an increase in average lake volume (Table 2.1). This apparent mean state hydrologic sensitivity to stochastic forcing can be explained by mechanisms controlling water delivery to the lake. In accordance with fundamental catchment hydrologic processes, the model calculates runoff on the basis of available water capacity (AWC) and the intra-annual water surpluses and deficits resulting from seasonal variability in precipitation and evapotranspiration. Specifically, when precipitation exceeds evapotranspiration, catchment AWC is reached (i.e, soils are saturated) and runoff to the lake occurs. Conversely, when precipitation does not exceed evapotranspiration, catchment AWC is not reached, and runoff does not occur. One consequence of this simple hydrologic process is a non-linear relationship between precipitation and runoff. For example, when soils are saturated, increasing precipitation will result in increasing runoff until precipitation rates decrease (or evapotranspiration rates increase) to a level at which soils are no longer saturated. At this point, further decreases in precipitation are irrelevant in determining the runoff rate, which remains zero until precipitation rates increase (or evapotranspiration rates decrease) to the point at which soils are again saturated. Long term average lake volume is therefore influenced to a greater extent by the magnitude of positive hydrologic forcing (i.e., precipitation increases) than by the magnitude of negative hydrologic forcing, such that increases in the variance of stochastic forcing result in more frequent high-volume precipitation and runoff events that increase long-term lake volume.

2.5 CONCLUSIONS

2.5.1 Implications for paleoclimate studies

In the interpretation of closed-basin lake sediment oxygen isotope records a frequent assumption is that long term (century- to millennial-scale) increases in $\delta^{18}\text{O}$ values correspond to decreases in effective moisture or precipitation-evaporation balance. The model simulations of stochastic and mean state precipitation changes presented here demonstrate that this assumption may not always be valid, as the interplay between outseepage rates and the effect of SA:V ratio changes with depth on evaporative flux proportions can influence steady state lake water $\delta^{18}\text{O}$ values. Specifically, in lakes with appreciable outseepage rates (such as CL), the extent to which volumetric adjustments will affect evaporation and seepage outflow proportions is in part controlled by the magnitude of the SA:V ratio change. Conversely, in lakes with minimal outseepage (such as SL), the SA:V ratio changes that result from volumetric adjustments will not affect steady state water $\delta^{18}\text{O}$ values because evaporation outflow proportions remain far greater than seepage outflow proportions (no matter the SA:V ratio). Simulation results additionally demonstrate that variability in lake water $\delta^{18}\text{O}$ values is largely controlled by total lake volume and the consequent percentage change in lake volume in response to stochastic variability in hydroclimate. The implications of this inference are two-fold, in that given similar catchments, smaller (volumetrically) closed-basin lakes (e.g., SL) will exhibit a larger standard deviation of annual lake water $\delta^{18}\text{O}$ values than will volumetrically larger closed-basin lakes (e.g., CL), and that the standard deviation of annual $\delta^{18}\text{O}$ values will increase as lake volume decreases and the consequent percentage changes in lake volume increase in response to stochastic forcing (and vice versa). This latter implication is especially relevant to paleoclimate studies, as changes in

the magnitude of closed-basin lake sediment core oxygen isotopic variability may reflect past variations in the mean state of hydroclimate and not stochastic variability. When mean state climate changes are not applied, however, model simulations suggest that lake volumes are controlled largely by stochastic variability, with increasing variance in precipitation resulting in increasing average lake volume (and vice versa) (Figures 2.8, 2.9; Table 2.1). Given large enough variance changes and, as a consequence, significantly greater lake volume, this relationship could result in a reduced lake water oxygen isotopic response to stochastic forcing (*see* Section 2.4.2).

Given the observations and constraints described above, records of stochastic variability in hydroclimate should ideally be generated from sedimentary deposits within closed basin lakes with low outseepage rates, high SA:V ratios, and low volumes, all characteristics that lead to large percentage volumetric changes and correspondingly large isotopic responses. Conversely, mean state changes in hydroclimate should be reconstructed using sediment records from closed-basin lakes with relatively high outseepage rates and SA:V ratios that vary considerably with changing lake level. In some cases, a lake may fulfill all of these requirements. CL, for example, has an outseepage rate high enough to cause strong responses to large-scale mean state climatic forcing, but does not respond to lesser mean state change due to a SA:V ratio that is approximately constant over a wide range of moderate depths.

In many cases, robust paleoclimatic reconstructions may not be developed without isolating the individual components of hydroclimatic change (i.e., mean state and stochastic variability) by coupling analyses from nearby closed-basin lakes with disparate morphologies, outseepage rates, and consequently varying responses to stochastic and mean state hydrologic forcing. In the cases such as Scanlon Lake and Castor Lake, which have differing morphologies

and outflow dynamics, analysis of sediment core $\delta^{18}\text{O}$ records can provide insight into past hydroclimatic conditions and, more importantly, controlling synoptic-scale climate patterns such as the Pacific Decadal Oscillation (generally, positive PDO phases generally correlate to drought in the Columbia River basin) (Mantua and Hare 2002; Gedalof et al. 2004; Knapp et al. 2004). This is only possible, however, when the hydrologic and isotopic responses of the analyzed lake systems to climate change are well understood.

3.0 HYDROLOGIC AND ISOTOPE MASS BALANCE MODEL SIMULATIONS OF LAKE OUTSEEPAGE AND IMPLICATIONS FOR LAKE RESPONSES TO HYDROCLIMATIC VARIATIONS

Model simulations of lake responses to precipitation variations using a variety of outseepage submodel configurations indicate that outseepage algorithms influence lake evaporation and outseepage fluxes and thereby control lake steady state isotopic sensitivity to hydrologic forcing. These tests also demonstrate that lake short term (i.e., transient) isotopic sensitivity is relatively unaffected by the outseepage submodel. In lakes with homogenous outseepage across the lakebed (i.e., outseepage rates decrease only slightly as offshore distance increases) lake steady state responses to hydrologic forcing are minimal, whereas in lakes with spatially heterogeneous outseepage rates (i.e., outseepage rates decrease extensively offshore), strong steady state isotopic responses to hydrologic forcing occur. Lake steady state isotopic responses to dry periods were similar between several exponential outseepage configurations and the volume-based accounting method, suggesting that volume based methods may accurately approximate lake isotopic responses to drought. Conversely, lake steady state isotopic responses to wet periods contrasted between the exponential and volumetric outseepage configurations, indicating that volume based methods, which are strongly influenced by lake surface area to volume (SA-V) ratios, may not be appropriate for simulating lake isotopic responses to lake level increase, especially in lakes in which the SA-V ratio increases as depth increases. The

simulation results presented here also indicate that lakes with spatially homogenous outseepage rates are less isotopically sensitive at steady to hydrologic forcing, and that lakes with a SA-V ratio that decreases with increasing lake level will exhibit stronger steady state isotopic responses to long term precipitation changes.

3.1 INTRODUCTION

Whether qualitative or quantitative, models are a useful tool for identifying hydroclimatic signals in lake sediment oxygen isotope records. One prevalent qualitative model relates lower lake water $\delta^{18}\text{O}$ values to higher lake level resulting from precipitation increases and vice versa (Benson et al. 2002; Leng and Marshal 2004; Shapley et al. 2009). The quantitative model of Steinman et al. (2010a), however, demonstrates that such qualitative methods may not apply in lakes with surface area to volume (SA-V) ratios that increase with increasing lake level. Steinman et al. (2010a) apply a simple seepage model in which the outseepage rate is proportional to the lake volume. Results from their simulations demonstrate that the primary control on the isotopic composition of closed-basin lake water is the proportioning of water between fractionating (evaporation) and non-fractionating (overflow and outseepage) outflow pathways. They further show that as the SA-V ratio increases, the fraction of water lost from the lake through evaporation will increase while the fraction lost through outseepage will decrease. This implies that in lakes with a SA-V ratio that increases at greater lake levels, isotopic enrichment could occur in response to an increase in lake volume. Other studies, however, have demonstrated that lake outseepage fluxes are not necessarily proportional to lake volume, and are instead related to the fraction of lake water exposed to littoral sediment (McBride and Pfannkuch

1975; Pfannkuch and Winter 1984; Cherkauer and Zager 1989; Shaw and Prepas 1990a; 1990b; Almendinger 1990; Bokuniewicz 1992). In accordance with these studies, a rise in lake level leads to increased lake inundation of permeable littoral sediment, causing an increase in the outseepage flux proportion, a decrease in the evaporation outflow proportion, and a consequent decrease in lake water $\delta^{18}\text{O}$ values. Here the potential influence of outseepage configurations on model predictions of lake sensitivity to hydroclimate change is investigated.

The primary objectives of this study are to describe the extent of control of two potentially competing influences on lake outseepage flux proportions, i.e. SA-V ratio change and spatial variation in lake sediment permeability, and to characterize outseepage submodel influences on model predictions of lake water isotopic responses to hydrologic forcing. Steady-state simulations were conducted to investigate Castor Lake responses to precipitation variations using the numeric hydrologic and isotope mass balance model of Steinman et al. (2010a) combined with five different outseepage submodel configurations. In each simulation precipitation was adjusted by $\pm 50\%$. In the first set of simulations, the model calculated outseepage as a simple, linear function of volume (Steinman et al. 2010a). In all remaining simulations the model calculated outseepage using an exponential decay function that relates the outseepage rate to offshore distance. To describe the influence of lake SA-V ratios, additional steady state simulations were conducted on Castor Lake with an altered hypsographic profile using an exponential decay equation to control outseepage similar to that applied in the standard hypsography simulations.

3.2 METHODS

3.2.1 Model development, study sites, and regional climate

Detailed descriptions of model structure, inputs, and calibration, as well as Castor Lake and regional climate can be found in Steinman et al. (2010a) (*see* Chapter 1).

3.2.2 Process based outseepage submodel structure

Four different exponential decay equations (EXP1–EXP4) were applied to approximate the relationship between lake outseepage rates and distance from the shoreline (Figure 3.1). In each case, outseepage rates were highest on the shoreline and decrease exponentially as offshore distance (toward the lake center) increases. Genereux and Bandopadhyay (2001) demonstrated that as the hydraulic conductivity of lake sediment decreases, outseepage rates become more spatially homogenous and can be described by exponential functions that more weakly decay, and vice versa. In order to simulate a wide range of lake sediment heterogeneity and hydraulic conductivities, exponential decay functions ranging from strongly to weakly decaying were applied.

The outseepage submodel applied here is based on calculations of lakebed surface area derived from hypsographic profiles. Using 3-D modeling software, lakebed surface area changes over one-meter depth intervals were calculated (Figure 3.2). The lake surface area at the depth interval of each slice was used to calculate an average radius, which was then subtracted from the maximum possible radius of the lake (200m) to determine the distance of the slice from maximum shoreline. This method ensured that outseepage rates remained constant at each point

in the lakebed regardless of lake level change. Equation 3.1 describes the model calculation for volumetric outseepage fluxes (F_{OSSx}) in the exponential configurations:

$$F_{OSSx} = OS_{EXPx} \times SA_{Sx} \quad (3.1)$$

where OS_{EXPx} represents the outseepage rate for each slice (calculated as a function of distance from maximum shoreline) and SA_{Sx} represents the surface area of the slice. Outseepage volumetric fluxes for lakebed slices from both the shallow lake and deep lake reservoirs (RES_{SL} and RES_{DL} , respectively) were calculated and applied in accordance with the outseepage structure defined in Equations 1.3 and 1.4 (above) and in Steinman et al. (2010a).

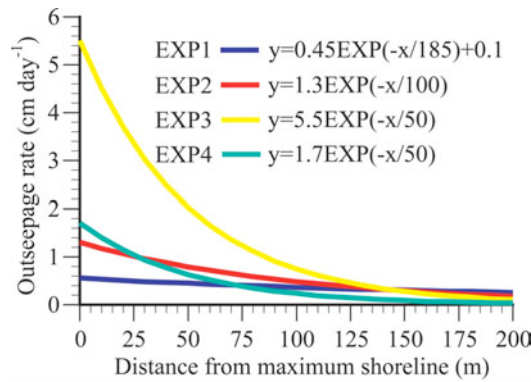


Figure 3.1 Exponential outseepage functions.

3.2.3 Altered hypsography simulations

Markedly, due to large littoral shelves on the northeastern and southwestern shorelines of Castor Lake, the SA-V ratio increases with both increasing and decreasing depth at ~11.5 meters (Figure 3.2). To investigate the influence of the SA-V ratio on lake hydrologic and isotopic responses to precipitation forcing, an altered hypsography configuration was applied in which the SA-V ratio decreases with increasing depth above 11.5 meters (Figure 3.2). Notably, a lower

exponential decay rate (relative to EXP3) was applied in these experiments to balance the lake at a pre-forcing level similar to that of the other simulations.

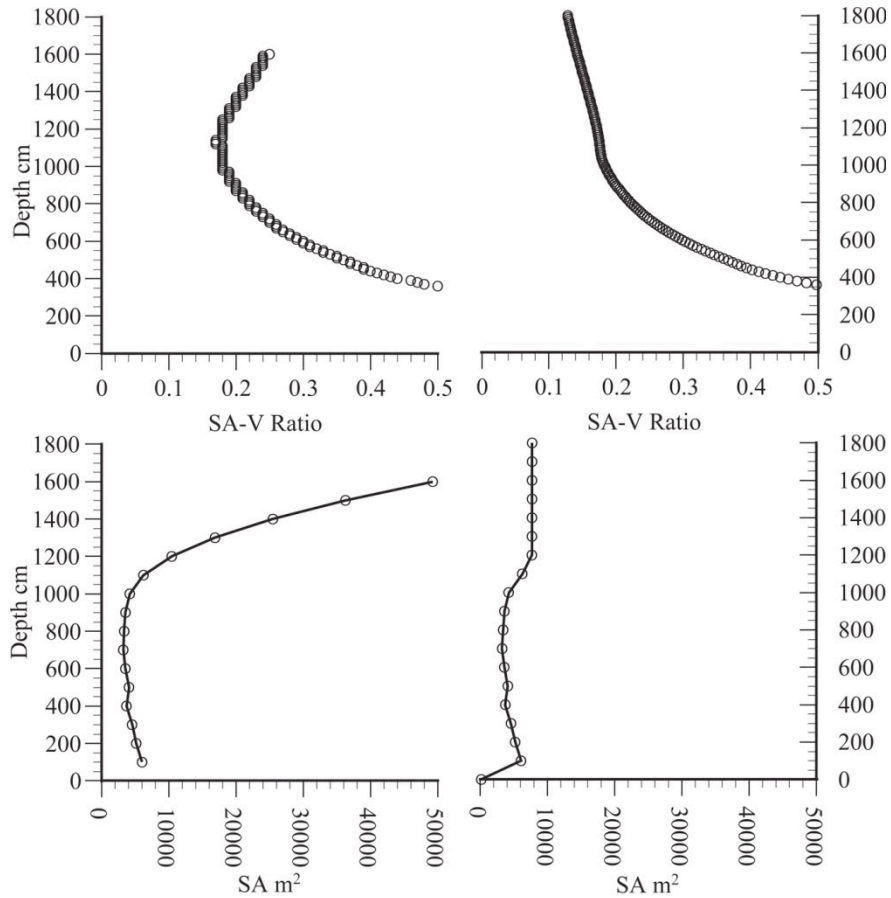


Figure 3.2 Observed Castor Lake hypsography (left) and adjusted Castor Lake hypsography (right) data. Upper panels display lake SA-V ratio changes as a function of depth. Lower panels display the surface area of one meter lakebed slices as a function of depth.

3.2.4 Steady state simulation structure

To simulate the transient and steady state sensitivity of the Castor Lake to precipitation forcing, we used monthly average climate data and modern catchment parameter datasets to approximate the monthly and seasonal variability of Castor Lake water levels. Each set of sensitivity simulations spanned 1000 months or ~83 model years. Following the 501st simulation

month (corresponding to the beginning (October) of the 42nd model hydrologic year) precipitation values either increased or decreased by 50% and remained at this level throughout the duration of the simulation.

3.3 RESULTS

3.3.1 Volumetric outseepage submodel configuration

In the first series of steady state simulations the model calculated outseepage as a function of lake volume. In this configuration, summer (June–August) average $\delta^{18}\text{O}$ values initially increased in response to a decrease in average precipitation occurring at model month 501 (Figure 3.3). Conversely, $\delta^{18}\text{O}$ values initially decreased at model month 501 in response to an increase in average precipitation. In both scenarios (i.e., -50% precipitation and +50% precipitation), the initial transient responses lasted until model month ~700 after which the model achieved equilibrium with $\delta^{18}\text{O}$ values of -1.5‰ and -2.5‰, respectively, considerably different than the preforcing steady state value of -3.7‰. In response to a precipitation decrease of 50% annual average lake evaporation and outseepage flux proportions changed by ~21% (i.e. evaporation outflow as percentage of total outflow increased by ~21% while outseepage decreased by 21%), a larger variation than occurred in the precipitation increase scenario where evaporation and outseepage flux proportions changed by ~6%. In the precipitation decrease simulation the annual average residence time decreased from 2.5 to 1.4 yrs, while in the precipitation increase simulation the annual average residence time decreased and from 2.5 to 2.2 yrs. In both precipitation forcing simulations the SA-V ratio increased (i.e., from 0.18 to 0.44 in

the increase scenario and from 0.18 to 0.23 in the decrease scenario). The equilibrium summer average lake level prior to precipitation forcing was 1166 cm with post-forcing values in the negative and positive precipitation forcing scenarios of 407 cm and 1488 cm, respectively.

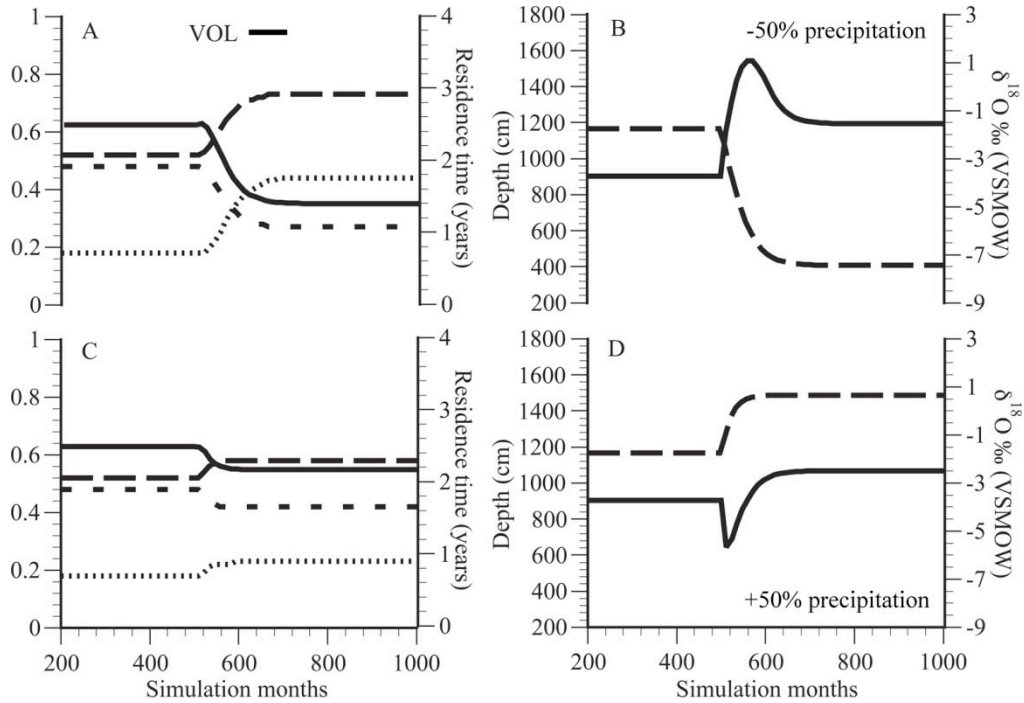


Figure 3.3 Volumetric (VOL) outseepage configuration results. Castor Lake annual average water residence time (solid line), SA-V ratio (fine dashed line), and percentage of outflow via evaporation (coarse dashed line) and seepage (medium dashed line) changes resulting from (A) a 50% decrease and (C) a 50% increase in precipitation. Castor Lake summer (June–August) average surface water $\delta^{18}O$ values (solid line) and lake level (coarse dashed line) resulting from (B) a 50% decrease and (D) a 50% increase in precipitation.

3.3.2 Exponential outseepage configuration 1

In the first exponential outseepage configuration (EXP1), lake outseepage rates decreased only slightly with increasing offshore distance (Figure 3.1). Under these conditions, $\delta^{18}O$ values initially (i.e., transiently) increased in response to a decrease in average precipitation occurring at model month 501, and vice versa (Figure 3.4). In the precipitation decrease scenario the transient response lasted until model month ~700, with the subsequent equilibrium $\delta^{18}O$ value (-

3.7‰) equal to the preforcing steady state value (-3.7‰). Precipitation increase scenario results were similar with pre- and post-forcing equilibrium $\delta^{18}\text{O}$ values of -3.7‰ and -3.8‰, respectively. Lake evaporation and outseepage flux proportions changed by less than 5% in response to both precipitation forcing settings. Residence time (from 2.5 to 0.7 yrs) and SA-V ratio (from 0.18 to 0.70) changes in the precipitation increase scenario were substantial, while in the precipitation decrease scenario, SA-V (from 0.18 to 0.22) and residence time (2.5 to 1.9 yrs) variations were relatively minimal. Pre- and post-forcing equilibrium depth values in the precipitation decrease scenario were 1165 cm and 274 cm, respectively; while in the precipitation increase scenario equilibrium lake depth values increased from 1165 cm to 1427 cm.

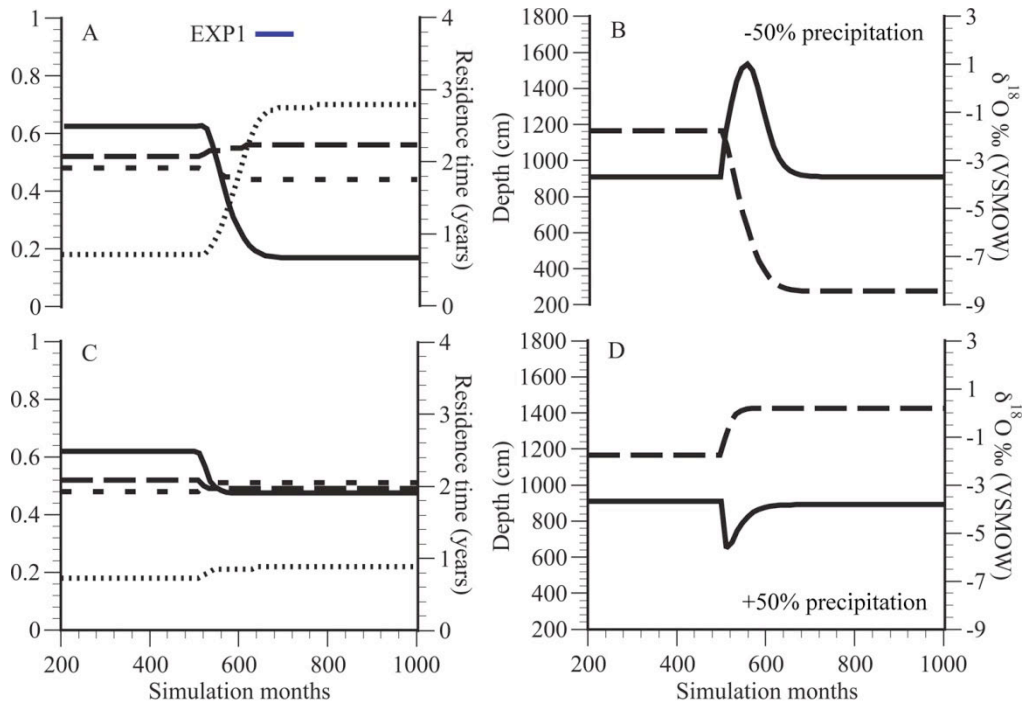


Figure 3.4 EXP1 configuration results. Castor Lake annual average water residence time (solid line), SA-V ratio (fine dashed line), and percentage of outflow via evaporation (coarse dashed line) and seepage (medium dashed line) changes resulting from (A) a 50% decrease and (C) a 50% increase in precipitation. Castor Lake summer (June–August) average surface water $\delta^{18}\text{O}$ values (solid line) and lake level changes (coarse dashed line) resulting from (B) a 50% decrease and (D) a 50% increase in precipitation.

3.3.3 Exponential outseepage configuration 2

In the second exponential outseepage configuration (EXP2), lake outseepage rates moderately decreased with increasing offshore distance (Figure 3.1). Under these conditions, as in the configurations described above, summer average $\delta^{18}\text{O}$ values transiently increased in response to a decrease in average precipitation, and vice versa (Figure 3.5). Equilibrium steady state values differed somewhat from results obtained in EXP1. For example, in response to a 50% precipitation decrease, steady state $\delta^{18}\text{O}$ values increased from -3.5‰ to -2.9‰; whereas in response to a 50% precipitation increase, steady state $\delta^{18}\text{O}$ values decreased from -3.5‰ to -4.5‰. Lake evaporation and outseepage flux proportions exhibited departures of less than 9% in response to both precipitation forcing scenarios. Both the residence time (from 2.5 to 0.9 yrs) and the SA-V ratio (from 0.18 to 0.59) changed considerably in the precipitation decrease simulations, while in the precipitation increase experiments, the residence time (from 2.5 to 1.8 yrs) and SA-V ratio (from 0.18 to 0.21) responses were relatively minimal. Pre- and post-forcing equilibrium depth values in the precipitation decrease scenario were considerably different (1170 cm and 317 cm, respectively), while in the precipitation increase scenario equilibrium lake depth values increased from 1170 cm to 1397 cm.

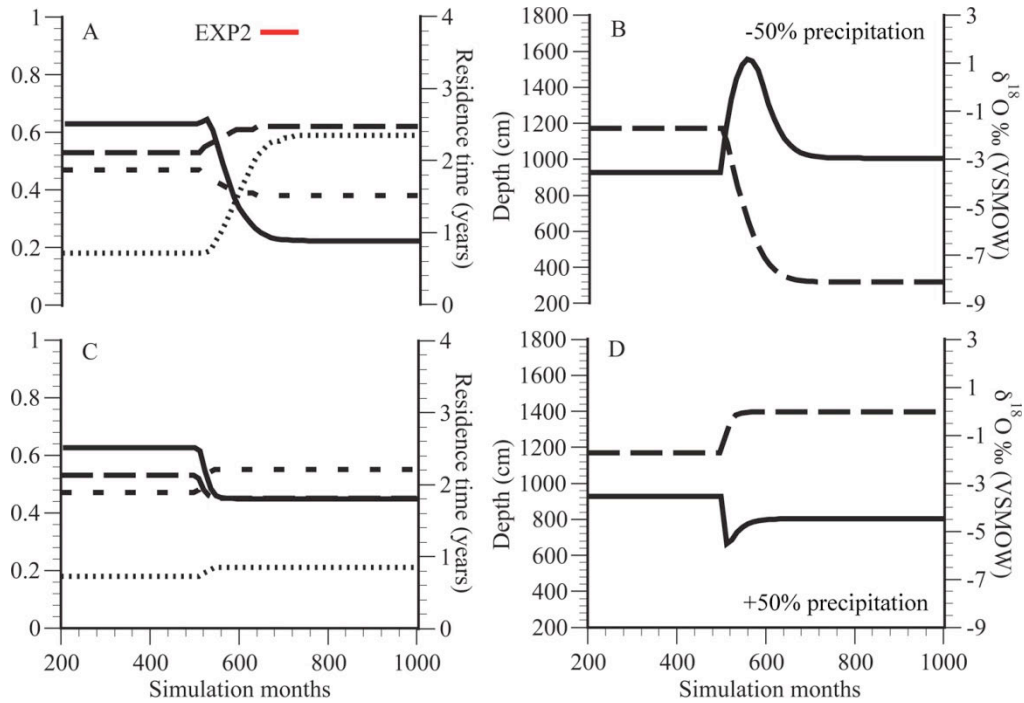


Figure 3.5 EXP2 configuration results. Castor Lake annual average water residence time (solid line), SA-V ratio (fine dashed line), and percentage of outflow via evaporation (coarse dashed line) and seepage (medium dashed line) changes resulting from (A) a 50% decrease and (C) a 50% increase in precipitation. Castor Lake summer (June–August) average surface water $\delta^{18}\text{O}$ values (solid line) and lake level changes (coarse dashed line) resulting from (B) a 50% decrease and (D) a 50% increase in precipitation.

3.3.4 Exponential outseepage configuration 3

In the third exponential outseepage configuration (EXP3), lake outseepage rates rapidly decreased with increasing offshore distance (Figure 3.1), leading to marked changes in lake hydrology and isotope dynamics relative to the other outseepage configurations (Figure 3.6). Under these conditions, $\delta^{18}\text{O}$ values transiently increased in response to a decrease in average precipitation, and vice versa. Equilibrium steady state values differed substantially from results obtained in both EXP1 and EXP2 and from the volumetric outseepage configurations. For example, in response to a 50% change in precipitation (either decrease or increase), summer average equilibrium $\delta^{18}\text{O}$ values changed by $\sim 1.6\text{‰}$, from a pre-forcing value of -3.5‰ to post-forcing values of -1.9‰ and -5.1‰ , respectively. Lake evaporation and outseepage flux

proportions also exhibited extensive departures from preforcing steady state values, changing by ~17% in the precipitation increase scenario and ~13% in the precipitation decrease scenario. Pre- and post-forcing annual average residence times ranged from 2.5 to 1.2 yrs and from 2.5 to 1.7 yrs, respectively, in the negative and positive precipitation forcing simulations, with average annual SA-V ratios ranging from 0.18 to 0.48 and 0.18 to 0.20, respectively. Average summer lake level values varied between a maximum of 1169 cm (pre-forcing) and a minimum of 379 cm (post-forcing), respectively, in the precipitation decrease scenario and 1169 cm (pre-forcing) and 1348 cm (post-forcing) in the precipitation increase scenario.

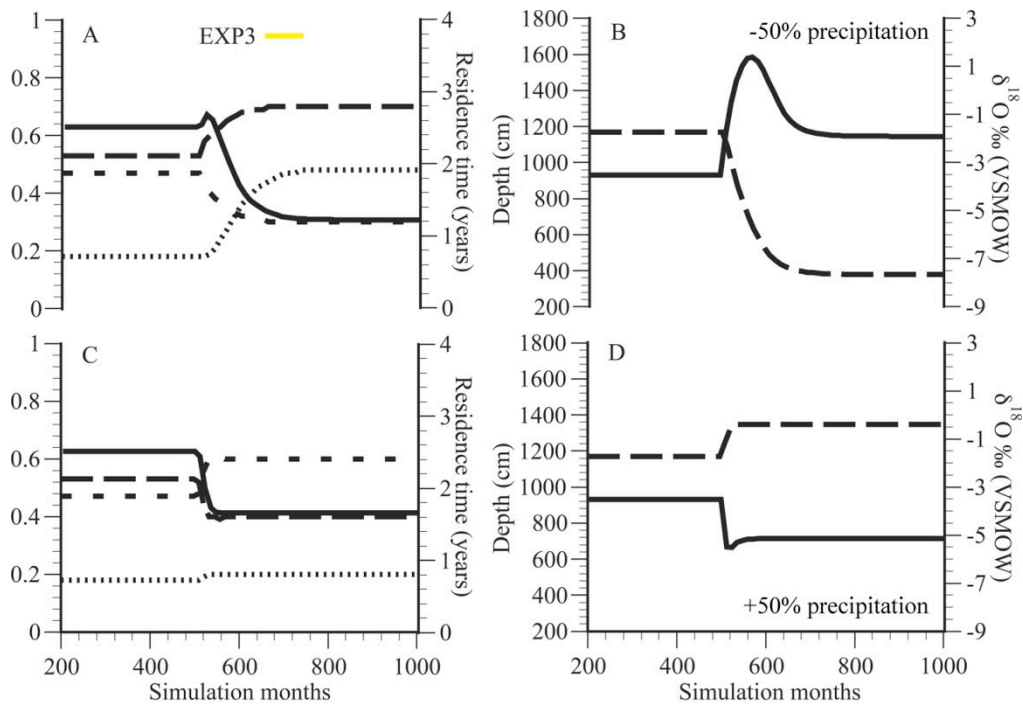


Figure 3.6 EXP3 configuration results. Castor Lake annual average water residence time (solid line), SA-V ratio (fine dashed line), and percentage of outflow via evaporation (coarse dashed line) and seepage (medium dashed line) changes resulting from (A) a 50% decrease and (C) a 50% increase in precipitation. Castor Lake summer (June–August) average surface water $\delta^{18}\text{O}$ values (solid line) and lake level changes (coarse dashed line) resulting from (B) a 50% decrease and (D) a 50% increase in precipitation.

3.3.5 Alternate hypsography configuration

In the alternate hypsography configuration (EXP4) in which the lake SA-V ratio was altered to decrease with increasing depth above 11.5 meters, lake responses to a precipitation increase were markedly different than in EXP3 (Figures 3.7, 3.8). For example, the steady state $\delta^{18}\text{O}$ value in the precipitation increase experiment decreased from a pre-forcing value of -3.8‰ to a post-forcing value of -5.8‰ . Further, outseepage and evaporation flux proportions changed by $\sim 13\%$ relative to pre-forcing steady state values.

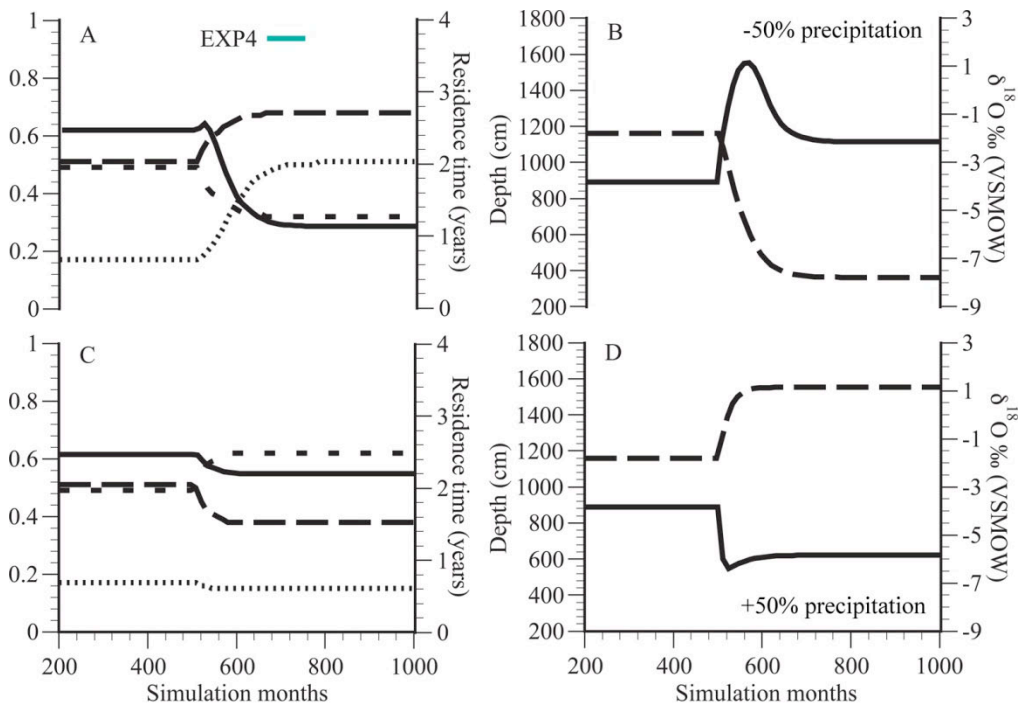


Figure 3.7 EXP4 configuration results. Castor Lake annual average water residence time (solid line), SA-V ratio (fine dashed line), and percentage of outflow via evaporation (coarse dashed line) and seepage (medium dashed line) changes resulting from (A) a 50% decrease and (C) a 50% increase in precipitation. Castor Lake summer (June–August) average surface water $\delta^{18}\text{O}$ values (solid line) and lake level changes (coarse dashed line) resulting from (B) a 50% decrease and (D) a 50% increase in precipitation.

3.4 DISCUSSION

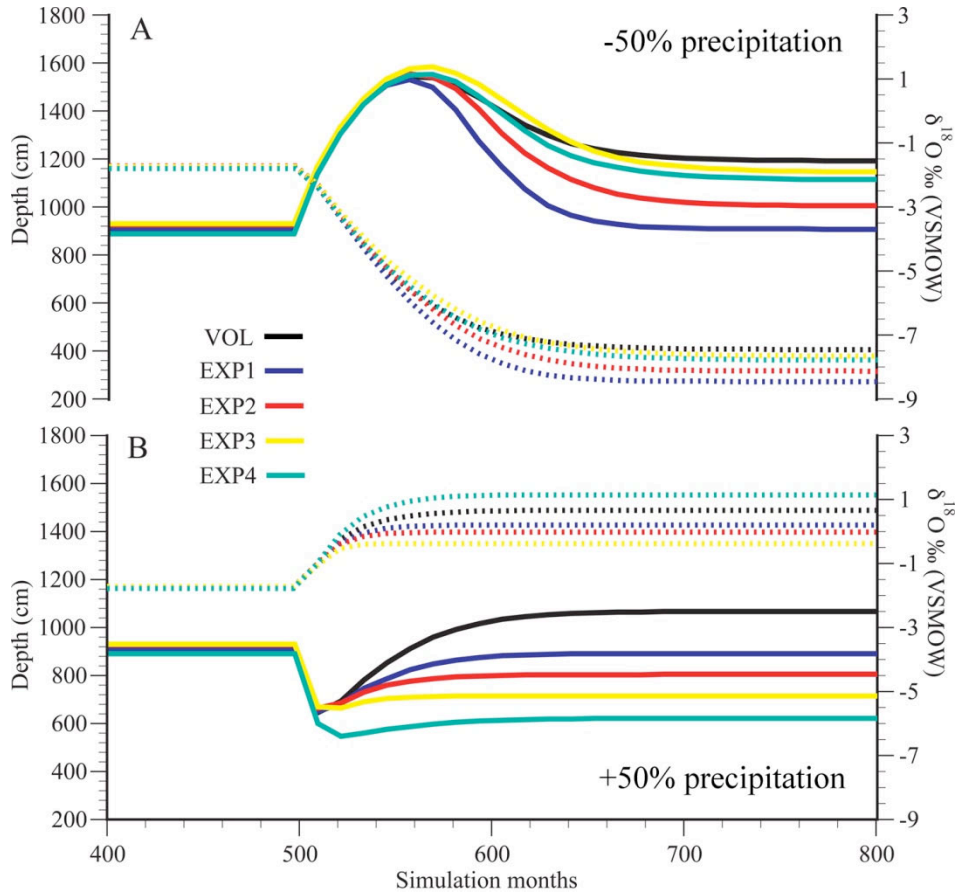


Figure 3.8 Combined Castor Lake summer (June–August) average lake level and $\delta^{18}\text{O}$ values from all simulations. (A) depicts results from the 50% precipitation decrease experiments and (B) depicts results from the 50% precipitation increase experiments.

3.4.1 The volumetric configuration

At Castor Lake, large littoral shelves on the northeast and southern shorelines create a hypsographic relationship in which the lake SA-V ratio increases with both increasing and decreasing depth at ~11.5 meters (Figure 3.2). In the volumetric outseepage configuration lake outflow proportions were largely mediated by lake SA-V ratio changes, leading to an increase and decrease in lake evaporation and outseepage flux proportions, respectively, in response to

both positive and negative hydrologic forcing. Volumetric outseepage results are, however, somewhat similar to EXP3 results in which outseepage from the lakebed is heterogeneous, in that large increases in lake water $\delta^{18}\text{O}$ values in response to precipitation decreases are predicted under both scenarios (Figure 3.8)

3.4.2 Exponential configurations

In the exponential outseepage configurations model steady state isotopic predictions widely varied in accordance with the decay rate of the exponential function. In the EXP1 configuration, in which the decay rate was low, steady state isotopic responses to precipitation changes of $\pm 50\%$ were minimal, with commensurately small responses in the evaporation and outseepage flux proportions. EXP1 approximates a lake with spatially homogenous outseepage rates due to an approximately even distribution of low conductivity lake sediment (rather than the typical trend of sediment fining toward the lake center) and minimal difference in head across the lake bed. Consequently, in the EXP1 scenario the average hydraulic conductivity and outseepage rate through the lakebed did not extensively change in response to lake level variations. Evaporation and outseepage flux also did not change and sensitivity to the direction of SA-V ratio changes became less pronounced, resulting in steady state lake water $\delta^{18}\text{O}$ values that were similar between the precipitation forcing scenarios.

In EXP2 the rate of exponential decay is larger than in EXP1, resulting in lakebed hydraulic conductivity and outseepage values that are more spatially heterogeneous. Under these conditions (unlike in EXP1) notable steady state lake water $\delta^{18}\text{O}$ responses to hydrologic forcing occurred, although to a lesser extent than in the volumetric outseepage configuration. For example, when precipitation rates were higher, simulated lake level consequently increased and

imbued shoreline lake sediment with higher hydraulic conductivity. The overall outseepage flux therefore increased, leading to a decrease in the evaporation outflux proportion. While the magnitude of the steady state $\delta^{18}\text{O}$ response in EXP2 may not have been large, the direction of the steady state isotopic change is clear and demonstrates the contrasting model predictions resulting from volumetric and exponential outseepage configurations.

EXP3 simulates lake responses when shoreline sediments have high a hydraulic conductivity that decreases rapidly with offshore distance. Under these conditions, model simulations predicted extensive variation in lake steady state responses to hydrologic forcing, with increases in lake level leading to large decreases in lake steady state $\delta^{18}\text{O}$ values, and vice versa. As in EXP2, lake outseepage rates increased as lake level raised, leading to a decrease in the evaporation outflow proportion. Similarly, in contrast to the volumetric outseepage configuration, the conductivity of the lake sediment was the primary control on the direction of the lake water $\delta^{18}\text{O}$ response rather than the SA-V ratio change.

Results of the EXP4 simulations help to clarify the influence of lake hypsography on lake water steady state $\delta^{18}\text{O}$ values. For example, the lake SA-V ratio in EXP4 decreases with increasing depth (and does not increase with increasing depth as in all other scenarios) leading to a lower average offshore distance for lakebed slices than in EXP1–3 and a consequently larger average outseepage rate.

The relationship between lakebed outseepage rates and hypsography revealed by these tests indicates that multiple lakes with varying shapes in identical hydrologic settings (i.e. similar aquifer characteristics and sediment hydraulic conductivities) should exhibit varying responses to hydrologic forcing. For example, in lakes with SA-V ratios that decrease with increasing lake level, the increase in proportional outseepage flux in response to rising lake level should be

greater than in lakes with an SA-V ratio that increases with lake level. The larger steady state isotopic response to a precipitation increase predicted by EXP4 (relative to EXP1 through EXP3) demonstrates that the SA-V ratio is an influential control on lake water steady state $\delta^{18}\text{O}$ values, and further that isotopic enrichment in response to a lake level increase is unlikely.

3.4.3 Transient $\delta^{18}\text{O}$ responses

In all outseepage configurations, transient responses to hydrologic forcing were approximately identical, in that peak $\delta^{18}\text{O}$ values were achieved soon after the precipitation change and persisted until model month ~ 700 . These results therefore suggest that lake transient responses to hydrologic forcing are controlled by factors other than lake the spatial distribution of lake outseepage.

3.4.4 Future work

To validate the modeling approach and conclusions developed herein, field experiments should be conducted to measure lake bed outseepage rates and then compared to model simulation results. Future work will include obtaining outseepage measurements and developing a flow net for Castor Lake using a series of minipiezometers.

3.5 CONCLUSIONS

Simulations of lake $\delta^{18}\text{O}$ responses to precipitation forcing under a variety of lake outseepage configurations demonstrate that the overall rate and spatial distribution of lake outseepage can profoundly affect lake water steady state isotopic values. Simulation results suggest that the extent of decay in lake outseepage with increasing offshore distance is a strong control on lake steady state isotopic responses to hydrologic forcing. In lakes with heterogeneous sediments and outseepage rates that are extensively higher near the shoreline, stronger isotopic responses to precipitation changes can be expected relative to lakes with more homogenous sediments. Simulation results additionally demonstrate that lake hypsography is an influential control on lake equilibrium isotopic values, in that the direction and magnitude of lake SA-V ratio changes with depth can amplify the magnitude of lake isotopic responses to lake level change. To that end, for lakes with SA-V ratios that increase with increasing lake level, smaller decreases in lake surface water $\delta^{18}\text{O}$ values can be expected in response to greater precipitation amounts. Conversely, for lakes with SA-V ratios that decrease with lake level increases, larger decreases in lake surface water $\delta^{18}\text{O}$ values can be expected as precipitation amounts increase.

The results presented here demonstrate that model predicted lake steady state sensitivity to hydrologic forcing is largely dependent on the structure of the applied outseepage submodel, and that for a single hydrologic forcing scenario, unique $\delta^{18}\text{O}$ predictions can be expected for each outseepage configuration. In the case of volumetric outseepage models, isotopic responses to precipitation change could be opposite that predicted in the exponential outseepage configurations (e.g., if the SA-V ratio of the lake increases with increasing depth). For example,

if outseepage is modeled exponentially, highly disparate results can be produced due to variations in the strength of decay of the exponential function, suggesting that some observational knowledge of lake seepage should be obtained prior to selecting a specific outseepage configuration in lake isotope mass balance models. While the volumetric method for calculating lake outseepage may be simplistic, it can be useful in model simulations of either drought conditions when lake levels are low, or pluvial conditions in lakes with SA-V ratios that decrease with increasing depth. Moreover, the universal similarity in the model prediction of transient lake water isotopic responses suggests that the outseepage configuration is not an important control on short-term lake water isotopic evolution, implying that model analyses of short-term lake sensitivity to climate forcing should not be affected by outseepage dynamics. This study demonstrates that lake-catchment model predictions of lake outflow proportions and consequent steady state isotopic responses to hydrologic forcing are highly dependent on the method of outseepage calculation, and that using such models to interpret lake sediment oxygen isotope records should be undertaken with caution if the outseepage characteristics of the study lake are not well understood.

4.0 SMALL LAKE ISOTOPIC AND HYDROLOGIC RESPONSES TO 20TH CENTURY CLIMATE VARIABILITY: COMPARISON OF OBSERVED AND MODELED SEDIMENT CORE OXYGEN ISOTOPE RECORDS AND LAKE LEVEL VARIATIONS

4.1 INTRODUCTION

Hydrologic and isotope mass balance models have long been used to quantitatively describe lake responses to climate forcing. Early predictive models (e.g., Dinçer 1968 and Gat 1970) applied steady state solutions to the common equations describing lake water and isotope mass balance. For many applications (e.g., when simulating isotopic responses to climate forcing in terminal and through-flow lakes with minimal annual and interannual volumetric changes) such steady state models are an adequate approximation of the lake system (Gibson et al. 2002). However, when simulating transient lake responses to climate forcing or modeling more complex lake-catchment systems, steady-state approaches are not appropriate and must be replaced by non steady-state methods. This often requires development of a system of ordinary or partial differential equations solved using numerical methods (Hostetler and Benson 1990; Benson et al. 2002; Rowe and Dunbar 2004).

Climate is seasonal in the rain shadow of the Cascade mountains, leading to lake hydrologic regimes that are largely controlled by dry season (i.e., summer) evapotranspiration

and wet season (i.e., late fall through early spring) precipitation. This persistent state of hydroclimatic variance produces large intra- and inter-annual volumetric fluxes in the lake catchment system. As a consequence, lakes exist in isotopic disequilibrium, with temperature and relative humidity influencing isotopic fractionation processes that occur during condensation and evaporation. Models must therefore incorporate non-steady state equations that can simulate intra-annual hydrologic and isotope dynamics as well as longer-term interannual to multidecadal lake responses to climate change. Specifically, such models must be able to simulate variations in both the mean state (i.e., multi-decade to century) and the stochastic (i.e., random, interannual) variability of climate.

Notably, evaluation of lake-catchment model performance within paleoclimate applications requires validation experiments in which model isotopic predictions are compared to measured lake water and/or sediment oxygen isotope values over a time period that sufficiently captures regional climate variability. Robust comparison requires accurate, continuous weather data for predictive model simulations (i.e., continuous weather station datasets for the most influential hydroclimatic variables, namely precipitation, relative humidity, and temperature), as well as dated sediment oxygen isotope records spanning the same time period.

In this study, recent lake surface elevation and sediment oxygen isotope value ($\delta^{18}\text{O}$) changes in Castor and Scanlon Lakes, north-central Washington are reconstructed using a modified version of the lake-catchment hydrologic and isotope mass balance model of Steinman et al. (2010a). Model simulations were conducted using continuous temperature and precipitation data sets spanning the 20th century (1900–2007) and validated using georeferenced air photos and lake sediment core records. To provide estimates of past lake levels, three-dimensional hypsographic models of the lake-catchment systems were coupled with historic air

photos. To provide estimates of past lake water and sediment $\delta^{18}\text{O}$ values 20th century oxygen isotope records using dated sediment cores from both lakes were developed.

4.2 METHODS

4.2.1 Study sites and regional climate

Scanlon Lake (SL) and Castor Lake (CL) are located in north-central Washington on a terrace margin of the Okanogan River. The small lake catchments ($< 1 \text{ km}^2$) are situated in the Limebelt region on a topographic high isolated from regional groundwater. Climate in the area is seasonal and semi-arid, largely controlled by the interaction between the Pacific westerlies and the Aleutian low- and north Pacific high-pressure systems. Additional detail on the study sites and regional climate can be found in Steinman et al. (2010a).

4.2.2 Lake and catchment elevation maps

Three-dimensional catchment representations for Scanlon and Castor Lakes were constructed from $\frac{1}{3}$ arc second ($\sim 10 \text{ m}$ resolution) National Elevation Data (NED) raster images. Using GIS software, polygon shapefiles delineating the boundary of each lake catchment were also created by tracing georeferenced 7.5-minute United States Geological Survey (USGS) topography maps. Catchment elevation datasets were converted to point shapefiles and clipped using the catchment boundary polygon shapefiles. The resulting catchment elevation point shapefiles were combined with near-lake catchment survey data collected in October 2008 and

bathymetric survey data collected in July 2007 to produce a complete lake catchment elevation model. Lake-catchment three-dimensional point data were then imported to 3-D modeling software and contoured to produce both 0.5 and 5 m contour maps of the lake-catchment system. Lake surface elevations were estimated on the basis of the USGS topographic maps and verified using catchment survey data. Bathymetric survey depths were adjusted by a fixed value equal to the change in lake level over the time between the bathymetric and catchment surveys. The NAD83 datum and UTM zone 11 coordinate system were applied to all GIS data.

Lake catchment surveys were conducted at CL and SL using a site level and handheld Garmin geographic positioning system (GPS). Specifically, 60 site elevations and locations were collected at CL, spaced at intervals near 10 m. Nearly 40 elevation values were collected at SL, also at points ~10 m apart. Point elevations at both sites were typically no higher than 5 m above lake level. Lake perimeter location data was also collected at CL and SL. Lake depth and location data were collected with a combination GPS receiver and chartplotter (Garmin® GPSMAP® 430S).

Eleven historic aerial photographs of the lakes (Table 4.1) were linearly corrected to a relatively recent (2006) National Agricultural Imagery Program (NAIP) orthophotograph ‘base’ image. Only minor linear corrections (less than 3 m) were applied to images collected over the last two decades. Images collected in 1983 and 1987 required larger adjustments but when properly scaled were only minimally distorted and closely matched the 2006 base image at all locations. All older aerial photographs (dating between 1945 and 1977) were aligned to the 2006 orthophotograph base layer using multiple lake shore tie points. Image positioning was a priority along the shallow, sloping northeast shoreline of both lakes, such that linear offset and scaling errors (less than ~0.25 m) in this location were minimized. Discrete historic lake level changes

were determined by overlaying the contour maps of the lake-catchment system and aerial photographs (Figures 4.1–4.6).

Table 4.1 Air photo data.

Year	Date	Agency/Program	Image Type	Scale	Resolution (m)	Source
1945	16-Aug	USACE	BW	unknown	n/a	US Army Corp of
1952	3-Jul	USGS	BW	1:37,400	n/a	USGS Earth Explorer
1954	15-Oct	USDA	BW	1:20,000	n/a	University of WA map
1973	18-Jul	USGS	BW	1:30,000	n/a	USGS Earth Explorer
1975	5-Sep	USGS	BW	1:78,000	n/a	USGS Earth Explorer
1977	22-Jul	WADNR	BW	1:63,360	n/a	University of WA map
1983	6-Aug	USGS-NHAP	CIR	1:58,000	n/a	USGS Earth Explorer
1987	25-Jun	WADNR	BW	1:24,000	n/a	University of WA map
1991	3-Jul	USGS-NAPP	BW DOQ	n/a	1	USGS Earth Explorer
1995	17-Jul	WADNR	BW DOQ	n/a	1	USGS Earth Explorer
1998	8-Aug	USFS-WMC	BW DOQ	n/a	1	USGS Earth Explorer
2006	1-Jul	USDA-NAIP	RGB DOQ	n/a	0.5	USGS Earth Explorer
United State Army Corp of Engineers (USACE)				BW (black and white)		
United States Department of Agriculture (USDA)				CIR (color infrared)		
Washington State Department of Natural Resources (WADNR)				DOQ (digital orthoquadrangle)		
National High Altitude Photography (NHAP)				RGB (red, green, blue)		
National Aerial Photography Program (NAPP)						
United States Forest Service (USFS)						
National Agricultural Imagery Program (NAIP)						

4.2.3 CL sediment core recovery and sampling

In January 2004, an undisturbed sediment-water interface core was recovered from CL using a freeze core assembly. The core was transported on dry ice to the University of Pittsburgh and sampled at 1–3 mm intervals for carbonate mineral oxygen isotope ($\delta^{18}\text{O}$) and X-ray diffraction analyses. Sediment samples for isotope analyses were disaggregated for ~24 hours in a ~7% H_2O_2 solution and sieved at $63\mu\text{m}$ to isolate authigenic (i.e., precipitated in-lake) carbonate mineral components and to limit contamination by biogenic carbonate shell material. The captured $<63\mu\text{m}$ portion of the disaggregated sediment was settled from rinse water, centrifuged, and the remaining liquid was decanted. The isolated fine-grained carbonate

sediment fraction was then bleached, freeze-dried, and gently homogenized using an agate mortar and pestle. Carbonate samples were reacted in 100% orthophosphoric acid at 70°C using a Finnigan™ MAT Kiel III automated preparation system and measured on-line with a Finnigan™ Mat 252 mass spectrometer at the University of Florida. Isotopic values are expressed in conventional delta (δ) notation as the per mil (‰) deviation from Vienna PeeDee Belemnite. Precision for $\delta^{18}\text{O}$ and samples was better than $\pm 0.06\text{‰}$. Sediment characterization by X-ray diffractometry was completed at the University of Pittsburgh's Materials Micro-Characterization Laboratory using a Phillips X'Pert Powder Diffractometer over a 2θ range of 10° to 80°.

4.2.4 CL sediment core chronology

Near-surface sediment chronology and sediment accumulation rates were determined by ^{210}Pb dating. ^{210}Pb and ^{137}Cs activities were measured at the Freshwater Institute at the University of Manitoba in Winnipeg, Canada. Sediment ages were determined using the constant rate of supply model (Appleby & Oldfield, 1978).

4.2.5 SL sediment core recovery and sampling

Surface sediments were collected from SL in July 2007 using a piston corer designed to retrieve undisturbed sediment-water interface profiles. The core was extruded in the field at 2 mm intervals (to a depth of 22.6 cm) by upward extrusion into a sampling tray fitted to the top of the core barrel.

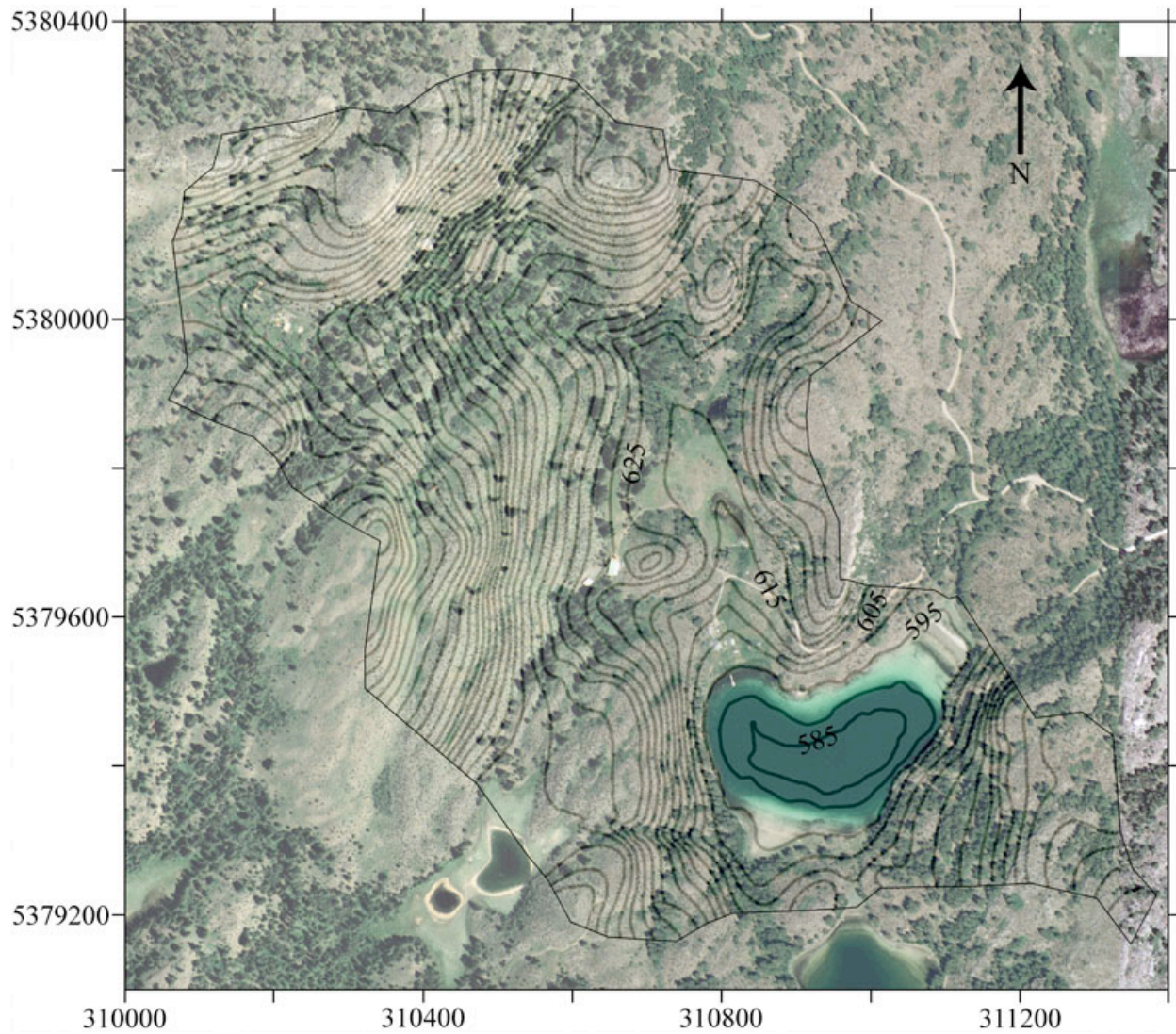


Figure 4.1 Air photo of the Castor Lake catchment on 07/01/2006 superimposed with catchment topography and lake bathymetry (5 m contours).

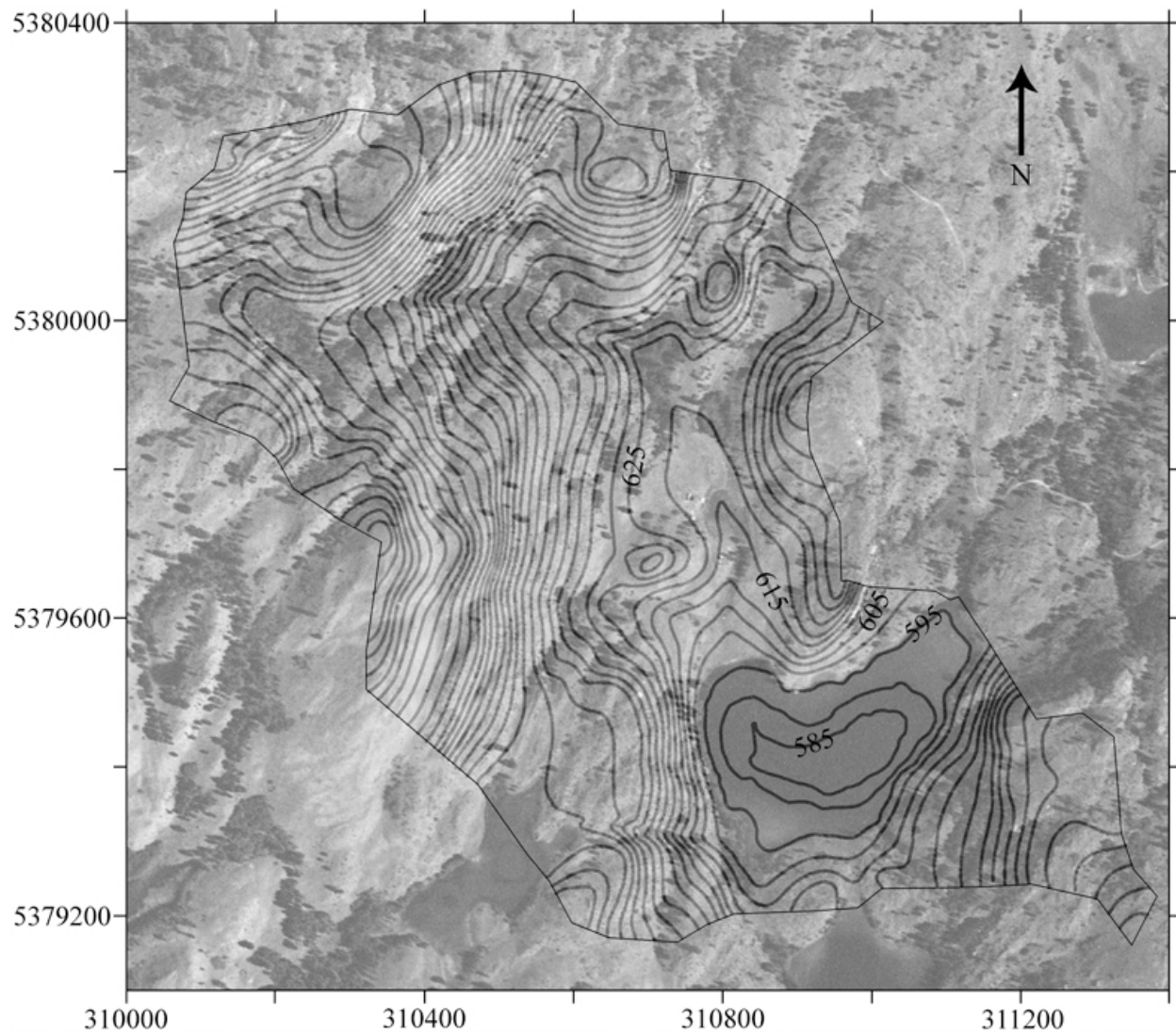


Figure 4.2 Air photo of the Castor Lake catchment on 07/03/1952 superimposed with catchment topography and lake bathymetry (5 m contours).

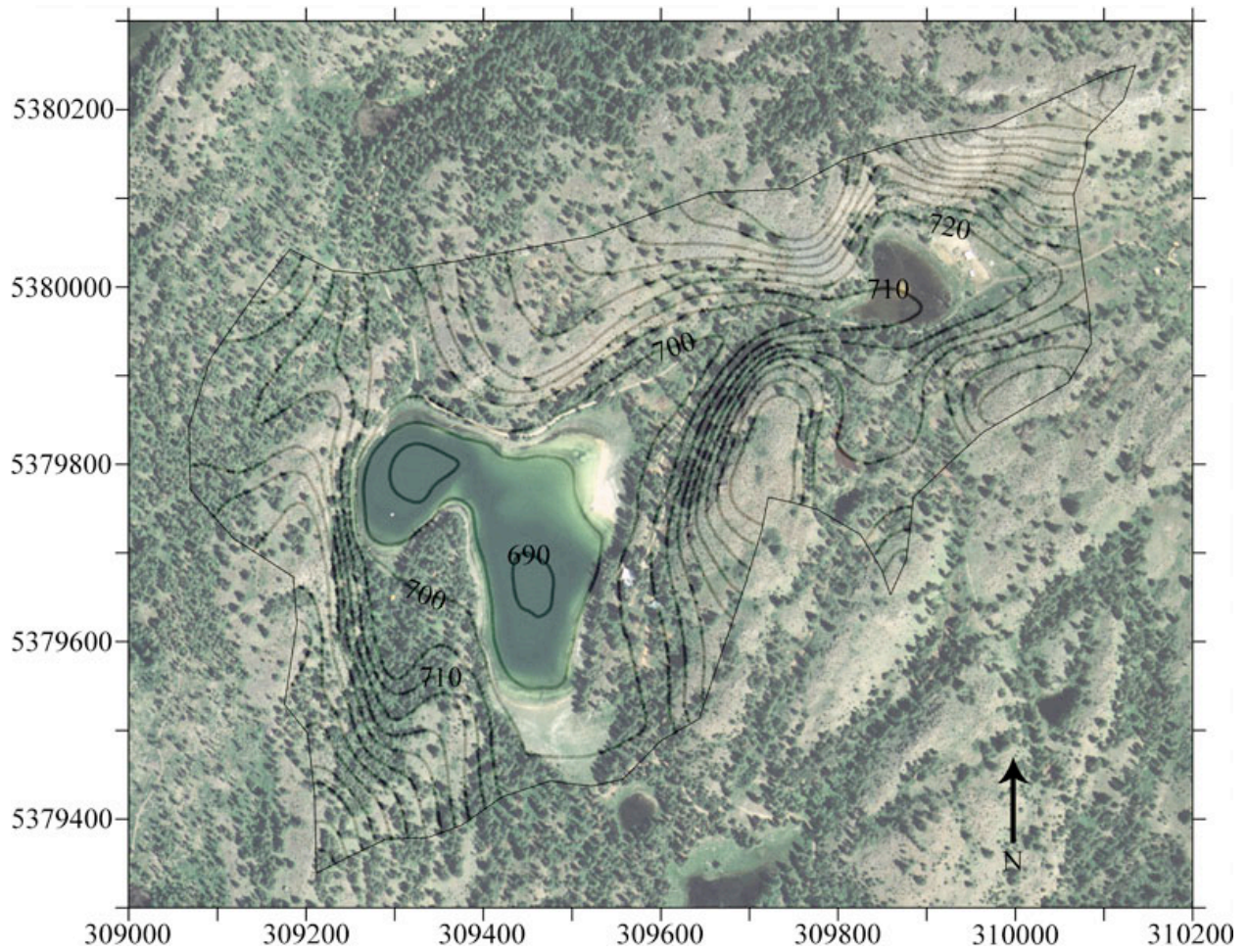


Figure 4.3 Air photo of the Scanlon Lake catchment on 07/01/2006 superimposed with catchment topography and lake bathymetry (5 m contours).

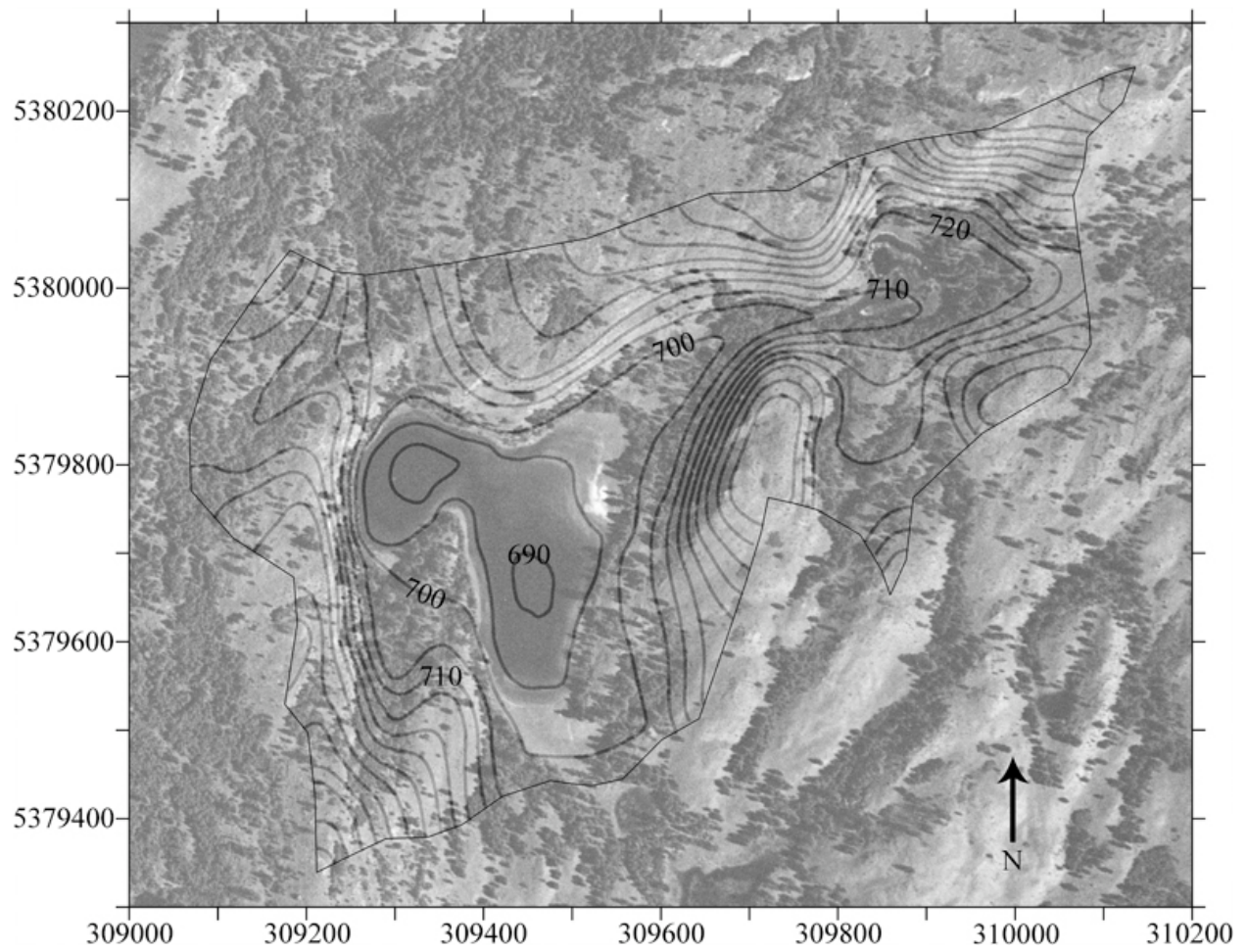


Figure 4.4 Air photo of the Scanlon Lake catchment on 07/03/1952 superimposed with catchment topography and lake bathymetry (5 m contours).



Figure 4.5 Air photo of Castor Lake on 07/03/1952 (left) and 07/01/2006 (right) superimposed with catchment topography and lake bathymetry (0.5 m contours). The “O” in the 1952 image marks active overflow at the northeastern corner of the lake. The solid line in the 2006 image marks the lake perimeter and surface elevation.

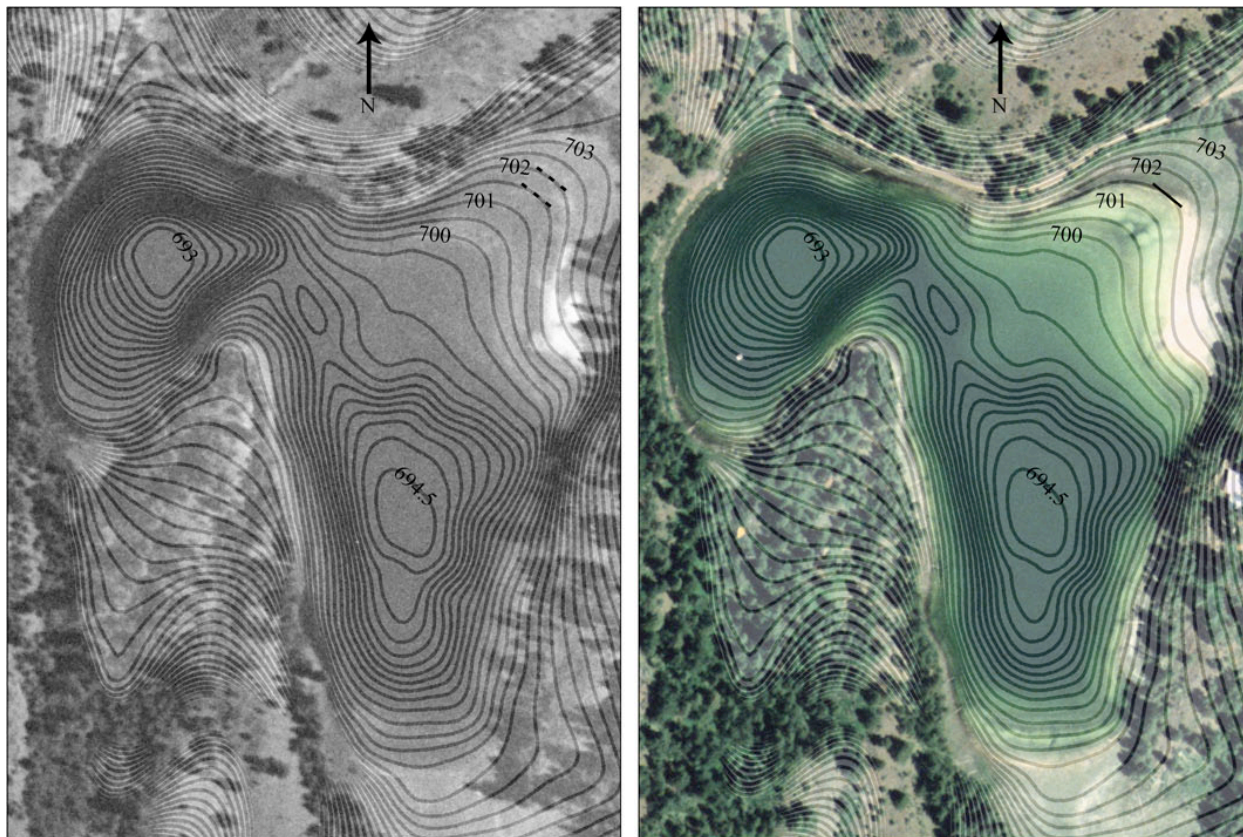


Figure 4.6 Air photo of Scanlon Lake on 07/03/1952 (left) and 07/01/2006 (right) superimposed with catchment topography and lake bathymetry (0.5 m contours). The solid line represents lake surface elevation with dashed lines representing upper and lower estimates.

Sediment samples were disaggregated in 7% H₂O₂ for ~24 hours and washed through a 63 µm sieve. Coarse material (>63 µm) was collected within filter paper and dried overnight at 60°C. Adult valves of the ostracod *Limnocythere Staplini* were picked under magnification from the dried samples and cleaned by hand using deionized water before drying. Oxygen isotopic ratios were measured on aggregate samples of ~20 ostracod valves from each 2 mm sediment sample. Only fully intact, thoroughly clean valves without discoloration or evidence of dissolution were selected for analysis. Isotopic ratios were measured at the University of Arizona Environmental Isotope Laboratory by CO₂ equilibration with a VG602C Finnigan™ Delta S isotope ratio mass spectrometer and at the University of Pittsburgh using a dual-inlet GV

Instruments, Ltd. (now Isoprime, Ltd.) IsoPrime™ stable isotope ratio mass spectrometer and MultiPrep™ inlet module. Isotopic values are expressed in conventional delta (δ) notation as the per mil (‰) deviation from Vienna PeeDee Belemnite. Analytical precision (based on repeated measurements of NBS-18 and NBS-19 carbonate standard materials) was better than 0.1‰ at both laboratories.

4.2.6 SL sediment core chronology

Sediment chronology and sediment accumulation rates at SL were determined by ^{210}Pb dating. Radioisotope (^{210}Pb , ^{137}Cs and ^{226}Ra activity) activities were determined by direct gamma counting (Appleby et al., 1986; Schelske et al., 1994) using an EG & G Ortec GWL well-type intrinsic germanium detector at the University of Florida's Land Use and Environmental Change Institute.

For the SL age model material was isolated for radiocarbon measurements from two terrestrial macrofossil samples (24 cm and 53 cm). Analyses were conducted at the W.M. Keck Carbon Cycle Accelerator Mass Spectrometry Laboratory at the University of California, Irvine (UCI). Samples were pretreated at the University of Pittsburgh following standard acid-base-acid procedures (Abbott and Stafford 1996). Radiocarbon ages were calibrated using the CALIB online software program version 6.0.0 (Stuiver et al. 1998; Reimer et al. 2004).

4.2.7 Model structure

CL and SL lake level and sediment core isotope ratio changes were simulated using the hydrologic and isotopic mass balance model of Steinman et al. (2010a) (*see* Chapter 1).

Generally, this model describes the hydrologic and isotope mass-balance of a lake using the following equations:

$$\frac{dV_L}{dt} = \Sigma I - \Sigma O \quad (1.1)$$

$$\frac{d(V_L \delta_L)}{dt} = \Sigma I \delta_i - \Sigma O \delta_o \quad (1.2)$$

where V_L is lake volume, ΣI and ΣO are the total surface and below ground inflows to and outflows from a lake, and δ is the isotopic composition of the inflows and outflows. Specifically, the hydrologic model is defined by six separate differential equations, each corresponding to a different theoretical water reservoir (e.g., catchment groundwater, snowpack, shallow and deep lake volumes). Model sub-routines for lake stratification, soil moisture availability, snowpack, and surficial and subsurface inflow control volumetric fluxes to the reservoirs.

To accommodate overflow at CL, a flux variable (F_{OF}) was added to the model differential equation describing the hydrologic balance of the surface lake reservoir (RES_{SL}) (see Equation 1.3):

$$F_{OF} = \begin{cases} RES_{SL} + RES_{DL} - 424562 & RES_{SL} + RES_{DL} > 424562 \\ 0 & RES_{SL} + RES_{DL} \leq 424562 \end{cases} \quad (4.1)$$

where RES_{DL} (deep lake reservoir) + RES_{SL} = total lake volume and 424562 (units of m^3) represents the overflow volume at a depth of 13.46 m. The complimentary differential equation describing the oxygen isotope mass balance of RES_{SL} was also modified.

Subroutines that calculate sediment $\delta^{18}O$ values on the VPDB (Vienna Pee Dee Belemnite) scale were also added to the model, in order to simulate the isotopic composition of authigenic carbonate sediments forming at CL and SL. The CL model calculates the equilibrium

fractionation factor for the aragonite water system in accordance with the equation of Zhou and Zheng (2003):

$$1000\ln\alpha_{\text{Aragonite-H}_2\text{O}} = 20.44(10^3 T^{-1}) - 41.48 \quad (4.2)$$

where $\alpha_{\text{Aragonite-H}_2\text{O}}$ is the equilibrium fractionation factor for aragonite and water and T is the water temperature in degrees Kelvin. The SL model determines the equilibrium fractionation factor for ostracod bio-calcite using the equation of Kim and O'Neil (1997):

$$1000\ln\alpha_{\text{Calcite-H}_2\text{O}} = 18.03(10^3 T^{-1}) - 32.42 \quad (4.3)$$

where $\alpha_{\text{Calcite-H}_2\text{O}}$ is the equilibrium fractionation factor for calcite and water and T is the water temperature in degrees Kelvin. In both cases, values for α are related to lake water $\delta^{18}\text{O}$ values on the VSMOW (Vienna Standard Mean Ocean Water) scale in accordance with the standard isotope fractionation relationship:

$$\alpha_{A-B} = \frac{1000 + \delta_A}{1000 + \delta_B} \quad (4.4)$$

where α_{A-B} is the fractionation factor of either the calcite-water or aragonite-water systems, δ_A is the isotopic composition of either aragonite or calcite, and δ_B is the isotopic composition of lake water. The model converts theoretical aragonite and calcite $\delta^{18}\text{O}$ values from the VSMOW to the VPDB scale using the following standard equation:

$$\delta_{\text{VSMOW}} = 1.03086 \times \delta_{\text{VPDB}} + 30.86 \quad (4.5)$$

The SL model also applies an isotopic offset of +0.8‰ to bio-calcite $\delta^{18}\text{O}$ values (von Grafenstein et al. 1999) to simulate the vital isotopic effect associated with carapace production of the *Limnocythere staplini* ostracod (see Section 4.4.2).

4.2.8 20th century weather datasets

Monthly precipitation and temperature datasets spanning the periods 1900–2007 and 1931–2007 were obtained from the Conconully and Omak National Climatic Data Center (NCDC) weather stations, respectively. Both of these weather stations are located within 14 km of Castor Lake and Scanlon Lake. Monthly relative humidity (RH) data collected from 1989 through 2008 were obtained from the Pacific Northwest Cooperative Agricultural Weather Network (AgriMet) weather station (also located in Omak). In May 2006, a Campbell® Scientific weather station was installed on the northwestern shoreline of Castor Lake, ~2 m above the lake surface. Since that time it has measured precipitation, temperature, RH, solar short wave radiation, barometric pressure and wind speed at 30 second intervals and recorded the average value of measurements every 30 minutes. The station measures precipitation amounts using a standard Campbell Scientific tipping bucket with an antifreeze, snowfall adaptor installed during winter months. In this study, data collected by the CL station between May 2006 and October 2008 were applied.

To develop continuous precipitation and temperature datasets spanning the 20th century, the Conconully and Omak weather station data was adjusted on the basis of strong linear correlations to the CL data (Figure 4.7). To produce the precipitation dataset, the Conconully data was regressed to the Omak data and the resulting linear equation was used to estimate values at Omak for the period 1900–1930 and for all other months for which there is no recorded data from the Omak station. This linear correlation was developed using monthly data for which non-zero precipitation totals were recorded at both stations and by eliminating all data points for which precipitation totals were either zero or not recorded. To produce the final precipitation dataset for model application, 30 minute precipitation totals recorded by the CL weather station

were summed to produce monthly totals and then used to linearly correct the adjusted Omak precipitation dataset (i.e., the Omak dataset was corrected a 2nd time on the basis of linear correlation to the CL data). To produce the temperature dataset, the Conconully data was adjusted on the basis of a linear correlation to the Omak data and then again on the basis of a linear correlation between the Omak and Castor datasets (30 minute temperature averages from the CL station were averaged to produce monthly values). Due to a lack of modern data from the Conconully station, direct correlation between the Conconully and CL data was not possible. For the 3 months prior to 1931 in which no temperature data were recorded, 20th century averages for that month were substituted.

The Conconully and Omak weather stations did not record continuous 20th century RH data. Consequently, monthly average RH values were calculated using a shorter dataset (1989–2008) from the Omak AgriMet station and this data was adjusted on the basis of a linear correlation to monthly average values from the CL weather station (Figure 4.7). The model applies these average monthly RH values in each year of the 20th century simulations. Monthly average wind speed values were calculated using data recorded at the CL station.

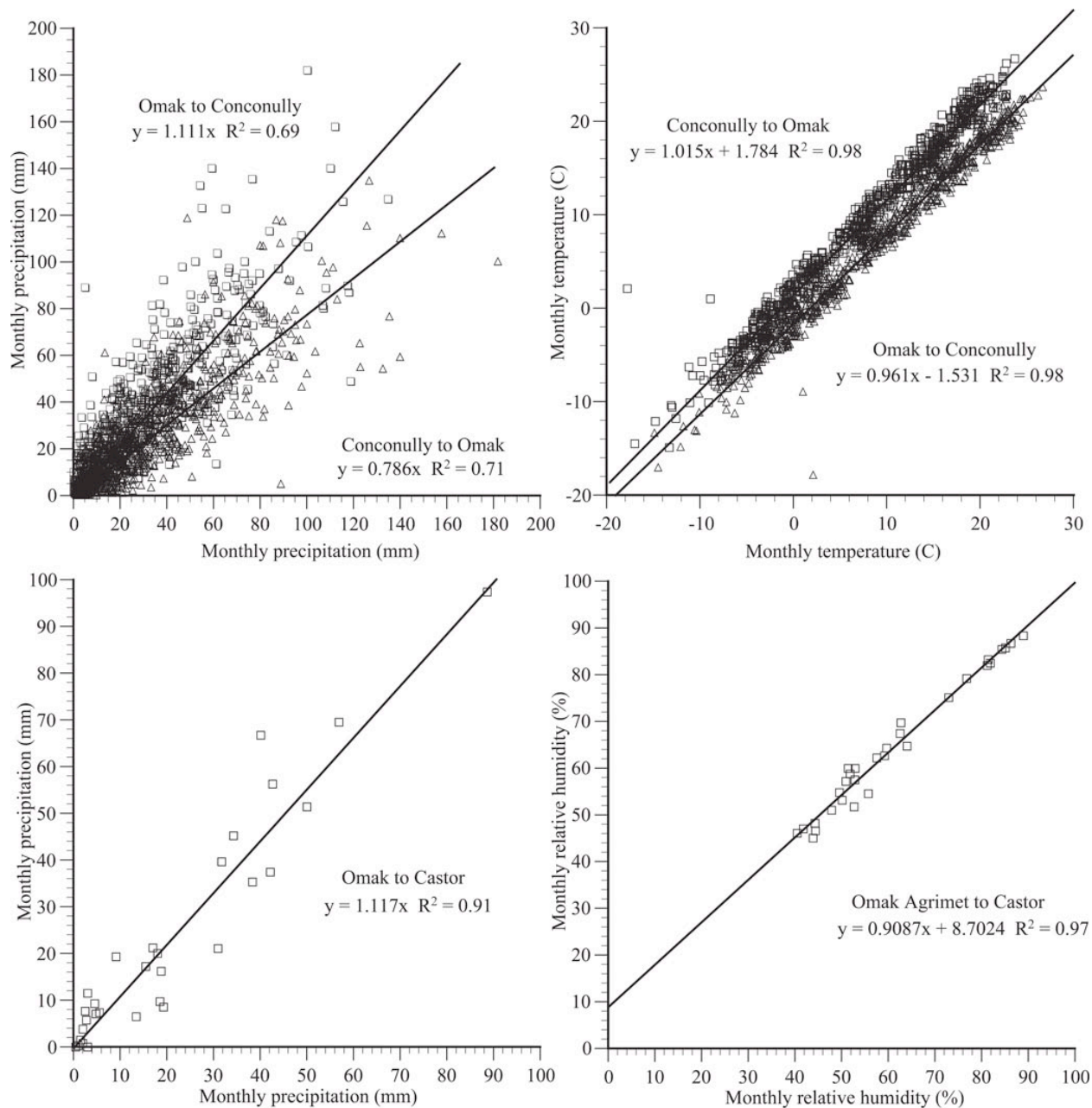


Figure 4.7 (A) Monthly precipitation data from the Omak and Conconully NCDC weather stations from 1930–2007 with the corresponding linear correlation equation used to estimate precipitation at Omak. (B) Monthly temperature data from the Omak and Conconully NCDC weather stations from 1930–2007 with the corresponding linear correlation equation used to estimate temperature at Omak. (C) Monthly precipitation data from the Omak and Castor weather stations from June 2006 to October 2008 with the corresponding linear correlation equation used to correct the Omak precipitation values for application to Castor Lake. (D) Monthly RH data from the Omak AgriMet and Castor NCDC weather stations from June 2006 to October 2008 with the corresponding linear correlation equation used to correct the Omak AgriMet RH values for application to Castor Lake.

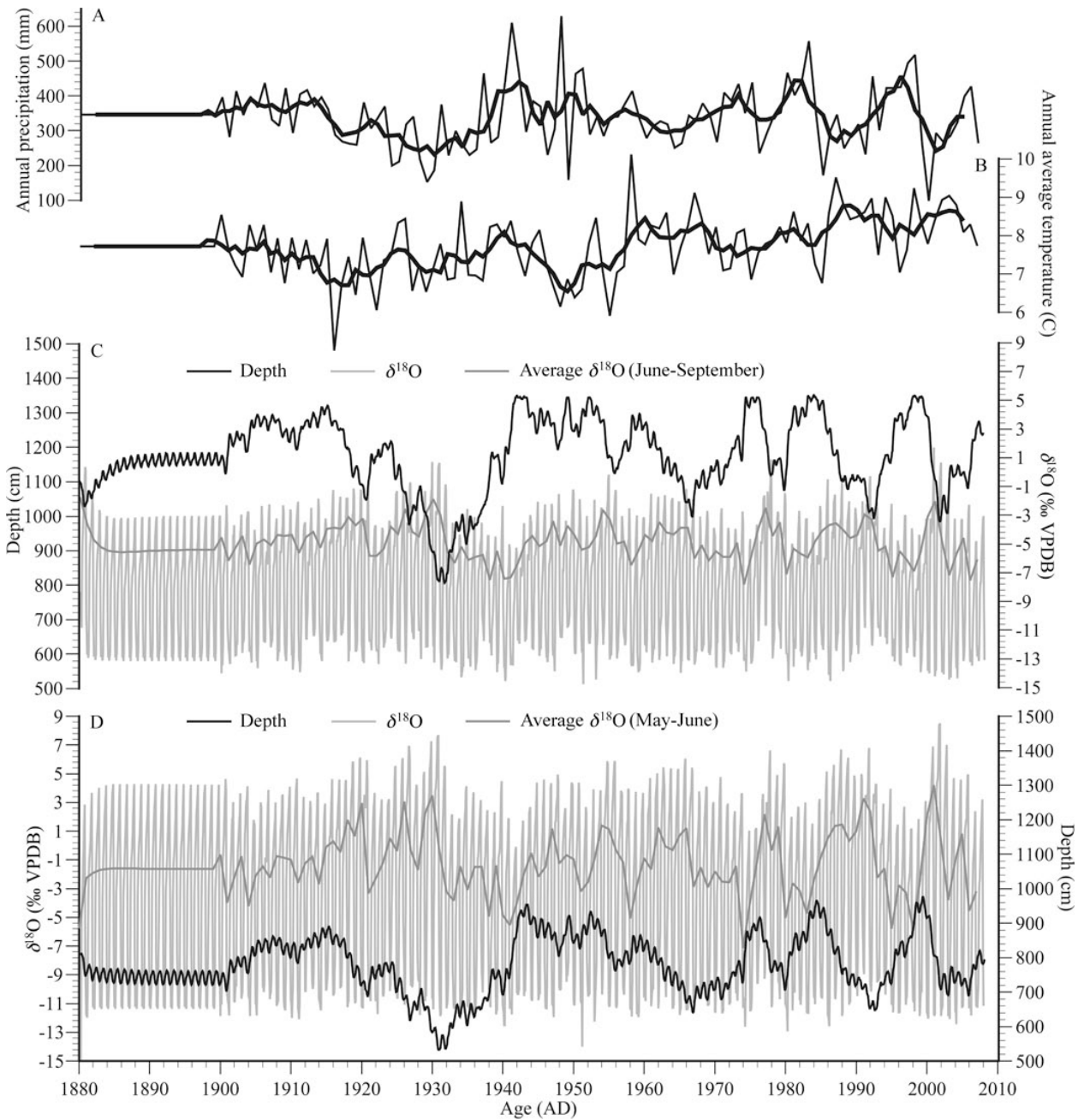


Figure 4.8 (A, B) 20th century annual (fine line) and five year average (coarse line) precipitation and average temperature values estimated for Castor and Scanlon lakes. (C) Castor Lake modeled 20th century depth (black line), monthly aragonite $\delta^{18}\text{O}$ values (light gray line), and average June–September aragonite $\delta^{18}\text{O}$ values. (D) Scanlon Lake modeled 20th century depth (black line), monthly ostracod $\delta^{18}\text{O}$ values (light gray line), and average May–June ostracod $\delta^{18}\text{O}$ values.

4.2.9 20th century simulations

Model simulations utilized continuous monthly temperature and precipitation datasets spanning the 20th century (Figures 4.7, 4.8) as inputs to reconstruct lake hydrologic and isotopic responses for comparison both to observations of 20th century lake level change from aerial photos and to sediment core oxygen isotope records. To simulate climate variables for which no long-term (i.e., multidecadal) continuous datasets exist (i.e., RH, solar insolation, and wind speed), monthly average values were applied as model inputs. In all simulations, catchment and lake parameters such as soil available water capacity were held constant. Each simulation (conducted on a monthly time step) lasted 128 years of which the first 20 were a model equilibration period in which average monthly values for all climate variables were continuously applied and the remaining 108 years represented the period 1900 through 2007.

4.3 RESULTS

4.3.1 Castor Lake age model

Despite the fine laminations in the surface sediment, the ²¹⁰Pb age model produced using the constant rate of supply (CRS) model does not include the ¹³⁷Cs peak at 1964 within a 2σ error range (Figure 4.9) (Oldfield and Appleby 1984). It is unlikely that ¹³⁷Cs is mobile at CL, given the relatively low organic matter content (10–20%) in the upper sequence of the core and the well preserved laminations. The ¹³⁷Cs profile was therefore applied instead of the ambiguous ²¹⁰Pb profile as the basis for the age model (Nelson et al. 2011).

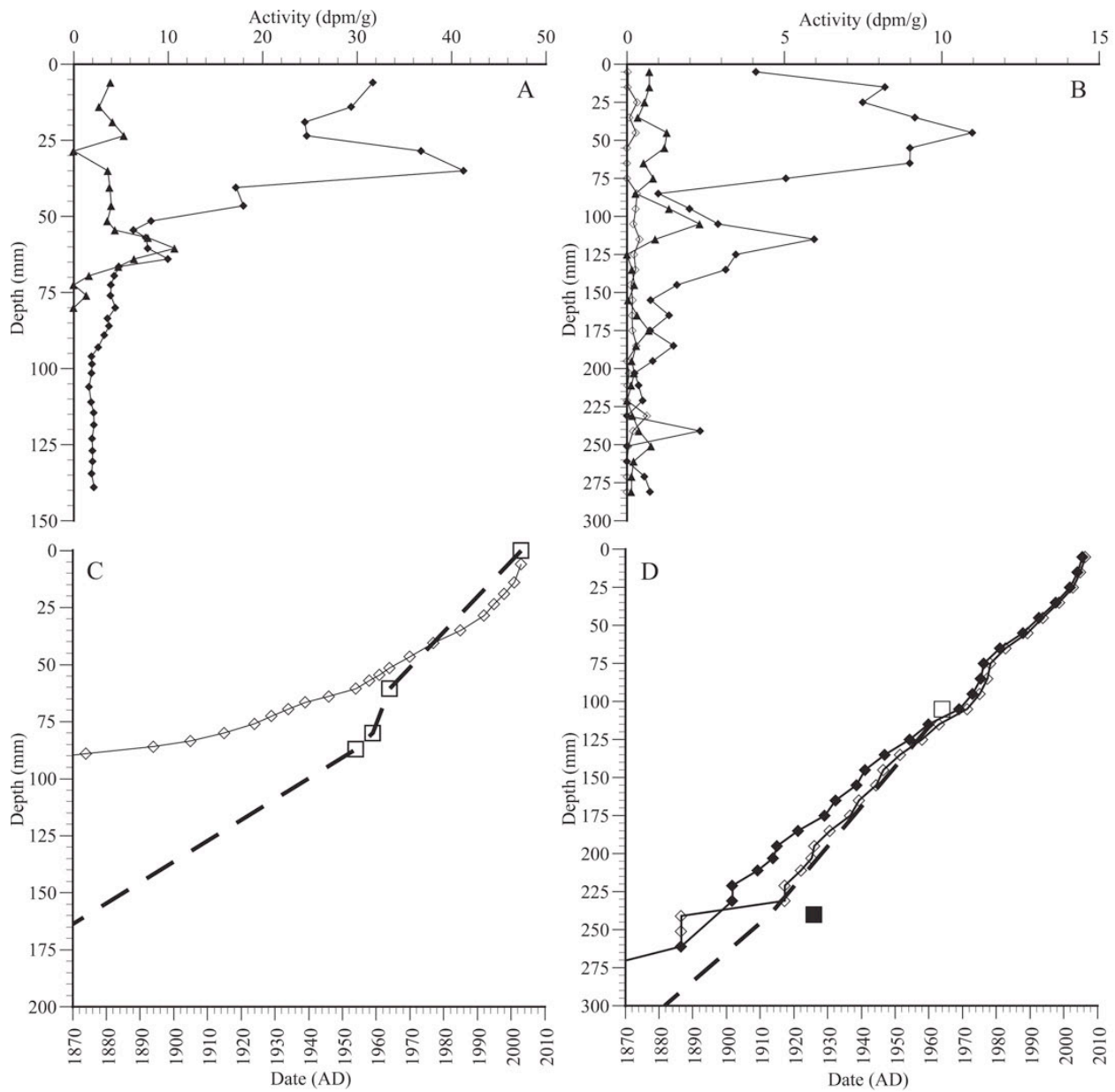


Figure 4.9 Castor Lake (A) and Scanlon Lake (B) total (closed diamonds) and unsupported (open diamonds) ^{210}Pb and ^{137}Cs (closed triangles) activity values. Supported ^{210}Pb was not measured on Castor Lake sediment. (C) Castor Lake age model. Open diamonds depict ^{210}Pb dates, and open squares depict dates inferred using ^{137}Cs . The dashed line represents the age model applied in this study. (D) Scanlon Lake age model developed using ^{210}Pb (open and closed diamonds) ^{137}Cs (open square) and ^{14}C (close square). The dashed line represents the age model for 1900–1964. ^{210}Pb data were used for 1964–2010. The age model applied in this study (dashed line) falls within the 2σ errors of both the ^{210}Pb and the ^{14}C data.

The ^{137}Cs profile matches the typical pattern of increase through the 1950s, peaking in 1964 AD when atmospheric nuclear testing was banned and ^{137}Cs levels began to decline. A date of 1964 AD was assigned to the ^{137}Cs activity peak and a date of 1959 AD to the beginning of the ^{137}Cs increase based on the shape of published atmospheric activity curves. A linear relationship was assumed between sediment age and depth from the top of the sediment (2003 AD), through the two cesium-inferred dates to the point corresponding to 1954 AD. The assumed linearity over this interval is based on trends in sediment density, which change at the 1954 AD level, indicating a probable end to the linear relationship between sediment age and depth in the upper ~50 years of the sequence. The Mount Saint Helens (MSH) W tephra, identified by electron microprobe at the Washington State University, provides a lower bounding age, determined by dendrochronology, of 1480 AD (470 BP) (Mullineaux 1986). A linear relationship was applied between the lowermost assumed age in the 20th century (1954) and the tephra inferred age of 1480 AD. To facilitate unbiased moving average analysis, the $\delta^{18}\text{O}$ data were resampled at an even 5 yr time step (average time step based on measured sampling interval) using linear interpolation.

4.3.2 Scanlon Lake age model

Sediment ages derived from ^{210}Pb dating methods were calculated using a constant rate of supply (CRS) model (Figure 4.9) (Oldfield and Appleby 1984). Errors in ages were propagated using first-order approximations and calculated in accordance with Binford (1990). Initial ^{210}Pb activity measurements were obtained on sediment sub-samples spanning 1 cm intervals from the surface to a depth of 22.6 cm. Because of the high activity (0.499 dpm/g) in the lowermost sample, six additional subsamples were extruded from a depth of 22.6 to 28.6 cm at the

University of Pittsburgh and submitted for analysis (*see* Section 3.2 for extrusion protocols). The bulk density of these samples (22.6–28.6 cm) changed through time and was not representative of the bulk density at the time of core collection. To calculate cumulative sediment accumulation at each depth interval, an equation of bulk density as a log function of depth from 0 to 22.6 cm was applied to the bottom section of the core. Average dry bulk density measurements from equivalent depths in other SL cores were used to verify the estimates for the 22.6 to 28.6 cm interval.

2σ calibration of the uppermost radiocarbon sample (24 cm) produced 5 possible ages, of which only one passed through the 2σ error ranges of the ^{210}Pb data. To produce the SL age model, a linear function was applied to connect the ^{137}Cs peak at 10.5 cm with the minimum possible age within the 2σ error range of the radiocarbon sample at 24 cm (Figure 4.9). This linear function passes through the 2σ error ranges of all ^{210}Pb measurements below 10.5 cm, and therefore represents the best possible compromise between the ^{210}Pb and ^{14}C data. We applied an additional linear function that connects the estimated age at 24 cm with the radiocarbon age at 54 cm to extend the age model to 1900. Support for the SL age model is provided by an additional ^{210}Pb chronology developed by assuming very small, non-zero unsupported ^{210}Pb activities for several of the lowermost samples (Figure 4.9). The SL $\delta^{18}\text{O}$ dataset was sampled at an even 1 yr time step using linear interpolation to facilitate unbiased moving average analysis for direct comparison to model reconstructed $\delta^{18}\text{O}$ values.

4.3.3 Modeled and orthophotograph derived lake surface elevation changes (1945–2007)

CL and SL lake surface elevation reconstructions based on georeferenced aerial photos and lake-catchment contour maps demonstrate considerable variability in interannual water

levels (Figure 4.10, Table 4.2). Minimum inferred lake elevation occurs at CL (592.5 m) and at SL (700.5 m) in 1991, with maximum lake elevation occurring at CL (595.5 m) during years of overflow in 1952, 1975, 1983 and 1998, and at SL (702.5 m) during 1983 and 1987. No long-term (multi-decadal) trends in lake level at CL or SL are apparent between 1945 and 2007.

Table 4.2 Observed and modeled 20th century lake surface elevation and volume data.

		Observed surface elevation (m amsl)	Error range of observed surface elevation ± (m)	Modeled surface elevation (m amsl)	Difference between modeled and observed surface elevation (m)	Observed volume (m ³)	Modeled volume (m ³)	Difference between modeled and observed vol. (m ³)	Difference between modeled and observed vol. (%)
CL	08/1945	594.00	0.4	594.86	0.86	320570	377370	56800	17.7
	07/1952	595.50	n/a	595.34	-0.16	427169	416354	-10814	-2.5
	10/1954	594.50	n/a	593.79	-0.71	351394	309435	-41958	-11.9
	08/1973	594.00	0.4	593.87	-0.13	320570	312946	-7623	-2.4
	09/1975	595.50	n/a	595.32	-0.18	427169	413978	-13190	-3.1
	08/1977	594.50	n/a	593.61	-0.89	351394	299913	-51480	-14.7
	08/1983	595.50	n/a	595.35	-0.15	427169	416515	-10653	-2.5
	07/1987	593.75	0.75	593.65	-0.10	306372	301481	-4890	-1.6
	07/1991	592.50	n/a	592.55	0.05	245387	247899	2512	1.0
	07/1995	594.38	0.38	594.87	0.49	343283	376791	33508	9.8
	08/1998	595.50	n/a	595.41	-0.09	427169	421797	-5371	-1.3
	07/2006	594.25	n/a	594.23	-0.02	335440	334297	-1142	-0.3
	07/2006*	594.64	n/a	n/a	n/a	n/a	n/a	n/a	n/a
SL	08/1945	700.88	0.38	701.26	0.38	144515	163023	18508	12.8
	07/1952	701.75	0.25	701.65	-0.10	190164	184471	-5692	-3.0
	10/1954	700.50	0.50	700.47	-0.03	127928	126724	-1203	-0.9
	08/1973	700.00	n/a	699.92	-0.08	106955	103979	-2975	-2.8
	09/1975	701.50	0.50	701.27	-0.23	175934	163527	-12406	-7.1
	08/1977	701.25	0.25	700.31	-0.94	162629	119724	-42904	-26.4
	08/1983	702.50	n/a	701.63	-0.87	248450	183192	-65257	-26.3
	07/1987	702.50	n/a	700.48	-2.02	248450	127096	-121353	-48.8
	07/1991	700.50	0.50	699.35	-1.15	127928	82615	-45312	-35.4
	07/1995	701.00	n/a	700.71	-0.29	150395	136910	-13484	-9.0
	08/1998	702.25	n/a	701.92	-0.34	226092	201071	-25020	-11.1
	07/2006	701.50	n/a	700.27	-1.23	175934	118063	-57870	-32.9
	07/2006*	701.20	n/a	n/a	n/a	n/a	n/a	n/a	n/a

*Observed using lake level sensors (Steinman et al. 2010a)

At CL model experiments utilizing modern instrumental weather observations between 1945 and 2007, resulted in lake surface elevation changes between ~595.4 m (1998) and ~592.6 m (1991) (Figure 4.10, Table 4.2). The average error between inferred and modeled lake volume and surface elevation at CL was ~0.3 m. At SL, maximum modeled lake surface elevation

(~701.9 m) was reached in 1998 with minimum lake surface elevation (~699.4 m) reached in 1991 (Figure 4.10, Table 4.2). The average error between inferred and modeled lake volume and surface elevation at SL was ~0.6 m. The 1987 air photo for SL is of poor quality and is the likely reason for the exceptionally large error observed during this year. If results from 1987 are removed, the average errors decreases to ~0.5 m.

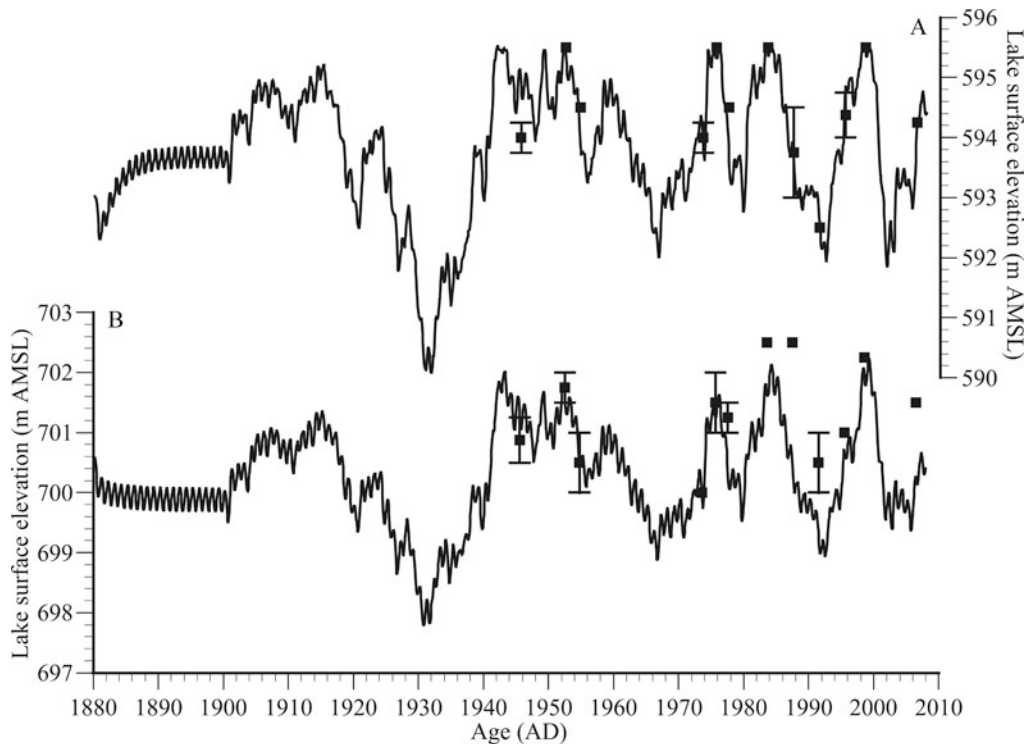


Figure 4.10 Castor Lake (top) and Scanlon Lake (bottom) 20th century modeled (lines) and observed (squares) water surface elevations and associated error estimates.

4.3.4 Modeled lake level changes (1900–2007)

Modeled average 20th century lake depths at CL and SL were ~11.8 m and ~8.0 m, respectively (Table 4.3). Lower lake elevations and reduced lake volumes occurred in model simulations at CL and SL between 1900 and 1950 (Figure 4.8, Table 4.3). Modeled decadal

average lake depth and volume were lowest at CL and SL between 1930 and 1940 (~9.8 m and 221,000 m³ and ~6.6 m and 75,000 m³, respectively) and highest between 1940 and 1950 (~12.8 m and 375,000 m³ and ~8.8 m and 166,000 m³, respectively). Average modeled lake depth and volume in the five years of the equilibration period (i.e., just prior to the application of 20th century precipitation and temperature data) were ~11.5 m and 292000 m³ at CL and ~7.6 m and 110000 m³ at SL.

Table 4.3 20th century lake model simulation results.

		Observed aragonite $\delta^{18}\text{O}$ (‰ VPDB)	Modeled aragonite $\delta^{18}\text{O}$ (‰ VPDB)	Surface lake $\delta^{18}\text{O}$ (‰ VSMOW)	Depth (cm)	Volume (m ³)	Residence time (yr)	Evaporation proportion	Outseepage proportion	Overflow proportion	SA:V ratio (m ²)	Precipitation (mm)	Temperature (°C)
CL	EP*	n/a	-5.40	-3.33	1145	291549	2.49	0.52	0.48	0.00	0.18		
	1900-2008	-4.87	-4.86	-3.07	1180	317303	2.39	0.52	0.46	0.02	0.18	343	7.67
	1900-1950	-4.23	-4.81	-3.09	1164	310370	2.42	0.53	0.46	0.01	0.19	332	7.36
	1950-2008	-5.51	-4.90	-3.06	1193	323280	2.38	0.52	0.46	0.02	0.18	355	7.95
SL	EP*	n/a	-1.64	-0.83	761	110320	1.92	0.84	0.16	n/a	0.37		
	1900-2008	-1.40	-1.35	-0.24	797	128538	1.99	0.83	0.17	n/a	0.36	355	7.95
	1900-1950	-0.77	-1.29	-0.29	784	123227	2.00	0.83	0.17	n/a	0.36	343	7.67
	1950-2008	-2.03	-1.42	-0.19	809	133117	1.98	0.83	0.17	n/a	0.35	332	7.36
CL	1900-1910	-4.30	-5.04	-3.35	1237	345156	2.44	0.53	0.47	0.00	0.18	370	7.62
	1910-1920	-4.15	-4.25	-2.60	1236	345449	2.46	0.53	0.47	0.00	0.18	332	7.07
	1920-1930	-3.45	-4.24	-2.46	1087	265472	2.50	0.52	0.48	0.00	0.18	283	7.29
	1930-1940	-3.53	-5.27	-3.51	982	220656	2.40	0.54	0.46	0.00	0.19	284	7.48
	1940-1950	-5.67	-5.26	-3.52	1279	375115	2.28	0.51	0.44	0.05	0.19	389	7.37
	1950-1960	-5.94	-4.71	-2.95	1242	350665	2.41	0.53	0.46	0.01	0.19	366	7.44
	1960-1970	-5.17	-4.61	-2.80	1130	285243	2.46	0.53	0.47	0.00	0.18	315	8.08
	1970-1980	-5.61	-5.03	-3.22	1203	328883	2.40	0.52	0.46	0.02	0.19	350	7.69
	1980-1990	-5.37	-4.88	-3.00	1235	348876	2.28	0.52	0.44	0.05	0.19	357	8.19
	1990-2000	-5.45	-5.27	-3.32	1197	329054	2.27	0.51	0.44	0.06	0.19	385	8.34
2000-2008	n/a	-5.13	-3.08	1137	290378	2.44	0.53	0.47	0.00	0.18	295	8.38	
SL	1900-1910	-1.55	-1.91	-0.92	818	134903	2.06	0.83	0.17	n/a	0.34	370	7.62
	1910-1920	-1.07	-0.61	0.29	841	145220	2.18	0.82	0.18	n/a	0.32	332	7.07
	1920-1930	-0.15	-0.05	1.09	720	95321	1.85	0.84	0.16	n/a	0.39	283	7.29
	1930-1940	0.57	-1.77	-0.80	658	75128	1.73	0.85	0.15	n/a	0.42	284	7.48
	1940-1950	-1.67	-2.12	-1.14	880	165563	2.15	0.82	0.18	n/a	0.32	389	7.37
	1950-1960	-3.27	-1.44	-0.35	857	153351	2.16	0.82	0.18	n/a	0.32	366	7.44
	1960-1970	-2.30	-0.70	0.46	752	107372	1.86	0.84	0.16	n/a	0.38	315	8.08
	1970-1980	-1.61	-1.71	-0.64	803	129211	1.99	0.83	0.17	n/a	0.36	350	7.69
	1980-1990	-1.94	-1.50	-0.37	855	154466	2.05	0.83	0.17	n/a	0.34	357	8.19
	1990-2000	-1.05	-1.74	-0.63	801	132265	1.92	0.84	0.16	n/a	0.37	385	8.34
2000-2008	n/a	-0.67	0.57	781	119267	1.90	0.84	0.16	n/a	0.37	295	8.38	

*Equilibration Period

4.3.5 Measured 20th century $\delta^{18}\text{O}$ records

Measured CL sediment core $\delta^{18}\text{O}$ values vary between -3.2‰ (~1927) and -6.7 (~1960) (Figures 4.8, 4.11). The interpolated sediment core $\delta^{18}\text{O}$ values vary between -3.2‰ (1928) and -6.5‰ (1958). The 20th century average value of the interpolated $\delta^{18}\text{O}$ data is -4.9‰, with

decadal maxima occurring between 1920 and 1930 and decadal minima occurring between 1950 and 1960 (Table 4.3). The average interpolated $\delta^{18}\text{O}$ values from 1900 to 1950 and 1950 to 2000 are -4.2‰ and -5.5‰ , respectively. Notably, the XRD results indicate that aragonite is the only detectable carbonate mineral in the sediment and therefore that $\delta^{18}\text{O}$ variations in the CL sediment core are not a result of changes in the carbonate mineral composition.

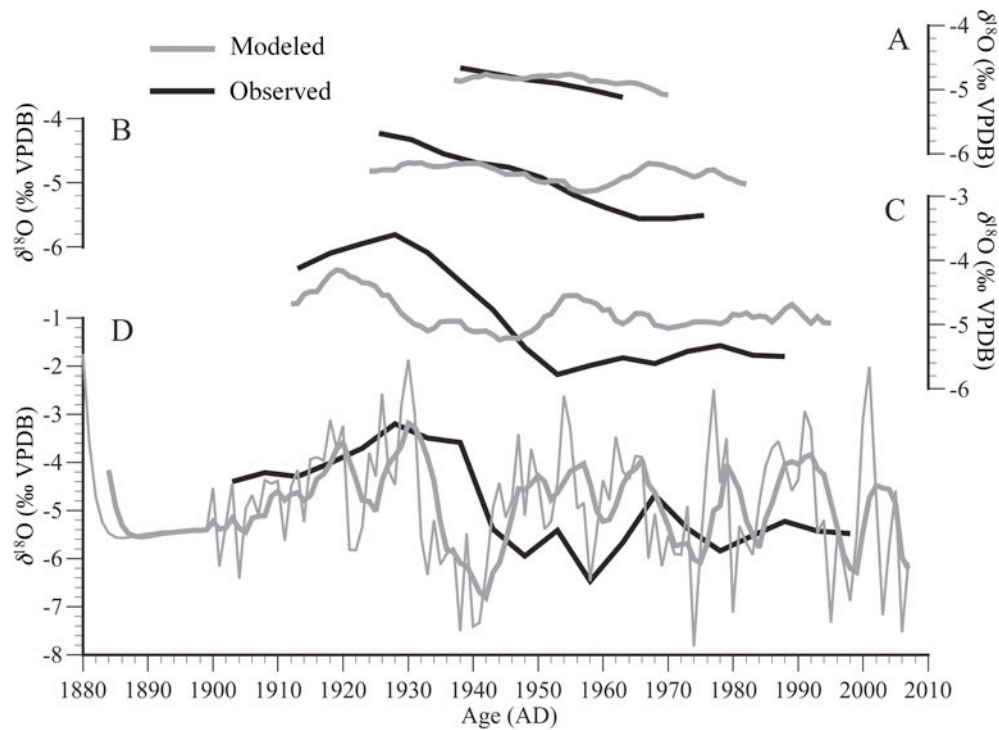


Figure 4.11 Modeled and observed sediment $\delta^{18}\text{O}$ values for Castor Lake. (A) 75 year moving average of both datasets. (B) 50 year moving average. (C) 25 year moving average. (D) Raw data (fine lines) with 5 year moving average (coarse lines) of the model results.

At SL, sediment core $\delta^{18}\text{O}$ values vary between 2.1‰ (~ 1934) and -4.9‰ (~ 1951) over the 20th century (Figures 4.8, 4.12) with interpolated sediment core $\delta^{18}\text{O}$ values varying between 2.1‰ (1933) and -4.6‰ (1950). The 20th century average value of the interpolated $\delta^{18}\text{O}$ data is -1.4‰ , with decadal maxima occurring between 1930 and 1940 and decadal minima occurring

between 1950 and 1960 (Table 4.3). The average interpolated $\delta^{18}\text{O}$ values from 1900 through 1950 and 1950 through 2006 are -0.8‰ and -2.0‰ , respectively.

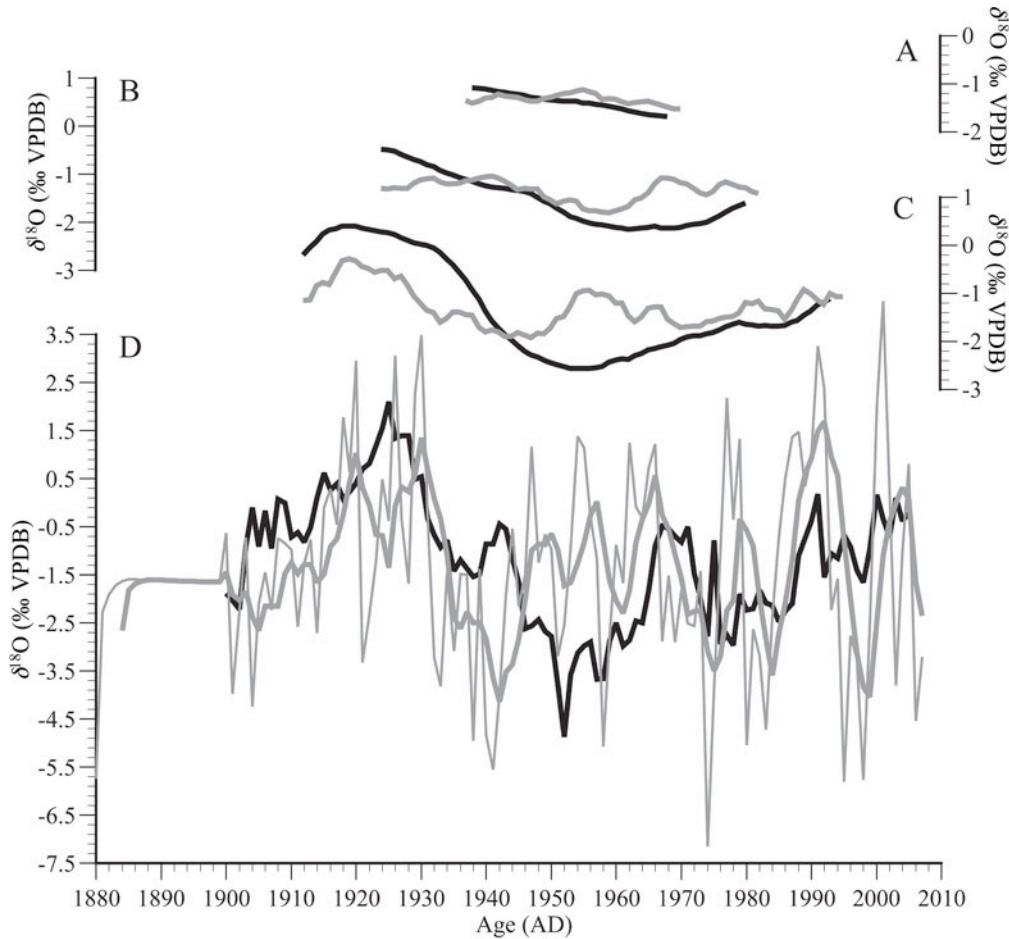


Figure 4.12 Modeled and observed sediment $\delta^{18}\text{O}$ values for Scanlon Lake. (A) 75 year moving average of both datasets. (B) 50 year moving average. (C) 25 year moving average. (D) Raw data (fine lines) with 5 year moving average (coarse lines) of the model results.

4.3.6 Modeled 20th century $\delta^{18}\text{O}$ records

At CL, model predicted intra-annual sediment core $\delta^{18}\text{O}$ values varied between 1.7‰ and -14.8‰ , with annual summer values (Jun–Sep) varying between 1.9‰ in 1930 and -7.8‰ in 1974 (Figures 4.8, 4.11). Five-year averages of the annual values reached a maximum of -3.2‰

in 1930 and a minimum of -6.8‰ in 1942. Decadal average modeled CL sediment core $\delta^{18}\text{O}$ values were highest between 1920 and 1930 with minimum values occurring between 1930 and 1940 and 1990 and 2000 (Table 4.3). The average $\delta^{18}\text{O}$ value over the first (1900 to 1950) and second (1950–2007) halves of the simulation period were -4.8‰ and -4.9‰ respectively. The average $\delta^{18}\text{O}$ value for the entire simulation period was -4.9‰ while summer $\delta^{18}\text{O}$ values prior to the application of 20th century precipitation and temperature data averaged -5.4‰.

At SL, model predicted intra-annual sediment $\delta^{18}\text{O}$ values varied between 8.5 and -14‰, with annual summer values (May–Jun) varying between 4.2 in 2002 and -7.1‰ in 1974 (Figures 4.8, 4.12). Five-year averages of the annual values reached a maximum of 1.7‰ in 1992 and a minimum of -4.1‰ in 1942. Decadal average $\delta^{18}\text{O}$ values at SL were highest between 1920 and 1930 with minimum values occurring between 1940 and 1950 (Table 4.3). The average $\delta^{18}\text{O}$ value over the first (1900–1950) and second (1950–2007) halves of the simulation period were -1.3‰ and -1.4‰, respectively. The average $\delta^{18}\text{O}$ value for the entire simulation period was -1.4‰ while summer $\delta^{18}\text{O}$ values prior to the application of 20th century precipitation and temperature data averaged -1.6‰.

4.4 DISCUSSION

4.4.1 CL authigenic carbonate formation

At CL aragonite precipitation from the water column likely occurs in the late spring and summer (June–September) as a result of physico-chemical and climatic control of the aragonite

solubility product (K_{sp}) and Ca^{2+} ion concentrations and through biological control of DIC (dissolved inorganic carbon) equilibria and carbonate species concentrations. Aragonite precipitates when the degree of saturation (Ω) exceeds a value of one:

$$\Omega = \frac{a_{Ca}a_{CO_3}}{K_{sp}} > 1 \quad (4.6)$$

where a represents ion activity of either Ca^{2+} or CO_3^{2-} . If seed crystals of aragonite are not present in solution, however, precipitation will not occur until a critical level of supersaturation is reached at which the formation energy of new phase aragonite is exceeded (Koschel 1997; Raidt and Koschel 1988; Koschel et al. 1983).

Climate can influence aragonite formation through seasonal and inter-annual temperature and precipitation variations. Temperature influences aragonite formation via two interrelated mechanisms: first, by controlling K_{sp} (higher temperatures result in lower K_{sp} values), and second, through control of primary productivity, which typically increases at higher temperatures resulting in removal of CO_2 and a shift in the DIC equilibria toward the CO_3^{2-} species (Kelts and Hsu 1978). Precipitation can influence aragonite formation by controlling the delivery of Ca^{2+} ions to the lake through runoff and baseflow. In small lakes in seasonal climatic settings, carbonate production is often limited by Ca^{2+} ion concentrations. At CL and other similar lakes, increased precipitation results in increased Ca^{2+} ion delivery to the lake and consequently greater ion availability for authigenic carbonate production in the water column. Grayscale analysis of CL sediment cores conducted by Nelson et al. (2011) revealed a close agreement between sediment color, carbonate content, and $\delta^{18}O$ values, hence confirming the applicability to CL of the Ca^{2+} limitation mechanism proposed by Shapley et al. (2005).

The biological mechanism that relates aragonite precipitation and primary productivity is not entirely understood but is thought to involve a combination of the both direct and indirect

influences of picoplankton. In the former case, picoplankton blooms can alter DIC equilibria and carbonate species concentrations and induce inorganic precipitation. In the latter case, they can provide nucleation points that reduce the formation energy of aragonite crystals (Thompson et al. 1997; Hodell et al. 1998; Sondi and Juracic 2010).

4.4.2 SL authigenic carbonate formation

At SL, *Limnocythere Staplini* ostracods hatch in the spring, molt and shed their calcite carapaces 8–9 times until reaching adulthood in the late spring/early summer. Limnocytherids form carapaces quickly, typically over several hours, and proceed through instar growth stages to adulthood within 4–6 weeks (Palacios-Fest et al. 2002). The short life cycle of *Limnocythere staplini* can potentially lead to several generations in one year, although the high alkalinity of SL waters (>9 meq/L on the basis of field alkalinity titrations) likely inhibits their growth past mid-summer (Smith et al. 1993).

All ostracod species form carapaces in isotopic disequilibrium with a constant, isotopic offset (or vital offset) from the equilibrium $\delta^{18}\text{O}$ value that is temperature and instar independent (see equations 4.3–4.5). This vital offset is constant among species within a genus. For *Limnocythere inopinata* von Grafenstein et al. 1999 calculated a value of $\sim 0.8\%$, which we apply here.

4.4.3 Model accounting for the timing of authigenic carbonate formation

The CL and SL models account for the timing of carbonate mineral formation by averaging the late spring and summer month aragonite and calcite $\delta^{18}\text{O}$ values to produce a

single value for each year that can be compared to sediment core data. At CL, aragonite is assumed to form in the water column exclusively from June through September via the processes outlined above; whereas at SL adult ostracod carapaces are assumed to form in May and then again in June after the first generation of adults reproduces. Given the alkalinity limits described by Smith et al. (1993) SL ostracods likely do not fully mature if they have not done so by the end of June. Undoubtedly, the distribution of ostracod formation at SL and aragonite formation at CL is not even over the months assigned above and is therefore a source of error that could explain discrepancies between the modeled and observed records over decadal time periods.

4.4.4 Comparison of observed and modeled lake surface elevation

Model predictions for lake surface elevation change from 1945 through 2007 were largely consistent with observations from aerial photos (Figure 4.10, Table 4.2). Modeled volumetric estimates were typically within 5% and 18% of the values inferred from lake surface elevation observations at CL and SL, respectively. The reasons for the discrepancy in the predictive accuracy of the CL and SL models are not entirely clear. One potential explanation lies in the conspicuous fact that, at SL, the model estimates for lake surface elevation are in most cases lower than observations. This underestimate could be related to several factors including inaccuracy in lake morphometry measurements (which would, in turn, lead to inaccuracy in the resulting contour maps and lake level observations) or subtle differences in precipitation, temperature, relative humidity, or wind speed at the lake, relative to the weather station-derived values used within the model simulations. The latter explanation is more probable given that precipitation, the most hydrologically significant climate variable in the lake models (i.e., the climate variable that is most influential in controlling lake levels) exhibits a spatial incoherence

that is uncharacteristic of temperature and RH. The relatively low correlation of the precipitation data (Figure 4.7) suggests that precipitation rates can considerably vary on monthly timescales over short distances such as the ~14 km separating the CL and Omak weather stations, or the ~1.5 km separating CL and SL. Therefore it is possible that precipitation rates at SL were higher than the estimates calculated on the basis of the correlation between the CL and Omak weather stations. Another possible explanation lies in the fact that SL is over 100 m higher than CL and is subject to slightly lower temperatures that result in lower evapotranspiration rates, higher snowpack, and increased spring runoff that lead to higher lake levels. These issues, coupled with the strong control of evaporation on SL hydrology (Steinman et al. 2010a) help to explain SL model underestimates of past lake surface elevation.

4.4.5 The influence of precipitation and temperature on lake level

Between 1900 and 1945 (i.e., prior to the period of orthophotograph based lake-level reconstruction) modeled lake levels and volumes were on average lower than during the period of observation (1945–2007), an expected result given that average annual precipitation rates were appreciably lower prior to 1945 (Figure 4.8, Table 4.3). Model simulations predicted high lake-stands between 1940 and 1950 and lake low-stands between 1920 and 1940. In both cases, decadal average precipitation rates were commensurate with the extent of the lake level and volume changes. For example, in the period of protracted lake lowstands (1920–1940), the lowest average decadal precipitation rates of the simulation period (1900–2007) occurred. Conversely, during the protracted highstands (1940–1950), the highest average decadal precipitation rates of the simulation period occurred. After ~1975, simulated lake level varied between relative high and low points on an approximately decadal basis in response to roughly

proportionate changes in precipitation.

The effect of temperature on lake level and volume is not as clear as that of precipitation. Highest average temperatures (and inferred increases in evaporation) occurred between 2000 and 2007 while the lowest lake levels occurred between 1930 and 1940 (Table 4.3). Similarly, average annual temperature over the period of observation was higher than over the period prior to observation when the highest modeled lake surface elevations occurred. These results support the assertions of Steinman et al. (2010a) that lake hydrologic variability on decadal timescales is primarily controlled by variations in precipitation with secondary control by temperature and RH.

4.4.6 The influence of stochastic variance on long term lake levels and $\delta^{18}\text{O}$ values

The average simulated lake level and sediment $\delta^{18}\text{O}$ values from the equilibration period (i.e., prior to the application of continuous data in 1900) were considerably different than average simulated (and observed) values from 1900 through 2007, an important observation given that 20th century average monthly climate data were applied during the equilibration period (Table 4.3). The likely explanation for this disparity lies in the catchment response to stochastic variations in precipitation-evaporation balance. Specifically, runoff and precipitation exhibit a non-linear relationship in which runoff occurs only when catchment soils are saturated such that runoff amounts are dependent on the magnitude of positive hydrologic forcing events (i.e., large precipitation events). In contrast, runoff amounts are relatively insensitive to the magnitude of negative hydrologic forcing (i.e., periods in which evapotranspiration rates exceed precipitation). Runoff amounts are therefore strongly controlled by variance in stochastic forcing, with greater variance resulting in more frequent large-scale precipitation events and consequently larger

runoff amounts and higher lake levels (Steinman et al. 2010b). These results suggest that average climate data cannot be used to accurately simulate lake hydrologic and isotopic steady states, and that stochastic variations must be applied to produce realistic long-term lake responses to changes in the mean state of climate (e.g., long term changes in precipitation or temperature).

4.4.7 Comparison of observed and modeled $\delta^{18}\text{O}$ records

At CL and SL, limitations in the temporal resolution of the sediment archives and dating methods reduce the covariance between modeled and observed sediment core $\delta^{18}\text{O}$ values over decadal timescales, restricting the evaluation of model performance over shorter time periods (e.g., investigations of modeled lake transient responses) (Figures 4.11, 4.12). Fifty to one-hundred year averages of the modeled and observed records are, however, similar in both cases (Figures 4.11, 4.12; Table 4.3), suggesting that model simulations are capable of reproducing multidecadal sediment core oxygen isotope variations. This implies that, in general, sediment oxygen isotope records lacking annually (or nearly annually) resolved age control, cannot be expected to strongly covary with model isotopic predictions over the short term (i.e., 5 to 10 years) because of dating uncertainties, but can be expected to covary over longer time periods when comparing averaged values.

4.5 CONCLUSIONS

The results presented here have important implications for paleolimnological studies, in that past hydroclimatic conditions could potentially be investigated through model analyses of multidecadal (or longer) average sediment core $\delta^{18}\text{O}$ values in lake systems for which modern climate and catchment data are available. For example, the strong control of hydroclimate on CL and SL sediment $\delta^{18}\text{O}$ values suggests that quantitative solutions of average, multidecadal hydroclimatic conditions could potentially be developed for north-central, WA using paleorecords from these lakes. Such simulations would have to include stochastic as well as mean state variations in the hydroclimatic variables and could be used to interpret multidecadal average sediment core $\delta^{18}\text{O}$ variations to estimate, for example, past precipitation rates within probabilistic limits defined by variance in the climatic variables and additional influences on the lake-catchment system (e.g., catchment vegetation on soil available water capacity or the effects of basin infill and morphology change through time). To successfully conduct such a study, however, several additional requirements will have to be met such as assessment of the relative influence of model initial conditions (i.e., lake hydrologic and isotopic states prior to the initiation of continuous climatic data) and comparison of resulting model derived quantitative predictions of hydroclimatic variables to direct climatological observations (e.g., weather station data spanning multiple decades) to assess the veracity of the quantitative reconstruction.

5.0 SMALL LAKE ISOTOPIC AND HYDROLOGIC RESPONSES TO 20TH CENTURY CLIMATE VARIABILITY: SIMULATIONS OF MEAN STATE AND STOCHASTIC CLIMATE VARIATIONS WITH NON-CONSTANT INITIAL CONDITIONS

5.1 INTRODUCTION

The isotopic composition of closed-basin lake water is influenced by multiple factors including lake morphology, groundwater throughflow rates, catchment size and hydrologic characteristics, and short term (i.e., stochastic) and longer term (mean state) climate variations. Past studies using lake-catchment hydrologic and isotope mass balance models have described the influence of many of these controlling factors and have established a basis for quantitative, paleoclimate interpretations of sediment oxygen ($\delta^{18}\text{O}$) and hydrogen (δD) isotope records (Gat 1979; Benson and Paillet 2002; Cross et al. 2004). Such interpretations have proven difficult due to the complexity in how mean state (i.e., multidecadal to century scale) and stochastic (i.e., random, interannual) changes in precipitation, temperature, and relative humidity (i.e., the primary hydroclimatic variables) influence lake hydrologic and isotopic evolution on varying time scales (Leng and Marshal 2004; Jones et al. 2007; Steinman et al. 2010a). For example, the $\delta^{18}\text{O}$ value of authigenic carbonate sediment forming within lake surface water is controlled by simultaneous hydrologic and isotopic processes such as volumetric changes in response to

precipitation evaporation balance and temperature control of calcite-water equilibrium fractionation (Gibson et al. 2002; Shapley et al. 2008; Jones and Imbers 2010). Model simulations of stochastic or mean-state variations in individual climate variables can therefore help to disentangle the many controls on lake hydrology and isotopic evolution and provide quantitative information for paleoclimate analysis of lake sediment isotope records.

Here the lake-catchment model of Steinman et al. 2010a is used to simulate the hydrologic and isotopic responses of Castor Lake (CL) and Scanlon Lake (SL) to hypothetical climate scenarios based on observed (1900–2007) weather data. In the first set of simulations altered 20th century average relative humidity (RH), temperature, and precipitation values are used to demonstrate the effects of mean-state climate change within the context of 20th century stochastic variations (i.e., average climate values were changed while maintaining the interannual standard deviations). In the second set of tests, the standard deviations of annual average 20th century temperature and precipitation were altered by a fixed percentage (i.e., the standard deviations were changed while maintaining the annual average values) to demonstrate the effects of changes in stochastic hydroclimate. In the 3rd series of simulations, the influence of initial hydrologic and isotopic conditions on model 20th century reconstructions were investigated by altering climate values during the equilibration period that preceded the application of the observed 20th century datasets. Two subsets of initial condition simulations were conducted. In the first subset, mean state precipitation was altered during the equilibration period by a fixed percentage ($\pm 50\%$) of the 20th century value and compared. The resulting 20th century $\delta^{18}\text{O}$ reconstructions was compared to the observed 20th century values of Steinman et al. (In prep. a.) (*see* Chapter 4) at moving average resolutions of 5 to 100 years. These comparisons allowed an investigation of the magnitude of potential error resulting from unknown mean state

initial conditions and provide a quantitative basis for error estimation when using lake models to interpret sediment core $\delta^{18}\text{O}$ records. In the second subset of initial condition tests, randomly generated RH, temperature, and precipitation data were applied during the equilibration period while maintaining the 20th century average and standard deviation of each climate variable. Results from these simulations provide further insight into the extent of error introduced by unknown initial conditions on 20th century model reconstructions and additionally provide information on the expected duration of the influence of past climatic events on current lake hydrologic and isotopic states.

5.2 METHODS

5.2.1 Study sites

Scanlon Lake (SL) and Castor Lake (CL) are located in north-central Washington within 14 km and 200 m elevation of two National Climatic Data Center (NCDC) and one Pacific Northwest Cooperative Agricultural Weather Network (AgriMet) weather stations. The seasonal, semi-arid climate in this region is largely controlled by the interaction between the Pacific westerlies and the Aleutian Low- and North Pacific High-pressure systems. Additional detail on study sites and regional climate can be found in Steinman et al. (2010a) (*see* Chapter 1).

5.2.2 Model structure

The following equations describe the hydrologic and isotope mass-balance of a lake:

$$\frac{dV_L}{dt} = \Sigma I - \Sigma O \quad (1.1)$$

$$\frac{d(V_L \delta_L)}{dt} = \Sigma I \delta_i - \Sigma O \delta_o \quad (1.2)$$

where V_L is lake volume, ΣI and ΣO are the total surface and below ground inflows to, and outflows from a lake, and δ is the isotopic composition of the inflows and outflows. The model applied in this study is based on a system of 12 ordinary differential equations compiled by numerical modeling software to describe water and isotope dynamics for the lake, catchment system. Detail regarding most aspects of the model is provided by Steinman et al. (2010a) (*see* Chapter 1). Additional detail regarding calculation of authigenic carbonate isotopic values is provided by Steinman et al. (In prep. a) (*see* Chapter 4).

5.2.3 Mean state RH, temperature, and precipitation forcing simulations

To explore the influence of mean state hydroclimatic changes on lake hydrologic and isotopic states (in the context of 20th century stochastic variability), simulations were conducted using altered, continuous temperature and precipitation datasets in which the annual 20th century average of each climate variable was changed by a fixed percentage while maintaining the interannual standard deviation. The resulting altered, continuous temperature and precipitation datasets allowed the estimation of lake hydrologic and isotopic responses to mean state hydroclimate forcing within the context of 20th century stochastic variability. Both positive and negative forcing simulations were conducted for precipitation ($\pm 50\%$), temperature ($\pm 20\%$) and RH ($\pm 10\%$), although in the latter case average monthly values were altered by a fixed percentage due to the lack of a continuous RH dataset spanning the 20th century.

5.2.4 Stochastic temperature and precipitation forcing simulations

To simulate lake responses to changes in the variance of stochastic hydroclimate, experiments were conducted using altered continuous temperature and precipitation datasets in which the interannual 20th century standard deviation was changed by a fixed percentage ($\pm 50\%$) while maintaining the annual average (Figure 5.1). To produce these data, average annual values for temperature and annual total values for precipitation were calculated for each year using the established 20th century datasets (Steinman et al. In prep. a) (*see* Chapter 4). An algorithm was then applied to each dataset that altered each annual value (either the annual average temperature or the annual total of precipitation) such that the 20th century average of the dataset remained unchanged while the standard deviation was either increased or decreased by 50%. Annual modifiers for each year were calculated in accordance with the following equations:

$$\left(\frac{\text{Annual total P in year X}}{\text{20th century average annual P}} - 1 \right) \times (1.5 \text{ or } 0.5) + 1 = \text{APM} \quad (5.1)$$

$$\left(\frac{\text{Annual average T in year X}}{\text{20th century average annual T}} - 1 \right) \times (1.5 \text{ or } 0.5) + 1 = \text{ATM} \quad (5.2)$$

where P is precipitation, T is temperature, APM is the annual precipitation modifier, and ATM is the annual temperature modifier. The annual modifiers for each year were then multiplied by the observed monthly values from that year to produce the final altered dataset.

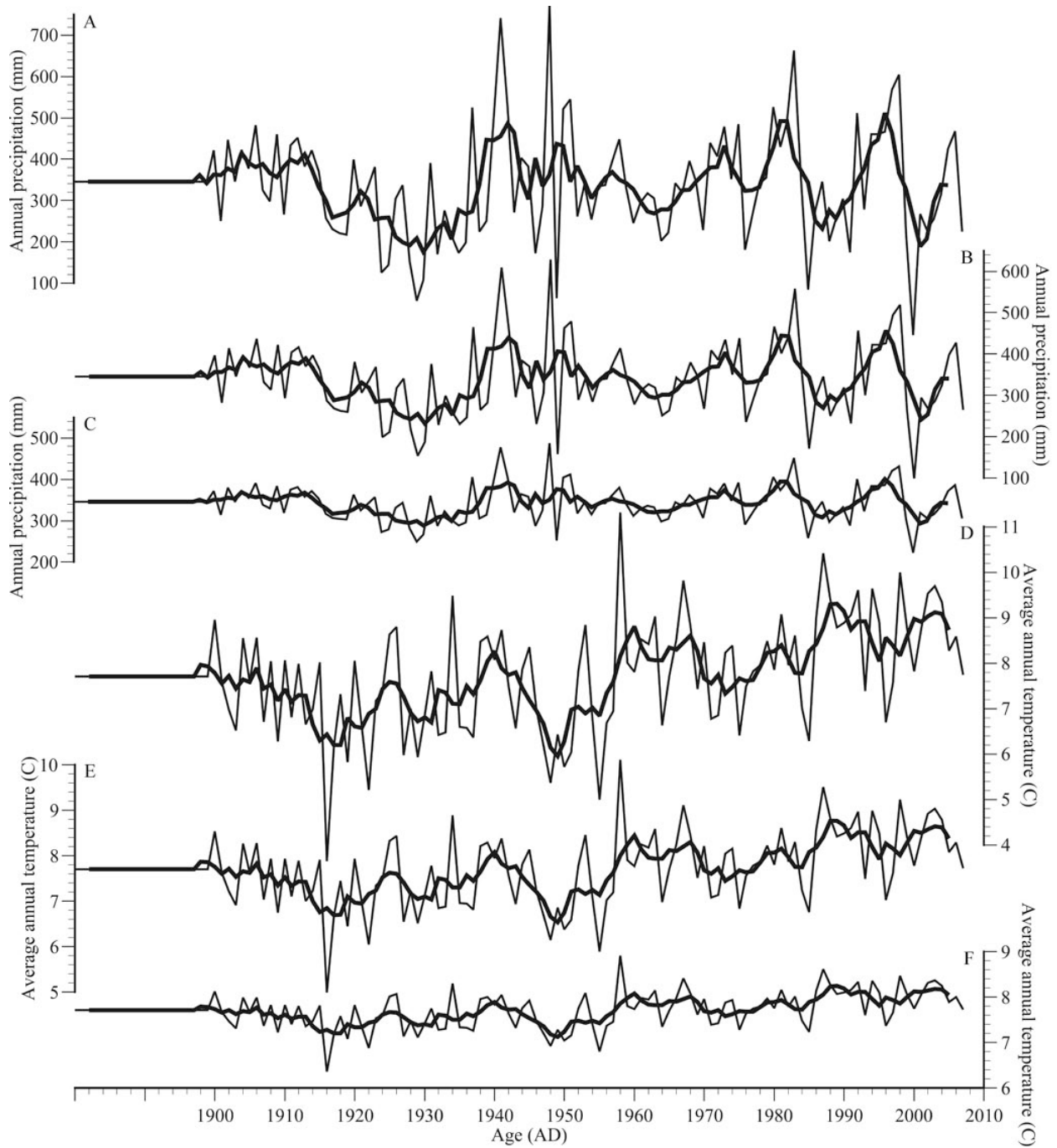


Figure 5.1 Continuous 20th century annual total precipitation and average temperature datasets modified by increasing (A, D) and decreasing (C, F) the standard deviation by 50%. (B, E) Unaltered 20th century precipitation and temperature.

5.2.5 Initial condition forcing simulations

To investigate the influence of unknown initial hydrologic and isotopic states, simulations designed to investigate the influence of unknown initial mean state and stochastic conditions representative of the 20th century were conducted. In the first subset of tests, precipitation rates were altered during the 20 year, preliminary equilibration period by a fixed percentage ($\pm 50\%$). Between year 0 and 20, average monthly precipitation was maintained at values altered by $\pm 50\%$, allowing the lakes to equilibrate at levels and isotopic values much different than those achieved using unaltered 20th century precipitation data. At model year 1900, the observed, monthly 20th century temperature and precipitation datasets were applied (Figures 1B, 1E). In the second subset of experiments, randomly generated monthly precipitation, temperature, and RH data were applied during the equilibration period. To produce each random dataset, a Gaussian distribution of annual climate modifier values was generated with an average of 1 and a standard deviation equal to the observed 20th century coefficient of variation (i.e., the interannual standard deviation divided by the annual average) for the respective climate variable. These random climate modifiers were then multiplied by the 20th century monthly average data to produce continuous, monthly datasets spanning a 20 year time period. To maintain consistency, identical randomly generated datasets were applied to both the CL and SL model configurations. For each lake 100 separate simulations were conducted.

5.3 RESULTS

5.3.1 Simulations of mean state change in hydroclimate

At CL RH changes of $\pm 10\%$ produced average 20th century sediment $\delta^{18}\text{O}$ values of -5.43‰ and -4.43‰, which differed by $\sim 0.6\%$ from the unaltered 20th century values of 4.86‰ (Figures 5.2, 5.4; Table 5.1). At SL mean RH changes produced average 20th century sediment $\delta^{18}\text{O}$ values of -2.07‰ and -0.52‰, which differed by $\sim 0.8\%$ from the unaltered 20th century values of $\sim -1.35\%$. Lake depth in the RH decrease scenario averaged 1163 cm at CL and 778 cm at SL. In the RH increase scenario lake depths averaged 1198 cm and 817 cm at CL and SL, respectively (Figures 5.3, 5.5; Table 5.1).

At CL mean state temperature changes of $\pm 20\%$ produced average sediment $\delta^{18}\text{O}$ values of -5.43‰ and -4.35‰ with an average difference of $\sim 0.5\%$ from the unaltered 20th century value. At SL, mean temperature changes produced average sediment $\delta^{18}\text{O}$ values of -2.07‰ and -0.53‰, which differed by $\sim 0.8\%$ from the unaltered 20th century value. In the temperature increase scenario lake depths averaged 1164 cm and 774 cm at CL and SL, respectively. In the temperature decrease scenario lake depths averaged 1197 cm and 823 cm.

A mean precipitation increase of 50% produced average 20th century sediment $\delta^{18}\text{O}$ values of -5.75‰ at CL and -0.91‰ at SL, which differ from the unaltered 20th century value by 0.89‰ and 0.44‰, respectively. A mean precipitation decrease of 50% produced average 20th century sediment $\delta^{18}\text{O}$ values of -2.59‰ at CL and -1.16‰ at SL, which differ from the unaltered 20th century value by 2.27‰ and 0.19‰. Lake depth in the precipitation decrease scenario averaged 440 cm at CL and 383 cm at SL. In the precipitation increase scenario lake depths averaged 1328 cm at CL and 987 cm at SL.

Table 5.1 20th century steady state and stochastic climate change simulation data.

		Average Carbonate $\delta^{18}\text{O}$ (‰ VPDB)	Surface lake $\delta^{18}\text{O}$ (‰ VSMOW)	Depth (cm)	Volume (m ³)	Res. time (yr)	Evap. Prop.	Outseep . Prop.	Over. Prop.	SA:V ratio (m ⁻¹)	
20 th century simulations											
CL	None	-4.86	-3.07	1180	317303	2.39	0.52	0.46	0.02	0.18	
SL	None	-1.35	-0.24	797	128538	1.99	0.83	0.17	0.00	0.36	
Mean state change simulations											
CL	RH	-10%	-4.33	-2.52	1163	307881	2.37	0.53	0.45	0.02	0.18
		+10%	-5.43	-3.62	1198	327087	2.42	0.51	0.46	0.03	0.19
	T	-20%	-4.35	-3.28	1197	326485	2.48	0.50	0.48	0.02	0.19
		+20%	-5.43	-2.91	1164	308336	2.31	0.54	0.44	0.02	0.18
	P	-50%	-2.59	-0.77	440	54555	1.47	0.72	0.28	0.00	0.45
		+50%	-5.75	-3.94	1328	410624	1.78	0.41	0.34	0.25	0.20
SL	RH	-10%	-0.52	0.57	778	120293	1.90	0.84	0.16	0.00	0.37
		+10%	-2.07	-1.02	817	137447	2.08	0.83	0.17	0.00	0.35
	T	-20%	-0.53	-0.12	823	139768	2.18	0.82	0.18	0.00	0.35
		+20%	-2.07	-0.36	774	118765	1.83	0.85	0.15	0.00	0.37
	P	-50%	-1.16	-0.09	383	19715	1.10	0.91	0.09	0.00	0.73
		+50%	-0.91	0.17	987	239578	1.97	0.83	0.17	0.00	0.36
Stochastic change simulations											
CL	T	-50%	-4.93	-3.12	1179	316851	2.40	0.52	0.46	0.02	0.19
		+50%	-4.83	-3.03	1178	316374	2.39	0.52	0.46	0.02	0.19
	P	-50%	-5.12	-3.32	1164	303926	2.46	0.53	0.47	0.00	0.18
		+50%	-4.83	-3.03	1209	336268	2.30	0.51	0.44	0.05	0.19
SL	T	-50%	-1.30	-0.23	796	127964	1.99	0.83	0.17	0.00	0.36
		+50%	-1.32	-0.25	797	128719	1.99	0.83	0.17	0.00	0.36
	P	-50%	-1.53	-0.47	766	113288	1.91	0.84	0.16	0.00	0.37
		+50%	-1.09	-0.02	836	148240	2.03	0.83	0.17	0.00	0.35

5.3.2 Simulations of variations in stochastic temperature

At CL changes of $\pm 50\%$ in the standard deviation of annual average temperature produced average 20th century sediment $\delta^{18}\text{O}$ values of -4.83‰ and -4.93‰ , which differed from the unaltered simulation value by $\sim 0.05\text{‰}$ (Figure 5.6, Table 5.1). CL depths averaged ~ 1180 cm in all three scenarios (i.e., increase, decrease, and unaltered). At SL temperature variance changes produced average 20th century sediment $\delta^{18}\text{O}$ values of -1.32‰ (50% increase scenario) and -1.30‰ (50% standard decrease scenario), which differed from the unaltered simulation value by $\sim 0.05\text{‰}$. SL depths averaged ~ 800 cm in all three scenarios.

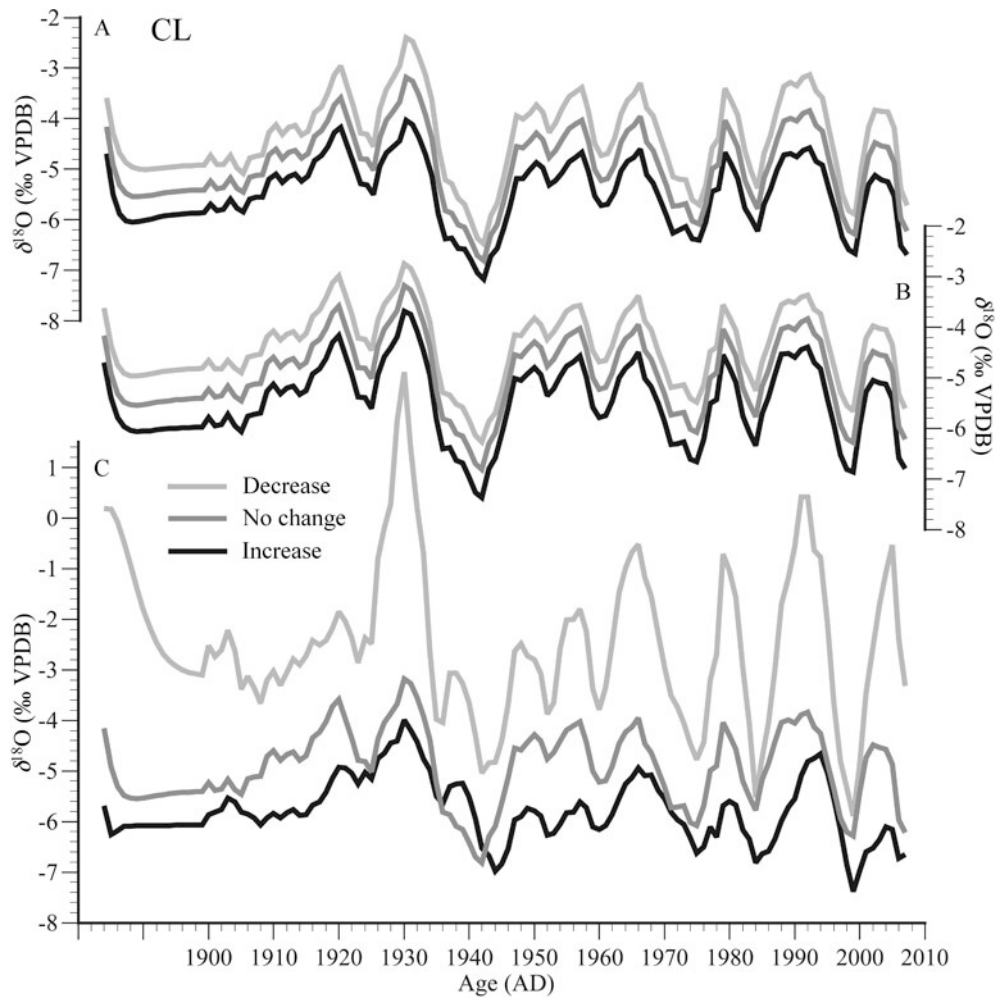


Figure 5.2 CL average summer (June–September) sediment $\delta^{18}\text{O}$ values from mean state sensitivity simulations in which monthly (A) RH ($\pm 10\%$), (B) temperature ($\pm 20\%$), and (C) precipitation ($\pm 50\%$) were increased (black line) or decreased (light gray line) by a percentage (*see above*) of their 20th century annual averages. 5 year moving averages are shown to facilitate comparison of multi-year trends. Monthly average climate data were applied during the equilibration period (i.e., during the 20 years prior to 1900).

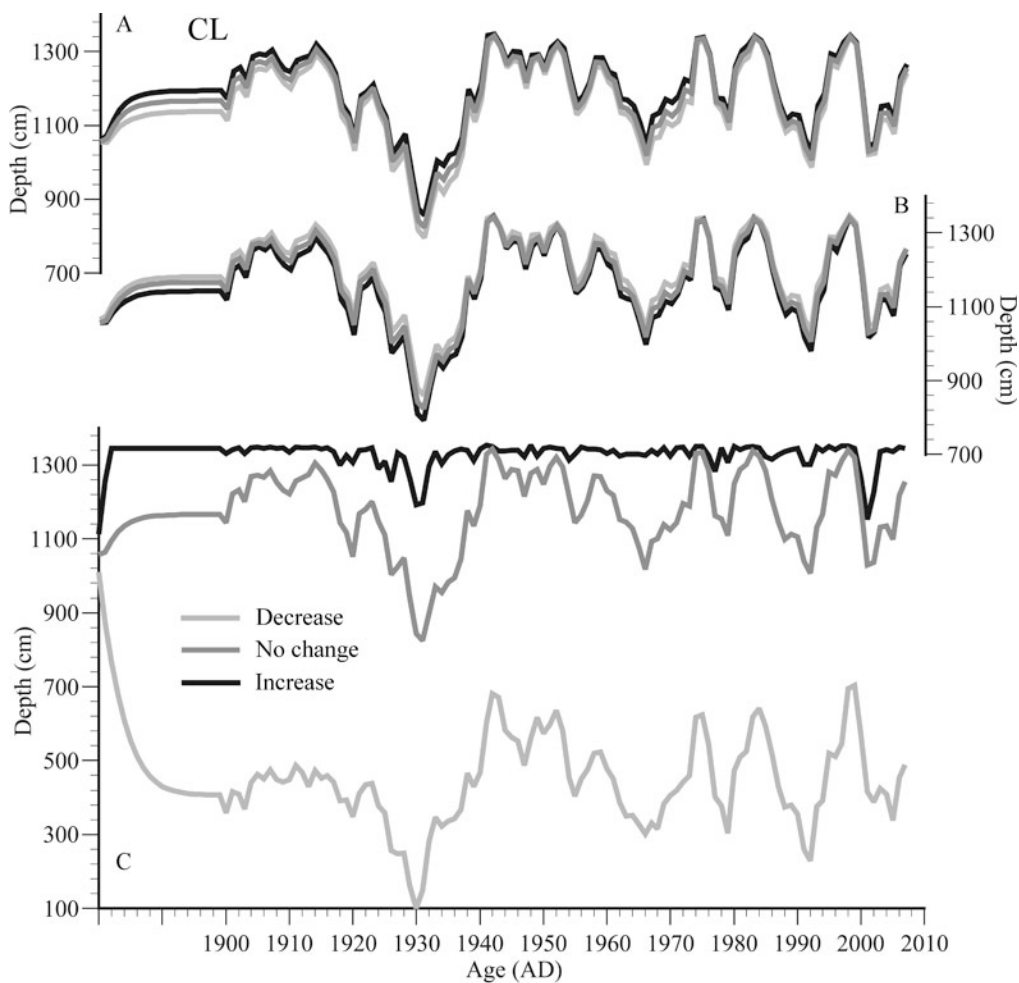


Figure 5.3 CL average summer (June–September) depth values from mean state sensitivity simulations in which monthly (A) RH ($\pm 10\%$), (B) temperature ($\pm 20\%$), and (C) precipitation ($\pm 50\%$) were increased (black line) or decreased (light gray line) by a percentage (see above) of their 20th century annual averages. 5 year moving averages are shown to facilitate comparison of multi-year trends. Monthly average climate data were applied during the equilibration period (i.e., during the 20 years prior to 1900).

5.3.3 Simulations of variations in stochastic precipitation

At CL a change of $\pm 50\%$ in the standard deviation of annual total precipitation produced average 20th century sediment $\delta^{18}\text{O}$ values of -4.83‰ and -5.12‰ , which differed from the unaltered simulation value by 0.03‰ and 0.26‰ , respectively (Figure 5.6, Table 5.1). At SL precipitation variance changes produced average 20th century sediment $\delta^{18}\text{O}$ values of -1.09‰ (50% increase scenario) and -1.53‰ (50% decrease scenario), which differed from unaltered

simulation values by 0.26‰ and 0.18‰. CL depths averaged 1209 cm in the variance increase scenario and 1164 cm in the decrease scenario, with an average difference of 23 cm from the unaltered 20th century depth of 1180 cm (Figure 5.7, Table 5.1). SL depths averaged 836 cm and 766 cm, respectively, with an average difference of 35 cm from the unaltered 20th century depth of 797 cm.

5.3.4 Initial condition sensitivity simulations (mean state)

In the initial precipitation increase and decrease scenarios initial 5 year average CL sediment $\delta^{18}\text{O}$ values were -4.59‰ and -7.70‰ respectively, a difference of 0.78‰ and 2.33‰ from the unaltered initial condition $\delta^{18}\text{O}$ value of -5.37‰ (Table 5.2). Modeled CL sediment isotopic values in both scenarios converged with $\delta^{18}\text{O}$ results from the unaltered initial condition scenario by 1911 (i.e., the difference between altered and unaltered scenario $\delta^{18}\text{O}$ values decreased to <0.25‰) (Figure 5.8). Modeled lake depths converged by 1909 (i.e., the difference between altered and unaltered scenario depths decreased to <10cm) (Figure 5.10). Application of 50 year moving averages reduced the differences between initial values of the initial precipitation decrease and increase scenarios to <0.5‰, with 100 year averages reducing the difference to <0.25‰.

At SL, the initial 5 year average $\delta^{18}\text{O}$ value in the initial precipitation increase and decrease scenarios were 0.02‰ and -5.42‰, respectively, which differ by ~2.7‰ from the unaltered initial condition $\delta^{18}\text{O}$ value of -2.36‰ (Table 5.2). Modeled sediment isotopic values and lake depths converged by 1912 (Figures 5.9, 5.10). Application of 50 year moving averages reduced the differences between initial values of the initial precipitation decrease and increase scenarios to ~0.75‰, with 100 year averages reducing the difference to <0.40‰.

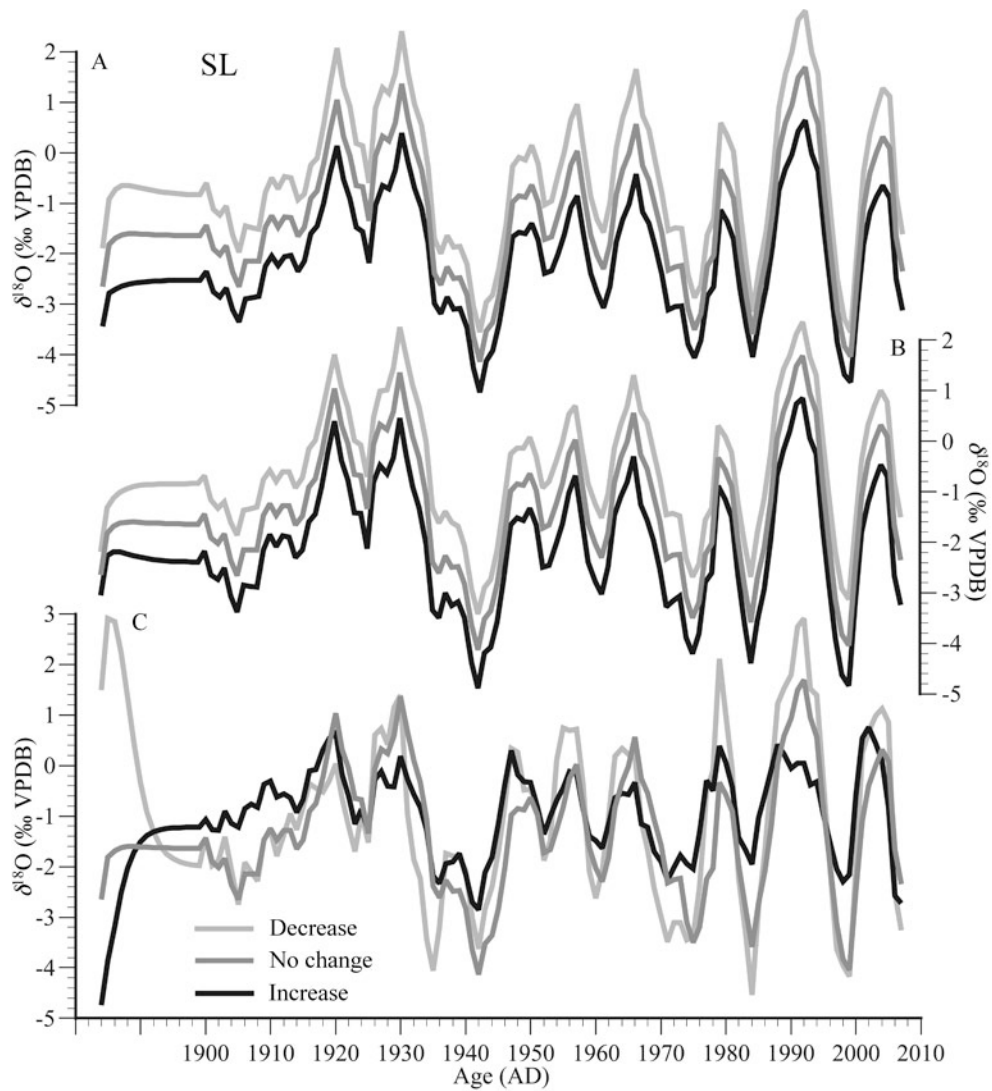


Figure 5.4 SL average spring/summer (May–June) sediment $\delta^{18}\text{O}$ values from mean state sensitivity simulations in which monthly (A) RH ($\pm 10\%$), (B) temperature ($\pm 20\%$), and (C) precipitation ($\pm 50\%$) were increased (black line) or decreased (light gray line) by a percentage (*see above*) of their 20th century annual averages. 5 year moving averages are shown to facilitate comparison of multi-year trends. Monthly average climate data were applied during the equilibration period (i.e., during the 20 years prior to 1900).

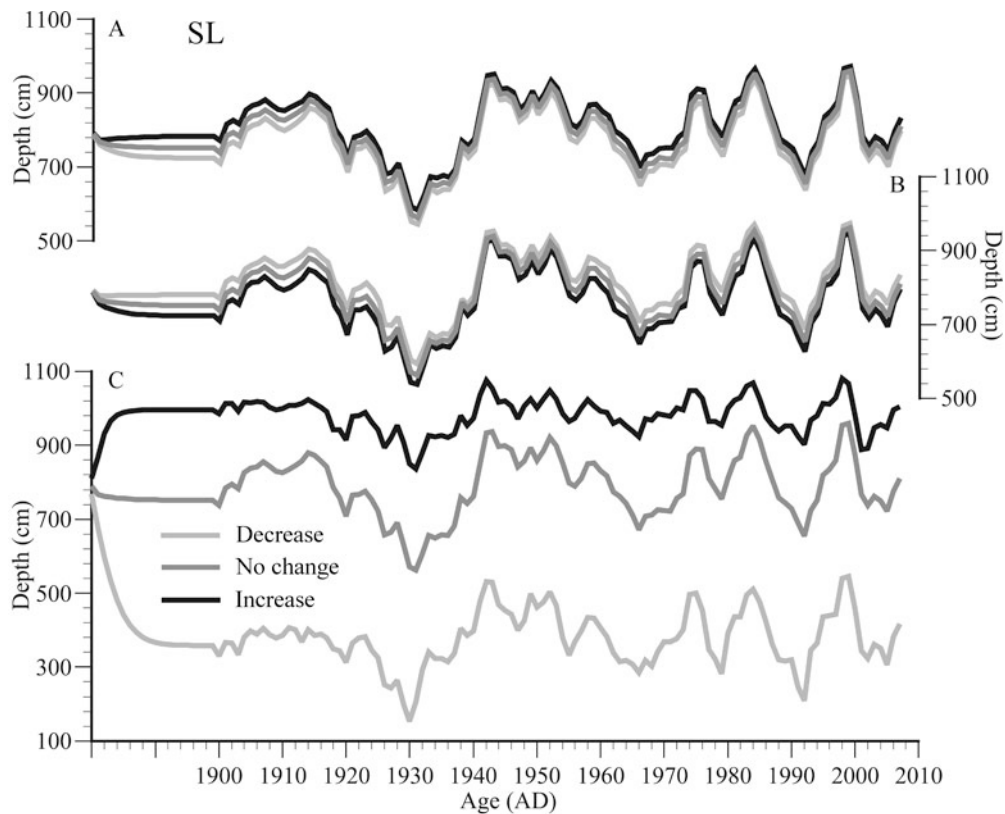


Figure 5.5 SL average spring/summer (May–June) depth values from mean state sensitivity simulations in which monthly (A) RH ($\pm 10\%$), (B) temperature ($\pm 20\%$), and (C) precipitation ($\pm 50\%$) were increased (black line) or decreased (light gray line) by a percentage (see above) of their 20th century annual averages. 5 year moving averages are shown to facilitate comparison of multi-year trends. Monthly average climate data were applied during the equilibration period (i.e., during the 20 years prior to 1900).

The difference between modeled and observed sediment $\delta^{18}\text{O}$ values generally decreased when moving averages were applied. At CL, the average difference between the 5 year moving average modeled and observed sediment $\delta^{18}\text{O}$ values was 0.96‰ in the unaltered initial condition scenario, 0.90‰ in the increased initial precipitation scenario, and 1.14‰ in the decreased initial condition scenario (Table 5.2). At SL, the average differences between the 5 year moving average modeled and observed sediment $\delta^{18}\text{O}$ values were 1.36‰ in the unaltered scenario, 1.29‰ in the increase scenario, and 1.48 in the decrease scenario. In contrast, at CL and SL, the average differences between the 50 year moving average modeled and observed sediment $\delta^{18}\text{O}$ values were 0.35‰ and 0.42‰ in the unaltered initial condition scenario, 0.34‰

and 0.39‰ in the increased initial precipitation scenario, and 0.39‰ and 0.45‰ in the decreased initial condition scenario, respectively.

5.3.5 Initial condition sensitivity simulations (random)

Modeled CL and SL sediment isotopic values produced through the application of randomly generated stochastic hydroclimate inputs converged in 1910 and 1912, respectively (i.e., the 2σ value for the 100 simulations of each lake decreased $<0.25\text{‰}$) (Figures 11, 12). Modeled CL and SL lake volumes converged in 1907 and 1913, respectively (i.e., the 2σ volume for all simulations decreased to $<2.5\%$ of average lake volume).

5.4 DISCUSSION

5.4.1 Simulations of mean state variations in RH, temperature, and precipitation

Results of the mean state forcing experiments indicate that long-term (i.e., 50–100 year) lake sediment isotopic values are controlled by RH, temperature, and precipitation and that in closed lakes with higher outseepage rates (e.g., CL) precipitation is the primary control. In lakes with lower outseepage rates where a greater proportion of water is lost through evaporation (e.g., SL), RH and temperature (which influence the isotopic composition of evaporated surface water) become more important long term isotopic influences.

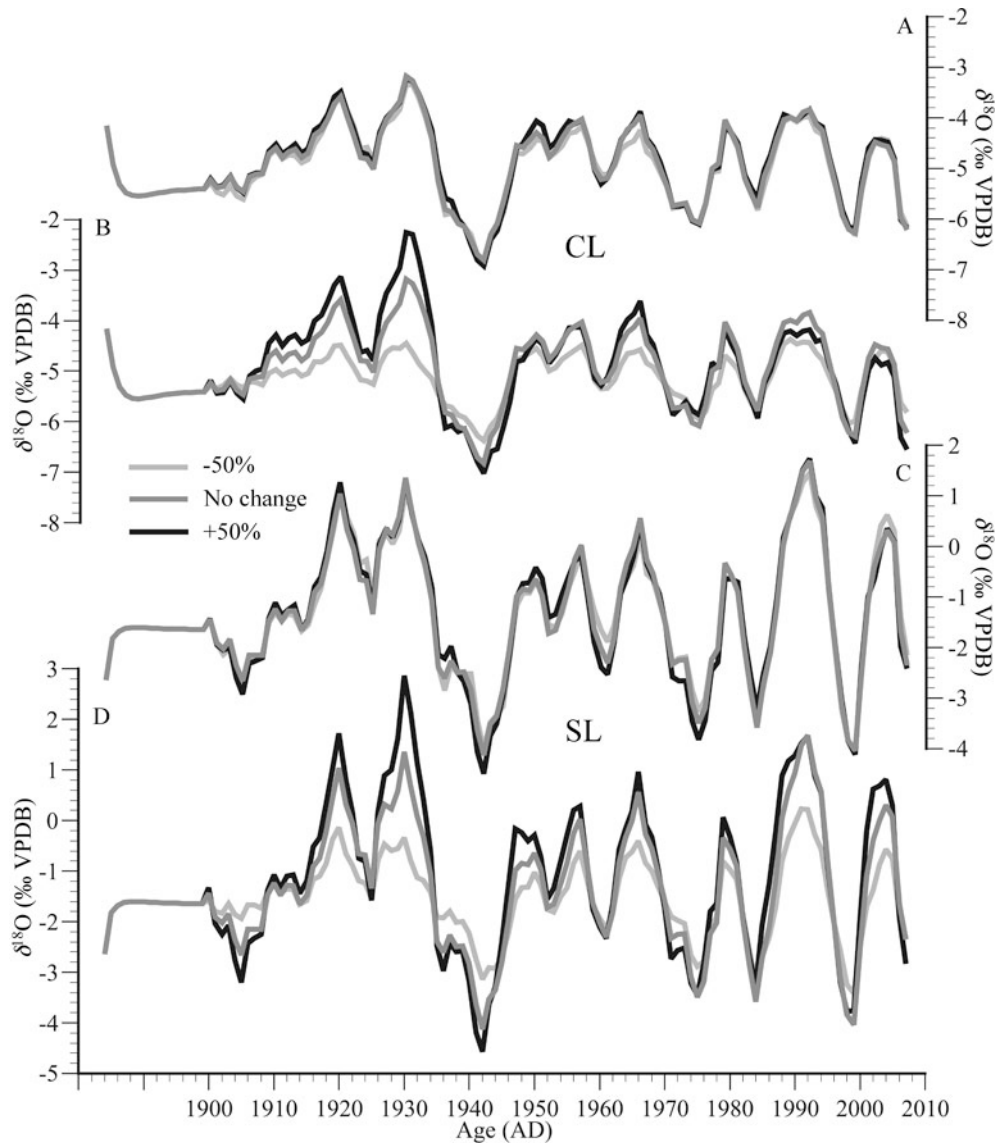


Figure 5.6 (A, B) CL and (C, D) SL average spring/summer (June–September for CL and May–June for SL) sediment $\delta^{18}\text{O}$ values from stochastic forcing simulations in which the standard deviation of 20th century (A, C) average annual temperature and (B, D) total annual precipitation were altered by a fixed percentage ($\pm 50\%$) (see Figure 5.1, above). 5 year moving averages are shown to facilitate comparison of multi-year trends. Monthly average climate data were applied during the equilibration period (i.e., during the 20 years prior to 1900).

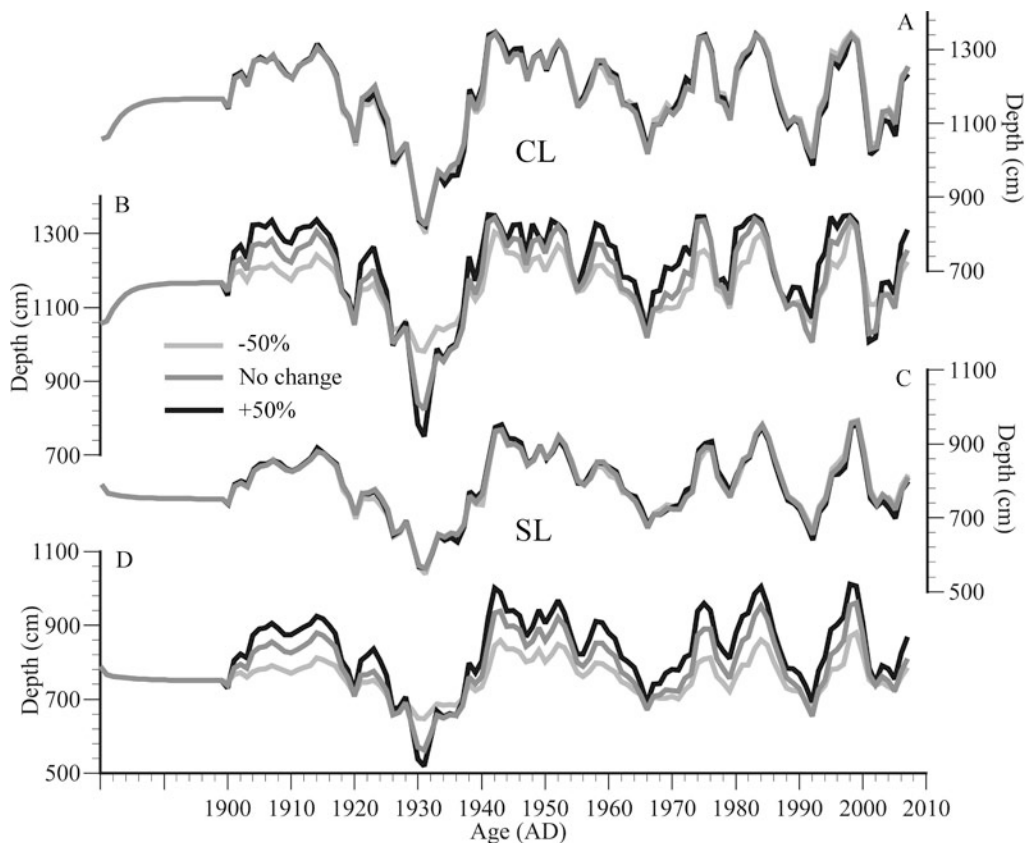


Figure 5.7 (A, B) CL and (C, D) SL average spring/summer (June–September for CL and May–June for SL) depth values from stochastic forcing simulations in which the standard deviation of 20th century (A, C) average annual temperature and (B, D) total annual precipitation were altered by a fixed percentage ($\pm 50\%$) (see Figure 5.1, above). 5 year moving averages are shown to facilitate comparison of multi-year trends. Monthly average climate data were applied during the equilibration period (i.e., during the 20 years prior to 1900).

The effects of mean precipitation change on average sediment $\delta^{18}\text{O}$ values were inconsistent between CL and SL and depended upon outseepage and basin characteristics. At CL, large increases in mean precipitation caused overflow (a non-fractionating outflow pathway) and consequently smaller $\delta^{18}\text{O}$ values, while large precipitation decreases caused greater water loss through evaporation (a fractionating outflow pathway) and larger $\delta^{18}\text{O}$ values (Figure 5.2, Table 5.1). At SL the SA:V ratio increased in both the P increase and decrease scenarios, leading to greater water loss through evaporation and isotopic enrichment of surface water and sediment (Figure 5.4, Table 5.1). In the precipitation decrease scenario, the larger $\delta^{18}\text{O}$

responses at CL relative to SL was a result of the contrasting outseepage rates of the two basins. At CL, where the outseepage rate is higher, a decrease in lake level leads to an increased SA:V ratio, and a corresponding increase in the proportion of water lost through evaporation. In contrast, at SL where the outseepage rate is lower, a decrease in lake level does not lead to a large change in the proportion of water lost through evaporation since the SA:V ratio is large at all lake levels (Table 5.1). These results lend further support to the hypothesis of Steinman et al. (2010a) that lake outseepage rates are a fundamental control of long term lake isotopic responses to hydrologic forcing (i.e., lower outseepage rates cause decreased lake isotopic sensitivity to mean state hydrologic forcing).

Table 5.2 Initial condition sensitivity simulation data.

Period of avg.	No initial condition precipitation change			Initial condition precipitation = -50%			Initial condition precipitation = +50%			
	Initial mod. $\delta^{18}\text{O}$ value (‰)*	Max. $\delta^{18}\text{O}$ diff. from sed. record (‰)*	Avg. $\delta^{18}\text{O}$ diff. from sed. record ^a (‰)*	Initial mod. $\delta^{18}\text{O}$ value (‰)*	Max. $\delta^{18}\text{O}$ diff. from sed. record (‰)*	Avg. $\delta^{18}\text{O}$ diff. from sed. record ^a (‰)*	Initial mod. $\delta^{18}\text{O}$ value (‰)*	Max. $\delta^{18}\text{O}$ diff. from sed. record (‰)*	Avg. $\delta^{18}\text{O}$ diff. from sed. record ^a (‰)*	
CL	none	-4.54	-0.13	0.13	-4.30	-3.77	1.14	-4.52	-2.83	0.90
	5	-5.37	-2.83	0.96	-7.70	-2.46	0.97	-4.59	-2.29	0.81
	10	-5.04	-2.29	0.85	-6.72	-1.27	0.70	-4.44	-1.22	0.63
	25	-4.68	-1.22	0.65	-5.40	-0.95	0.39	-4.69	-0.46	0.34
	50	-4.81	0.80	0.35	-5.17	-0.20	0.09	-4.77	-0.13	0.10
	75	-4.85	0.22	0.12	-5.09	-0.17	-0.17	-4.80	0.07	0.07
	100	-4.86	0.01	0.01	-5.04	-0.17	-0.17	-4.80	0.07	0.07
SL	none	0.63	3.27	1.36	-3.26	1.48	0.02	3.27	1.29	1.29
	5	-2.36	2.55	1.06	-5.42	1.14	-0.21	2.55	0.99	0.99
	10	-1.91	1.63	0.70	-3.79	0.74	-0.40	1.63	0.65	0.65
	25	-1.15	1.04	0.42	-1.95	0.45	-0.92	1.04	0.39	0.39
	50	-1.29	0.16	0.16	-1.69	0.23	-1.16	0.28	0.13	0.13
	75	-1.40	0.06	0.06	-1.63	0.18	-1.17	0.08	0.04	0.04
	100	-1.35	0.06	0.06	-1.56	0.18	-1.17	0.08	0.04	0.04

^aAbsolute values of differences were averaged.

* VPDB

At both CL and SL mean temperature increases produced lower average sediment $\delta^{18}\text{O}$ values due largely to the method applied in this study to adjust monthly temperature (Figures 5.2, 5.4; Table 5.1). Steinman et al. (2010a) demonstrate that an increase in average air temperature

should cause an increase in surface water $\delta^{18}\text{O}$ values due both to greater evaporation rates (and consequent isotopic enrichment of surface water) and higher precipitation $\delta^{18}\text{O}$ values (Rozanski et al. 1992). These two effects are balanced by temperature control of equilibrium fractionation for the calcite/aragonite-water system in which increasing temperature decreases fractionation and consequently lowers calcite $\delta^{18}\text{O}$ values (Kim and O'Neil 1997; Zhou and Zheng 2003). Because monthly climate values were altered by a fixed percentage, however, the lower temperature winter months were adjusted by a smaller absolute amount than were the higher temperature summer months, causing summer control of the calcite/aragonite-water fractionation factor to overwhelm winter control of the isotopic composition of precipitation. This effectively produced a pattern of seasonality in temperature that may not reflect lake responses to constant, non-seasonal offsets in average monthly temperature.

Lake hydrologic responses to mean state changes in the hydroclimatic variables, RH, temperature, and precipitation, were generally consistent between CL and SL, in that altered precipitation rates more strongly influenced average lake level and volume than did altered RH and temperature (Figures 5.3, 5.5; Table 5.1). There were however inconsistencies between the two sites. At CL for example RH and temperature adjustments produced less extensive average lake level changes than at SL. This greater sensitivity of SL lake level and volume to mean state changes in RH and temperature is caused by the lower outseepage rate at SL and the fact that evaporation is a greater proportion of total outflow at SL than at CL. These results suggest that RH and temperature control of long-term lake level and volume is in part a function of the lake outseepage rate, which in lakes without surficial outflow (e.g., SL), is main control on the evaporation outflow proportions.

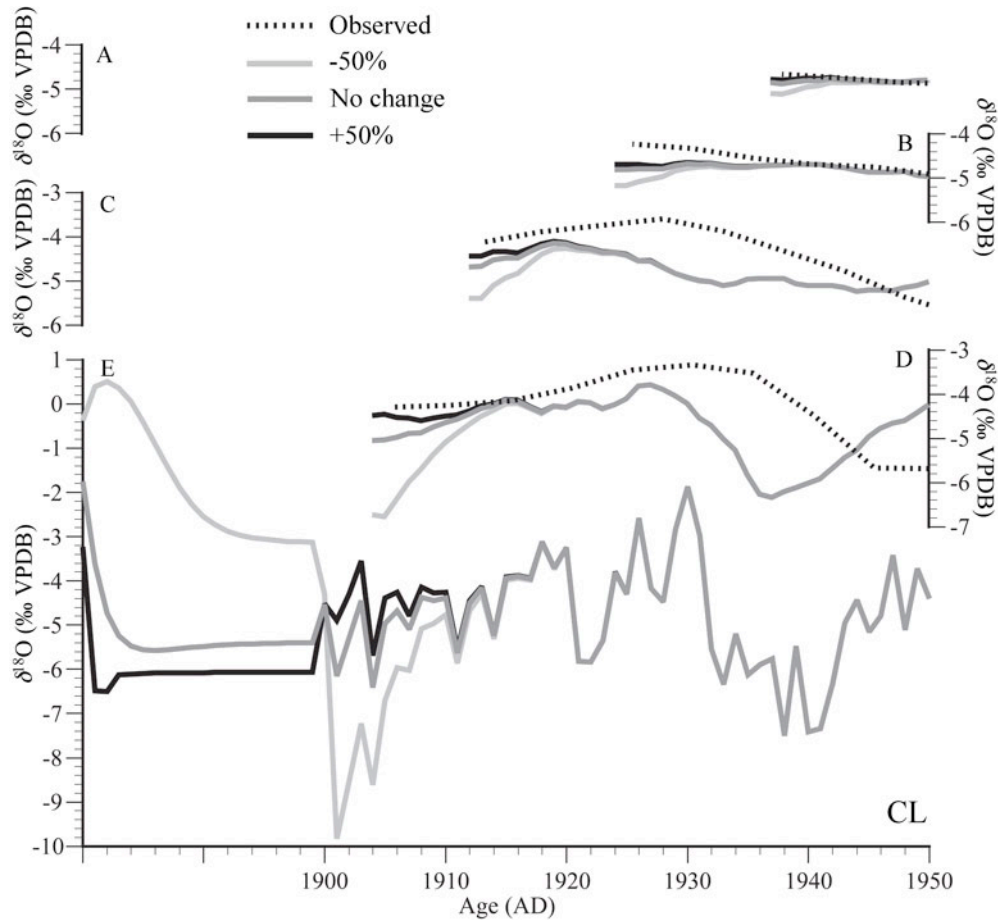


Figure 5.8 CL $\delta^{18}\text{O}$ average summer month (June–September) $\delta^{18}\text{O}$ values from initial condition sensitivity simulations and observed sediment core $\delta^{18}\text{O}$ measurements. (A) 75-year (B) 50-year (C) 25-year and (D) 10-year moving average modeled (solid lines) and observed (dashed lines) $\delta^{18}\text{O}$ values. (E) represents raw model data. Black (light gray) lines depict modeled sediment $\delta^{18}\text{O}$ values with average monthly precipitation increased (decreased) by 50% during the equilibration period and unaltered thereafter. Gray lines depict modeled sediment $\delta^{18}\text{O}$ values with unaltered precipitation rates during the equilibration period.

An additional, notable result is that the variance of interannual sediment $\delta^{18}\text{O}$ values in model simulations was dependent in part on lake level and volume, with decreased lake level resulting in increased variance in interannual $\delta^{18}\text{O}$ values. This result supports the conclusion of Steinman et al. (2010b) that interannual percentage changes in lake volume will be greater at lower lake levels, resulting in comparably larger isotopic variations in response to stochastic precipitation.

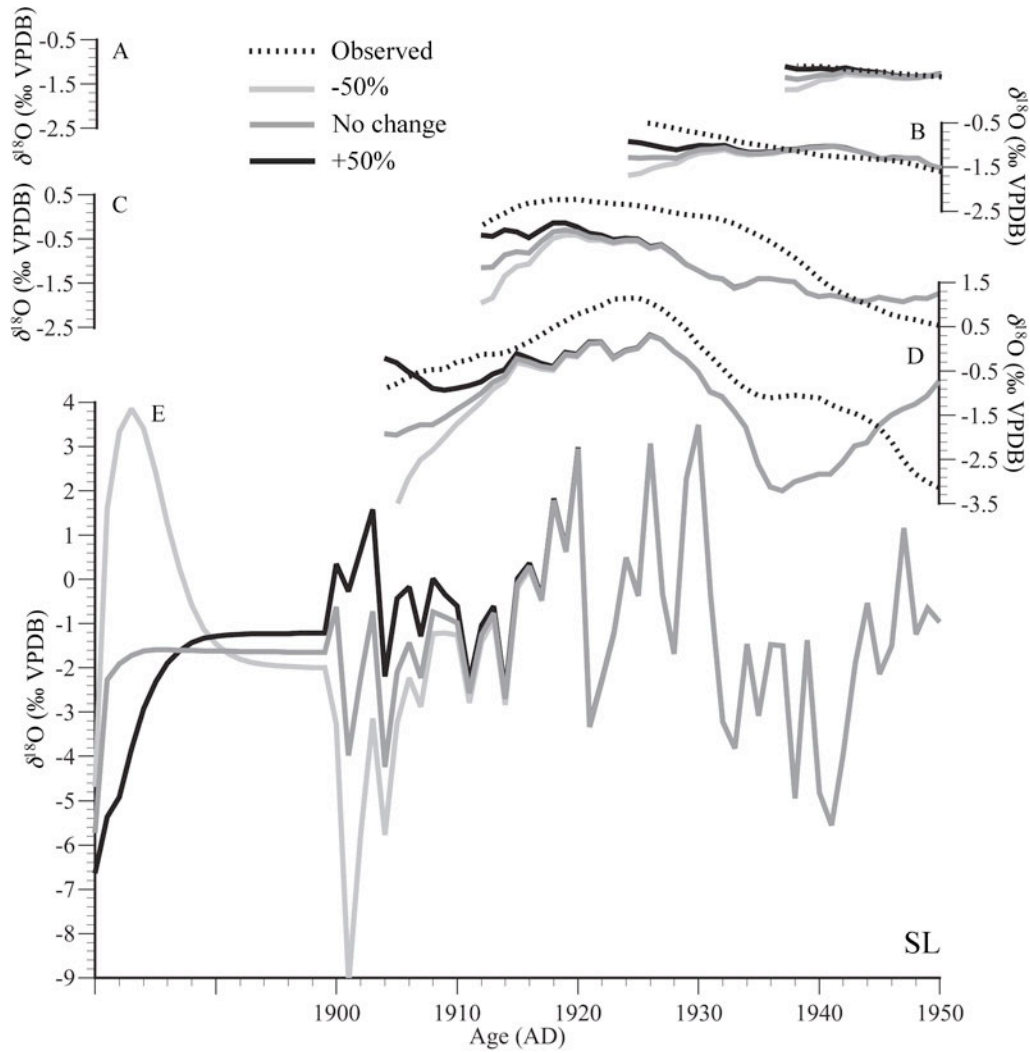


Figure 5.9 SL average spring/summer month (May–June) $\delta^{18}\text{O}$ values from initial condition sensitivity simulations and observed sediment core $\delta^{18}\text{O}$ measurements. (A) 75-year (B) 50-year (C) 25-year and (D) 10-year moving average modeled (solid lines) and observed (dashed lines) $\delta^{18}\text{O}$ values. (E) represents raw model data. Black (light gray) lines depict modeled sediment $\delta^{18}\text{O}$ values with average monthly precipitation increased (decreased) by 50% during the equilibration period and unaltered thereafter, i.e., at simulation year 1900, the continuous, observed climate data were applied. Gray lines depict modeled sediment $\delta^{18}\text{O}$ values with unaltered precipitation rates during the equilibration period.

5.4.2 Simulations of variations in stochastic RH, temperature, and precipitation

At both CL and SL, the variance of modeled, interannual sediment isotope values was largely commensurate with the variance of annual precipitation, an expected result given the control that precipitation exerts over water and sediment $\delta^{18}\text{O}$ values on an interannual to decadal time scale (Figure 5.6, Table 5.1). Conversely, simulations of changes in the standard deviation of temperature demonstrate an almost complete lack of stochastic temperature control on decadal to subdecadal sediment $\delta^{18}\text{O}$ values. This result can be explained by the much lower standard deviation of average annual temperature relative to that of precipitation in north-central Washington (Steinman et al. 2010a).

The 20th century average $\delta^{18}\text{O}$ value at CL was greater in the decreased (rather than the increased) variance scenario, suggesting that variability in stochastic forcing can influence multi-decade to century scale lake isotope values (Table 5.1). The same cannot be said for stochastic variance in temperature, however, as the average of 20th century $\delta^{18}\text{O}$ values did not significantly vary in either of the temperature variance scenarios. The former of these two results is in part supported by data from Steinman et al. (2010b) (i.e., small changes in mean state water $\delta^{18}\text{O}$ values result from changes in the standard deviation of interannual precipitation), although the changes in stochastic variance applied in their study were half the magnitude of those applied in this study (25% versus 50%, respectively).

Altering the standard deviation of temperature produced minimal change in both short-term and long-term lake levels (Figure 5.7, Table 5.1), while altering stochastic precipitation produced relatively extensive changes in lake level at all time scales. At both CL and SL the average modeled 20th century lake level and volume was greater in the increased precipitation

standard deviation scenario (and vice versa), suggesting that variability in stochastic precipitation can influence long term lake hydrology. This result is supported by Steinman et al. (2010b), who demonstrated that changes in long term lake level and volume can result from variations in the standard deviation of interannual precipitation due to non-linear catchment runoff responses to large precipitation events.

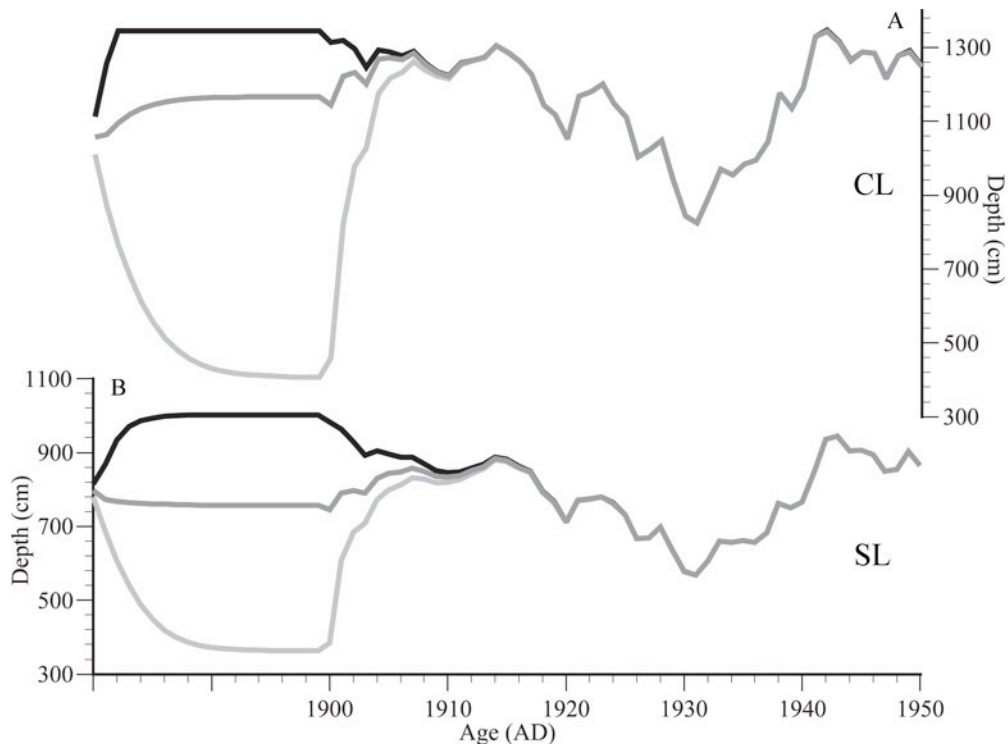


Figure 5.10 (A) CL and (B) SL average summer month (June–September/May–June) depth values from initial condition sensitivity simulations. Black (light gray) lines depict modeled sediment $\delta^{18}\text{O}$ values with average monthly precipitation increased (decreased) by 50% during the equilibration period and unaltered thereafter (i.e., at simulation year 1900, the continuous, observed climate data were applied). Gray lines depict modeled sediment $\delta^{18}\text{O}$ values with unaltered precipitation rates during the equilibration period.

Results from the mean state and stochastic sensitivity simulations demonstrate that changes in average RH and temperature produce approximately constant isotopic shifts in water and sediment $\delta^{18}\text{O}$ values, while changes in mean precipitation produce inconsistent responses

that depend on the lake basin morphometry and outseepage characteristics. In lakes with low outseepage rates (e.g., SL) mean precipitation change does not affect average long term average water and sediment $\delta^{18}\text{O}$ values because evaporation outflow proportions remain much higher than outseepage proportions at all lake levels. Conversely, in lakes with high outseepage (e.g., CL) mean precipitation changes affect long term water and sediment $\delta^{18}\text{O}$ values by influencing the proportion of water lost through evaporation (a fractionating outflow pathway) and outseepage (a non-fractionating outflow pathway). Mean precipitation change also influences the standard deviation of interannual $\delta^{18}\text{O}$ values through control of average lake levels, and consequent control of the percentage change in volume resulting from stochastic precipitation (Steinman et al. 2010b). In volumetrically smaller lakes with high SA-V ratios, a larger standard deviation of interannual isotopic responses to stochastic hydroclimate can be expecting than in volumetrically larger lakes with low SA-V ratios. Similarly, the magnitude of the isotopic response of smaller lakes (such as SL) to individual precipitation events will be larger than the response of volumetrically larger (lakes such CL).

5.4.3 Simulations of unknown initial conditions

At both CL and SL, modeled sediment $\delta^{18}\text{O}$ values and lake levels in the 1st decade of the 20th century were extensively different in all three mean state change initial condition scenarios (i.e., in the +50%, -50%, and unaltered initial precipitation simulations) (Figures 5.8–5.10). Not until ~1912 did the modeled $\delta^{18}\text{O}$ values from all three simulations converge to within ~0.1‰. Results of the random initial condition simulations were largely comparable, suggesting that lake responses to unknown mean state and stochastic initial conditions are similar (Figure 5.11). For instance, at both CL and SL, extensive variance in lake volume and $\delta^{18}\text{O}$ values between

individual model runs persisted for approximately 12 years, as defined by the 2σ threshold for $\delta^{18}\text{O}$ and volume values of 0.25‰ and 5% of total volume, respectively. This ~ 12 year persistence of extensive variance in the $\delta^{18}\text{O}$ values indicates that initial conditions can strongly influence model isotopic predictions over the first ~ 12 years of the simulation and do not significantly affect model results thereafter.

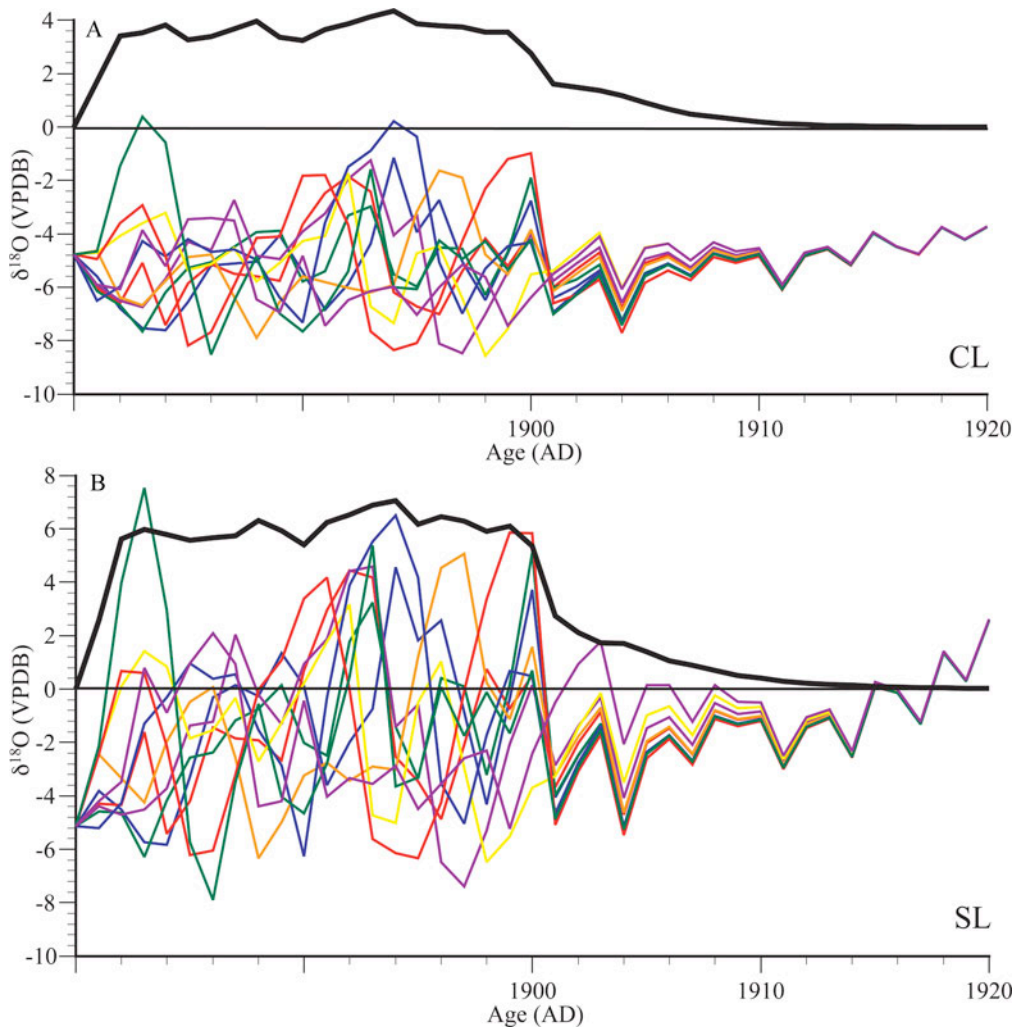


Figure 5.11 (A) CL and (B) SL average summer month (June–September/May–June) $\delta^{18}\text{O}$ values (colored lines) from initial condition sensitivity simulations in which random precipitation, temperature, and RH data were applied during the equilibration period. The black line depicts the annual 2σ value of the $\delta^{18}\text{O}$ data. All randomly generated weather datasets maintained the standard deviation and average observed in 20th century. 100 simulations were conducted but results from only 10 are shown to maintain clarity.

The residence time and proportion of volumetric change in response to climate forcing determine the duration of the influence of initial hydrologic conditions. In volumetrically smaller lakes (e.g., SL) with shorter residence times, the percentage volumetric change, and consequently, the isotopic response to hydrologic forcing is larger than in volumetrically larger lakes (e.g., CL) with longer residence times. In larger lakes, however, the longer residence time prolongs the influence of the initial condition relative to smaller lakes. The combination of these two characteristics (i.e., longer residence times in the case of volumetrically larger lakes, and larger percentage changes in volume in the case of smaller lakes) leads to a lake memory (i.e., duration of initial lake response to climatic forcing) of ~12 years (~6 residence times) for closed lakes with volumes similar to those of this study.

If moving averages of ~50 years or longer are applied to modeled $\delta^{18}\text{O}$ values, differences between the initial condition simulation results become small (Figures 5.8, 5.9; Table 5.2). This suggests that model simulations can be used to quantitatively analyze sediment oxygen isotope records over discrete time periods without regard to preceding sediment isotopic values and associated climatic states. For example, if 50 year moving averages are applied to sediment oxygen isotope records from small lakes similar to CL and SL, model simulations can be conducted to analyze hydroclimatic conditions within each 50 year window with limited regard for the preceding isotopic or hydrologic conditions.

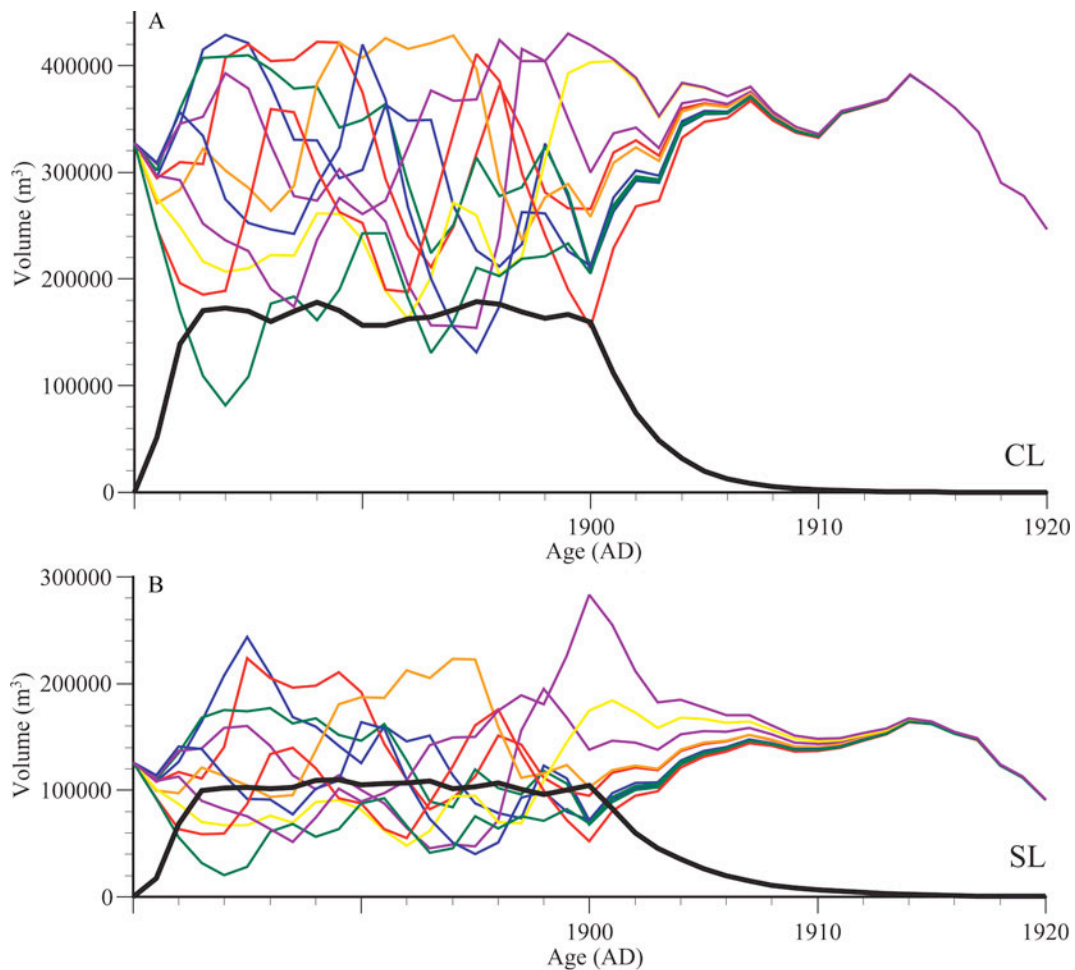


Figure 5.12 (A) CL and (B) SL average summer month (June–September/May–June) volume values (colored lines) from initial condition sensitivity simulations in which random precipitation, temperature, and RH data were applied during the equilibration period. All randomly generated weather datasets maintained the standard deviation and average observed in 20th century. The black line depicts the annual 2σ value of the $\delta^{18}\text{O}$ data. 100 simulations were conducted but results from only 10 are shown to maintain clarity.

5.5 CONCLUSIONS

The hydrologic and isotopic state of a lake is dependent upon the hydrologic and isotopic states of the lake in many prior years, with the duration of this influence controlled in part by the volume and residence time of the lake. Consequently, interpretations of average sediment oxygen isotope values cannot be limited to the state (i.e., the stochastic and average values) of

hydroclimate, but must instead include the initial conditions as a controlling variable. Extracting useful hydroclimate information from sediment isotope records therefore requires analysis of average $\delta^{18}\text{O}$ values over time periods long enough to minimize the potential error contributed by the unknown initial hydrologic and isotopic conditions. In the case of CL and SL, 50 year averages reduce this error to less than 0.25%. Effectively, this means that applying a 50 year moving average to CL and SL sediment core data will minimize the influence of initial conditions on each individual averaged data point, such that one can extract climatic information alone from the data. This conclusion has significant implications for both qualitative and quantitative interpretations of sediment core isotope records. In the qualitative case, short term variations in sediment isotope values should not necessarily be ascribed to weather during the year (or several preceding years) in which the sediment formed. In the specific case of high resolution stable isotope records (i.e., $\delta^{18}\text{O}$ or δD records with annual or near-annual resolution) large magnitude sub-decadal droughts or wet periods may not always produce proportionate isotopic excursions and vice versa (i.e, short-term, large scale isotopic variations may not in all cases be representative of equivalently large climate variations). This latter result may in part explain why short-term CL sediment isotope values do not perfectly track the tree-ring based reconstructed PDSI values of Cook et al. (2004) over the past ~1500 years (Nelson et al. 2011). When conducting quantitative analyses, modelers could potentially extract climate information from averaged sediment core records using stable isotope mass balance models configured to simulate both stochastic and mean state hydroclimate change. A Monte Carlo approach to model simulations in which mean and stochastic precipitation, temperature, and RH are randomly varied on an iterative basis could address the problem of equifinality, which prevents the assignment of a specific hydroclimatic state to each individual sediment $\delta^{18}\text{O}$ value. Such

simulations could be conducted with limits on past temperature, RH, and precipitation rates inferred from regional multi-proxy, paleoclimate studies, and analyzed using multiple-regression methods to extract a probabilistic range of climate variable values for each averaged sediment isotope value. Such a study would represent a considerable advancement in the interpretation of sediment core isotope records and could produce quantitative paleoclimate datasets with widely ranging applications including climate sensitivity parameterization in global climate model simulations (Goosse et al. 2006; 2010) or the refinement of water management policies in drought stressed regions such as upper Columbia River basin.

6.0 CENTURY SCALE PRECIPITATION IN THE PACIFIC NORTHWEST FROM OXYGEN ISOTOPES IN LAKE SEDIMENT

6.1 INTRODUCTION

Water resources in the American west are under increasing stress because of higher demand and reduced availability from recent drought conditions (Mote 2003; Barnett et al. 2004; Cook et al. 2007). Developing temporal and spatial records of the timing, frequency, and magnitude of drought can provide information on synoptic climate pattern variability and may help to improve model predictions of climate responses to projected future warming (Goosse et al. 2006; 2010). Modern drought patterns in western North America are affected by Pacific ocean-atmosphere dynamics such as the El Niño Southern Oscillation (ENSO) and the Pacific Decadal Oscillation (PDO). Generally, drought occurs in the northwestern and southwestern United States during El Niño and La Niña events, respectively (Dettinger et al. 1998; Cayan et al. 1999; Clark et al. 2001). Here past relationships between Pacific Ocean dynamics and precipitation in the Pacific Northwest are investigated through a model based analysis of sediment oxygen isotope ($\delta^{18}\text{O}$) values from Castor Lake and Lime Lake, Washington (Figure 6.1). The $\delta^{18}\text{O}$ records are interpreted using an ensemble of Monte Carlo simulations conducted with a lake-catchment mass balance model, and produce a probabilistic, quantitative reconstruction of winter and spring (November–June) precipitation for the past 1500 years.

Results from this study contrast with the PDSI reconstructions of Cook et al. (2004) and suggest that the Medieval Climate Anomaly (MCA) was a period of exceptional wetness in the Pacific Northwest, and that the Little Ice Age (LIA) was relatively dry in this region. Given the observed relationship between ENSO and precipitation in eastern Washington, this further suggests that the MCA (950–1250 AD) and the LIA (1450–1850 AD), respectively, were characterized by enhancement of La Niña and El Niño like conditions in the tropical Pacific.

$\delta^{18}\text{O}$ records from lake sediment cores have long been used to provide qualitative and/or semi-quantitative information on past hydroclimatic conditions (Benson et al. 1996; Hammarlund et al. 2003; Leng and Marshall 2004). Advances in mass balance modeling methods allow us to estimate the relative influence of the hydroclimatic variables (i.e., temperature, relative humidity, and precipitation) on lake water $\delta^{18}\text{O}$ values (Hostetler and Benson 1994; Shapley et al. 2008; Jones and Imbers 2010) and to extract quantitative paleoclimate information from lake sediment $\delta^{18}\text{O}$ records (Ricketts and Johnson 1996; Cross et al. 2001; Benson and Paillet 2002). Such modeling studies demonstrate that closed-basin lakes, in which evaporation is the primary water loss pathway, exhibit large steady state isotopic responses to mean state hydroclimatic change (e.g., long-term shifts in average precipitation or temperature) and the consequent variations in water-balance as determined by winter precipitation and summer evaporation amounts (Steinman et al. 2010a; 2010b). In contrast, modeling research and observations have shown that open-basin lakes are characterized by extensive overflow or groundwater outflow and therefore exhibit water $\delta^{18}\text{O}$ values that are primarily controlled by the isotopic composition of inflowing water (Abbott et al. 2000; Leng and Marshall 2003; Henderson and Shuman 2009). Although subject to limitations, (e.g., imprecise age control), lake sediment $\delta^{18}\text{O}$ records have considerable potential as recorders of

century-scale climate change because they can be quantitatively interpreted using physically based rather than statistically based models (i.e., in the case of tree rings). In the small lakes presented here, the physical processes that control lake-catchment hydrology and isotope dynamics on decadal time scales also control lake responses on century long time scales. The ability of models to accurately describe decadal processes should therefore be equivalent to their ability to describe century scale processes, a case that cannot be made for methods of tree ring analysis.

Here $\delta^{18}\text{O}$ records from open-basin Lime Lake and closed-basin Castor Lake are analyzed (Figure 6.2). After mean centering the records, the Lime Lake record was subtracted from the Castor Lake record producing a $\Delta\delta^{18}\text{O}$ record of precipitation-evaporation balance that is unaffected by non hydrologic controls (i.e., shifts in the isotopic composition of source water). More positive $\Delta\delta^{18}\text{O}$ values indicate a relative deficit of catchment water and drier conditions while more negative $\delta^{18}\text{O}$ values indicate a surplus of catchment water and wetter conditions. To quantitatively interpret the $\Delta\delta^{18}\text{O}$ record, an ensemble of Monte Carlo simulations are conducted using a combined lake-catchment, hydrologic and isotope mass balance model that simulated Castor Lake isotopic evolution over discrete 20-year periods in response to randomly generated changes in monthly precipitation, temperature and relative humidity. To produce modeled $\Delta\delta^{18}\text{O}$ estimates (and eliminate the influence of source water $\delta^{18}\text{O}$ variations), a constant source water isotopic composition was applied in the model simulations. Polynomial regression was used to determine the relationship between the modeled $\Delta\delta^{18}\text{O}$ values and precipitation amounts. The regression equation was then applied to the observed lake sediment $\Delta\delta^{18}\text{O}$ record to produce a continuous reconstruction of winter and spring precipitation for the past 1500 years (*see* Section 6.3)

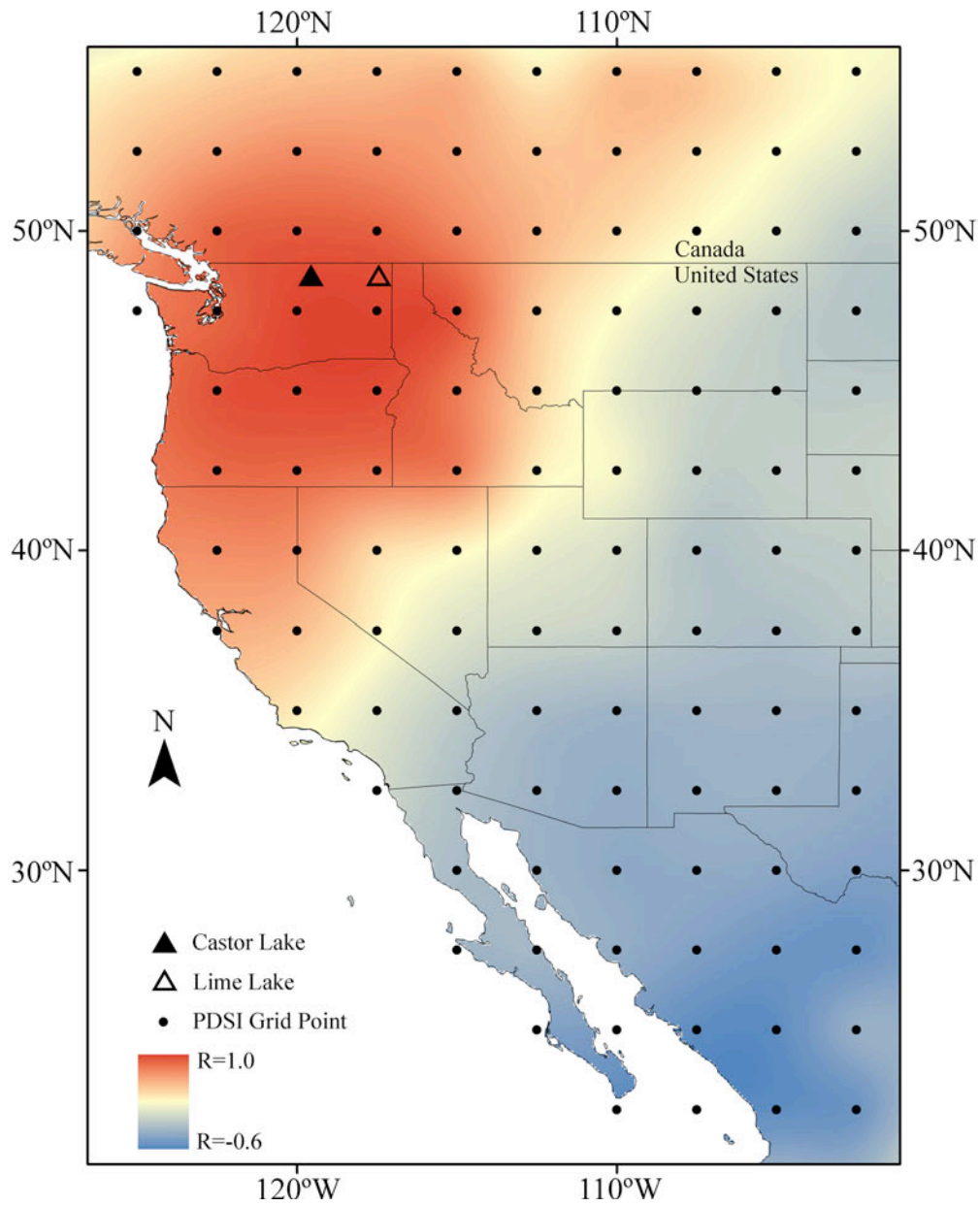


Figure 6.1 PDSI reconstruction correlation map for the western United States. Correlations between eastern Washington (i.e., the average of grid points 43 and 55) and all other individual grid points were calculated using 20 year moving average data from the period common to all grid points (1645–2003). A contrasting aridity pattern has existed between the Pacific Northwest and southwest for the last ~350 years.

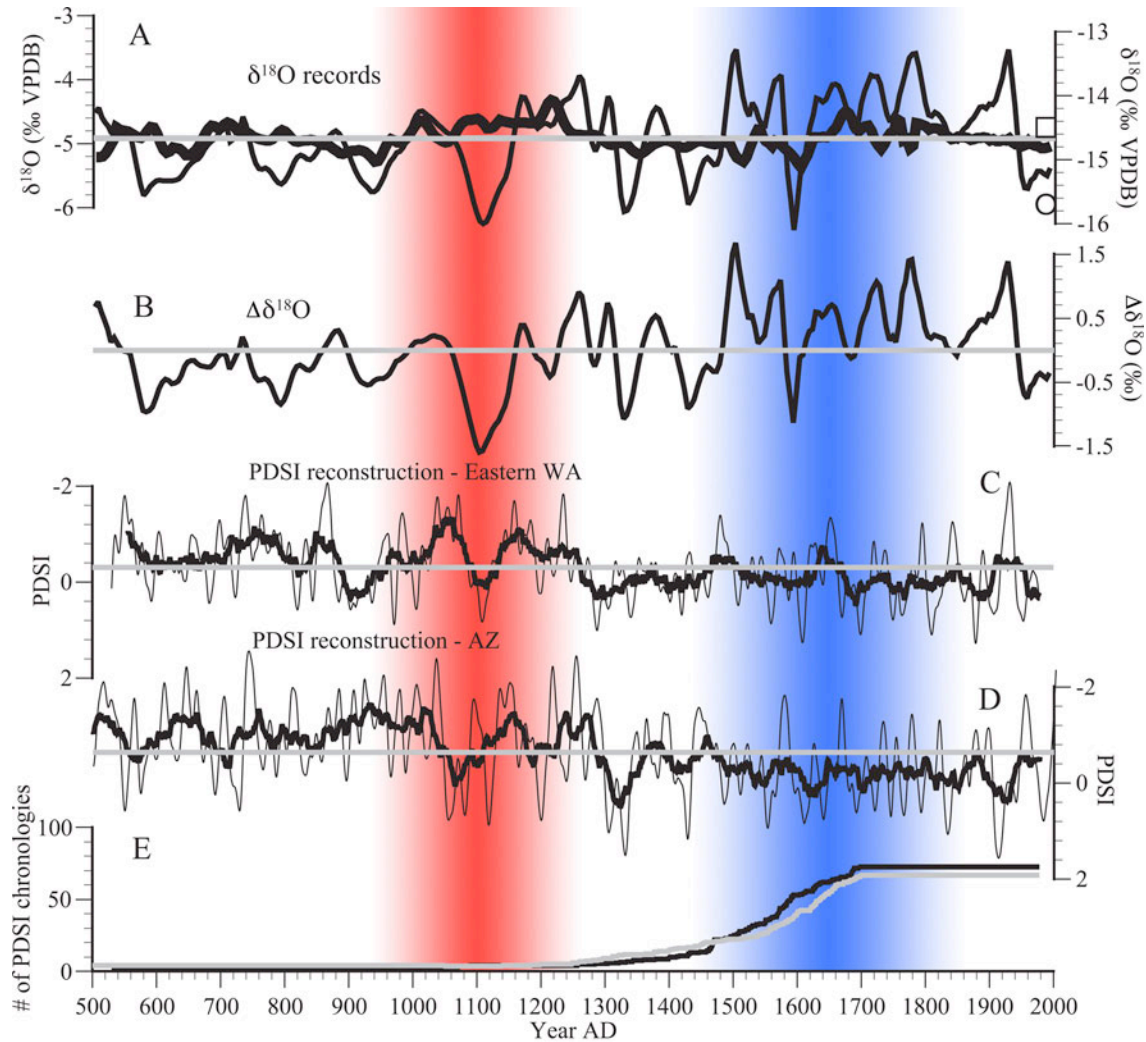


Figure 6.2 (A) Castor Lake (fine line) and Lime Lake (coarse line) sediment $\delta^{18}\text{O}$ records. 20 year moving averages of Castor Lake values vary between -3 and -6% . 20 year moving averages of Lime Lake values vary between -13 and -16% . Theoretical modern calcite values for Lime Lake were calculated using the interpolated precipitation $\delta^{18}\text{O}$ values of Bowen and Revenaugh (2003) (open square) and observations over a 5 year period (open circle). (B) $\Delta\delta^{18}\text{O}$ record calculated by mean centering the Lime Lake and Castor Lake $\delta^{18}\text{O}$ records and subtracting the Lime record from the Castor record. The $\Delta\delta^{18}\text{O}$ represents the Castor Lake isotopic response to hydroclimatic forcing without the influence of variations in the $\delta^{18}\text{O}$ of precipitation. $\Delta\delta^{18}\text{O}$ values suggest a wet MCA (950–1250 AD) and a dry LIA (1450–1850). (C) PDSI reconstructions (average) from grid points 43 and 55 (eastern Washington). 50 year moving average (coarse line) and 20 year low pass filter values (fine line) suggest a wet LIA and a dry MCA in the Pacific Northwest, opposite the pattern indicated by the $\Delta\delta^{18}\text{O}$ record. Negative (positive) PDSI values represent drought (wet) conditions. (D) PDSI reconstructions (average) from grid points 88, 89, 104 and 105 (Arizona). 50 year moving average (coarse line) and 20 year low pass filter values (fine line) suggest a wet LIA and a dry MCA in the southwestern United States, similar to the PDSI trend identified for eastern Washington. The similarity in long term aridity trends in the American southwest and Pacific Northwest is conspicuous given the anticorrelation between drought patterns observed in the PDSI records over the past ~ 350 years (Figure 6.1). (E) The number of chronologies used in the PDSI reconstructions for eastern WA (black line) and Arizona (gray line). Note the much larger number of chronologies in both regions for the LIA relative to the MCA.

6.1.1 Study Sites

Castor and Lime Lakes are both of late Wisconsinian glacial origin, with small surface areas ($<0.1 \text{ km}^2$) and maximum depths of $\sim 12 \text{ m}$ and $\sim 15 \text{ m}$, respectively. Castor Lake is located east of the Cascade Range (48.54° N , 119.56° W , elevation 594 m) in the semi arid brush steppe of north-central Washington (Figure 6.1). The lake catchment is on a plateau several hundred meters above the Okanogan river valley isolating it from distal groundwater sources. Modeling and observational studies demonstrate that evaporation is the primary water loss pathway and that input to the lake is limited to precipitation and catchment derived groundwater (Steinman et al. 2010a). Lime Lake is located in northeastern WA (48.87° N , 117.34° W , elevation 780 m) in the Selkirk Mountains (Figure 6.1). The lake catchment is on the eastern flank of the Pend Oreille River Valley, positioned well above regional groundwater. Surficial outflow occurs on a permanent basis from the southern shoreline through a bog that flows into an incised drainage. The lake catchment to lake surface area ratio is high, producing large runoff amounts and a rapid rate of groundwater throughflow. Observations of lake and local meteoric water $\delta^{18}\text{O}$ values obtained over a five year period (2005–2010 AD) demonstrate that Lime Lake water is relatively unaffected by evaporation (Figure 6.S1).

The $\delta^{18}\text{O}$ values of Castor Lake water are largely controlled by precipitation, temperature, and relative humidity and the resulting influence of these climate variables on catchment water balance, i.e. runoff and groundwater inputs to the lake, soil moisture, and evapotranspiration. Prior to analysis Nelson et al. (2011) detrended the Castor Lake $\delta^{18}\text{O}$ record and thereby removed century scale variability that contained information about long term hydroclimatic changes. Here analyses are conducted on the unaltered Castor Lake record to investigate trends in century scale hydroclimatic variations and to compare these results with the

regional paleoclimate reconstructions. The Castor Lake age model and sediment core collection methods are described in detail by Nelson et al. (2011).

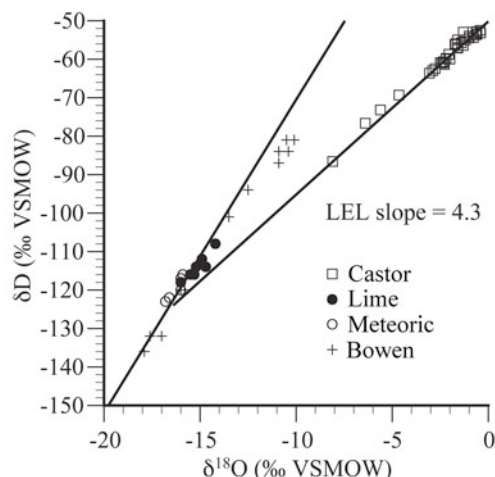


Figure 6.S1 Global meteoric water line, local evaporation line and water sample $\delta^{18}\text{O}$ measurements from the period of observation (2005–2011). Lime Lake $\delta^{18}\text{O}$ measurements plot on the Global Meteoric Water line, demonstrating that Lime Lake is open and primarily influenced by changes in precipitation $\delta^{18}\text{O}$ values.

The geochemical conditions of both Castor and Lime Lakes lead to carbonate mineral precipitation from the water column in the late spring and summer. X-ray diffraction was used to identify aragonite at Castor Lake and calcite at Lime Lake as the only abundant carbonate minerals in the sediment. $\delta^{18}\text{O}$ values of these minerals are primarily controlled by the $\delta^{18}\text{O}$ value of lake water at the time of mineral formation (Kim and O’Neil 1997; Zhou and Zheng 2003). Both calcite and aragonite precipitate at similar temperatures during late spring and summer months as a result of biomediation and physicochemical effects, which consequently reduces the influence of temperature on carbonate $\delta^{18}\text{O}$ values (Steinman et al. In prep. a) (*see* Chapter 4). Hypolimnetic anoxia at both lakes prohibits bioturbation, allowing the formation of fine carbonate sediment laminations that preserve the lake water $\delta^{18}\text{O}$ signal.

6.2 DISCUSSION AND CONCLUSIONS

Modeling studies confirm that catchment water balance variations resulting from precipitation forcing are the primary control on Castor Lake $\delta^{18}\text{O}$ values (Steinman et al. 2010a; 2010b; In prep. a) (*see* Chapter 4). Lime Lake $\delta^{18}\text{O}$ values, however, are primarily controlled by shifts in the isotopic composition of rain and snowfall, which are related to the seasonality of precipitation and temperature. The isotopic composition of precipitation is influenced by several factors including the origin of atmospheric moisture, air mass trajectories and air temperature (Rozanski et al. 1992). The combined effects of isotopic variations in source water establish a baseline for the Castor Lake water $\delta^{18}\text{O}$ variability in response to purely hydrologic (rather than isotopic) processes, such as evaporation and meteoric water inflow. By subtracting variations in the open basin Lime Lake record from the closed basin Castor Lake record, the isotopic influence of purely hydrologic forcing on the Castor catchment system was isolated. The resulting $\Delta\delta^{18}\text{O}$ record reflects the cumulative isotopic effects of evaporation and groundwater and runoff input to Castor Lake and is not reflective of changes in the isotopic composition of lake source water.

Precipitation in the Pacific Northwest is largely controlled by the strength and position of the Aleutian Low and North Pacific High pressure systems and the resulting westerly winds that deliver wet air to the continental interior (Bryson and Hare 1974). Dry years, for example, typically occur when a high-pressure ridge forms over the northeastern Pacific and prevents wet air from entering the region. ENSO and PDO influence precipitation amounts in the western United States by modulating ocean-atmosphere interactions and corresponding temperature and pressure gradients in the Pacific Basin. A relationship between ENSO and PDO has been

described through analysis of 20th century Pacific Ocean temperature patterns (Newman et al. 2003) and through the comparison of paleorecords (Verdon and Franks 2006). These analyses demonstrate a positive correlation between El Niño events and warm PDO phases over the past 400 years (Verdon and Franks 2006), and further suggest that PDO can be described as the extratropical Pacific Ocean response to ENSO forcing combined with atmospheric noise (Newman et al. 2003). Logically, if the PDO does represent the mid-latitude Pacific Ocean response to ENSO, then changes in the tropical Pacific will lead to changes in the mid-latitudes that affect precipitation amounts in eastern Washington. Comparison of regional precipitation amounts and 20th century $\Delta\delta^{18}\text{O}$ values (WRCC) with the instrumental PDO and ENSO indices confirms this assertion (Figure 6.3). Instrumental PDO and Southern Oscillation Index (SOI) data are generally correlated to precipitation rates in eastern Washington with a residual component likely related to noise in Pacific ocean-atmosphere system and secondary influence by the Northern Annular Mode and Atlantic Multidecadal Oscillation (McCabe et al. 2004). La Niña years (and negative PDO index years) for example, are distinctively wet, while El Niño years (and positive PDO index years) are typically dry, although less predictable (Figure 6.3) (Cayan 1996; Cayan et al. 1999; Clark et al. 2001). ENSO control of winter temperature accentuates water balance trends by affecting snowpack amounts and stream flow volumes during the spring and summer. For example, lower than average winter temperatures occur during La Niña years and higher than average winter temperatures often occur during El Niño years, with corresponding higher and lower spring and summer stream flow volumes, respectively (Cayan 1996; Cayan et al. 1999; Clark et al. 2001).

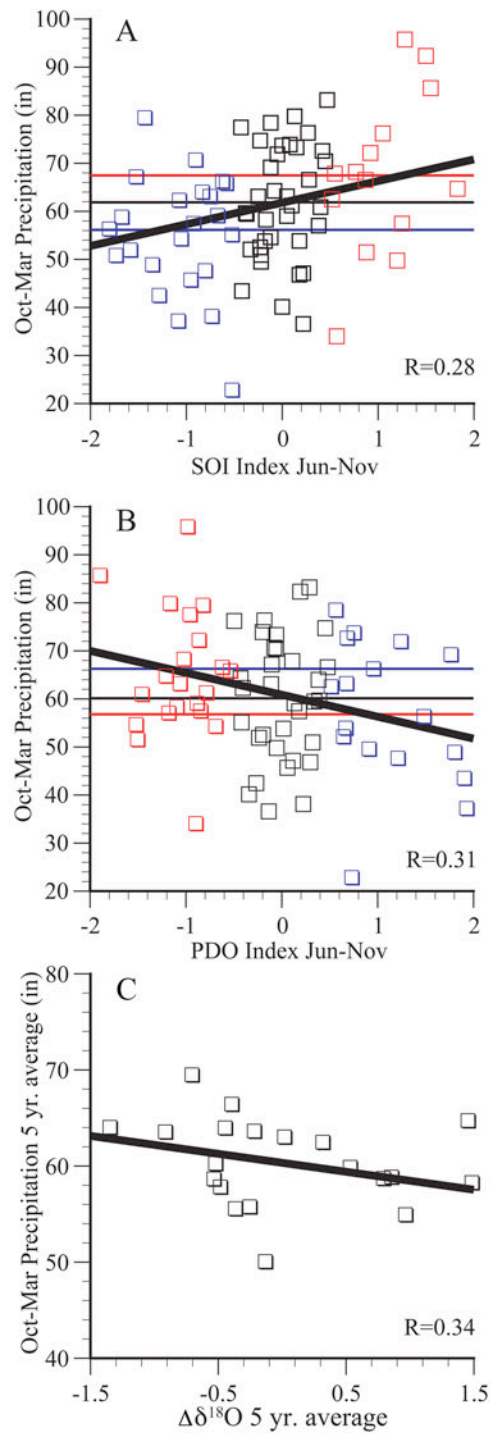


Figure 6.3 SOI (A) and PDO (B) index values (June – November average) and associated precipitation amounts (October – March total) in eastern Washington. Data span the period from 1933 to 2005. SOI index values greater than 0.5 and less than -0.5 represent La Niña (red open squares) and El Niño (blue open squares) conditions, respectively. PDO index values greater than 0.5 (blue open squares) and less than -0.5 (red open squares) represent warm phase and cool phase conditions, respectively. A positive SOI index and a negative PDO index are associated with wetter conditions in eastern Washington. (C) 20th century $\Delta\delta^{18}\text{O}$ values related to precipitation amounts in eastern Washington, indicating that more positive $\Delta\delta^{18}\text{O}$ values are associated with lower precipitation amounts and vice versa.

The 20th century is too short a time period to effectively investigate century scale correlations between precipitation and synoptic climate indices. Multi-century paleorecords must therefore be used to conduct such analyses. The temperature reconstructions of Mann et al. (2009) incorporate most of the paleotemperature datasets from the tropical and extratropical Pacific, and thus better describe the general temporal and spatial characteristics of ENSO and the PDO than do individual records. Comparison of the $\Delta\delta^{18}\text{O}$ and model derived precipitation reconstruction with the Mann et al. (2009) PDO reconstruction reveals a century scale relationship between higher precipitation amounts in eastern Washington and positive PDO temperature anomalies (i.e., a “cool” phase of the PDO) over the past 1500 years (Figure 6.4). During the MCA, for example, PDO values were generally more positive and precipitation amounts correspondingly greater than during the LIA. A similar century scale relationship exists during the MCA between negative Niño3 values (i.e., La Niña like conditions in the tropical Pacific), and higher than normal precipitation. Notably, the reduced precipitation of the LIA was not associated with exceptionally positive Niño3 values, a result that can potentially be explained by the relatively lesser coherence between negative (rather than positive) SOI index values and precipitation over the 20th century (Figure 6.3). These results confirm that the multidecadal relationships between ENSO and PDO observed over the 20th century are represented on century long time scales.

Interestingly, the drought reconstructions of Cook et al. (2004) do not support the results presented here. Although the Castor Lake $\delta^{18}\text{O}$ record and the regional PDSI records of Cook et al. (2004) (grid points 44 and 55) are well (anti)correlated on multidecadal time scales (Nelson et al. 2011), they do not exhibit similar longer term trends (Figure 6.1). During and the MCA, for example, the Cook et al. (2004) data suggest relatively dry conditions in the Pacific Northwest,

while the Castor data suggest wetter conditions. Notably the tree ring data also point to a dry MCA in the southwest, a result that contradicts the contrasting multidecadal responses in the PDSI data observed in the northwest and southwest over the past ~350 years (Figure 6.1). The temporal distribution of PDSI chronologies may explain this discrepancy. In both eastern Washington and Arizona for example, no more than 4 tree ring chronologies span the last millennium in each region, with over 12 spanning the LIA. Combined, the lack of consistency in the tree-ring data on varying timescales, the potential error introduced by detrending methods (Cook et al. 1995; Briffa 2000; Hughes 2002; Jones et al. 2009), and the small number of chronologies during the MCA indicate that the PDSI reconstruction of Cook et al. (2004) may not be ideal for defining drought patterns in the Pacific Northwest on century long time scales.

Climate modeling studies of past changes in the tropical Pacific during globally warmer periods, such as the MCA, inform us about the potential for Pacific Ocean responses to anthropogenic radiative forcing. The model simulations of Mann et al. (2005), for example, suggest that the MCA and LIA were characterized by La Niña and El Niño like conditions, respectively. The Zebiak-Cane climate model (Zebiak and Cane 1987; Cane et al. 1997) applied in this and other (e.g., Clement et al. 1996) studies is based on atmospheric processes that are simplified such that atmospheric circulation does not weaken in response to warming. This allows the ocean thermostat mechanism to dominate, producing a La Niña like response in the tropical Pacific to increased radiative forcing. In contrast, coupled global climate models (CGCM) that more accurately represent atmospheric physics (at the expense of simplified representations of oceanic mixing) predict an El Niño like response in the tropical Pacific to future greenhouse gas increases. These models do not simulate the ocean thermostat mechanism and thus allow the weaker Walker circulation to dominate, leading to weakened easterly winds

and a reduction in the equatorial Pacific SST gradient (Knutson and Manabe 1995; Held and Soden, 2006). Additional CGCM simulations (e.g., Vecchi et al. 2008) in which both ocean and atmospheric processes are fully represented indicate yet another outcome to future warming that is less El Niño like than indicated by CGCM simulations in which oceanic mixing is simplified.

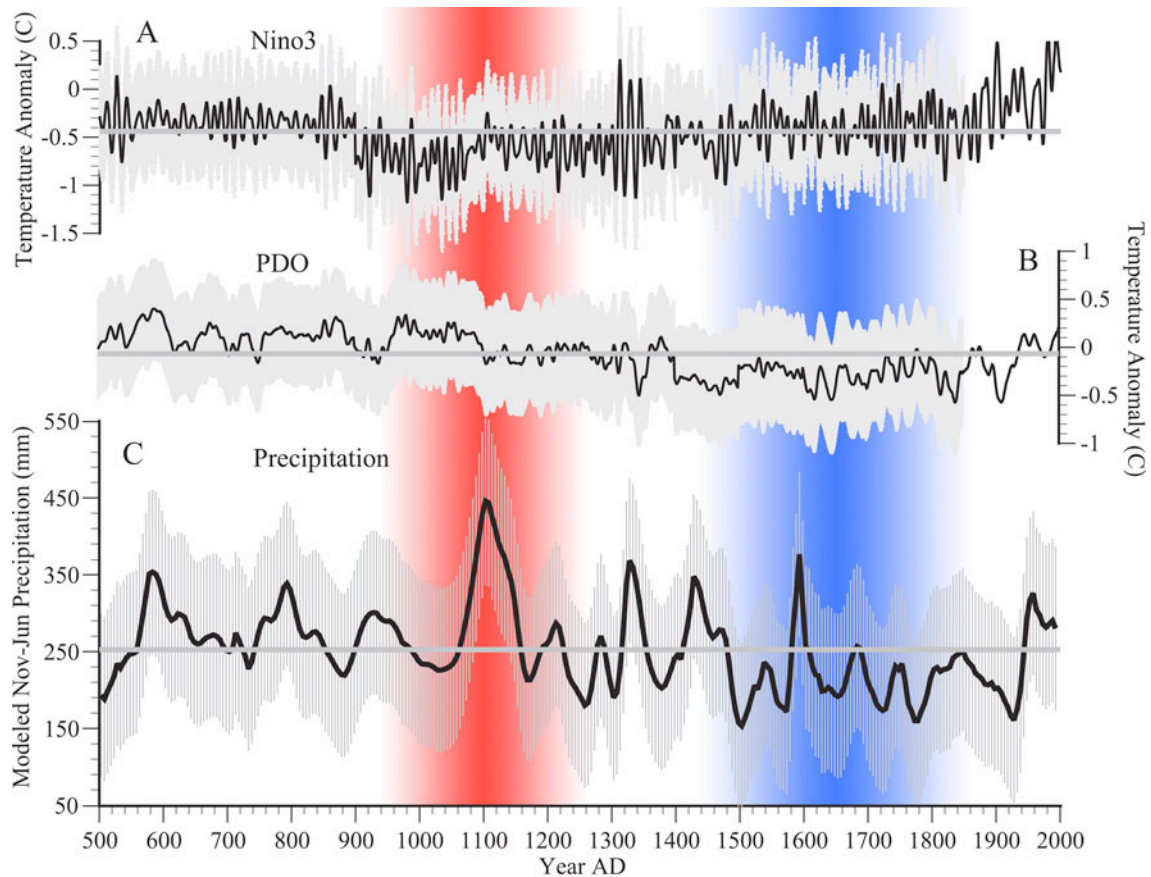


Figure 6.4 Niño3 (A) and PDO (B) reconstructions of Mann et al. (2009) compared to (C) the lake sediment and model derived precipitation reconstruction. During the MCA (950–1250 AD) more positive PDO values combined with negative Niño3 temperature anomalies and increased precipitation amounts in eastern Washington suggest La Niña like conditions in the tropical Pacific. During the LIA (1450–1850) negative PDO temperature anomalies combined with more positive Niño3 values and decreased precipitation amounts in eastern Washington suggest more El Niño like conditions in the tropical Pacific. Gray shading represents estimated 95% confidence limits for the temperature and precipitation reconstructions. PDO reconstruction area is based on the SST averaged over the central North Pacific region 22.5°N–57.5°N, 152.5°E–132.5°W as defined by Mantua et al. (1997). The Niño3 region is 2.5°S–2.5°N, 92.5°W–147.5°W.

The lake sediment derived precipitation reconstruction presented here holds important

implications for estimating Pacific Northwest drought responses to projected future warming. Given the lack of reconciliation among state of the art climate models (Merryfield 2006; Meehl et al. 2007) we cannot predict with confidence the future response of the tropical Pacific to greenhouse gas increases and consequently cannot make assertions about future continental drought patterns. We can however be fairly certain that century scale precipitation in the Pacific Northwest is closely related to long term changes in tropical Pacific Ocean dynamics, and that future perturbations in the state tropical Pacific Ocean will likely produce commensurate evolution in the hydroclimate of the western United States.

6.3 MATERIALS AND METHODS

6.3.1 Castor Lake model structure

The following equations generally describe the hydrologic and isotopic mass balance of the lake-catchment system:

$$\frac{dV_L}{dt} = \Sigma I - \Sigma O \quad (1.1)$$

$$\frac{d(V_L \delta_L)}{dt} = \Sigma I \delta_i - \Sigma O \delta_o \quad (1.2)$$

where V_L is lake volume, ΣI and ΣO are the total surface and below ground inflows to and outflows from a lake, and δ is the isotopic composition of the inflows and outflows. These equations provide the basis for a system of twelve ordinary differential equations solved using numerical modeling software that describe water and isotope dynamics for the lake, catchment system. The hydrologic model is defined by six separate differential equations (Equations 1.3–

1.8), each corresponding to a different water reservoir (*RES*). Volumetric fluxes (*F*) to the reservoirs include model sub-routines for lake stratification, soil moisture availability, snowpack, and surficial and subsurface inflow. Steinman et al. (2010a) provides additional detail regarding calculation of the flux (*F*) components and other aspects of the model (*see* Chapter 1). All equation solutions were obtained using the 4th order Runge-Kutta numerical integration method.

6.3.2 Hydrologic mass-balance equations

The water mass-balance of the lake is controlled by the following equations:

$$\frac{dRES_{SL}}{dt} = F_P + F_{IN} + F_{DLM} - F_E - F_{SLM} - F_{SOS} \quad (1.3)$$

$$\frac{dRES_{DL}}{dt} = F_{SLM} - F_{DLM} - F_{DOS} \quad (1.4)$$

where RES_{SL} and RES_{DL} are near surface and deep lake waters, respectively, F_P is direct precipitation over the lake surface area, F_{IN} is inflow from the catchment, F_E is lake water evaporation, and F_{SOS} and F_{DOS} are outseepage through shallow lake and deep lake sediments. Surface and deep water mixing fluxes (F_{SLM} and F_{DLM} , respectively), associated with the establishment and breakdown of lake stratification, also control the movement of water between the near surface and deep lake reservoirs.

Soil water mass-balance is determined by the amount of rainfall and snowmelt over the catchment surface area (excluding the lake surface area), catchment evapotranspiration, infiltration, and losses to sub-surface flow and/or runoff to the lake and is defined by two reservoir and flux systems:

$$\frac{dRES_{SS}}{dt} = F_{SSI} - F_{SSE} - F_{SSD} \quad (1.5)$$

$$\frac{dRES_{DS}}{dt} = F_{SSD} - F_{DSE} - F_{DSD} \quad (1.6)$$

where RES_{SS} and RES_{DS} are the volume of water stored within surface and deeper soil reservoirs, respectively, and F_{SSI} , F_{SSE} , F_{SSD} , F_{DSD} and F_{DSE} denote surface soil infiltration from precipitation, evapotranspiration from the soil surface, surface soil drainage to the deep soil reservoir, deep soil drainage to the inflow reservoir, and evapotranspirative loss from deep soil.

The partitioning of catchment water between soil storage, runoff, and subsurface flow is controlled by a soil model sub-routine, which is derived, in part, from the two layer soil models of Palmer (1965) and Vassiljev et al. (1995).

Hydrologic mass-balance within the inflow reservoir is controlled by runoff (F_{RO}) generated by catchment rainfall (F_R) and/or melt of the catchment snowpack (F_{SM}) in excess of soil water storage:

$$\frac{dRES_{IN}}{dt} = F_{RO} + F_{DSD} - F_{IN} \quad (1.7)$$

with excess water ultimately reaching the lake via combined surface and sub-surface inflows (F_{IN}) following a fixed retention time in the catchment. Snow cover (i.e., snowpack reservoir size, RES_{SP}) in the catchment is determined by a balance between accumulation and melt:

$$\frac{dRES_{SP}}{dt} = F_{SF} - F_{SM} \quad (1.8)$$

where F_{SF} is snowfall and F_{SM} is a temperature-controlled snowmelt flux component based on the model of Vassiljev et al. (1995).

Evaporation from the lake surface is estimated by a combination radiation-aerodynamic Penman equation developed by Valiantzas (2006):

$$E = \left(\begin{array}{l} 0.051(1 - ALB) \times R_s \times (T_a + 9.5)^{(1/2)} - 2.4 \left(\frac{R_s}{R_a} \right)^2 + \\ 0.052(T_a + 20) \times \left(1 - \frac{RH}{100} \right) \times (a_u - 0.38 + 0.54WS) \end{array} \right) \times 30 \quad (1.22)$$

where E is evaporation in mm day^{-1} , ALB is the albedo of the lake surface (0.08), T_a is average daily temperature in $^{\circ}\text{C}$, R_s is average daily incoming solar radiation in $\text{MJ m}^{-2} \text{d}^{-1}$, R_a is average daily extraterrestrial radiation in $\text{MJ m}^{-2} \text{d}^{-1}$, RH is average daily relative humidity expressed as a percentage, a_u is the Penman wind function constant, and WS is average daily wind speed in m s^{-1} .

Similarly, evapotranspirative flux from the surface and deeper soil (F_{SSE} and F_{DSE}) is determined by potential evapotranspiration and the total availability of water stored within the catchment in accordance with the combination radiation-aerodynamic Penman equation developed by Valiantzas (2006):

$$PET = \left(\begin{array}{l} 0.051(1 - ALB) \times R_s \times (T_a + 9.5)^{(1/2)} - 2.4 \left(\frac{R_s}{R_a} \right)^2 + \\ 0.048(T_a + 20) \times \left(1 - \frac{RH}{100} \right) \times (0.5 + 0.536WS) \end{array} \right) \times 30 \quad (1.23)$$

where ALB is the albedo of the grass surface (0.25) and all other terms are defined above.

6.3.3 Isotope mass-balance equations

The equations of Dincer (1968), Gonfiantini (1986), and Gat (1995) define the isotope mass balance model within which, oxygen isotopic values, in standard delta (δ) notation are calculated for each reservoir at each time step and are multiplied by the corresponding hydrologic flux to determine the isotope mass-balance of any given water mass.

The linear resistance model of Craig and Gordon (1965) was used to estimate the isotopic composition of moisture evaporating from the lake surface (δ_E):

$$\delta_E = \frac{\alpha^* \delta_L - h_n \delta_A - \varepsilon_{tot}}{1 - h_n + 0.001 \varepsilon_{kin}} \quad (1.24)$$

where a^* is the reciprocal of the equilibrium isotopic fractionation factor (Horita and Wesolowski 1994), δ_L is the isotopic composition of lake water, h_n is the ambient humidity normalized to lake water temperature, δ_A is the isotopic composition of atmospheric moisture (Gibson et al. 2002), ε_{tot} is the total per mil isotopic separation ($\varepsilon_{eq} + \varepsilon_k$), and ε_{eq} and ε_k are the equilibrium and kinetic (Merlivat and Jouzel 1979) isotopic separations, respectively.

6.3.4 Removal of source water $\delta^{18}\text{O}$ influences

To simulate $\Delta\delta^{18}\text{O}$ values at Castor Lake, isotopic variability in source water was removed by setting precipitation $\delta^{18}\text{O}$ to a constant value of -5‰ in all simulations. The choice of -5‰ was arbitrary, as all constant values produce identical $\Delta\delta^{18}\text{O}$ anomalies. Removal of source water $\delta^{18}\text{O}$ variations (that result from temperature and seasonality variations) isolated the effects of climate driven hydrologic forcing on sediment $\delta^{18}\text{O}$ values and thereby isolated the effective water balance signal from the model simulation results.

6.3.5 Authigenic carbonate formation

At Castor Lake and Lime Lake, carbonate mineral precipitation from the water column occurs in the late spring and summer (June–September) as a result of physico-chemical and climatic control of the solubility product (K_{sp}) and Ca^{2+} ion concentrations and biological control

of DIC (dissolved inorganic carbon) equilibria and carbonate species concentrations (Kelts and Hsu 1978; Koschel 1997). Temperature influences carbonate mineral formation via two interrelated mechanisms: firstly by controlling K_{sp} (higher temperatures result in lower K_{sp} values), and secondly through control of primary productivity, which increases at higher temperatures resulting in removal of CO_2 and a shift in the DIC equilibria toward the CO_3^{2-} species (Kelts and Hsu 1978). Rain and snowfall, likewise, can influence carbonate mineral formation by controlling the delivery of Ca^{2+} ions to the lake through runoff and baseflow (Shapley et al. 2005).

Model subroutines calculate the equilibrium fractionation factors for the aragonite-water system at Castor Lake for each time step to determine sediment $\delta^{18}O$ values on the VPDB (Vienna Pee Dee Belemnite) scale (*see* Chapter 4). The model calculates the equilibrium fractionation factor for the aragonite water system in accordance with the equation of Zhou and Zheng (2003):

$$1000 \ln \alpha_{Aragonite-H_2O} = 20.44(10^3 T^{-1}) - 41.48 \quad (4.2)$$

where $\alpha_{Aragonite-H_2O}$ is the equilibrium fractionation factor for aragonite and water and T is the water temperature in degrees Kelvin. The model relates values for α to lake water $\delta^{18}O$ values on the VSMOW (Vienna Standard Mean Ocean Water) scale in accordance with the standard isotope fractionation relationship:

$$\alpha_{A-B} = \frac{1000 + \delta_A}{1000 + \delta_B} \quad (4.4)$$

where α_{A-B} is the fractionation factor of either the calcite-water or aragonite-water systems, δ_A is the isotopic composition of either aragonite or calcite, and δ_B is the isotopic composition of

lake water. Theoretical aragonite $\delta^{18}\text{O}$ values are converted from the VSMOW to the VPDB scale using the following standard equation:

$$\delta_{VSMOW} = 1.03086 \times \delta_{VPDB} + 30.86 \quad (4.5)$$

6.3.6 Lime Lake sediment core recovery and sampling

In October 2006 sediment cores were collected from Lime Lake using piston and modified Livingstone corers. The uppermost sediments were extruded in the field at 0.5 cm intervals and returned to the University of Pittsburgh where they were kept in storage at 4 °C. The Lime Lake sediment consists of fine bands and laminations, indicating the preservation of decadal scale lake water $\delta^{18}\text{O}$ variations. The remaining Lime Lake sediment cores were sampled at ~1–5 mm intervals for carbonate mineral stable isotope analysis. After disaggregating the samples for ~24 hours with ~7% H_2O_2 solution, they were sieved at 63 μm to isolate the precipitated, authigenic calcite component of the sediment and to limit contamination by biogenic, carbonate shell material. The captured <63 μm portion of the sediment was allowed to settle from the rinse water and was concentrated by centrifuging. After bleaching and freeze-drying the samples, they were gently homogenized using an agate mortar and pestle. $\delta^{18}\text{O}$ measurements were conducted at the University of Arizona Environmental Isotope Laboratory by CO_2 equilibration with a VG602C Finnigan® Delta S isotope ratio mass spectrometer. Samples were measured against National Institute of Standards and Technology (NIST) carbonate standard material NBS-18 and NBS-19 and reported relative to the VPDB isotope scale in standard ‰ notation. Internal precision averaged 0.05‰ for oxygen.

6.3.7 Lime Lake chronology

Radiometric measurements of ^{210}Pb , ^{137}Cs , and ^{226}Ra activity were obtained at the University of Pittsburgh Department of geology and Planetary Science using low-background gamma counting systems with well-type intrinsic germanium detectors (Appleby and Oldfield 1983; Schelske et al. 1994). Sediment ages were calculated using a constant rate of supply (CRS) model (Oldfield and Appleby 1984). Errors in ages were propagated using first-order approximations and calculated in accordance with Binford (1990). Initial activity measurements were obtained on sediment sub-samples spanning 0.5 cm intervals from the surface to a depth of 24 cm, which represents the lowermost depth of samples extruded in the field.

Table 6.S1 Lime Lake age model data.

Depth from surface (cm)	Material	^{14}C age (yr BP)	^{14}C age \pm (yr)	Calibrated 2 σ -high (yr BP)	Calibrated 2 σ -low (yr BP)	Calibrated median age (yr BP)
0.0		-56		-56	-56	-56
37.5	Charcoal	250	15	285	307	297
43.0	Charcoal	800	100	632	927	744
54.3	tephra	470		470	470	470
63.5	Charcoal	920	25	778	920	852
75.5	Charcoal	1220	25	1064	1185	1146
105.5	Charcoal	2035	30	1921	2065	1988

Five terrestrial macrofossil samples and one tephra of known age were used to produce radiocarbon dates for sediment age control (Table 6.S1). Analyses were conducted at the W.M. Keck Carbon Cycle Accelerator Mass Spectrometry Laboratory at the University of California, Irvine (UCI). Samples were pre-treated at the University of Pittsburgh following standard acid-base-acid procedures (Abbott and Stafford 1996). Radiocarbon ages were calibrated using the CALIB online software program version 6.0.0 (Stuiver et al. 1998; Reimer et al. 2004). The Mount Saint Helens (MSH) W tephra was identified in the Castor Lake core by electron

microprobe at the Washington State University and has an age, determined by dendrochronology, of 470 BP (1480 AD) (Mullineaux 1986). To produce the Lime Lake age model, one date (43 cm) was removed from the profile due to its small size, large standard deviation, and lack of correspondence with the MSH-W tephra. A linear point to point interpolation was applied between the ^{210}Pb , median ^{14}C , and tephra ages to relate depth from the surface with age before present (Figure 6.S2).

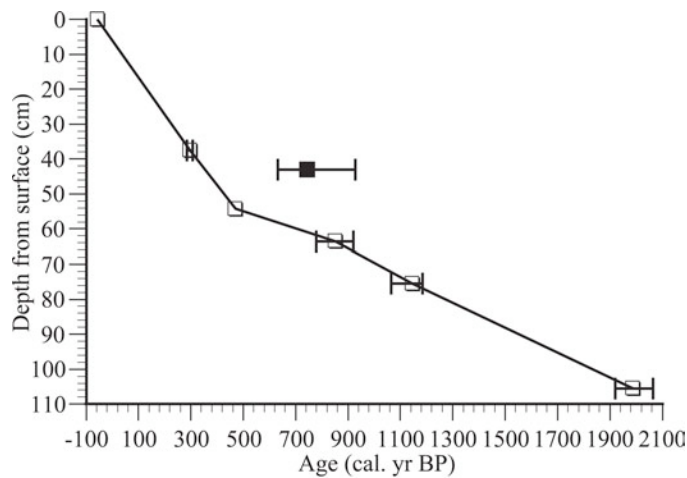


Figure 6.S2 Lime Lake age model. Accepted (open squares) and rejected (closed squares) dates with associated 2σ errors related to depth from the water surface in the sediment core.

6.3.8 Lime Lake $\delta^{18}\text{O}$ record

20 year average $\delta^{18}\text{O}$ values at Lime Lake vary within a range of $\sim 1.1\text{‰}$ over the 1500 year time span of the record (Figure 6.2). In comparison, 20 year average $\delta^{18}\text{O}$ values at Castor Lake vary by $\sim 2.8\text{‰}$. As an open-basin system, Lime Lake is not subject to the large isotopic sensitivity to hydrologic forcing that characterizes closed-basin systems. $\delta^{18}\text{O}$ anomalies in the Lime Lake record suggest several possible climate change scenarios involving shifts in the

seasonality of precipitation and/or air temperature. For example, positive $\delta^{18}\text{O}$ anomalies result from an increase in air temperature, an increase in warm season precipitation, or a decrease in cold season precipitation (or some combination thereof). Conversely, negative $\delta^{18}\text{O}$ anomalies imply cooler temperatures, a decrease in warm season precipitation, or an increase in cold season precipitation. Lime Lake $\delta^{18}\text{O}$ anomalies are distinctly positive during the MCA, suggesting higher air temperatures. The increase in precipitation suggested by the $\Delta\delta^{18}\text{O}$ record during this time implies that either winter temperature were considerably warmer, or an increase in spring precipitation occurred.

As a test of the controls on Lime Lake sediment $\delta^{18}\text{O}$ values, a simplified open-basin lake model was applied to simulate water isotopic evolution in response to hydroclimatic forcing. The model is based on two assumptions: first, that Lime Lake water $\delta^{18}\text{O}$ values are controlled by the weighted average isotopic composition of annual precipitation, and second that evaporation does not influence lake surface water $\delta^{18}\text{O}$ values. To conduct this study, average monthly precipitation data from the Boundary Dam NCDC weather station (~5 km west of Lime Lake) and the inferred $\delta^{18}\text{O}$ values of precipitation (Bowen and Revenaugh 2003) were used to calculate a weighted average theoretical isotopic composition of Lime Lake sediment using the calcite water equilibrium fractionation factor equation of Kim and O'Neil (1997). Water temperature was estimated at the time of calcite formation on the basis of several lake water temperature profiles measured over the 5 year period of observation (2005–2010). Results obtained using this method compare favorably to observations of Lime Lake sediment core $\delta^{18}\text{O}$ values (Figure 6.2), with a difference of ~0.2‰. Notably, theoretical calcite values calculated using measurements of Lime Lake surface water $\delta^{18}\text{O}$ values (rather than the meteoric water estimates of Bowen and Revenaugh (2003) do not compare as favorably to sediment core $\delta^{18}\text{O}$

observations (Figure 6.2), with a difference of $\sim 0.9\%$. One reason for this discrepancy could be that the surface sediment cores were collected at the beginning of the period of observation and therefore are not representative of lake water $\delta^{18}\text{O}$ values during this time. Another consideration is that the period of observation is not long enough to characterize the full range of Lime Lake surface water $\delta^{18}\text{O}$ variability and therefore may not be representative of the decadal scale average values represented by the sediment core. The interpolated $\delta^{18}\text{O}$ values of Bowen and Revenaugh (2003) are derived from measurements obtained over a considerably longer time period (monitoring began between 1960 and 1969) than the Lime Lake period of observation and are therefore more representative of average meteoric water $\delta^{18}\text{O}$ values than are the Lime Lake surface water samples.

In this study the $\delta^{18}\text{O}$ record from Lime Lake is interpreted as a proxy for regional (i.e., eastern Washington), decadal scale variations in small lake source water $\delta^{18}\text{O}$ values, implying that decadal scale variations in Lime Lake $\delta^{18}\text{O}$ values are representative of similar scale variations in the $\delta^{18}\text{O}$ values of Castor Lake source water. This does not mean, however, that interannual scale variations in Lime Lake $\delta^{18}\text{O}$ values are representative of source water changes at Castor Lake, as the two lakes are far enough apart (~ 170 km) to be subject to short term, noise related climatic discrepancies.

6.3.9 20th century weather datasets

Monthly precipitation and temperature datasets spanning 1900–2007 and 1931–2007 were obtained from the Conconully and Omak National Climatic Data Center (NCDC) weather stations, respectively. Monthly relative humidity (RH) data spanning 1989–2008 were obtained

from the Pacific Northwest Cooperative Agricultural Weather Network (AgriMet) weather station located in Omak. In May 2006, a Campbell Scientific weather station was installed on the northwestern shoreline of Castor Lake at an elevation ~2 m above the lake surface. The station was programmed to measure precipitation, temperature, RH, solar short wave radiation, barometric pressure, and wind speed at 30 second intervals and record the average value of measurements every 30 minutes. The station measures precipitation amounts using a standard tipping bucket with a snowfall adaptor installed during winter months.

To develop precipitation and temperature datasets for application to model simulations, the Conconully and Omak weather station data were adjusted on the basis of linear correlations to both one another and to the Castor Lake weather station data (Steinman et al. In prep. a) (*see* Chapter 4). These adjustments were applied to produce datasets that more accurately reproduce 20th century weather variations at Castor Lake, which is situated far enough from Omak and Conconully to have a slightly different climate. Additional detail regarding the development of 20th century weather datasets is provided by Steinman et al. (In prep. a) (*see* Chapter 4).

6.3.10 Monte Carlo simulations

Closed-basin lakes are subject to considerable intra- and inter-annual variability in climate (e.g., stochastic, year-to-year changes in precipitation), and hence never truly exist in an equilibrium state (Gibson et al. 2002; Steinman et al. 2010a; 2010b). As a consequence, transient isotopic responses to stochastic, inter-annual climate change are typically more important than steady state responses in determining short term variability in the isotopic composition of closed basin lake sediment (Steinman et al. In prep. a) (*see* Chapter 4). Over the long term however, transient responses combine to produce average isotopic values that are

primarily a function of mean state (i.e., the long term average) climate conditions and to a lesser extent the stochastic state of climate (Steinman et al. In prep. b) (*see* Chapter 5). This complexity in the lake-climate system creates a condition of equifinality where many possible climate solutions, or the lack of a unique climatic solution, exist for each observed sediment $\delta^{18}\text{O}$ value. To address the issue of equifinality Monte Carlo experiments were conducted as part of this study to produce a probabilistic, quantitative precipitation reconstruction.

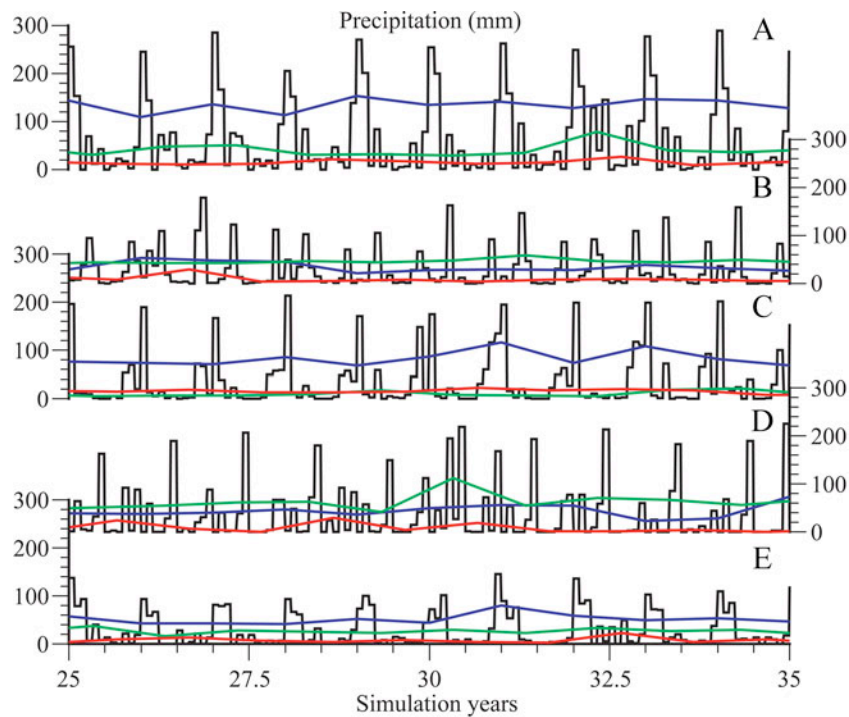


Figure 6.S3. Monthly precipitation data (coarse lines) applied in the Monte Carlo simulations. Each panel (A–E) depicts a sample of the random data produced during one simulation. Winter (November–February), spring (March–June) and summer (July–October) average monthly precipitation amounts are represented by blue, green, and red fine lines, respectively. $\delta^{18}\text{O}$ results for each simulation (A–E) are presented in Figure 6.S6.

To simulate lake hydrologic and isotopic responses to random climate variability, the model was forced using Gaussian white noise applied to monthly climate variables, namely precipitation (Figure 6.S3), temperature (Figure 6.S4) and relative humidity (Figure 6.S5). To

construct the random climate change algorithms, monthly variability in precipitation and temperature was characterized using continuous weather observations. For example, for each calendar month the average and standard deviation were calculated over the period of record (1900–2007 for precipitation and temperature, 1989–2007 for relative humidity). To simulate randomness in each month from year to year a statistical distribution algorithm was applied that produced continuous random numbers with an average and standard deviation equal to the values calculated for each calendar month using the 20th century datasets. A normal distribution was applied to define monthly temperature and relative humidity values, and a lognormal distribution was applied to define precipitation. The model maintained a logical relationship between precipitation, temperature, and relative humidity, whereby in months for which precipitation is higher than average and temperature is lower, relative humidity could not be lower than average, and vice versa. If such a scenario did occur, the algorithm applied a default relative humidity value that was as close as possible to the original, randomly selected value while satisfying the relative humidity logic.

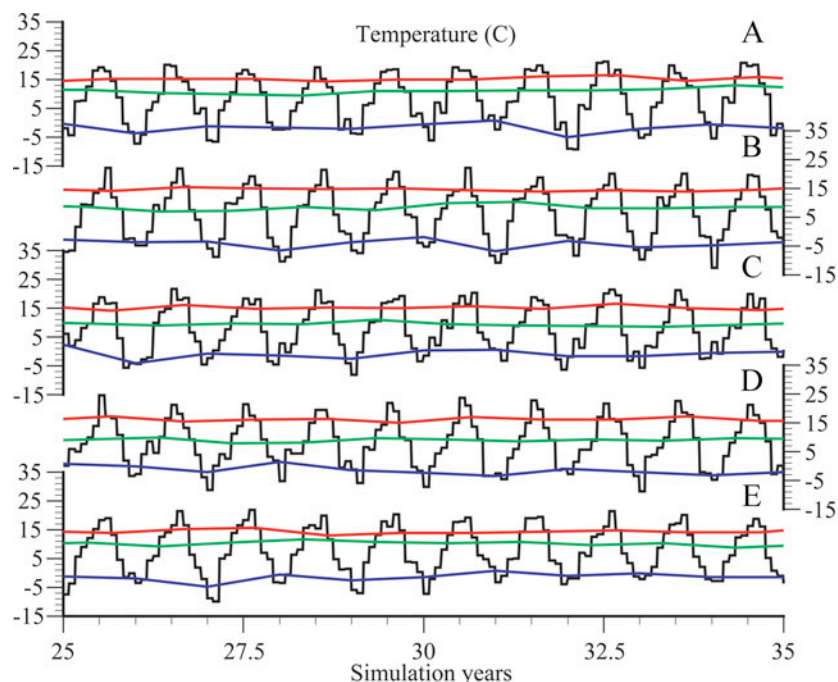


Figure 6.S4 Monthly temperature data (coarse lines) applied in the Monte Carlo simulations. Each panel (A–E) depicts a sample of the random data produced during one simulation. Winter (November–February), spring (March–June) and summer (July–October) average monthly temperatures are represented by blue, green, and red fine lines, respectively. $\delta^{18}\text{O}$ results for each simulation (A–E) are presented in Figure 6.S6.

To adequately address changes in seasonality, the model simulated mean changes in hydroclimatic conditions on a monthly basis. Prior to each simulation the model randomly selected an average value for each climate variable for each calendar month (within limits), and thereby established the baseline for random, interannual variance over the remainder of the simulation. The model generated the average monthly value for each simulation using an even distribution random number algorithm with established limits. These user defined limits, i.e., the domain of the Monte Carlo simulations, were carefully chosen to produce a realistic distribution of changes in mean climate values. Twenty year sections of climate data were analyzed over the 20th century to ensure that the mean climate value limits exceeded the observed values of the 20th century without being unrealistic in the context of likely climate variability over the past 1500 years. Based on these analyses, potential mean precipitation changes were set to range between

0 and 200%. Effectively, therefore, prior to each simulation the model adjusted the average monthly value of precipitation for each calendar month between 0 and 200%. If November and December precipitation averaged 50 mm and 60 mm over the 20th century, for example, the model selected an average precipitation amount of 0–100 mm for November and 0–120 mm for December. Similarly, average monthly temperature values were allowed to range between ± 2 °C, and average monthly relative humidity was allowed to change by $\pm 5\%$.

In all simulations, catchment and lake parameters such as soil available water capacity and outseepage (calculated as a linear function of volume) were held constant. Likewise, each simulation was conducted on a monthly time step over 60 years of which the first 40 were a model equilibration period and the remaining 20 years represented the period of analysis. The short residence time (~ 2.5 years) (Steinman et al. 2010a) of Castor Lake produces an isotopic memory effect that limits the influence of weather in any one particular year to approximately 10 years (Steinman et al. In prep. b) (*see* Chapter 5). Effectively, this means that the state of climate prior to 10 years in the past has no influence on current lake water isotopic values. A 20 year window of analysis was selected to ensure that the resulting average isotopic values from each simulation integrated as much of the past state of climate as possible and to strike a balance between temporal resolution and a lack of precision in results produced by interannual randomness in climate. Had from the final 10 years of each simulation been analyzed, added resolution would have been attained but precision would have been lost (and hence would have expanded the error in the final precipitation estimates) due simulated interannual randomness. Extending the analysis to 30 years or longer would have increased precision (and hence error would have been reduced) through smoothing of climate noise, but temporal resolution would

have been lost which would have compromised validation of the results through comparison to 20th century observations.

By averaging the late spring and summer model predicted $\delta^{18}\text{O}$ values, a single $\delta^{18}\text{O}$ value was produced for each year in the model simulations (Figure 6.S6). For each individual simulation the final 20 of these annual $\delta^{18}\text{O}$ values were averaged to produce the average 20 year $\Delta\delta^{18}\text{O}$ value applied in the regression analyses. The 20 year average of annual November through June precipitation was calculated for each simulation and related to the corresponding 20 year average $\Delta\delta^{18}\text{O}$ in the regression analysis (Figure 6.S7). Over 3000 simulations were conducted and then downsampled by eliminating values that fell outside the range of $\Delta\delta^{18}\text{O}$ values ($\sim \pm 1.6\text{‰}$) observed in the sediment record. To establish an even distribution within the observed range of $\Delta\delta^{18}\text{O}$ values, data were further downsampled on the basis of the normal distribution of simulation results. Specifically, the average number of samples falling within the ranges 1.6 to 1.5‰ and -1.5 to -1.6‰ were determined. Simulation results were then randomly removed from all other 0.1‰ intervals until the distribution of values between -1.6 and 1.6‰ was even. This was done to ensure that values more likely to be produced by the Monte Carlo simulations did not more heavily weight the resulting relationship between $\Delta\delta^{18}\text{O}$ values and precipitation. The final dataset included results from ~185 simulations.

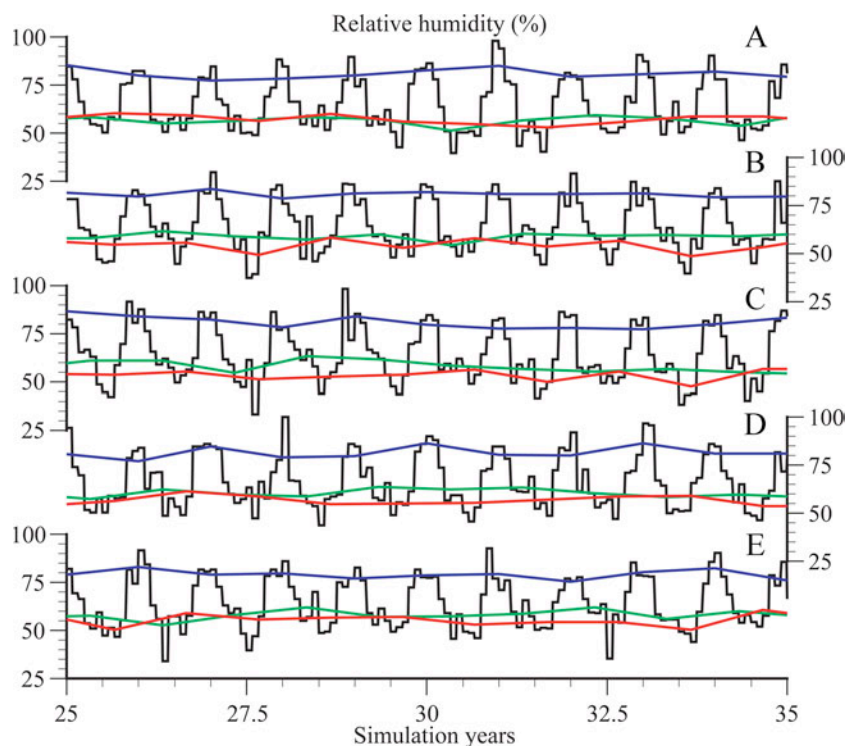


Figure 6.S5 Monthly relative humidity data (coarse lines) applied in the Monte Carlo simulations. Each panel (A–E) depicts a sample of the random data produced during one simulation. Winter (November–February), spring (March–June) and summer (July–October) average monthly relative humidity values are represented by blue, green, and red fine lines, respectively. $\delta^{18}\text{O}$ results for each simulation (A–E) are presented in Figure 6.S6.

6.3.11 Monte Carlo results and comparison to 20th century observations

A 2nd order polynomial regression was applied to the simulated $\Delta\delta^{18}\text{O}$ and annual Nov–June precipitation values (Figure 6.S7) and used to calculate precipitation on the basis of the sediment core $\Delta\delta^{18}\text{O}$ record. Model predicted precipitation values for the 20th century positively correlate to observations, with an R^2 value of 0.52 (Figure 6.S8). All observations fall within 95% prediction confidence limits. Some of the discrepancy between the observed and modeled values likely is due to age model errors in sediment core records, as well as sedimentation rate variance, which can lead to over- and under-representation of individual years in the sediment core record. Additional error in model predictions potentially lies in the outseepage

configuration used to describe Castor Lake groundwater throughflow (Steinman et al. In prep. c) (see Chapter 3). Further assessment of Castor Lake hydrology through direct observation (e.g., measurements of outseepage) will help to better characterize lake hydrologic and isotopic responses to hydroclimatic forcing and will thereby improve the accuracy and precision of future model based estimates of paleoprecipitation.

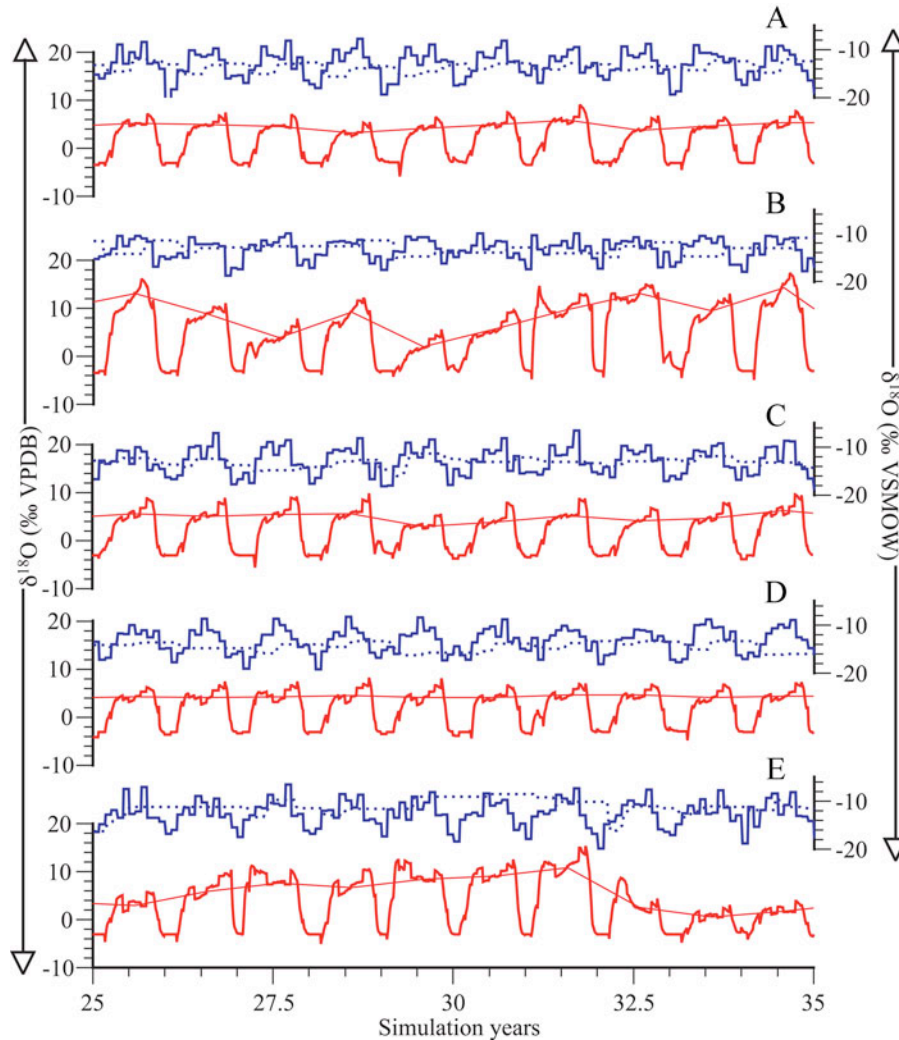


Figure 6.S6 $\delta^{18}\text{O}$ results from the Monte Carlo simulations. Modeled monthly (coarse red line) and summer average (June–September) (fine red line) $\Delta\delta^{18}\text{O}$ values are depicted with corresponding monthly precipitation (blue line) and source water (groundwater inflow + catchment runoff) $\delta^{18}\text{O}$ values (blue lines). Each panel (A–E) depicts a sample of the random data produced during one simulation.

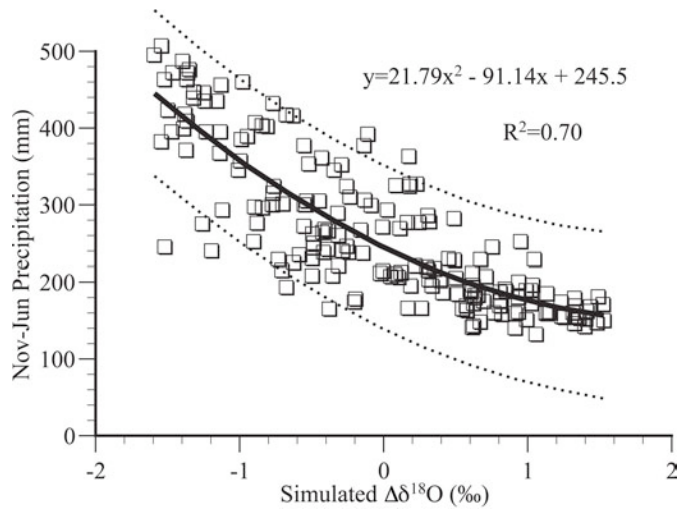


Figure 6.S7 Monte Carlo simulation results relating 20 year average $\Delta\delta^{18}\text{O}$ values to 20 year average winter/spring precipitation amounts (November–June). The 2nd order polynomial function and associated 95% confidence limits (dashed lines) was applied to the sediment core $\Delta\delta^{18}\text{O}$ record to produce the quantitative precipitation reconstruction.

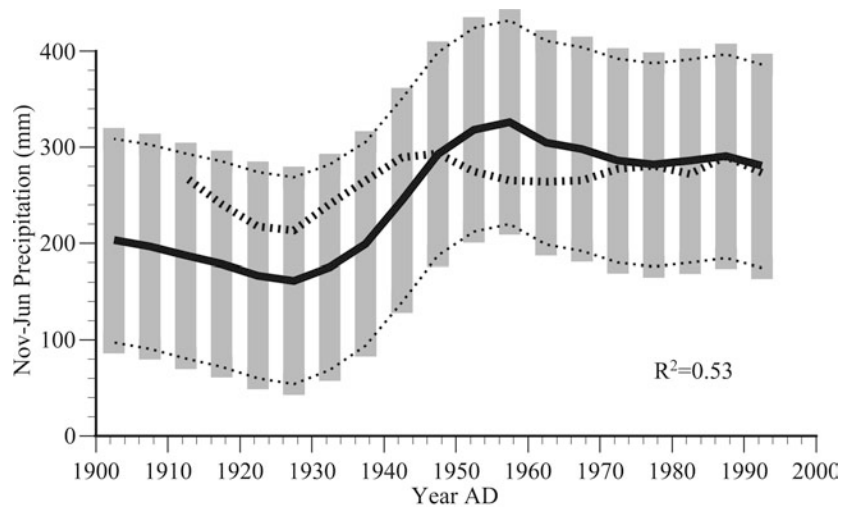


Figure 6.S8 20 year average observed (dashed line) and modeled (solid line) winter/spring precipitation for the Castor Lake region over the 20th century. Dashed lines and vertical gray lines depict estimated 95% confidence limits for the precipitation reconstruction. Note that observed values fall within the range of error for the model predictions.

BIBLIOGRAPHY

- Abbott, M.B., and T.W. Stafford. 1996. Radiocarbon geochemistry of ancient and modern Arctic lakes, Baffin Island. *Quaternary Res.* 45: 300–311.
- Almendinger, J. E. 1990. Groundwater control of closed-basin lake levels under steady-state conditions. *J. Hydrol.* 112: 293–318.
- Almendinger, J. E. 1993. A groundwater model to explain past lake levels at Parkers Prairie, Minnesota, USA. *Holocene* 3: 105–115, doi:10.1177/ 095968369300300202
- Appleby, P.G., and F. Oldfield. 1983. The assessment of ^{210}Pb data from sites with varying sediment accumulation rates. *Hydrobiologia* 103: 29–35.
- Araguás-Araguás, L., K. Froehlich, and K. Rozanski. 2000. Deuterium and oxygen-18 isotope composition of precipitation and atmospheric moisture. *Hydrol. Process.* 14: 1341–1355.
- Barnett, T., R. Malone, W. Pennell, D. Stammer, B. Semtner, and W. Washington. 2004. The effects of climate change on water resources in the west: Introduction and overview. *Climatic Change* 62: 1–11.
- Benson, L., L.D. White, and R. Rye. 1996. Carbonate deposition, Pyramid Lake Subbasin, Nevada: 4. Comparison of the stable isotope values of carbonate deposits (tufas) and the Lahontan lake-level record. *Palaeogeogr. Palaeocl.* 122: 45–76.
- Benson, L., M. Kashgarian, R. Rye, S. Lund, F. Paillet, J. Smoot, C. Kester, S. Mensing, D. Meko, and S. Lindström. 2002. Holocene multidecadal and multicentennial droughts affecting Northern California and Nevada. *Quaternary Sci. Rev.* 21: 659–682.

- Benson, L., and F. Paillet. 2002. HIBAL: a hydrologic-isotopic-balance model for application to paleolake systems. *Quaternary Sci. Rev.* 21: 1521–1539.
- Binford, M.W. 1990. Calculation and uncertainty of ^{210}Pb dates for PIRLA project sediment cores. *J. Paleolimnol.* 3: 253–267.
- Bokuniewicz, H.J. 1992. Analytical Descriptions of Subaqueous Groundwater Seepage. *Estuaries* 15: 458–464.
- Bowen, G.J., and J. Revenaugh. 2003. Interpolating the isotopic composition of modern meteoric precipitation. *Water Resour. Res.* 39: 1299. doi:10.1029/2003WR002086.
- Bowen, G. J., L. I. Wassenaar, and K. A. Hobson. 2005. Global application of stable hydrogen and oxygen isotopes to wildlife forensics. *Oecologia* 143: 337–348, doi:10.1007/s00442-004-1813-y.
- Bowen, G. J., and B. Wilkinson. 2002. Spatial distribution of $\delta^{18}\text{O}$ in meteoric precipitation. *Geology* 30: 315–318.
- Briffa, K.R. 2000. Annual climate variability in the Holocene: interpreting the message of ancient trees. *Quaternary Sci. Rev.* 19: 87–105.
- Bryson, R.A., and K.F. Hare. 1974. Climates of North America, p. 5–12. In H. E. Landsberg [ed.], *World survey of climatology*. Elsevier Scientific Publishing Company.
- Cane, M.A., A.C. Clement, A. Kaplan, Y. Kushnir, D. Pozdnyakov, R. Seager, S.E. Zebiak, and R. Murtugudde. 1997. Twentieth-century sea surface temperature trends. *Science* 275: 957–960. doi:10.1126/science.275.5302.957

- Cayan, D.R. 1996. Interannual climate variability and snowpack in the western United States. *J. Climate* 9: 928–948.
- Cayan, D.R., M.D. Dettinger, H.F. Diaz, N.E. Graham. 1998. Decadal variability of precipitation over western North America. *J. Climate* 11: 3148–3166.
- Cayan, D.R., K.T. Redmond, and L.G. Riddle. 1999. ENSO and hydrologic extremes in the western United States. *J. Climate* 12: 2881–2893.
- Cherkauer, D.S., Zager, J.P., 1989. Groundwater interaction with a kettle-hole lake: relation of observations to digital simulations. *Journal of J. Hydrol.* 109: 167–184.
- Clark, M.P., M.C. Serreze, and G.J. McCabe. 2001. Historical effects of El Niño and La Niña events on the seasonal evolution of the montane snowpack in the Columbia and Colorado River Basins. *Water Resour. Res.* 37: 741–757. doi: 10.1029/2000WR900305.
- Clement, A.C., R. Seager, M.A. Cane, and S.E. Zebiak. 1996. An ocean dynamical thermostat. *J. Climate* 9: 2190–2196.
- Cook, E.R., K.R. Briffa, D.M. Meko, D.A. Graybill, and G. Funkhouser. 1995. The 'segment length curse' in long tree-ring chronology development for palaeoclimatic studies. *Holocene* 5: 229–237.
- Cook., E.R., C. Woodhouse, D.M. Meko, and D.W. Stahle. 2004. Long-term Aridity Changes in the Western United States. *Science* 306: 1015–18.
- Cook, E.R., R. Seager, M.A. Cane, D.W. Stahle. 2007. North American drought: Reconstructions, causes, and consequences. *Earth-Sci. Reviews* 81: 93–134. doi:10.1016/j.earscirev.2006.12.002

- Craig, H., and L.I. Gordon. 1965. Isotopic oceanography: deuterium and oxygen 18 variations in the ocean and the marine atmosphere. *Marine Geochemistry Occasional Publication 3*: 277–374.
- Cross, S.L., P.A. Baker, G.O. Seltzer, S.C. Fritz, and R.B. Dunbar. 2001. Late Quaternary climate and hydrology of tropical South America inferred from an isotopic and chemical model of Lake Titicaca, Bolivia and Peru. *Quaternary Res.* 56: 1–9.
- Dettinger, M.D., D.R. Cayan, H.F. Diaz, D.M. Meko. 1998. North-south precipitation patterns in western North America on interannual-to decadal timescales. *J. Climatol.* 11: 3095–3111.
- Dincer, T. 1968. The use of oxygen 18 and deuterium concentrations in the water balance of lakes. *Water Resour. Res.* 4: 1289–1306.
- Donovan, J. J., A. J. Smith, V. A. Panek, D. R. Engstrom, and E. Ito. 2002. Climate-driven hydrologic transients in lake sediment records: calibration of groundwater conditions using 20th Century drought. *Quat. Sci. Rev.* 21: 605–624.
- Gat, J. R. 1979. Environmental isotope balance of Lake Tiberias, p. 109–127. *In* *Isotopes in hydrology*. IAEA.
- Gat, J.R. 1995. Stable isotopes in fresh and saline lakes, p. 139–165. In A. Lerman, D. M. Imboden and J. R. Gat [eds.], *Physics and chemistry of lakes*. Springer-Verlag.
- Gedalof, Z., D. L. Peterson, and N. J. Mantua. 2004. Columbia River flow and drought since 1750. *J. Am. Water Resour. As.* 40: 1579–1592.
- Genereux, D., and I. Bandopadhyay. 2001. Numerical investigation of lake bed seepage patterns: effects of porous medium and lake properties. *J. Hydrol.* 241: 286–303.

- Gibson, J.J., E.E. Prepas, and P. McEachern. 2002. Quantitative comparison of lake throughflow, residency, and catchment runoff using stable isotopes: modeling and results from a regional survey of Boreal lakes. *J. Hydrol.* 262: 128–144.
- Gonfiantini, R. 1986. Environmental isotopes in lake studies, p. 113–168. In P. Fritz and J. C. Fontes [eds.], *Handbook of environmental geochemistry*, vol. 2: The terrestrial environment. B. Elsevier Science Publishing Company.
- Goosse, H., E. Cressin, A. de Montety, M.E. Mann, H. Renssen, and A. Timmermann. 2010. Reconstructing surface temperature changes over the past 600 years using climate model simulations with data assimilation. *J. Geophys. Res.* 115: D09108. doi:10.1029/2009JD012737
- Goosse, H., H. Renssen, A. Timmermann, R.S. Bradley, and M.E. Mann. 2006. Using paleoclimate proxy-data to select optimal realizations in an ensemble of simulations of the climate of the past millennium. *Clim. Dynam.* 27: 165–184. doi: 10.1007/s00382-006-0128-6
- Hammarlund, D., S. Björck, B. Bucharadt, C. Israelson, and C. Thomsen. 2003. Rapid hydrological changes during the Holocene revealed by stable isotope records of lacustrine carbonates from Lake Igelsjön, southern Sweden. *Quaternary Sci. Rev.* 22: 353–370.
- Held, I.M., and B.J. Soden. 2006. Robust responses of the hydrological cycle to global warming. *J. Climate* 19: 5686–5699.
- Henderson, A.K., and B.N. Shuman. 2009. Hydrogen and oxygen isotopic compositions of lake water in the western United States. *Geol. Soc. Am. Bull.* 121: 1179–1189.
- Hodell, D.A., C.L. Schelske, G.L. Fahnenstiel, and L.L. Robbins. 1998. Biologically induced calcite and its isotopic composition in Lake Ontario. *Limnol. Oceanogr.* 43: 187–199.

- Horita, J., and D. Wesolowski. 1994. Liquid-vapour fractionation of oxygen and hydrogen isotopes of water from the freezing to the critical temperature. *Geochim. Cosmochim. Ac.* 47: 3425–3437.
- Hostetler, S. W., and P. J. Bartlein. 1990. Simulation of lake evaporation with application to modeling lake variations of Harney-Malheur Lake, Oregon. *Water Resour. Res.* 26: 2603–2612.
- Hostetler, S., and L. Benson. 1990. Paleoclimatic implications of the high stand of Lake Lahontan derived from models of evaporation and lake level. *Clim. Dynam.* 4: 207–217.
- Hostetler, S.W., and L.V. Benson. 1994. Stable isotopes of oxygen and hydrogen in the Truckee River-Pyramid Lake surface-water system. 2. A predictive model of $\delta^{18}\text{O}$ and $\delta^2\text{H}$ in Pyramid Lake. *Limnol. Oceanogr.* 39: 356–364.
- Hughes, M. 2002. Dendrochronology in climatology – the state of the art. *Dendrochronologia* 20: 95–116.
- Johnson, D. L., and D. Watson-Stegner. 1987. Evolution model of pedogenesis. *Soil Sci.* 143: 349–366.
- Jones, M.D., and J. Imbers. 2010. Modeling Mediterranean lake isotope variability. *Global Planet. Change* 71: 193–200.
- Jones, M. D., M. J. Leng, N. Roberts, M. Turkes, and R. Moyeed. 2005. A coupled calibration and modeling approach to the understanding of dry-land lake oxygen isotope records. *J. Paleolimnol.* 34: 391–411.
- Jones, M. D., C. N. Roberts, and M. J. Leng. 2007. Quantifying climatic change through the last glacial-interglacial transition based on lake isotope palaeohydrology from central Turkey. *Quaternary Res.* 67: 463–473.

- Jones, P.D., K.R. Briffa, T.J. Osborn, J.M. Lough, T.D. van Ommen, B.M. Vinther, J. Luterbacher, E.R. Wahl, F.W. Zwiers, M.E. Mann, G.A. Schmidt, C.M. Ammann, B.M. Buckley, K.M. Cobb, J. Esper, H. Goosse, N. Graham, E. Jansen, T. Kiefer, C. Kull, M. Küttel, E. Mosley-Thompson, J.T. Overpeck, N. Riedwyl, M. Schulz, A.W. Tudhope, R. Villalba, H. Wanner, E. Wolff, and E. Xoplaki. 2009. High-resolution palaeoclimatology of the last millennium: a review of current status and future prospects. *Holocene* 19: 3–49. doi: 10.1177/0959683608098952
- Katz, R. W. 1996. Use of conditional stochastic models to generate climate change scenarios. *Climatic Change* 32: 237–255.
- Kelts, K., and K.J. Hsu. 1978. Freshwater carbonate sedimentation. In Lerman, A. (Ed.), *Lakes – Chemistry, Geology, Physics*. New York, Heidelberg, Berlin, pp. 295–323.
- Kim, S., and J.R. O’Neil. 1997. Equilibrium and nonequilibrium oxygen isotope effects in synthetic carbonates. *Geochim. Cosmochim. Ac.* 61: 3461–3475.
- Knapp, P. A., P. T. Soulé, and H. D. Grissino-Mayer. 2004. Occurrence of sustained droughts in the interior Pacific northwest (A.D. 1733–1980) inferred from tree-ring data. *J. Climate*. 17: 140–150.
- Knutson, T.R., and S. Manabe. 1995. Time-mean response over the tropical Pacific to increased CO₂ in a coupled ocean-atmosphere model. *J. Climate* 8: 2181–2199.
- Koschel, R. 1997. Structure and function of pelagic calcite precipitation in lake ecosystems. *Verh. Internat. Verein. Limnol.* 26: 343–349.
- Koschel, R., J. Benndorf, G. Proft, and F. Recknagel. 1983. Calcite precipitation as a natural control mechanism of eutrophication. *Arch. Hydrobiol.* 98: 380–408.

- Leng, M., P. Barker, P. Greenwood, N. Roberts, and J. Reed. 2001. Oxygen isotope analysis of diatom silica and authigenic calcite from Lake Pinarbasi, Turkey. *J. Paleolimnol.* 25: 343–349.
- Leng, M.J., and J.D. Marshall. 2004. Paleoclimate interpretation of stable isotope data from lake sediment archives. *Quaternary Sci. Rev.* 23: 811–831.
- Mann, M.E., M.A. Cane, S.E. Zebiak, and A. Clement. 2005. Volcanic and solar forcing of the tropical Pacific over the past 1000 years. *J. Climate* 18: 447–456.
- Mann, M.E., Z. Zhang, S. Rutherford, R.S. Bradley, M.K. Hughes, D. Shindell, C. Ammann, G. Faluvegi, and F. Ni. 2009. Global signatures and dynamical origins of the Little Ice Age and Medieval Climate Anomaly. *Science* 326: 1256–1260.
- Mantua, N. J., and S. R. Hare. 2002. The Pacific decadal oscillation. *J. Oceanogr.* 58: 33–44.
- Mantua, N. J., S.R. Hare, Y. Zhang, J.M. Wallace, and R.C. Francis. 1997. A Pacific decadal climate oscillation with impacts on salmon. *Bull. Amer. Meteor. Soc.* 78: 1069–1079.
- McBride, M.S., H.O. Pfannkuch. 1975. The distribution of seepage within lake beds. *U.S. Geological Survey Journal of Research* 3: 505–512.
- McCabe, G.J., M.A. Palecki, and J.L. Betancourt. 2004. Pacific and Atlantic Ocean influences on multidecadal drought frequency in the United States. *P. Natl. Acad. Sci USA* 101: 4136–4141.
- Mearns, L. O., C. Rosenzweig, and R. Goldberg. 1997. Mean and variance change in climate scenarios: Methods, agricultural applications, and measures of uncertainty. *Climatic Change* 35: 367–396.

- Meehl, G.A., et al. 2007. Global Climate Projections, in *Climate Change 2007: The Physical Science Basis. Contribution of Working Group I to the Fourth Assessment Report of the Intergovernmental Panel on Climate Change*, edited by S. Solomon, et al., pp. 747–845, Cambridge University Press, Cambridge, United Kingdom and New York, NY, USA.
- Merlivat, L., and J. Jouzel. 1979. Global climatic interpretation of the deuterium-oxygen 18 relationship for precipitation. *J. Geophys. Res.* 84: 5029–5033.
- Merryfield, W.J. 2006. Changes to ENSO under CO₂ doubling in a multimodel ensemble. *J. Climate* 19: 4009–4027.
- Meyers, P.A. 1997. Organic geochemical proxies of paleoceanographic, paleolimnologic, and paleoclimatic processes. *Org. Geochem.* 27: 213–250.
- Mote, P.W. 2003. Trends in snow water equivalent in the Pacific Northwest and their climatic causes. *Geophys. Res. Lett.* 30: 1601–1604.
- Mullineaux, D.R. 1986. Summary of pre-1980 tephra-fall deposits erupted from Mount St. Helens, Washington State, USA. *B. Volcanol.* 48: 17–26.
- Nelson, D.B., M.B. Abbott, B.A. Steinman, P.J. Polissar, N.D. Stansell, J.D. Ortiz, M.F. Rosenmeier, B.P. Finney, and J. Riedel. 2011. A 6,000 year lake record of drought from the Pacific Northwest. *P. Natl. Acad. Sci USA*. doi/10.1073/pnas.1009194108
- Newman, M., G.P. Compo, and M.A. Alexander. 2003. ENSO-forced variability of the Pacific Decadal Oscillation. *J. Climate* 16: 3853–3857.
- Oldfield, F., and P.G. Appleby. 1984. Empirical testing of ²¹⁰Pb-dating models for lake sediments, p. 93–124. In E.Y. Haworth and W.G. Lund [eds.], *Lake Sediments and Environmental History*. University of Minnesota Press, Minneapolis, Minnesota.

- Palacios-Fest, M.R., A.L. Carreño, J.R. Ortega-Ramirez, and G. Alvarado-Valdéz. 2002. A paleoenvironmental reconstruction of Laguna Babicora, Chihuahua, Mexico based on ostracode paleoecology and trace element shell chemistry. *J. Paleolimnol.* 27: 185–206.
- Palmer, W.C. 1965. Meteorological drought. Weather Bureau Research Paper 45. U. S. Department of Commerce, Washington, DC.
- Pfannkuch, H.O., T.C. Winter. 1984. Effect of anisotropy and groundwater system geometry on seepage through lake beds: 1. Analog and dimensional analysis. *J. Hydrol.* 75: 213–237.
- Pham, S. V., P. R. Leavitt, S. McGowan, B. Wissel, and L. I. Wassenaar. 2009. Spatial and temporal variability of prairie lake hydrology as revealed using stable isotopes of hydrogen and oxygen. *Limnol. Oceanogr.* 54: 101–118.
- Phillips, J. D. 1993. Progressive and regressive pedogenesis and complex soil evolution. *Quaternary Res.* 40: 169–176.
- Raidt, H., R. Koschel. 1988. Morphology of calcite crystals in hardwater lakes. *Limnologica* 19: 3–12.
- Reimer, P.J., M.G.L. Baillie, E. Bard, A. Bayliss, J.W. Beck, C.J.H. Bertrand, P.G. Blackwell, C.E. Buck, G.S. Burr, K.B. Cutler, P.E. Damon, R.L. Edwards, R.G. Fairbanks, M. Friedrich, T.P. Guilderson, A.G. Hogg, K.A. Hughen, B. Kromer, F.G. McCormac, S.W. Manning, C.B. Ramsey, R.W. Reimer, S. Remmele, J.R. Southon, M. Stuiver, S. Talamo, F.W. Taylor, J. van der Plicht, and C.E. Weyhenmeyer. 2004. IntCal04 Terrestrial radiocarbon age calibration, 26 – 0 ka BP. *Radiocarbon* 46: 1029–1058.
- Richardson, C. W. 1981. Stochastic simulation of daily precipitation, temperature, and solar radiation. *Water Resour. Res.* 17: 182–190.

- Ricketts, R.D., and T.C. Johnson. 1996. Climate change in the Turkana basin as deduced from a 4000 year long $\delta^{18}\text{O}$ record. *Earth Planet. Sc. Lett.* 142: 7–17.
- Roberts, N., M. D. Jones, A. Benkaddour, W. J. Eastwood, M. L. Filippi, M. R. Frogley, H. F. Lamb, M. J. Leng, J. M. Reed, M. Stein, L. Stevens, B. Valero-Garcés, and G. Zanchetta. 2008. Stable isotope records of Late Quaternary climate and hydrology from Mediterranean lakes: the ISOMED synthesis. *Quaternary Sci. Rev.* 27: 2426–2441.
- Rosenberry, D. O., T. C. Winter, D. C. Buso, and G. E. Likens. 2007a. Comparison of 15 evaporation methods applied to a small mountain lake in the northeastern USA. *J. Hydrol.* 340: 149–166.
- Rosenberry, D. O., T. C. Winter, D. C. Buso, and G. E. Likens. 2007b. Reply to comment by J. Szilagyi on “Comparison of 15 evaporation methods applied to a small mountain lake in the northeastern USA” [*J. of Hydrol.* 340 (3–4) (2007) 149–166]. *J. Hydrol.* 348: 566–567, doi:10.1016/j.jhydrol.2007.09.050.
- Rosenmeier, M. F., M. Brenner, D. A. Hodell, J. B. Martin, and M. W. Binford. In press. Quantitative assessments of Holocene environmental change in Petén, Guatemala: Predictive models of catchment hydrology and lake water $\delta^{18}\text{O}$ values. *Quaternary Res.*
- Rowe, H.D., and R.B. Dunbar. 2004. Hydrologic-energy balance constraints on the Holocene lake-level history of lake Titicaca, South America. *Clim. Dynam.* 23: 439–454, doi:10.1007/s00382-004-0451-8.
- Rozanski, K., L. Araguás-Araguás, and R. Gonfiantini. 1992. Relation between long-term trends of oxygen-18 isotope composition of precipitation and climate. *Science* 258: 981–985.
- Sacks, L. A. 2002. Estimating ground-water inflow to lakes in central Florida using the isotope mass-balance approach. U.S. Geological Survey Water Resources Investigations Report 02-4192.

- Schelske, C.L., A. Peplow, M. Brenner, and C.N. Spencer. 1994. Low-background gamma counting: applications for ^{210}Pb dating of sediments. *J. Paleolimnol.* 10: 115–128.
- Shapley, M.D., E. Ito, and J.J. Donovan. 2005. Authigenic calcium carbonate flux in groundwater-controlled lakes: Implications for lacustrine paleoclimate records. *Geochim. Cosmochim. Ac.* 69: 2517–2533.
- Shapley, M.D., E. Ito, and J.J. Donovan. 2008. Isotopic evolution and climate paleorecords: modeling boundary effects in groundwater-dominated lakes. *J. Paleolimnol.* 39: 17–33.
- Shapley, M.D., E. Ito, and J.J. Donovan. 2009. Lateglacial and Holocene hydroclimate inferred from a groundwater flow-through lake, Northern Rocky Mountains. *Holocene* 19: 523–535.
- Shaw, R.D., E.E. Prepas. 1990a. Groundwater-lake interactions 1. Accuracy of seepage meter estimates of lake seepage. *J. Hydrol.* 119: 105–120.
- Shaw, R.D., Prepas, E.E., 1990b. Groundwater-lake interactions 2. Nearshore seepage patterns and the contribution of groundwater to lakes in central Alberta. *J. Hydrol.* 119: 121–136.
- Smith, A. 1993. Lacustrine ostracodes as hydrochemical indicators in lakes of the north-central United States. *J. Paleolimnol.* 8: 121–134.
- Smith, A. J., J. J. Donovan, E. Ito, and D. R. Engstrom. 1997. Ground-water processes controlling a prairie lake's response to middle Holocene drought. *Geology* 25: 391–394.
- Smith, A. J., J. J. Donovan, E. Ito, D. R. Engstrom, and V. A. Panek. 2002. Climate-driven hydrologic transients in lake sediment records: multiproxy record of mid-Holocene drought. *Quat. Sci. Rev.* 21: 625–646.

- Sondi, I., and M. Juracic. 2010. Whiting events and the formation of aragonite in Mediterranean karstic marine lakes: new evidence on its biologically induced inorganic origin. *Sedimentology*. 57: 85–95.
- Steinman, B.A., M.F. Rosenmeier, M.B. Abbott, and D.J. Bain. 2010a. The isotopic and hydrologic response of small, closed-basin lakes to climate forcing from predictive models: Application to paleoclimate studies in the upper Columbia River basin. *Limnol. Oceanogr.* 55: 2231–2245.
- Steinman, B.A., M.F. Rosenmeier, and M.B. Abbott. 2010b. The isotopic and hydrologic response of small, closed-basin lakes to climate forcing from predictive models: Simulations of stochastic and mean state precipitation variations. *Limnol. Oceanogr.* 55: 2246–2261.
- Steinman, B.A., M.B. Abbott, M.F. Rosenmeier, and D.B. Nelson. In preparation a. Small lake isotopic and hydrologic responses to 20th century climate variability: Comparison of observed and modeled sediment core oxygen isotope records and lake level variations. *Limnol. Oceanogr.*
- Steinman, B.A., M.B. Abbott, and M.F. Rosenmeier. In preparation b. Small lake isotopic and hydrologic responses to 20th century climate variability: Simulations of mean state and stochastic climate variations with non-constant initial conditions. *Limnol. Oceanogr.*
- Steinman, B.A., D.J. Bain, M.B. Abbott, and M.F. Rosenmeier. In preparation c. Hydrologic and isotope mass balance model simulations of lake outseepage and implications for lake responses to hydroclimatic variations. *J. Hydrol.*
- Stuiver, M., P.J. Reimer, and T.F. Braziunas. 1998. High-precision radiocarbon age calibration for terrestrial and marine samples. *Radiocarbon* 40: 1127–1151.

- Thompson, J.B., S. Schultze-Lam, T.J. Beveridge, and D.J. Des Marais. 1997. Whiting events: Biogenic origin due to the photosynthetic activity of cyanobacterial picoplankton. *Limnol. Oceanogr.* 42: 133–141.
- United States Geological Survey. 1981. “Riverside, Washington” [map]. 1:24,000. 7.5 minute series. United States Geological Survey. <http://rocky.ess.washington.edu/data/raster/drg/okanogan/index.html>
- Valiantzas, J.D. 2006. Simplified versions for the Penman evaporation equation using routine weather data. *J. Hydrol.* 331: 690–702.
- Vassiljev, J., S.P. Harrison, and A. Haxeltine. 1995. Recent lake-level and outflow variations at Lake Viljandi, Estonia: validation of a coupled lake-catchment modeling scheme for climate change studies. *J. Hydrol.* 170: 63–77.
- Vassiljev, J. 1998. The simulated response of lakes to changes in annual and seasonal precipitation: implication for Holocene lake-level changes in northern Europe. *Clim. Dynam.* 14: 791–801, doi:10.1007/s003820050255
- Vecchi, G.A., A. Clement, and B.J. Soden. 2008. Examining the tropical Pacific’s response to global warming. *Eos* 89(9): 26.
- Verdon, D.C., S.W. Franks. 2006. Long-term behavior of ENSO: Interactions with the PDO over the past 400 years inferred from paleoclimate records. *Geophys. Res. Lett.* 33: L06712.
- Vogt, H. J. 1976. Separation of isotopes in the evaporation of water. Staatsexamensarbeit, Universität Heidelberg.
- von Grafenstein, U., H. Erlernkeuser, and P. Trimborn. 1999. Oxygen and carbon isotopes in modern fresh-water ostracod valves: assessing vital offsets and autecological effects of interest for paleoclimate studies. *Palaeogeogr. Palaeoclimatol.* 148: 133–152.

Zebiak, S.E., and M.A. Cane. 1987. A model El Niño/Southern Oscillation. *Mon. Wea. Rev.* 115: 2262–2278.

Zhou, G., and Y. Zheng. 2003. An experimental study of oxygen isotope fractionation between inorganically precipitated aragonite and water at low temperature. *Geochim. Cosmochim. Ac.* 67: 387–399.